Understanding and Prediction of Stable Atmospheric Boundary Layers over Land

G.J. Steeneveld

Promotor:

Prof. dr. A.A.M. Holtslag   Hoogleraar in de Meteorologie,

Wageningen Universiteit

Co-promotor:

Dr. ir. B.J.H. van de Wiel   Wetenschappelijk onderzoeker,

Leerstoelgroep Meteorologie en Luchtkwaliteit,

Wageningen Universiteit

Samenstelling promotiecommissie:

Dr. A.C.M. Beljaars   ECMWF, Reading, Engeland

Prof. dr. ir. B.J.J.M. van den Hurk Universiteit Utrecht, KNMI

Prof. dr. M.C. Krol   Wageningen Universiteit, Stichting voor

Ruimteonderzoek Nederland

Prof. dr. G. Svensson   Stockholm Universiteit, Zweden

Understanding and Prediction of Stable Atmospheric Boundary Layers over Land

G.J. Steeneveld

Voorwoord

Daar is-ie dan, het eerste MAQ proefschrift uit de "netkous", de koosnaam voor ons nieuwe Atlasgebouw. Na vele uren van schrijven, knippen, plakken, opmaken en heropmaken is het dan eindelijk gereed.

Allereerst wil ik mijn promotor en initiatiefnemer voor dit promotieonderzoek Bert Holtslag bedanken voor zijn stimulerende vragen, ideeën en discussies. Vooral als je weer eens terug-kwam van een conferentie, stond mijn computer daarna snel te loeien om weer een nieuw idee uit te werken, of weer nieuwe berekeningen uit te voeren. Verder wil ik je bedanken voor het stroomlijnen van menig van mijn teksten en titels, wat de kwaliteit erg ten goede kwam. Toen dit promotieonderzoek begon, stond GABLS net in de kinderschoenen, maar door jouw initia-tief is het uitgegroeid tot een volwassen project en een mooi platform waarin het vakgroeps-werk kan worden (h)erkend.

Graag wil ik Bas van de Wiel bedanken voor zijn begeleiding van het promotieonderzoek. Jouw theoretische blik op de zaak en wetenschappelijke manier van schrijven geven altijd weer nieuw initiatief en scherpte aan het artikel.

Naast mijn directe begeleiders wil ik ook een aantal andere mensen bedanken met wie ik heb samengewerkt: Jordi Vila, Thorsten Mauritsen, Gunilla Svensson, Larry Mahrt, Sukanta Ba-su, Carmen Nappo, Cisco de Bruijn, Erik van Meijgaard, Thijs Heus, en de participanten in de GEWEX Atmospheric Boundary Layer Study (GABLS). En natuurlijk ben ik ook veel dank verschuldigd aan hen van wie ik metingen heb mogen 'lenen' (tsja ik ben zelf nu eenmaal niet zo handig/practisch): Oscar Hartogensis, Wouter Meijninger, de deelnemers in het CASES-99 experiment, Marku Kangas, Sylvain Joffre, Daan Vogelezang, Fred Bosveld, Bert Heusink-veld, Willy Hillen, Frits Antonysen, en Wim van den Berg. Verder verdienen Gerrie van den Brink en Kees van den Dries speciale waardering voor hun ondersteunende werk waardoor de vakgroep draait als een geoliede machine. Verder was de week niet compleet zonder Adrie's humoristische weekafsluiter.

Naast alle collega's wil ik ook de studenten (Marcel de Vries, Sander Pijlman, Marcel Wokke, Miranda Braam, Christine Groot Zwaaftink, Peter Baas en Bram van Kesteren) bedanken voor de leerzame samenwerking gedurende afstudeervakken en Bachelorafsluitingen.

Op deze plaats wil ik graag een aantal fondsen, instellingen en bedrijven bedanken voor de sponsoring door middel van reisbeurzen en andere subsidies. Hierdoor werd het bezoeken van cursussen, workshops en symposia aanzienlijk vergemakkelijkt. Het fonds Landbouw Export Bureau 1916/1918 heeft bijgedragen aan mijn bezoeken aan het ECMWF, het *17th Symposium on Boundary Layers and Turbulence* (San Diego) en de GABLS workshop in Stockholm.

Abstract

The main objective of this thesis is to contribute to further understanding of the stable boundary layer (SBL) over land, and its representation in atmospheric models. A SBL develops during night due to radiative surface cooling. Observations in the SBL, and their interpretation are difficult since many different physical processes can play a role. These processes are turbulent mixing, radiative transport, a coupling of the atmosphere with the vegetation and underlying soil, drainage flows, gravity waves, fog, and aspects of land use heterogeneity. Therefore, the understanding and the representation of the SBL in weather forecast and climate models is relatively poor, especially for calm nights.

In this thesis, a detailed column model of the atmosphere-land surface system is used to represent the atmospheric boundary layer over land and ice. As such, Large Eddy Simulation results and CASES-99 field observations are used for comparison and model evaluation. It turns out that the degree of land-surface coupling plays a key role in forecasting the SBL. Also, the sensitivity of the radiation transfer model to vertical resolution is examined. It is found that the SBL can be satisfactorily modelled (except for the low-level jet (LLJ) and intermittency of the turbulence) if the geostrophic wind speed, advection, subsidence, and vegetation and soil properties are known, and if relatively high vertical resolution is used near the surface (both in the soil and in the atmosphere).

Furthermore, the column model is used to study the nighttime 2 meter temperature increase due to additional CO_2 as function of wind speed. Observations show that the temperature increase is similar for windy and calm nights, although this is somewhat counterintuitive. Model results confirm that the temperature increase is indeed similar for windy and calm nights.

Next, an intercomparison study of limited area weather forecast models (COAMPS, MM5, HIRLAM) is performed for CASES-99. Large errors occur in the forecasted minimum temperature, SBL height and diurnal temperature range. Models that account for a realistic interaction with the land surface are advantageous. A sufficient large model domain is required to forecast the LLJ, and the forecasted surface cooling is very sensitive to the choice of the radiation scheme, especially for calm nights. Overall, it is possible to upgrade the model performance by using the lessons learnt with the column model.

This thesis also explores the role of orographic drag on the SBL. It is shown that orography of 10 m amplitude can generate gravity wave drag as large as the turbulent drag. Accounting for this in a forecast model gave the required cyclones filling, and a better forecast of the SBL structure and LLJ.

The thesis concludes with studies of the SBL height. Dimensional analysis is used to derive a new and robust formulation for the SBL height for a broad range of latitude and land-use conditions.

Contents

Chapter 1

Introduction and research questions

1.1 The role of the Atmospheric Boundary Layer in the land surface climate

This thesis deals with the subject of Understanding and Prediction of the Stable Atmospheric Boundary Layer over Land. In this general introduction first the main diurnal structure and development of the boundary layer and its role in the land-surface climate is sketched. Next, the most relevant processes in the boundary layer, our current understanding and the current status and problems of stable boundary-layer modeling are addressed. Finally the research questions are formulated.

The Atmospheric Boundary Layer (ABL) is the turbulent atmospheric layer adjacent to the Earth's surface that directly 'feels' the effect of the diurnal cycle at the surface. In principle, the ABL is a turbulent layer, characterized by irregular swirls of motions, so called eddies. Usually turbulence consists of many different eddy sizes superimposed on each other. These turbulent eddy motions are generated by two mechanisms: forced convection and buoyancy. Forced convection occurs when a flow travels over a rough area (with obstacles as grass, trees, cities), and is forced to pass these objects. Wind shear is the source for turbulence in this case. Buoyancy is the effect that warm air parcels have a smaller density than surrounding colder parcels, and therefore they start to drift upward. A characteristic property of turbulence is its effectiveness in transportation. Therefore, the ABL plays a vital role in the exchange of heat, momentum, moisture and natural (e.g. CO_2 and other greenhouse gases) and anthropogenic (e.g. pollutant emission) contaminants from the Earth's surface to the free atmosphere above the ABL.

In the daytime ABL, the sun heats the surface and the turbulence is dominantly driven by buoyancy. The boundary layer rapidly grows in the morning, and large convective eddies provide vigorous vertical mixing over typically 1-2 km depth.

In contrast, at night, buoyancy suppresses the turbulence intensity (sink), so only forced convection is a source of turbulence. Therefore, the nighttime ABL is much shallower, typically 100-200 m deep. However, during weak winds the suppression of turbulence by buoyancy is larger than the production by wind shear, so as a result the turbulence vanishes. Then, other transport processes than turbulence appear to govern the boundary-layer structure. These are radiation divergence (Ha and Mahrt, 2003), gravity waves (Nappo, 2002), drainage flows, the low-level jet (Garratt, 1985), fog (Teixeira and Miranda, 2001), and heat conduction from the soil (Holtslag and De Bruin, 1988).

Stable boundary layers prevail at night, but also during daytime in winter in mid-latitudes as well as in polar regions (Yagüe and Redondo, 1995), and during daytime over irrigated regions with advection. In addition to daily weather forecasts, the stable boundary layer is especially relevant for agriculture (minimum temperatures, surface frost, dew, fog), road traffic (fog and frost), air traffic (fog, low-level jet), and wind energy engineering. Bony et al. (2006) found that the polar regions, that are dominantly stably stratified during a long part of the season, warm 1.4-4 times faster than the global average, but a clear reason for this is unknown. Further research to stable boundary layer processes is thus necessary.

1.2 Stable boundary layer processes and their basic interactions

The stably stratified atmospheric boundary layer is governed by many physical processes, although their role is not a priori clear for each process until now, and some of them has been only qualitatively understood. Questions such as "What determines the nocturnal cooling timescale at 2 m?" have still not been completely answered (Pattantyús-Ábrahám and Jánosi, 2004). After sunset during clear skies, the Earth surface starts to cool due to net emission of long wave radiation. As such, the virtual potential temperature increases with height, which we call stable stratification. We will now briefly point out the relevant processes and explain their role (if understood).

-Turbulence
A key characteristic of the atmospheric boundary layer is the turbulent nature of the flow. A turbulent flow consists of swirls (eddies) of different scales. Large eddies absorb energy from the mean flow. These large eddies break up to smaller eddies and finally these eddies are so small that they are dissipated by molecular viscosity. All eddy motions of different length scales, from millimetres to the scale of the boundary-layer height, transport momentum, heat, humidity and contaminants. The turbulence intensity is influenced by wind shear and stratification (the Brunt-Väisälä frequency). During daytime the solar insolation heats the surface, and creates thermal instability and thermals. In contrast, in the SBL turbulence is suppressed by the stable stratification during calm nights. Then the turbulence is only produced by the mean wind shear; it is destroyed by buoyancy effects and (at a larger rate) viscous dissipation. As a result its energetics can be in a delicate and precarious balance, and extremely sensitive to changes in the mean wind profile (which shear is its energy source) and the mean temperature profile (which lapse rate severely limits its vertical motions). Not surprisingly, the similarity statements we can make about the structure of the PBL are then of different nature from those in a convective case (Wyngaard, 1985).

-Long-wave radiative transfer
Every object in nature that is above the absolute temperature minimum of 0 K, emits radiation. This also holds for the air in the ABL. The amount of radiation that is absorbed or emitted by an air layer depends on the emissivity of the air layer and its temperature. The emissivity depends on the concentration of absorbing gases such as water vapour, carbon dioxide, ozone. Due to temperature and emissivity differences between air layers, the emitted absorbed long wave radiation differs between the different layers, resulting in a net radiative flux. Especially in the stable boundary layer, the temperature gradients near the surface can become extremely large, and consequently the emitted radiation differs strongly between the different layers. The potential temperature at a certain level in the atmosphere is amongst others governed by the *divergence* of turbulent flux and the *divergence* of the net long wave radiative flux (Rodgers, 1967; Anfossi et al., 1976).

-Soil and vegetation

On clear nights with weak winds, the boundary-layer energy budget is governed by radiative cooling and the compensating soil heat flux. The soil heat flux depends on the thermal conductivity and on the temperature gradient in the soil. Local soil properties, such as density, soil material, and soil moisture content, determine the conductivity. These properties can vary substantially in time and in space. However, in atmospheric models the soil is assumed to be homogeneous. In this thesis we will also assume a homogeneous soil.

-Low-Level Jet

Above the stable boundary layer, the wind speed profile is in the idealized case characterized by a small air layer with wind speeds larger than the geostrophic wind speed in the free atmosphere above the ABL. During daytime, the mean flow is determined by the pressure gradient force, the Coriolis force and the friction that is generated by the ABL turbulence. However, during sunset the turbulent drag suddenly decreases and the equilibrium is disturbed. As a consequence, the air accelerates in response to the lack of friction in the ABL. The low-level jet can act as a second source (beyond the production by near surface wind shear) of turbulence in the stable boundary layer due to the shear above and below the wind speed maximum. However, the nocturnal jet can also be formed or influenced by baroclinicity (i.e. the change of the geostrophic wind with height due to horizontal temperature gradients).

-Gravity waves

A general property of stably stratified geophysical flows is their ability to support and propagate gravity waves (Nappo, 2002). Einaudi et al. (1978) define gravity waves as essentially coherent structures (mainly horizontally propagating) with a speed mostly much less than of the mean wind with horizontal scales less than 500 km and times scales less than a few hours. Gravity waves can be generated by a variety of features: sudden surface roughness changes, convection, and undulating topography, on which we will focus here. Indeed these wave (type) motions are widely observed during special observational campaigns (e.g. CASES-99, Newsom and Banta, 2003). Since gravity waves are able to redistribute energy and momentum, they are important in determining the vertical structure of the atmosphere and the coupling of mesoscale motions to the micro scale phenomena.

In essence, these waves transport positive momentum downwards. At a certain level, a so-called critical level can be reached (Fig. 1.1). Here the wind speed in the direction of the wave motion vanishes and consequently the wave breaks into turbulence. A similar mechanism can be present at the top of the stable boundary layer. In fact, this mechanism removes momentum from the mean flow, and thus acts as a drag on the flow (Chimonas and Nappo, 1989). Gravity waves can be generated by the topography of the land surface. These waves are standing waves, and the wave perturbations are not measured using standard eddy covariance technique, because the perturbations do not pass the sensor.
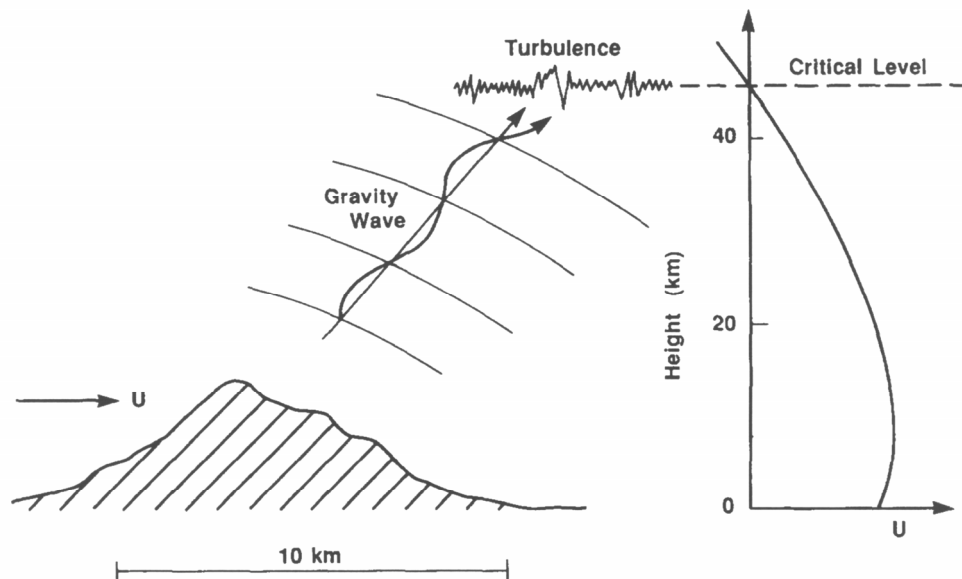
Figure 1.1: Illustration of propagating gravity waves caused by orography. At a critical level (where the wind speed is 0), the waves starts to break up into turbulence. From Chimonas and Nappo (1989).

-Fog/ Moist processes

When the surface cooling is strong enough, the air becomes saturated, and radiation fog starts to form over a certain layer. Next to the effect of the condensational heat release, the fog onset also rigorously modifies the radiative transport within the boundary layer and consequently the energy budgets of the boundary layer. The long-wave emission to space occurs at the top of the fog layer, which consequently cools rapidly. This destabilizes the fog layer, and the fog layer starts mixing. The final temperature profile follows the saturated-adiabatic lapse rate, with the surface now being warmer than the overlying atmosphere. Fog can prevail over large areas for a long time in polar regions.

-Aspects of heterogeneity

Land-surface heterogeneity (apart from orographic effects) can impact on the stable boundary layer. Natural landscapes are covered with patches of different vegetation and soil properties. Each of them will become in equilibrium with the local net radiative cooling. As such it might occur that differently stably stratified and unstably stratified patches exist next to each other. However, weather forecast models need to represent all patches within a single grid cell. Due to the non-linear nature of the turbulent exchange (e.g. Mahrt 1987; Ronda and De Bruin, 1999; Nakamura and Mahrt, 2006), grid cell averaging results in different and uncertain exchange coefficients compared to the local approach.

Secondly, differential cooling due to land surface inhomogeneities might generate small-scale baroclinicity and consequently mesoscale circulations. These cannot be resolved in Numerical Weather Prediction (NWP) models, although these flows can generate wind shear and as such additional turbulent exchange.

All small-scale processes as listed above need to be effectively represented in large-scale weather and climate models. It is clear that the parameterization of these processes is difficult. The present study focuses on a detailed modeling of the separate SBL regimes (according to the wind speed and surface cooling) and also aims to find the main physical cause of the transitions between the regimes (possibly in terms of external forcing parameters). To this end, we use a column-model with a detailed description of the transport by 1) turbulent exchange processes, 2) radiative processes and 3) soil-vegetation processes. This model has a parameterization of turbulence and the parameterization of radiative transport (emissivity approach). Furthermore a basic description is given for the atmosphere-vegetation/soil interaction by following the force-restore method (Deardorff, 1978) in combination with a canopy-resistance law. This description of the atmosphere-surface interaction will be improved by solving the diffusion equation for heat in the soil.

An important aspect of the research is the comparison of the model results with observational data. For this purpose an excellent dataset is provided by the CASES-99 field experiment. The extensive cooperative field experiment CASES-99 (Cooperative Atmospheric Surface-Exchange Study) was carried out by various groups (Poulos et al., 2002), including the Meteorology and Air Quality Group of Wageningen University (e.g. Hartogensis and De Bruin, 2005). CASES-99 was especially designed to tackle the vexing scientific problems in stable and/or nocturnal atmospheric conditions (Nappo and Johansson, 1998). The experiment lasted for a full month, under various meteorological conditions, which makes the experiment extremely suitable to study the development of different SBL regimes.

Fig. 1.2 illustrates the above mentioned processes, and their interactions. The main SBL forcings are the pressure gradient force, the Coriolis force, cloud cover, and free flow stability. For example, an increased geostrophic wind speed will enhance the turbulent mixing, and thus give reduced stratification (which can also occur due to incoming clouds). A reduced stratification will reduce the magnitude of the surface sensible heat flux in the weakly stable regime, and also limit the radiation divergence and thus the clear air radiative cooling. However, in the very stable regime, a reduction of the stratification might result in increased surface sensible heat flux. In both cases the surface energy budget is also altered, resulting in a modified soil heat flux. In the case of ceasing turbulence, the magnitude of the soil heat flux increases and vice versa. Moreover, this will alter the surface temperature and therefore the outgoing long wave radiation, and so the stratification.

In addition, increased geostrophic wind will under certain conditions increase the impact of wave drag due to the orography, which at first increases the cyclone filling and thus reduces the geostrophic wind. On the other hand, it will also enhance the low-level jet wind speed (see chapter 5). This consequently might result in additional downward turbulent mixing from the jet. This starts to impact on the stratification again.

The picture becomes even more complicated when radiation fog occurs. In principle, surface cooling can generate radiation fog when the air is sufficiently moist. However, with some wind, the latent heat flux will result in dew deposition, and heading off fog onset. Then in-

creased wind and turbulent mixing are necessary to transport moist air from above downwards for fog formation. Finally, when the fog becomes optically thick, the long wave cooling is at the top of the fog layer, instead of at the surface. Then the whole fog layer can become unstable with strong turbulent mixing. Overall it is clear that many complex interactions are present in the stable boundary layer.
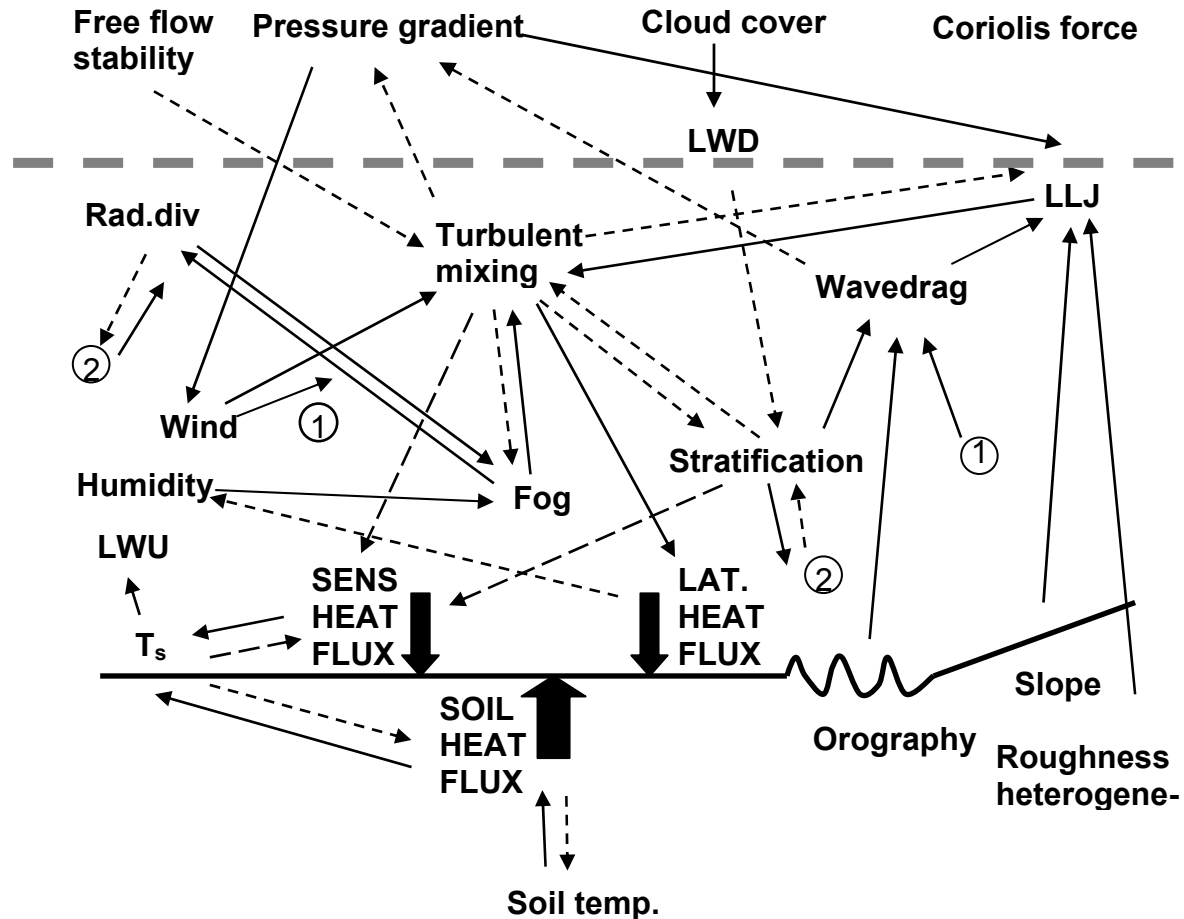
Figure 1.2: Overview of the relevant processes in the stable atmospheric boundary layer and their interactions. LWU and LWD are the upward and downward long-wave radiative fluxes, and LLJ the low-level jet. Positive interactions are full lines, negative feedbacks are dashed lines, and long dashed lines indicate a feedback that can either be positive or negative.

1.3 Problems in stable boundary layer modeling (partly adapted from Holtslag, 2006)

For various applications in meteorology, agriculture and hydrology there is need for a better understanding and a better description of the ABL and of the energy and mass balance at the earth surface under stable conditions. It is commonly known that, currently, the poor parameterizations of the stable boundary layer (SBL) in weather and climate prediction models (Beljaars and Viterbo, 1994, 1998) are a direct consequence of the poor knowledge of the physical processes in the SBL (Mahrt 1999, 2001; Derbyshire, 1999). One reason for this is that a multiplicity of processes in the SBL and their coupling.

At the same time it is realized that the current parameterisation of the SBL is still rather

poor, and that progress is slow (e.g. Beljaars and Holtslag, 1991; Holtslag and Boville, 1993; Beljaars and Viterbo, 1998). Unfortunately regional and global climate models show great sensitivity to the model formulation of mixing in stratified conditions. As an example, Viterbo et al. (1999) studied the vertical mixing in the ECMWF model in stable conditions. From two model runs with the same forcing conditions, but with (slightly) different stability functions in the mixing scheme, they noticed that differences in the mean winter temperatures at a height of 2 meters between the two model runs can be as large as 10 K over the continental areas!

In addition, King et al. (2001, 2007) found similar results between model runs for winter climate over Antarctica. Also over Europe, it was found that significant differences occur between the 2-meter temperatures of a 30-year regional climate simulation with observations for present day winter climate (e.g. Lenderink et al., 2003). It also appears that the magnitude of the diurnal temperature cycle is typically underestimated over land. These results are to a large extent influenced by the boundary-layer scheme in stable conditions though other atmospheric processes (like clouds and radiation) and land-surface processes obviously also play a role (Viterbo et al., 1999). On the topic of stable boundary-layer diffusion it can be concluded that further research is needed to get more insight in how diffusion should be present at the grid scale of a large-scale model. Terrain heterogeneity, subgrid-scale orography and the coupling with the subsoil through the land surface scheme are major issues (Beljaars, 2001). This will be studied here.

Climate models and weather forecast models need to make an overall representation of the smaller-scale boundary-layer and near surface processes. Besides the many different relevant processes in the stable boundary layer, the phenomenology of stable atmospheric boundary layers is also quite divers, e.g. shallow and deep boundary layers with continuous turbulence through most of their depth, and boundary layers with intermittent turbulence or even laminar flow. The small-scale processes influence the vertical and horizontal exchange of quantities between the surface and the atmosphere as well as the mixing in the atmosphere on a variety of scales. The overall representation of these processes and the related 'spatial averaging' is highly non-trivial due to the fact that there are many non-linear processes, and also because the environment has often a heterogeneous character on a variety of scales (Mahrt, 1987; Mahrt and Vickers, 2003). This normally is a motivation to allow for some 'enhanced-mixing' in models as compared with tower observations (e.g. Beljaars and Holtslag, 1991; Holtslag, 2006). Fig. 1.3 shows the model performance for the 500 hPa. geopotential height of the ECMWF model with enhanced mixing (28R1_oper) and a turbulence parameterization based on field observations (MO_ejav). The model performance on the synoptic scale improves when the non-physical enhanced mixing is applied. On the other hand it is realized that the performance on the boundary-layer scale is less with enhanced mixing, since in that case the SBL is typically too warm, the LLJ is too weak and the SBL too deep.

Another reason for having enhanced mixing is to prevent the models to enter an unphysical decoupled mode, which in turn may lead to run-away cooling close to the ground (Derbyshire, 1999; Steeneveld et al., 2006). In addition, it is known that turbulent mixing in stratified flow

has an inherent non-linear character and may, as such, trigger positive feedbacks. These positive feedbacks, in turn, may cause unexpected transitions between totally different SBL regimes (e.g. Derbyshire, 1999; Delage, 1997; Van de Wiel et al., 2002).

Furthermore, we should realize the balance in building models: How much weight should be given should one give to the surface energy budget, to horizontal resolution, to turbulence closure, to PBL depth, or to the effect of stability on PBL structure? This is a difficult question. The complexity of all these components should match. We should perhaps be surprised if the first generation of experimenters had been able to perceive much order in the structure of the stable PBL (Wyngaard, 1985).
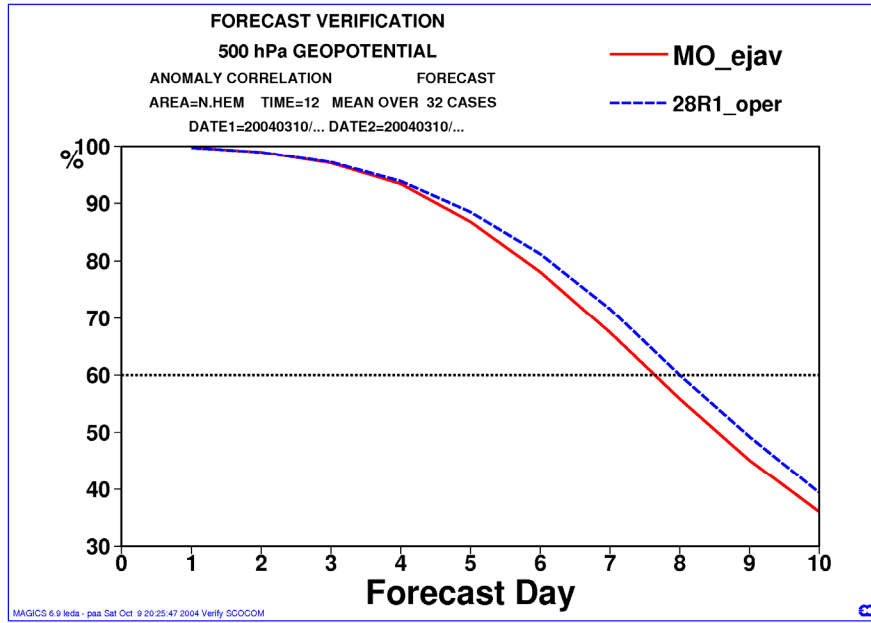
Figure 1.3: Anomaly correlation of the forecasted 500 hPa geopotential height in the ECMWF model for two different stable boundary-layer parameterizations (courtesy Anton Beljaars, ECMWF).

1.4 Research Tools

The research tool we use in this thesis is a single column model (see Fig 1.4). Such a model represents only one column of the atmosphere, and is a prime tool for parameterization development and testing. This model type was chosen because it has some clear advantages compared to alternative model approaches. Its main advantages are that parameterizations can be tested without interference/feedback from the dynamics or other model components such as in 3D forecast models, and thus the physics can be tested in an isolated environment. In addition, the model is computationally fast compared to three-dimensional models (e.g. weather forecast models). Finally, a column model was preferred to Large-Eddy Simulation (LES) because the LES only resolves large eddies which are in minority in the SBL (especially for low wind speed), and thus with LES we would rely on the subgrid model. A recent paper by Beare and MacVean (2004) showed that for a moderately stable boundary layer, the turbulence statistics in LES starts to converge around 2 meter grid size, and thus requires large computational resources. Thus LES is only useful for strong winds. In addition, existing LES models

lack a coupling with the land surface and also radiative divergence is neglected.
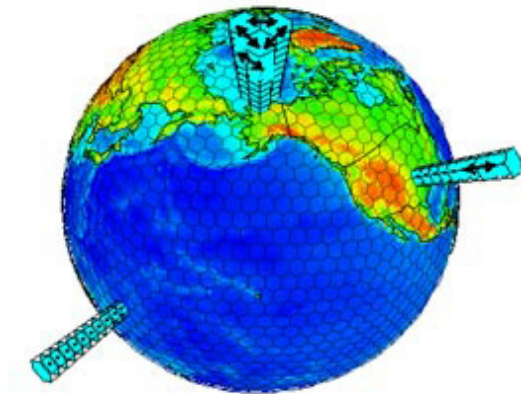
Figure 1.4: Illustration of a single column representation of the atmosphere.

1.5 GEWEX-Atmospheric Boundary-Layer Study (GABLS)

A part of the current work has been done in the context of GABLS, a project with the aim to improve the representation of the ABL in weather prediction and climate models. Within GABLS various single-column models from several research groups and operational weather centres, and ranging from first-order closure operational models to higher order closure research models, have done the same prediction task for a case with high wind speed. The results have been intercompared and also compared with LES simulations. These intercomparisons have the strong advantage that they improve the current knowledge in a way that could not be achieved by a single group.
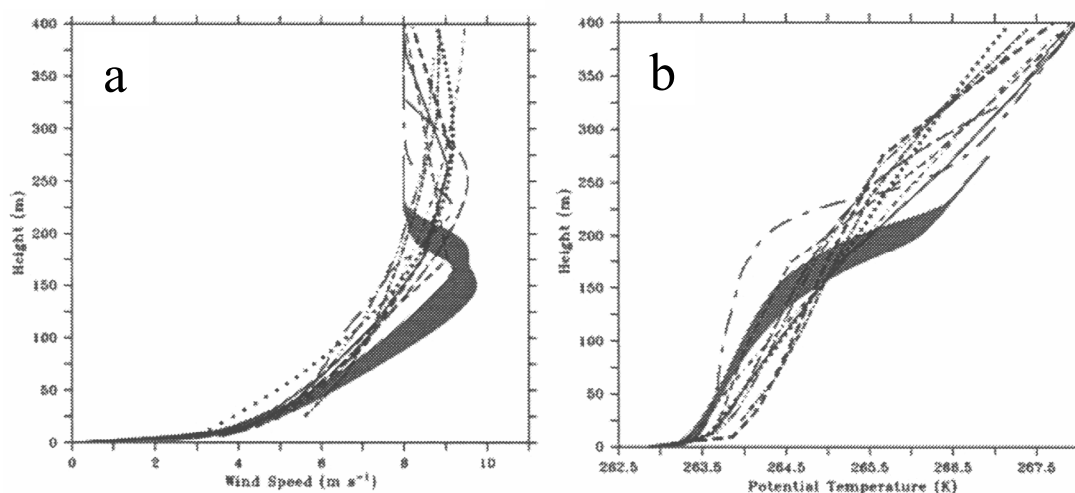
Figure 1.5: Model results (after 9 hours) for a stable boundary layer (a) potential temperature, b) wind speed as realized with several different parameterizations for the turbulent closure. The grey area indicates the ensemble mean results from LES (figures from Cuxart et al., 2006).

As an illustration of the GABLS results, Fig. 1.5 shows the model results for the first GABLS intercomparison study. This case is inspired by the LES study in Kosovic and Curry

(2000) for a SBL over ice, with a geostrophic wind of 8 ms^{-1} and prescribed surface cooling rate of 0.25 Kh^{-1}. It is immediately clear that (even for a prescribed surface temperature) the models results diverge strongly. Also, most models produce a deeper SBL than the LES, and the LLJ is absent, or too weak, or at a higher altitude. In Chapter 2, we explore this case study with a more realistic boundary condition, i.e. for solving the surface energy budget.

1.6 Research questions and contents

As sketched above, the prediction of the stable boundary layer in large-scale models has been a problematic feature for several decades. Despite the power of general circulation models in calculating the large-scale atmospheric flow, including advection and the effects of baro-clinicity, they use too coarse resolution (both horizontally and vertically) to give a proper representation of the important small-scale processes in the stable boundary layer. Consequently, the parameterizations for the SBL in these large-scale models do not work satisfactorily. Before implementation of new parameterizations for large-scale models, these parameterizations should be tested in column mode against field observations. We want to know if the poor performance of large-scale models in stable conditions is a direct consequence of a poor understanding of real physical processes or that it is caused (merely) by problems of model resolution/computational restrictions. To investigate whether the stable boundary-layer physics can be modeled fruitfully on a local scale, we simulate three diurnal cycles of the CASES-99 measurement campaign with a single-column model, with very high resolution. Therefore, these simulations can be seen as a proof of principle of the current understanding of stable boundary-layer modeling. Only with a proper simulation of the stable boundary layer without constraints on the resolution, we gain confidence in our ability to understand the SBL. This will be discussed in Chapter 3.

The confidence found in Chapter 3 was fair, and therefore we concluded that the physical processes at the local scale are well understood. Therefore an intercomparison and verification study with mesoscale models was conducted and reported in Chapter 4. Considering the physical processes, we shift to the following question: which physical process is lacking to forecast the stable boundary layer well in large-scale models? It is clear that the parameterized fluxes of momentum are highly uncertain, at one hand because of inaccurate boundary conditions (roughness length, subgrid orography parameter) and on the other hand due to uncertainties in the formulation for the stable boundary layer and subgrid orographic scheme. Quantitative verification on the level of momentum fluxes is virtually impossible (Beljaars, 2001). In Chapter 5, the role of orographically generated gravity wave drag is discussed as a possible missing mechanism in large-scale forecast models, and it will be shown that already small-scale orography can produce similar drag as the turbulence during calm nights.

Finally, air quality prediction model results strongly rely on the calculated stable boundary-layer height. Pollutions released in the SBL cannot be transported over the inversion height that acts as a lid on the boundary layer and inhibits exchange with the free atmosphere.

The other way around, contaminants released above the boundary-layer height are confined to the free atmosphere and cannot be mixed into the boundary layer. Proper SBL height prediction is therefore a key issue in air quality predictions. This height is in practice calculated from meteorological variables at the surface and from atmospheric soundings. A well established SBL height formula is evaluated against four data sets with a broad range of latitude, surface roughness and land use. Consequently, by means of dimensional analysis an alternative model for the stable boundary-layer height is developed and validated with observations.

Loosely speaking the thesis follows three paths. The first path considers the SBL from the one-dimensional perspective. The second path deals with the SBL in three-dimensional models, and the third part treats aspects and the modelling of the stable boundary-layer height. Thus the research questions and subquestions for this thesis are:

Main question 1:

To what extent do we understand the relative importance of the physical processes that govern the stable boundary layer, and can we model the stable boundary layer for different stability classes on the local scale?

Subquestions

- *To what extent is the stable boundary layer modelling sensitive to the coupling with the land surface?*
- *To what extent is stable boundary layer modelling sensitive to resolution in the atmosphere and in the soil.*

Main question 2:

Is evaluation and intercomparison of three-dimensional limited area models useful and what do we learn?

Subquestions

- *How can we transfer forecasting skill on the local scale to the 3D large scale? Do we miss a physical process?*
- *Which model descriptions are in favour for which atmospheric conditions?*

Main question 3:

How can we model the stable boundary-layer height?

Subquestions

- *How do diagnostic expressions for the stable boundary-layer height compare with observations, and can their performance be improved?*
- *How should the relevant length scales in the stable boundary layer be combined to obtain an equation for the stable boundary-layer height?*

Chapter 2

Modelling the Arctic stable boundary layer and its coupling to the surface

Abstract

The impact of coupling the atmosphere to the surface energy balance is examined for the stable boundary layer, as an extension of the first GABLS (GEWEX Atmospheric Boundary-Layer Study) one-dimensional model intercomparison. This coupling is of major importance for the stable boundary-layer structure and its development, because a coupling enables a realistic physical description of the interdependence of the surface temperature and the surface sensible heat flux. In the present case, the incorporation of a surface energy budget results in stronger cooling (surface decoupling), more stable and less deep boundary layers. The proper representation of this is a problematic feature in large-scale Numerical Weather Prediction and Climate models. To account for the upward heat flux from the ice surface beneath, we solve the diffusion equation for heat in the underlying ice as a first alternative. In that case, we find a clear impact of the vertical resolution in the underlying ice on the boundary-layer development: coarse vertical resolution in the ice results in stronger surface cooling than with fine resolution. Therefore, because of this impact on stable boundary layer development, the discretization in the underlying medium needs special attention in numerical modeling studies of the nighttime boundary layer. As a second alternative, a bulk conductance layer with stagnant air near the surface is added. The stable boundary-layer development appears to depend heavily on the bulk conductance of the stagnant air layer. This result re-emphasizes that the interaction with the surface needs special attention in stable boundary-layer studies. Furthermore, we perform sensitivity studies to atmospheric resolution, the length-scale formulation and the impact of radiation divergence on the stable boundary-layer structure for weak windy conditions.

Keywords: Decoupling, GABLS, Radiation divergence, Resolution, Stable boundary layer, Surface energy balance.

2.1 Introduction

In the first GABLS (GEWEX Atmospheric Boundary-Layer Study) model intercomparison study (Holtslag et al., 2003) a large variation for the outputs of single column models is found (Cuxart et al., 2006). As such, a simple stable boundary layer is studied with a prescribed constant cooling rate of -0.25 K h^{-1} at the surface. Such a forcing method for the stable boundary layer (SBL) is quite common (see e.g. Delage, 1974, 1997; Nieuwstadt and Driedonks, 1979; Kosovic and Curry, 2000). Alternatively, the surface turbulent heat flux $\overline{w'\theta'}_s$ can be prescribed (Galmarini et al., 1998, Viterbo et al., 1999). Although both methods are classical in the sense that they are easy to apply (especially in theoretical studies), there seems no direct physical justification for either one. In fact, the presence of feedbacks between the surface temperature (T_s), the surface sensible heat flux and the heat flux from the underlying medium towards the surface is essential (Derbyshire, 1999). Changes in surface-layer stability will affect the sensible heat flux through the stability functions, and consequently, the surface temperature will be affected through a coupled surface energy budget.

In the case of a surface energy budget, we can raise the question how the turbulent sensible heat flux in the SBL will react on surface cooling (Derbyshire, 1999; Delage et al., 2002). In fact the sensible heat flux may react in two different ways, corresponding to two regimes (compare also De Bruin, 1994 and Derbyshire, 1999):

- The weakly stable case, in which the sensible heat flux increases with stability. A sudden increase in stratification leads to a larger heat flux, opposing the increased stratification (negative feedback).

- The very stable case, in which an increase in stratification leads to a reduction of the sensible heat flux and therefore intensifying the increased stratification (positive feedback). This may lead to a collapse of turbulence so that the actual SBL decouples from the surface (ReVelle, 1993; Coulter and Doran, 2002; Delage et al., 2002; Van de Wiel et al., 2004).

Note that besides of this subdivision, alternative SBL classifications have been proposed by Beyrich (1997), Mahrt et al. (1998), Van de Wiel et al. (2003) and Mahrt and Vickers (2002) and others. At present no general classification picture of the SBL exists. Therefore, in the current work we use the pragmatic subdivision indicated above, i.e: weakly stable and very stable conditions.

From observations it is known that the SBL may either remain in a decoupled state, or recouple after a certain time, leading to turbulence of intermittent character (Van de Wiel et al., 2002a). From a modelling perspective, this very stable regime often leads to practical problems: for example large-scale atmospheric models tend to decouple and remain decoupled in an *unphysical sense* (e.g. Louis, 1979; Derbyshire, 1999). This can result in a serious cold model bias, especially during conditions where strong stratification exists for longer periods such as in the polar region in winter time (Viterbo et al., 1999). To circumvent this problem,

large-scale atmospheric models apply artificial enhanced mixing formulations for turbulence in the case of strong stability (e.g. Louis, 1979; Beljaars and Holtslag, 1991).

The importance of the surface-energy balance feedback was indicated by theoretical considerations above. The relevance of this feedback can also directly be inferred from typical observations of the surface temperature. Van de Wiel et al. (2003) illustrate from observations during the CASES-99 experiment that the surface temperature T_s, the turbulent heat flux and the soil heat flux may show simultaneous rapid changes during the night, revealing their interdependence. These fluctuations (with a rather high frequency compared to the daily cycle) are important for the dynamics of the SBL as a whole and cannot be modelled without taking into account the mutual interactions between the surface temperature, the sensible heat flux and the underlying soil. Derbyshire (1999) concludes: "Even the simplest valid analysis needs to couple the wind profile, the temperature profile and the surface heat budget".

Steeneveld et al. (2004) reveal that one-dimensional modelling results are largely improved as compared by detailed in situ observations when:

a) an accurate vegetation layer and fine soil discretization are applied, and

b) radiation divergence is included, at least for low geostrophic winds.

Fig. 2.1 shows results of the modelled vegetation temperature (full line) for three consecutive diurnal cycles during the CASES-99 experiment (Steeneveld et al., 2004). The first night is intermittent turbulent (moderate stable), the second continuously turbulent (weakly stable) and the third night is 'non-turbulent' (very stable), with suppressed turbulence. Thus we cover a wide range of stability conditions in this experiment. A clear agreement is found between the model results and the observations for these three different types of nights. This result is remarkable given the fact that the surface temperature is a difficult quantity to predict accurately with an off line model, especially for such a broad range of stability classes (Best, 1998). Additionally, we find that (not shown) the modelled potential temperature (θ) profiles also compare well with boundary-layer observations for these particular case studies.

The dash-dotted line in Fig. 2.1 shows the modelled surface temperature when the enhanced mixing approach is applied in the single column model, as is common practice in operational NWP and climate prediction models (e.g. Beljaars and Viterbo, 1998). Then the surface temperature is overestimated with about 5 K for the first two nights and the first half of the third night. Thus even from a practical point of view (as in NWP), the enhanced mixing approach is not appropriate over a large stability range. Fig. 2.1 shows that an accurate prediction of in situ observations is possible, using a sound physical representation of the soil-vegetation, heat exchange processes, without the need for an (artificial) enhanced mixing formulation. Note that in our current comparison with local observations, we disregard possible enhanced mixing as a consequence of spatial averages issues such as addressed by Mahrt (1987) that may play an important role in NWP of SBL under heterogeneous conditions.

The foregoing motivates us to pose the research question: what is the impact on the GABLS case study when we include realistic features of a surface energy balance? Therefore, we compare the outcome of the *reference case* (i.e. with prescribed surface cooling) with the

results of *two alternative surface coupled cases*. Both alternatives explicitly solve the surface energy budget equation and apply

- the diffusion equation for heat in the underlying ice (Alternative I), or
- use a bulk-conductance law at the surface (Alternative II),

in our extension of the single column model by Duynkerke (1991, 1999) to account for the heat flux from the underlying medium. This model also participated in the GABLS *reference case* comparison of various single column models (Cuxart et al., 2006).

Section 2.2 gives a short overview of the model description and additional results for the reference case study. Section 2.3 presents the results for a coupled system with a heat diffusion scheme (Alternative I). Results for Alternative II are presented in Section 2.4. Conclusions and recommendations are given in Section 2.5.
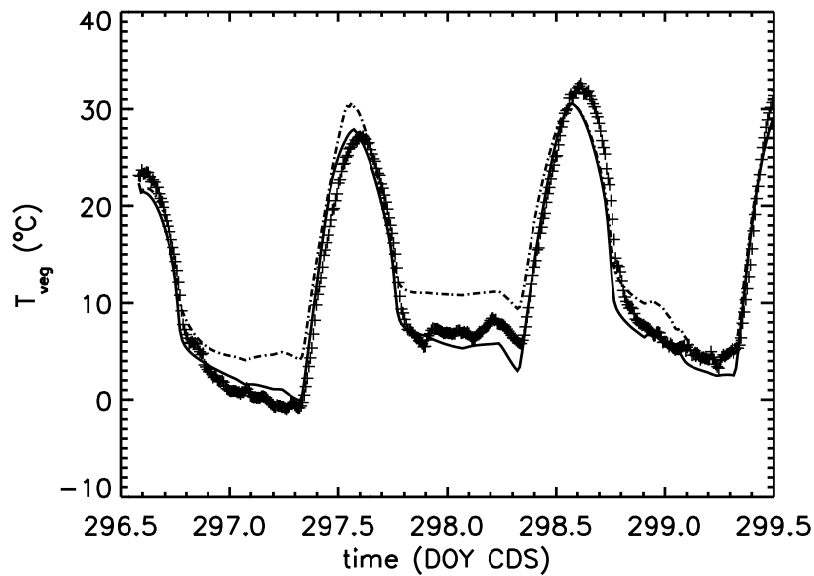
Figure 2.1: Modelled (full line) and observed (+) vegetation temperature for the period 23-26 October 1999 (Day of Year (DOY) = 296.5-299.5) for the CASES-99 experiment. The dash-dotted line indicates the model performance when enhanced mixing is applied.

2.2 Reference case: model description and results

a) Model description

Our model is an extension of the model by Duynkerke (1991, 1999). Turbulent mixing is parameterised in terms of local gradients (assuming local equilibrium of the TKE budget):

$$\overline{w'\chi'} = -K_x \frac{\partial X}{\partial z}, \tag{2.1}$$

where X is a mean quantity and $\overline{w'\chi'}$ the turbulent flux of X and z the height above the surface. The eddy diffusivity (K) is given by first order closure, expressed as (see also Holtslag, 1998):

$$K_x = \frac{l^2}{\phi_m \phi_x} \left| \frac{\partial \vec{V}}{\partial z} \right| \qquad x \in \{m, h\} \qquad\qquad (2.2)$$

with the mixing length $l = k\,z$ and $x = m$ for momentum and $x = h$ for heat, k the Von Kármán constant and $\partial \vec{V}/\partial z$ the vector wind shear. Based on reanalysis of the Cabauw tower observations from Nieuwstadt (1984), Duynkerke (1991) proposed the stability function

$$\phi_x(\zeta) = 1 + \beta_x \zeta \left(1 + \frac{\beta_x}{\alpha_x} \zeta \right)^{\alpha_x - 1} , \qquad\qquad (2.3)$$

where $\zeta = z/\Lambda$, Λ the local Obukhov length, defined as $\Lambda = -\overline{\theta} u_{*L}^{\,3} / (kg\overline{w'\theta'})$, and u_{*L} the local friction velocity. Coefficients were found to be $\beta_m = 5$, $\alpha_m = 0.8$, $\beta_h = 7.5$ and $\alpha_h = 0.8$, as compared to the original findings by Nieuwstadt (1984) who found $\alpha_h = \alpha_m = 1$, and $\beta_m = \beta_h = 5$. Note that the coefficients used in the present study (viz. as in Duynkerke, 1991) are in close agreement with the prescribed coefficients for the surface layer in the intercomparison case, especially for the weakly stable part.

Thus a simple first order closure model for turbulence is used in the present model, because the main aim of this paper is to illustrate the impact of coupling the atmosphere to the surface. Moreover, as shown by Brost and Wyngaard (1978), TKE transport terms in the SBL are usually relatively small so that the local equilibrium assumption is often applicable. Radiation divergence is neglected in the reference case.

The GABLS reference case study is defined over an ice surface with a relatively large roughness length for momentum and heat of $z_0 = z_{0h} = 0.1$ m. The geostrophic wind is $u_g = 8$ m s^{-1} and $v_g = 0$ m s^{-1} and the Coriolis parameter $f = 1.39 \times 10^{-4}$ s^{-1} (equivalent with 73 ºN). The initial mean state is given by $\theta = 265$ K for $0 < z < 100$ m and 0.01 K m^{-1} increasing above $z > 100$ m, and the atmosphere is considered to be dry. The model integration is for 9 hours and for the current study we apply a 40-layer logarithmically spaced grid. This provides fine resolution near the surface ($\Delta z = 0.7$ m) and coarser near the top of the domain (800 m in total). For additional information we refer to Beare et al. (2006) and Cuxart et al. (2006).

b) Results reference case.

Fig. 2.2 shows the evolution of the potential temperature (a) and wind speed (b) profile for the GABLS intercomparison study with prescribed surface temperature, shown as *a reference*. For convenience we use the integrated cooling (*IC*) of the boundary layer as a useful measure to compare several model runs. *IC* is defined as:

$$IC = \int_{z=0}^{z=z_{TOP}} \{ \theta_{start}(z) - \theta_{final}(z) \} dz \qquad\qquad (2.4)$$

in which z_{TOP} is the top of the model domain. For the reference case study *IC* amounts −342 K m after 9 hours (Table 2.1).

The reference case uses the classical length scale $l = k\,z$ which is valid near the surface. Besides this length scale, several additional turbulent length scale (*l*) formulations are cur-

rently in use (Cuxart et al., 2006). The rationale behind this, is the fact that z is not the only governing length scale when the stratification becomes strong. One of the simplest extensions to this neutral length scale ($l = k z$) is (conform Nieuwstadt, 1984; Hunt et al., 1985):

$$\frac{1}{l} = \frac{1}{kz} + \frac{N}{\sigma_w},\tag{2.5}$$

in which N is the Brunt-Vaisälä frequency. We *a priori* parameterize σ_w by $\sigma_w = 1.3u_{*L}$ (Nieuwstadt, 1984).
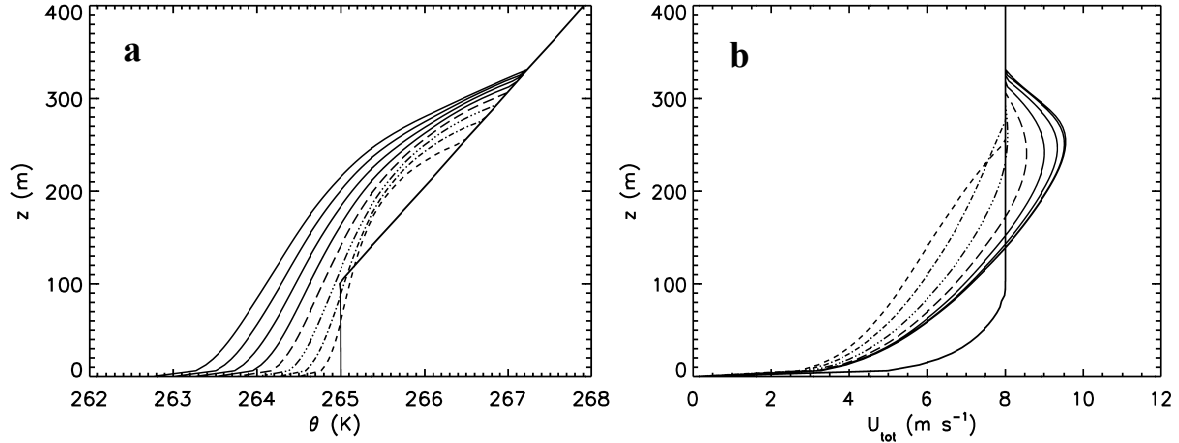
Figure 2.2: Potential temperature (a) development and structure for the reference GABLS case study with prescribed surface temperature, (b) for wind speeds (vector sum). Profiles are drawn every hour, (dashes: after one hour, dash dot after 2 hours, dash dot dot dot after 3 hours, long dashes after 4 hours, after 5 hours: full lines).

Fig. 2.3 gives the comparison of the final profiles for potential temperature (a) and wind speed (b) in comparison with the LES results for the GABLS case study (ensemble mean) and the LES of Wageningen University. Naturally, the strongest impact of mixing length formulation is found at the top where the inversion is strongest.

The results of Eq. (2.5) are in surprisingly good agreement with the LES models. This contrasts with the original length scale formulation in which $l = k z$, that causes too much vertical mixing. Note that in principle, it is expected that modification of Eq. (2.3) for high stabilities would be equivalent to our mixing length modifications. Using Eq. (2.5), *IC* amounts -242 K m (Table 2.1). For the remainder of this paper we keep the original formulation Eq. (2.3) as this was also used in the GABLS model intercomparison study.

The impact of vertical resolution for the *reference* case was examined by performing model simulations at a 6.25-m and a 40-m linear grid mesh (typical resolution for operational model) and a 40-layer stretched grid with fine grid mesh near the surface. No significant differences between these model runs were found (not shown). This agrees with the results of Delage et al. (1997) and Cuxart et al. (2006). However, care must be taken by interpreting these results, since this invariance may be caused by the prescribed surface temperature, which fixes partly the structure of the SBL.
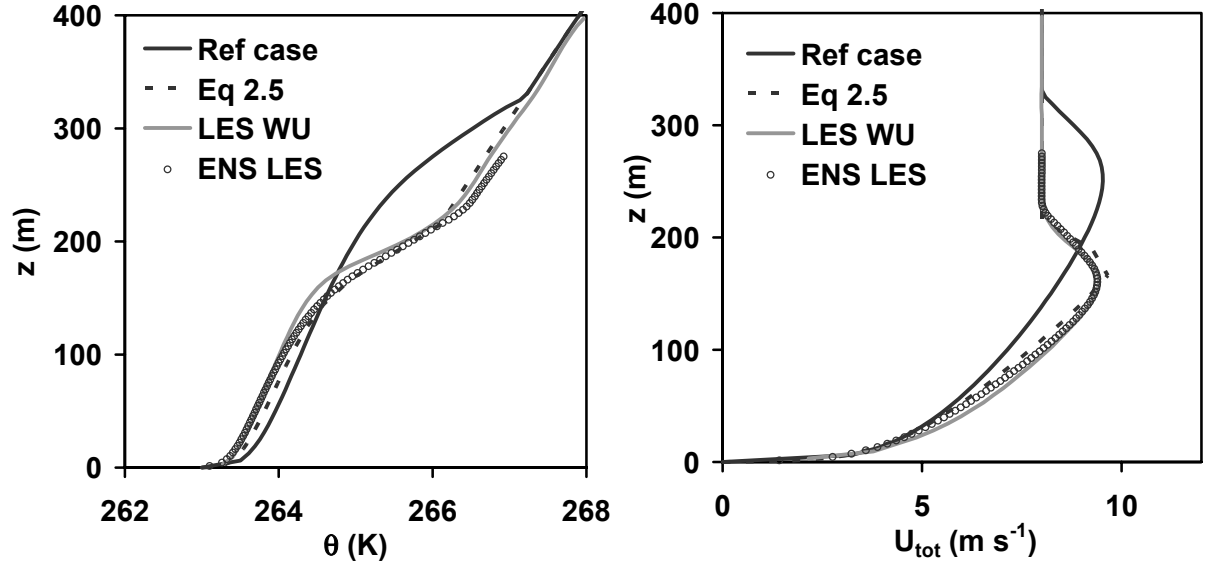
Figure 2.3: Final profiles of potential temperature (a) and wind speed (b) for the reference case, LES and Eq. (2.5).

Table 2.1: Overview of integrated cooling in the SBL for the different methods.

Case study	Integrated cooling (K m)
Reference study	-342
Equation (2.5)	-242
Diffusion scheme	-611
Bulk conductance ($\lambda_m / \delta_m = 5$)	-736

2.3 Coupling to the surface: a heat diffusion scheme (Alternative I)

The reference case study (see before in Section 2.2 and in Cuxart et al., 2006) uses a pre-scribed surface-cooling rate of -0.25 K h^{-1}. As mentioned before, this method gives only a limited degree of freedom, and therefore may limit our understanding of real SBL dynamics. Therefore, the current study goes one step further and focuses on the interdependence of the surface temperature (T_s) and the surface sensible heat flux $\overline{w'\theta'}_s$, by introducing the surface energy budget. The net radiation as computed by the radiation scheme is an essential element in the coupling to the boundary-layer scheme. The long-wave radiation components (upward and downward) are calculated using the grey-body approximation of Garratt and Brost (1981, from now on referred to as GB81). As a first test the current model set-up has been evaluated with the cases of Estournel and Guedalia (1985), and the results were found to be similar. For the present study we use a surface emissivity $\varepsilon_s = 0.96$ for ice (Oke, 1978). A uniform specific humidity profile of $q = 1.10^{-4}$ kg kg^{-1} was used. To consider the heat flux from the underlying medium towards the surface, we solve the diffusion equation for heat in a massive block of ice underneath the atmosphere (Fig. 2.4). Both the air temperature and surface temperature are

free variables in this configuration and $\overline{w'\theta'}_s$ and T_s are related interdependently, as in reality. The ice has a vertical dimension of 0.75 m (sufficient for short time integrations) and is initialised as $\theta_{ice} = 265$ K $\forall z$. θ_{ice} is held constant at the lower boundary during the simulation. In this manner, the ice supplies heat from below to the surface as a reaction to the surface cooling. The material properties used in the current study (using ice, see next section) are summarized in Table 2.2.
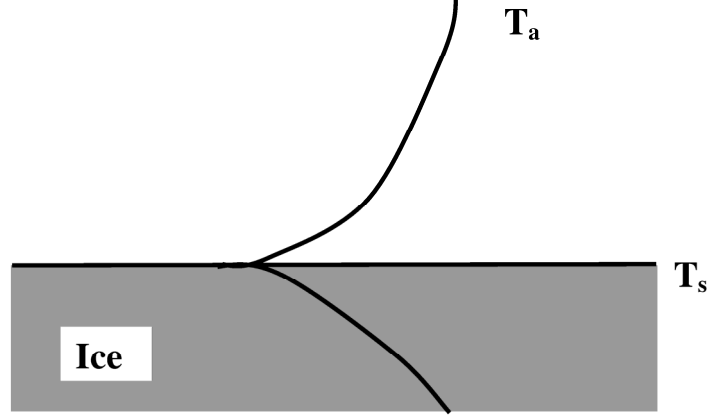
Figure 2.4: Model set-up for the SBL coupled with the ice through a heat diffusion scheme.

The results of this simple atmosphere-surface coupling (Fig. 2.4) on the development of the SBL are shown in Fig. 2.5. Compared to the reference case, this extension with a simple surface scheme results in a rather different SBL structure. Especially in the first hours, the surface cooling is much stronger than in the reference case (Fig. 2.2). We observe the boundary layer is less deep (220 m after 9 hours) and experiences a stronger total surface cooling than in the reference case ($\theta_{final} = 259.3$ K instead of 262.75 K after 9 hours). The vertical structure of the SBL is modified: the LLJ maximum is slightly weaker, at a lower level (160 m altitude) and sharper. The coupling with the surface for the present set-up causes a doubling of the extracted energy compared to the reference case, since *IC* equals −611 K m.
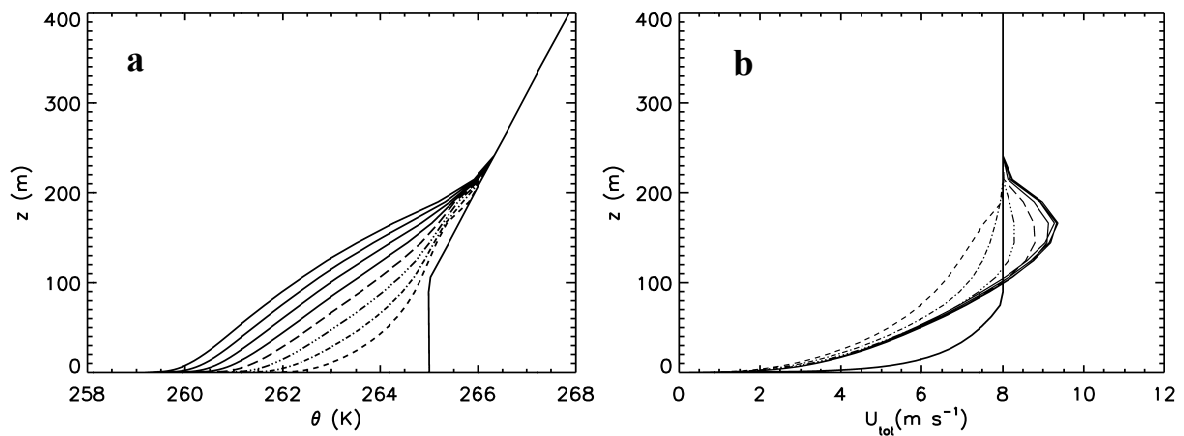
Figure 2.5: Potential temperature (a) and wind speed (b) development and structure for the alternative of solving the surface energy balance with a diffusion scheme for the ice heat flux.

Table 2.2: Material properties of ice (Oke, 1978).

Property	Value
Density ρ kg m^{-3}	920
Diffusivity K_s m^2 s^{-1}	$1.16.10^{-6}$
Heat capacity C_v J kg^{-1}K^{-1}	2100
Conductivity λ_g W m^{-1} K^{-1}	2.24

Impact of resolution

For the reference study without coupling, no serious dependence on vertical resolution in the atmosphere was found (see previous section). Interestingly, we will see that this is not true for the heat diffusion scheme in the ice. To examine the impact of resolution in further detail, we perform a sensitivity study on vertical resolution in the atmosphere and in the ice. As such, five model simulations are made with different kinds of vertical resolution (that apply both to the radiation scheme and the turbulence scheme, Table 2.3):

• Both atmosphere (with a stretched grid typically Δz = 0.5 m near the surface) and ice (Δz_{ice} = 0.005 m) at fine resolution. This provides the reference run for the coupled case.

• Atmosphere at operational (Δz = 40 m) and ice at fine (Δz_{ice} = 0.005 m) resolution.

• Atmosphere at operational (Δz = 40 m) and ice at coarse (five layers with Δz_{ice} = 0.25 m) resolution. State-of-the-art NWP and climate models adopt this typical configuration.

• Atmosphere at fine resolution near the surface (with a stretched grid typically Δz = 0.5 m near the surface) and the ice at coarse (Δz_{ice} = 0.25 m) resolution.

• Atmosphere at operational resolution (Δz = 40 m) applying *enhanced turbulent mixing* and the ice at coarse resolution (Δz_{ice} = 0.25 m).

Fig. 2.6 shows the final potential temperature (a) and wind speed profiles (b) for these five permutations. When we compare the final profile of the fine resolution and the operational resolution in the atmosphere, only a small difference is found *as long as a fine resolution in the ice is used in both cases*. This supports the results of Delage (1997) who explains that the altitude of the first grid point is less important for calculating the turbulent fluxes at the surface, due to compensating effects. By choosing the first model level at higher altitude, the gradients of temperature and wind speed are smaller which causes an underestimation of the flux. This is compensated by a larger mixing length (since it is proportional to z) and a slower increase of the bulk Richardson number with height. Both effects increase the estimated surface flux and more or less counteract for the first effect.

With the ice at coarser grid (both for the atmosphere at fine and operational grid mesh), the surface cooling is considerably stronger and the SBL is less deep compared with the case with fine resolution in the ice. Two counteracting effects are present:

- thick ice slabs will cause the ice to cool more slowly because of its large heat capacity, therefore slow down the surface cooling;

- the temperature gradients in the ice are smaller due to the larger grid length and conse-

quently only a small heat flux to the surface can be maintained, resulting in a smaller heat flux from the ice to the surface. Overall, this gradient effect of a coarse resolution seems to dominate the heat capacity effect, leading to stronger surface cooling.

Apparently, the model results appear to be most sensitive to vertical resolution in the underlying medium when the model is in coupled mode. For completeness we mention that for the extreme case, when we compare the total system at fine resolution with the total system at coarse resolution, we find a surface temperature difference of about 2 K for this case study.

We can hypothesize whether the stronger surface cooling in the case coarse resolution in the ice may be compensated in practice, e.g. by (artificial) enhanced turbulent mixing in the atmosphere (as in Louis, 1979). This is explored in Fig. 2.6: When turbulent mixing is enhanced (by setting $\alpha_m = \alpha_h = 0.85$ and $\beta_m = \beta_h = 2.5$), together with a coarse resolution both in the atmosphere and the ice, the surface cooling is reduced partly and the boundary layer has thickened 30 m compared to the case without the enhanced mixing. However, from this figure it seems that lack of resolution in the ice *can not* be cancelled out by enhanced turbulent mixing in the atmosphere.

The excess atmospheric cooling in the case of grid coarsening in the underlying medium can be attributed to either turbulent cooling (divergence of sensible heat flux) or cooling by the radiation scheme. In this study, the enhanced cooling due to the grid coarsening in the ice, is mainly caused by the turbulence scheme (increased flux divergence, not shown) and could not be attributed to the radiation scheme.
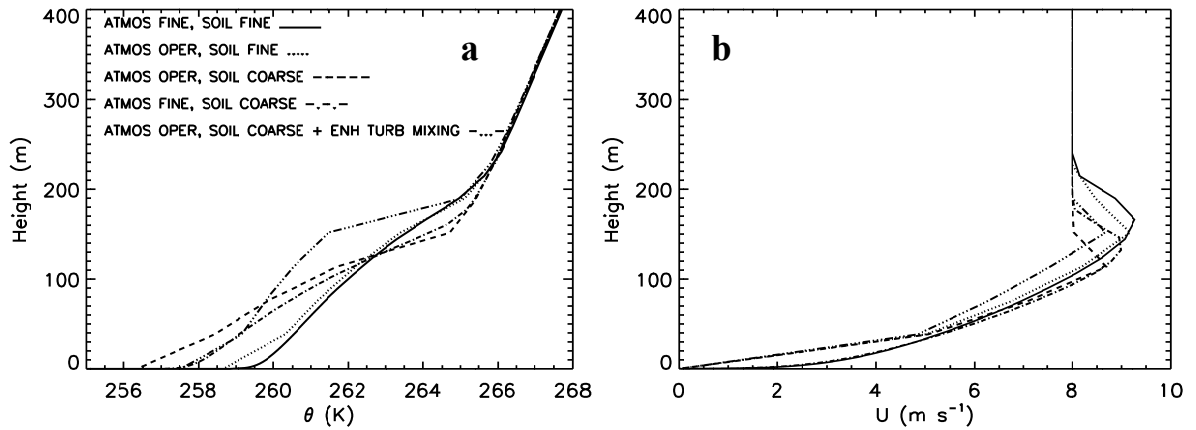
Figure 2.6: Final potential temperature (a) and wind speed (b) profiles as function of vertical resolution in the atmosphere and the underlying ice.

2.4 Coupling to the surface: a bulk conductance layer (Alternative II)

A second approach to incorporate the surface energy budget that is widely applied in numerical models (see for example Holtslag and De Bruin, 1988; Duynkerke, 1991; Viterbo and Beljaars, 1995), is to incorporate a small isolating layer of stagnant air (see Fig. 2.7) with a small heat capacity (Viterbo et al., 1999). For the current study, we will use a conductance layer to mimic the isolating properties of the stagnant layer. However, note that our intention

Table 2.3: Overview of integrated cooling in the SBL for the different methods.

Run	Near surface atmospheric resolution (m)*	Soil resolution (m)	Remark
I	0.5	0.005	Reference for coupled case
II	40	0.005	
III	40	0.25	Typical for NWP
IV	0.5	0.25	
V	40	0.25	Enhanced Turbulence

* using a 40 layer stretched grid.

is not to model the total mass and energy budget of a snow layer. For that purpose, we refer to Koivusalo et al. (2001). In the current approach both the surface temperature and the air temperature are free variables and similar reasoning as in Section 2.3 is valid for $\overline{w'\theta'}_s$.

This additional layer enables the surface temperature to react rapidly on imposed sudden changes in the surface cooling. The prognostic equation for the surface temperature in this case holds

$$C_v \frac{\partial T_s}{\partial t} = Q^* - \rho C_p \overline{w'\theta'}_s - \frac{\lambda_m}{\delta_m}(T_s - T_d),$$ (2.8)

in which C_v (J m^{-2} K^{-1}) is the heat capacity of the stagnant air layer, λ_m/δ_m (W m^{-2} K^{-1}) is the bulk heat conductance for that layer and T_d (K) the deep ice temperature (Fig. 2.7).

In this study we took T_d constant for simplicity; however, for long time scales a prognostic equation for T_d is required. The air density is given by ρ (kg m^{-3}) and the air heat capacity C_p (J kg^{-1} K^{-1}). For grassland C_v was found in the range between 2.10^3 and 2.10^4 J m^{-2} K^{-1}. For the bulk conductance λ_m/δ_m, values between 3 and 7 W m^{-2} K^{-1} are reported (Duynkerke, 1991; Van de Wiel et al., 2003). See Table 2.4 for an overview of proposed λ_m/δ_m values. For the current study with an isolating resistance layer, we adopted $C_v = 2090$ J m^{-2} K^{-1} and $\lambda_m/\delta_m = 5$ W m^{-2} K^{-1}. Although the heat capacity of the isolating layer depends on various factors and is a rather uncertain variable, we adopt the range 2000 – 20000 J m^{-2} K^{-1} in our sensitivity analysis.

The introduction of a stagnant air layer (Fig. 2.7) in the model leads also to strong surface cooling, resulting in a final temperature of 256.2 K (Fig. 2.8). The boundary layer has become less deep (170 m instead of 220 m with the heat diffusion equation) with a LLJ of 9.1 m s^{-1} at 125 m above the surface. The integrated cooling aggregates to $IC = -736.3$ K m. Fig. 2.9 shows the sensitivity of the final potential temperature and wind speed profiles to the bulk conductance coefficient λ_m/δ_m . For the range of $2 < \lambda_m/\delta_m < 20$, the modelled surface temperature varies between 261.2 K and 252.9 K. This large sensitivity that appears from Fig. 2.9, is an important result since a conductance layer is actually required in the model for a realistic behaviour of T_s in the case that vegetation is present (see Section 2.1).
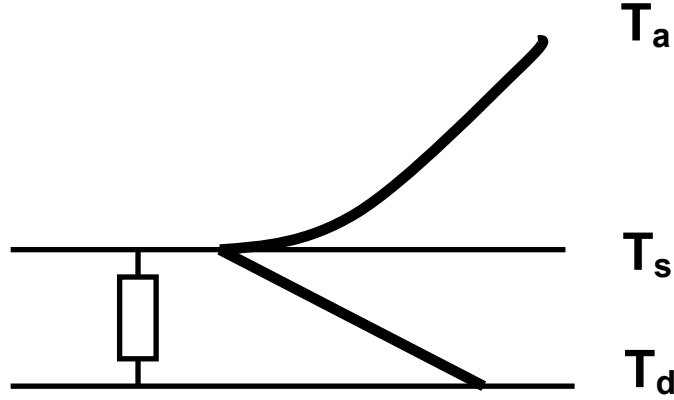
Figure 2.7: Model set-up for the SBL coupled with the ice through a bulk conductance layer of stagnant air.

The boundary-layer depth and stability also depend heavily on this bulk conductance parameter as well as the strength and altitude of the LLJ maximum. For a full representation of the SBL in atmospheric models, an adequate estimate of this surface parameter is therefore of major importance. Note that this parameter is also a key-parameter in modelling intermittent turbulence and oscillatory behaviour of the SBL temperature, as indicated by modelling results of Van de Wiel et al. (2002a, 2003). Interestingly, the present multi-layer single column model revealed oscillations of similar type (amplitude and period, not shown) as the model by ReVelle (1993) and the simple bulk model by Van de Wiel et al. (2002a). This is currently under investigation and is beyond the scope of the present study.

Besides the processes represented by the surface energy budget and the turbulent mixing processes, radiation divergence has an important impact on the structure of the SBL (see André and Mahrt, 1982 and GB81). Both studies report a three layer structure during the
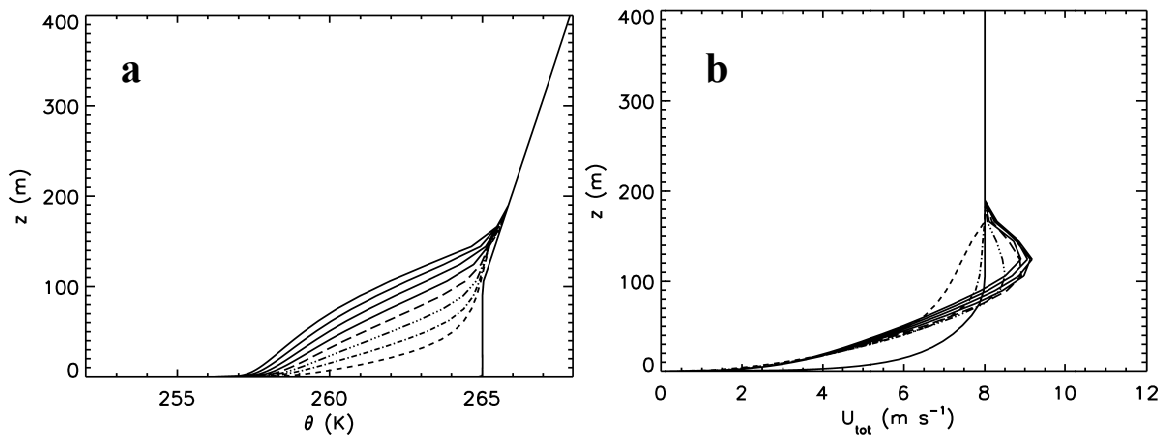
Figure 2.8: Potential temperature (a) and wind speed (b) development and structure in the alternative of solving the surface energy balance with a bulk conductance method and a stagnant air layer.

Table 2.4: Overview of reported bulk heat conductance values.

Reference	Bulk heat conductance (W m^{-2} K^{-1})
Van de Wiel et al. (2002a)	2.5
Duynkerke (1999)	3.0
Van Ulden and Holtslag (1985)	5
Steeneveld et al. (2004)	6.8
Viterbo and Beljaars (1995)	7

quasi-steady state of the SBL: a strong inversion near the surface, dominated by radiation divergence, a thick layer in the middle of the SBL dominated by turbulence, and an inversion layer dominated by radiative transport. For the current case study with moderate mechanical forcing $U_g = 8$ m s^{-1}, the impact of radiation divergence, applying the model of GB81 (with a uniform specified specific humidity of 0.1 g kg^{-1}) is small (not shown). With this strong mechanical forcing, the impact of radiation divergence is slightly noticeable near the surface: the inversion near the surface is smoother than in the reference case. In the 'bulk' of the boundary layer, hardly any impact is seen. However, it is to be expected that for weaker mechanical forcing the relative impact of radiation will increase. Fig. 2.10 shows the potential temperature development for $U_g = 3$ m s^{-1}, with and without radiation calculations incorporated for the bulk conductance method (using $C_v = 20900$ J m^{-2} K^{-1}) an a vertical resolution of 2 meters. The boundary layer is very thin in this case, but the structure is heavily dominated by radiation. In the latter case, the temperature inversion is more elevated and the vertical temperature gradients are weaker (radiative averages tend to smooth out large temperature gradients). Thus during weak wind conditions radiation divergence is an important process in SBL development, and is required to take into account for nights when turbulence is nearly absent (e.g. the third night in Fig. 2.1). This is in agreement with the work of Ha and Mahrt (2003) and earlier findings.
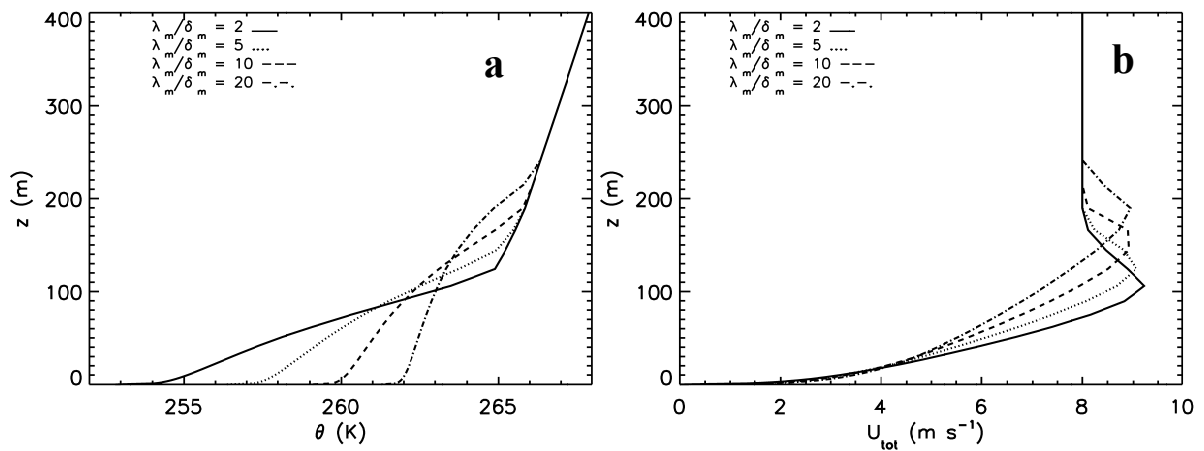
Figure 2.9: Sensitivity of the final profiles for potential temperature (a) and wind speed (b) as function of the bulk heat resistance (λ_m/δ_m).

To examine the impact of vertical resolution in the radiation scheme, Fig. 2.10c shows the cooling profiles due to radiation divergence for the last run, after 4 hours of cooling. One result is based on the original grid mesh of 2 meters and the same profile, and one result is obtained by using a 20 meter grid mesh. A clear distinction is seen: coarser grid mesh results in an underestimate of the cooling due to radiation divergence. This is in close agreement with the findings of Ha and Mahrt (2003).

2.5 Conclusions

Point of departure in the current paper is the reference GABLS single column model inter-comparison study that uses a prescribed surface cooling rate as a boundary condition (Cuxart et al., 2006). Both theory and observations in the literature indicate that a simple extension of this reference case by taking into account the surface energy budget, is necessary to attain a realistic boundary condition (since in reality the surface temperature T_s and surface sensible heat flux $\overline{w'\theta'}_s$ are dynamically interdependent). In the present study, this extension is pioneered in two different ways:

- At first, we include the surface energy balance and solve the heat diffusion equation in the ice. This coupling between the atmosphere and the land surface results in stronger surface cooling and thinner boundary layers compared to the reference case. A clear dependence on the vertical grid spacing in the ice is found. Coarse resolution in the ice gives a stronger surface cooling, thinner boundary layers that are on average more stable. In contrast, a coarser resolution in the atmosphere had only little effect on the results as was also found by Delage (1997).

- In the second method we introduce a bulk conductance layer of stagnant air at the surface. This is a realistic extension representing cases when (low) vegetation or snow cover is present. Moreover, from previous studies (Van de Wiel et al., 2002a) it is clear that such a coupling may lead to additional internal dynamics. In the present study, the implementation of a bulk conductance layer results in stronger surface cooling and thinner boundary layers compared to the reference case. Also, the SBL development shows strong sensitivity to the numerical value of the bulk conductance of the stagnant air layer. So, the impact of this particular surface boundary condition is large, even in its most simple form.

 Naturally, the bulk conductance depends on the land use, vegetation cover and snow/no snow cover as well and is required as input in large-scale models (from some land use classification). Additionally, the current study confirms that the impact of clear air radiation divergence (as compared to turbulence flux divergence) is mostly relevant at low geostrophic forcing (consistent with the findings of Estournel and Guedalia, 1985 and others).
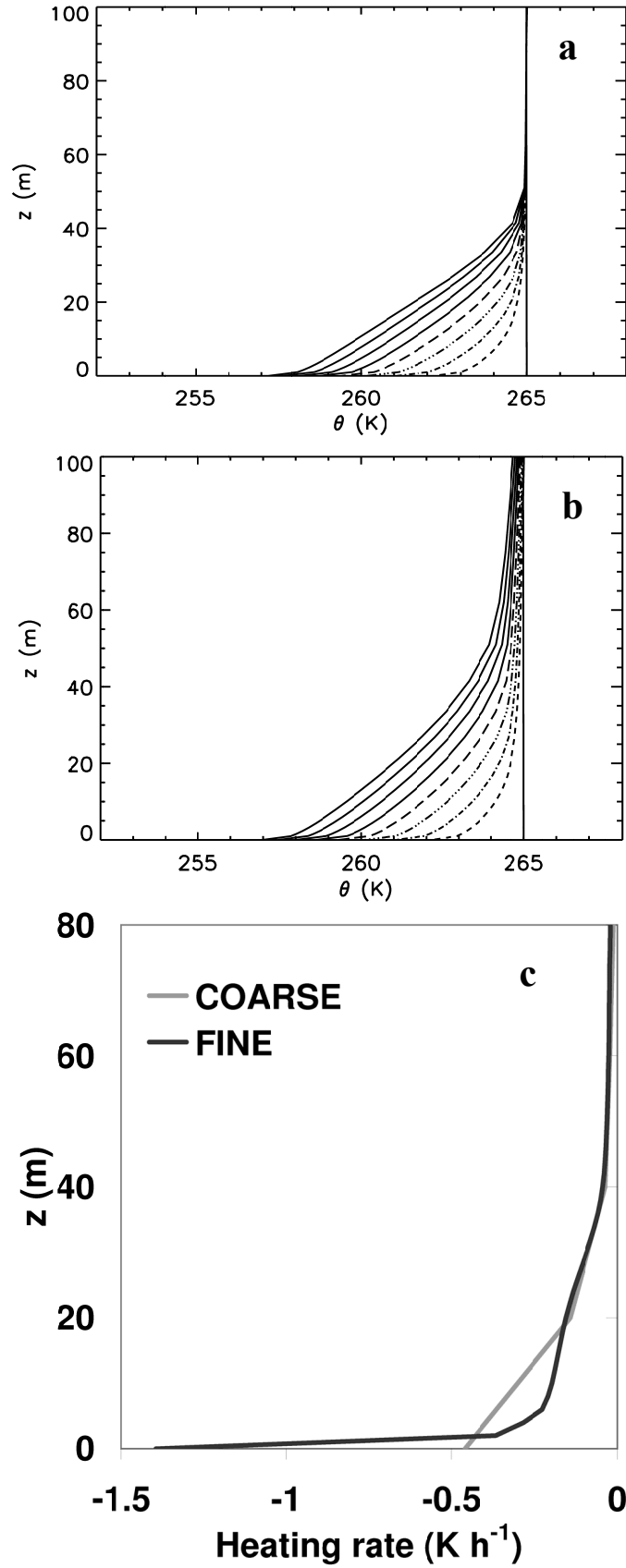
Figure 2.10: Potential temperature development with (a) and without (b) the radiation scheme for a geostrophic wind speed of 3 m s^{-1} and C_v = 20900 J m^{-2} K^{-1}. Figure c) shows radiative cooling for high (2 m) and low (20 m) vertical resolution after four hours cooling.

The present study on atmosphere-surface coupling (and similar studies on length scale formulations) show an evident impact on the structure and development of the SBL. These issues call for additional validation with detailed observations including surface fluxes, vertical temperature soundings, and boundary-layer depths, e.g. available for CASES-99 (Poulos et al., 2002), SABLES-98 (Cuxart et al., 2000), for Cabauw (Beljaars and Bosveld, 1997), or for more heterogeneous characteristics such as in Lindenberg, Germany (Beyrich et al., 2002). For modelling these real cases special attention should be paid to the interaction of the SBL with the surface and soil.

Chapter 3

Modelling the evolution of the atmospheric boundary layer coupled to the land surface for three contrasting nights in CASES-99

Abstract

The modeling and prediction of the stable boundary layer over land is a persistent problematic feature in weather, climate and air quality topics. Here, the performance of a state-of-the-art single column boundary-layer model is evaluated with observations from the CASES-99 field experiment. Very high model resolution in the atmosphere and the soil is utilized to represent three different stable boundary-layer archetypes, namely: a fully turbulent night, an intermittently turbulent night and a radiative night with hardly any turbulence (all at clear skies). Each archetype represents a different class of atmospheric stability. In the current model, the atmosphere is fully coupled to a vegetation layer and the underlying soil. In addition, stability functions (local scaling) are utilized based on local observations.

Overall it is found that the vertical structure, the surface fluxes (apart from the intermittent character) and the surface temperature in the stable boundary layer can be satisfactorily modeled for a broad stability range (at a local scale) with our current understanding of the physics of the stable boundary layer. This can also be achieved by the use of a rather detailed coupling between the atmosphere and the underlying soil and vegetation, together with high resolution in both the atmosphere and the soil. This is especially true for the very stable nights, where long-wave radiative cooling is dominant. Both model outcome and observations show that in the latter case the soil heat flux is a dominant term of the surface energy budget.

3.1 Introduction

After sunset with clear skies, the surface starts to cool due to long-wave radiation emission, and consequently the atmospheric boundary layer (ABL) becomes stably stratified. Understanding the physics of the stable boundary layer (SBL) is relevant to weather forecasting (Viterbo et al., 1999), climate modeling (Holtslag and Boville, 1993), air quality modeling (Neu, 1995) and CO_2 budget studies (Pattey et al., 2002). In this study we focus on the nighttime stable boundary layer, although the daytime is also considered to some extent.

Three distinct physical processes mainly govern the evolution and the structure of SBL: turbulence, radiative cooling and the interaction of the SBL with the vegetation and the underlying soil. Additional features such as gravity waves, drainage flows, katabatic flows, density currents (Sun et al., 2003a), downward transport of residual-layer turbulence and processes related to spatial heterogeneity are also relevant (Mahrt, 1987, 1999; Mahrt et al., 1998, Acevedo and Fitzjarrald, 2001), besides advection and thermodynamic processes including water vapor.

One of the following three SBL-archetypes may occur, depending on the relative importance of radiation and turbulence: 1) fully turbulent, 2) intermittently turbulent and 3) radiative SBL (Van de Wiel et al., 2003, henceforth W03). The very stable boundary layer, as defined by Mahrt et al. (1998) includes the intermittent and radiative archetypes. Wind shear is dominant during a continuously turbulent night, and radiative flux divergence and the soil heat flux dominate during the radiative archetype. The intermittent archetype consists of alternating dominance of turbulence and radiative flux divergence. The challenge is to develop an ABL model which is able to predict all three archetypes.

Current large-scale models encounter serious problems with SBL modeling (See Section 3.2, Beljaars, 1995; Beljaars and Viterbo, 1998; Holtslag, 2003; Cuxart et al., 2006). On one hand, the process descriptions of the physics can be inaccurate or incomplete. On the other hand, more resolution than is currently used may be needed to solve the SBL. If the latter is true, then to what physical process (turbulence, radiation or soil and vegetation) more allocation of computational efforts is needed to achieve the best results?

The aim of this paper is to answer the question whether the SBL can be satisfactorily modeled when resolution in both the atmosphere and the soil is not a limiting factor. Therefore, we evaluate the performance of a single-column model for all three SBL-archetypes (fully turbulent, intermittently turbulent and radiative) at high vertical resolution as a proof of principle. We will in particular explore the modeling of soil and vegetation, because the soil heat flux is a relatively large component of the surface energy budget during nighttime. We will compare our results with observations from the extensive CASES-99 data set (Poulos et al., 2002).

In Section 3.2, background information and additional motivation for the present study is given. In Section 3.3, the observational data is examined, including the surface energy budget

closure. Section 3.4 describes the model configuration, and Section 3.5 presents the results. Conclusions are drawn in Section 3.6.

3.2 Background

Current SBL parameterizations in large-scale numerical weather prediction (NWP) and climate models encounter problems with predicting the near surface atmospheric structure (Beljaars and Holtslag, 1991; Betts et al., 1998; Derbyshire 1999; Chen et al., 2004). Turbulence transport parameterizations in these models are based on similarity theory (McVehil, 1964; Oke, 1970; Businger et al., 1971; Louis, 1979; Kot and Song, 1998; Howell and Sun, 1999). However, the prerequisites of homogeneity and stationarity for applying similarity theory are often not met for very stable conditions (e.g. Caughey et al., 1979). Several studies report a significant model bias of predicted surface fluxes for very stable conditions (Carson and Richards, 1978; Louis, 1979, and Poulos and Burns, 2003).

For very stable (weak wind) conditions and during the day-night transition, radiative flux divergence significantly influences the SBL structure (mainly by decreasing the inversion strength) in governing the atmospheric cooling rate near the surface as shown by Funk (1960), André and Mahrt (1982), Garratt and Brost (1981, hereafter GB81), Nkemdirim (1978, 1988), Gopalakrishnan et al. (1998) and discussed by Andreas (2002). The coupling between the lower atmosphere and the land surface is of major importance, especially under very stable conditions (Deardorff, 1976; Best, 1998, and Van de Wiel, 2002).

As an illustration of current parameterization problems in meso- and large-scale models for stable conditions, we analyze a typical result of a mesoscale model (MM5, version 3.5, with U.S. Geological Survey (USGS) land use classification) for the CASES-99 campaign for 23-26 October 1999. We use both the first order closure model with prescribed diffusion profile form, MRF (Medium Range Forecast, Hong and Pan, 1996) and a 1.5 order TKE-*l* closure model, ETA (Janjić, 1990). Horizontal resolution is set to 1 km for the innermost grid nest (in total three nested grids were used), and using 30 vertical model layers of which 20 are located in the lowest 600 m. The ECMWF operational analysis provided the initial and boundary conditions every six hours.

In general the model results for both turbulence schemes agree with each other. The model overestimates the wind speed near the surface and near surface stability is underestimated. The modeled surface temperature is several degrees too high (Fig. 3.1), especially for the weak wind nights (first and third night). Furthermore, the intermittent character observed in the turbulent fluxes in the first night is absent in both model versions. This example from a typical state-of-the-art mesoscale model shows a clear discrepancy with local observations, even at high horizontal and vertical resolution. Similar discrepancies are found by Hanna and Yang (2001) and Zhong and Fast (2003) with MM5 and Viterbo et al. (1999) for routine use of NWP.

Besides the impact of turbulent diffusion, observations indicate that the soil heat flux is extremely important during nighttime (W03), especially during weak winds, since the turbulent fluxes are then small or absent (Fig. 3.2). Fig. 3.2 also shows that if the sensible heat flux changes, the soil heat flux reacts immediately on a similar time scale as the change of the sensible heat flux. We conclude that special attention to the coupling of the atmosphere and the surface is necessary (Deardorff, 1976; Derbyshire, 1995, 1999; Best, 1998, Van de Wiel, 2002a and Steeneveld et al., 2006a).

Although we expect three-dimensional models to consider advection and effects of spatial heterogeneity better than a single-column model (SCM), the parameterization problems in large-scale models mentioned above motivated us to use a SCM with 'state-of-the-art' physics for turbulent diffusion, long-wave radiation transfer and coupling of the atmosphere with the vegetation and the soil. Several SCM studies on the SBL were performed in the past, but many of them are limited to weak stratification with a strong geostrophic wind V_g. For example, Brost and Wyngaard (1978) modeled a SBL with $V_g = 10$ m s^{-1} with prescribed surface temperature as a boundary condition. In this manner, however, the dynamic interaction with the soil and the vegetation is not considered. In addition, radiative flux divergence was neglected, which is only allowed for large wind speed (e.g. Steeneveld et al., 2006a).

Similar SCM studies (i.e. without radiative flux divergence and/or prescribed surface temperature) were performed by Delage (1974), Nieuwstadt and Driedonks (1979), Mailhot and Benoit (1982), Basu and Raghavan (1986), Sharan and Gopalakrishnan (1997) with similar results. Finally, Galmarini et al. (1998) found good agreement between LES simulations and their SCM for large V_g.
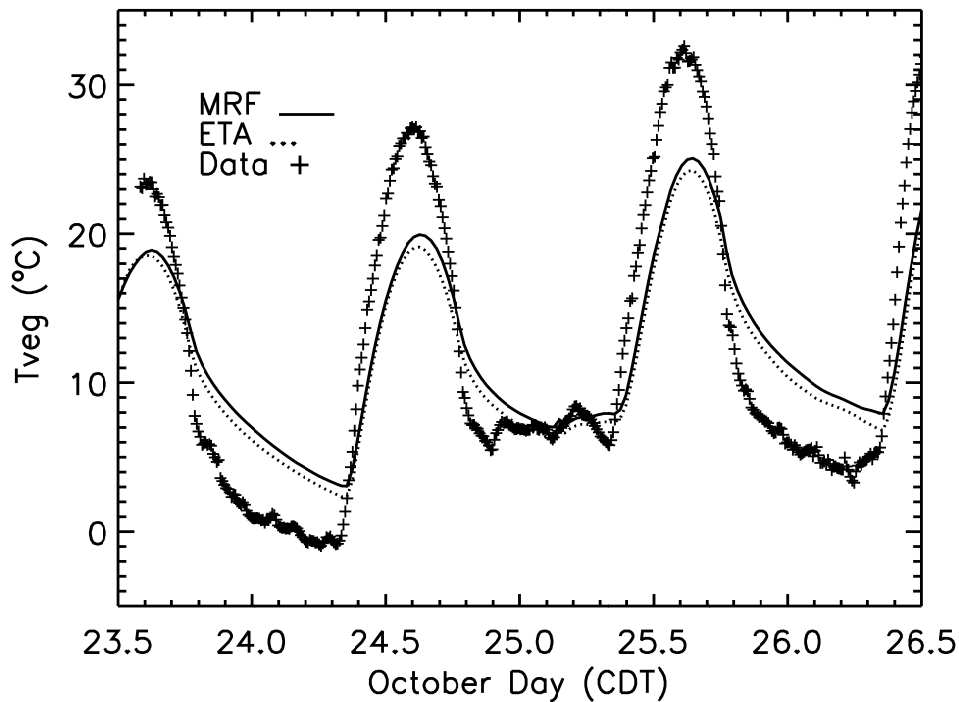
Figure 3.1: Estimated vegetation surface temperature using the mesoscale model MM5 with the MRF (full line) and ETA (dashed line) boundary-layer scheme, compared with CASES-99 observations (+), (23-26 October 1999).
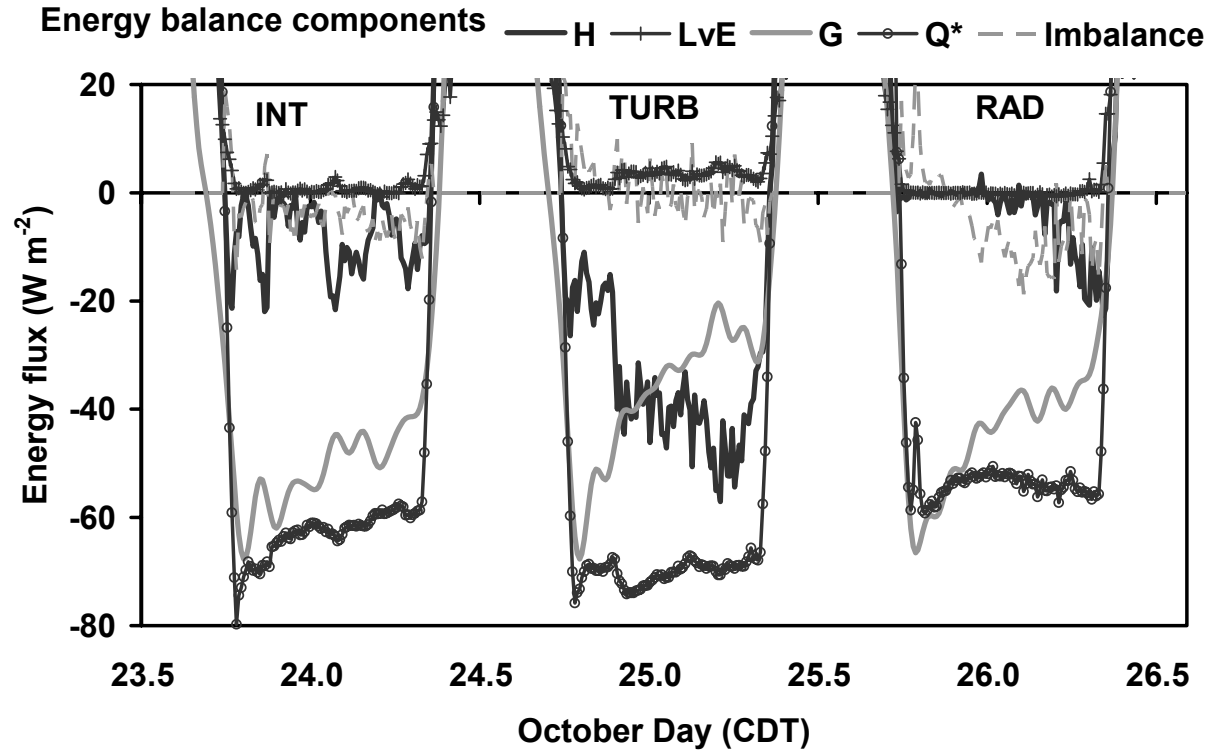
Figure 3.2: Energy partitioning for the period of 23-26 October 1999 for CASES-99. *H* is sensible heat flux (full black line), L_vE latent heat flux (thin black line with plusses), *G* soil heat flux (thick grey line) and Q^* the net radiation (thin black line with open circles). The first night is classified as intermittent, the second as fully turbulent and the last as radiative.

Recently, Rama Krishna et al. (2003) extended the former studies by simulating three different wind regimes: strong winds, moderate winds and weak winds. They used a detailed radiation transfer model and 1.5-order turbulence closure. However, they also prescribed the surface temperature, and consequently, the interdependence of the surface temperature and the sensible and soil heat fluxes were not considered.

Tjemkes and Duynkerke (1989, referred to as TD89) simulated SBLs with strong and moderate $\mathbf{V_g}$. With a narrow-band model for long-wave radiation transfer and a force-restore method at the surface, they obtained good agreement with the Cabauw tower and energy budget observations.

Duynkerke (1991, hereafter D91), Musson-Genon (1987), Vogelezang and Holtslag (1996), Steeneveld et al. (2006a) and others recognized the vital role of the interaction with the surface, and coupled the atmosphere to the surface with either a bulk conductance layer or a force-restore method.

To summarize, former studies generally concentrated on the modeling of fully turbulent nights with a strong mechanical forcing (allowing radiative flux divergence to be neglected safely, e.g. Estournel and Guedalia, 1985) and typically surface temperatures were prescribed. Since the atmosphere-land surface coupling is essential for SBL evolution, we will emphasize this topic in this study.

3.3 Observational data

In this paper, CASES-99 observations are used to validate the model. The CASES-99 measurement campaign was organized to study the relevant processes in the SBL and to improve SBL model parameterizations (Poulos et al., 2002). The experiment was conducted near Leon, Kansas, U.S.A. (37.6486º N, -96.7351º E, 436 m ASL) and lasted from 1-31 October 1999. The area consisted of relatively flat homogeneous terrain (average slopes are 0.2º) with a relatively dry soil, and lacks obstacles in the near surroundings. The roughness length for momentum (z_0) was 0.03 m.

Ground based observations consist of profiles of temperature, humidity and wind along a 60 m mast, and turbulent and radiative fluxes near the surface. The eddy-covariance measurements of the surface sensible heat flux (H) and friction velocity (u_*) were obtained at 2.6 m. Because the soil heat flux (G) becomes a key process during strong stability, special emphasis was given to the observations of this quantity by using simultaneous information of the temperature at 3 and 8 cm below the surface and soil heat flux plates at 5.4 cm depth (W03). We fitted a Fourier series (150 components to account also for the high frequency changes – without fitting the noise – as is shown below) through the 3 cm data and determined the soil diffusivity (κ) by translating this series to the 8 cm level. Consequently, the soil temperature T_s (z,t) is known. Here we assumed a homogeneous soil, since no spatial information on the soil structure is available. In reality soil properties may vary in space considerably. Differentiating T_s (z,t) with respect to z and substituting $z = 0$ provides the surface soil heat flux G_0 (for details see W03; Heusinkveld et al., 2004 and Van Wijk, 1963). The surface energy balance closure is rather good for all selected nights (Fig. 3.3), especially considering the fact that nighttime turbulent fluxes are often small and hence difficult to measure accurately. The closure provides confidence in the observations, for comparison with the model.

Hourly launched radiosondes provided information on the structure of temperature, wind speed and direction above 60 m AGL. Wind speed structure below 200 m was obtained with sodar. The data are available at http://www.atd.ucar.edu/rtf/projects/CASES-99/.

The observed vegetation surface temperature (T_{veg}) was determined from the 'apparent radiation temperature' T_{IRT} from the observed long-wave up- and downwelling radiation, assuming an emissivity of $\varepsilon = 0.98$, both for dry grass and the underlying soil (Oke, 1978). With the vegetation covering a fraction of the surface, $f_{veg} = 0.9$ (based on visual inspection of the field), we obtain for T_{veg}:

$$\sigma T_{IRT}^{4.5} = \varepsilon f_{veg} \sigma T_{veg}^{4.5} + \varepsilon (1 - f_{veg}) \sigma T_{s0}^{4.5} , \tag{3.1}$$

with σ the Stefan-Boltzmann constant. We use a 4.5 power law because we are observing in the atmospheric window, where the integral over the Planck-curve $B(\lambda)$ can be approximated

with $M = \int_{\lambda_1}^{\lambda_2} B(\lambda) = cT^b$ for a certain temperature range. In this expression c is a proportionality constant and $b = 4.5$ (not 4) in this case (De Bruin, pers. comm.).

We selected three consecutive, clear nights, 23-24, 24-25 and 25-26 October 1999 (Fig. 3.2, Table 3.1). Each night was classified as one of the archetypes discussed in Section 3.1. The first night is intermittently turbulent, with several turbulent mixing events (Sun et al., 2003a). Banta et al. (2002) reports a low-level jet (LLJ) with mean speed of 7.6 m s^{-1}, typically at a height of 100 m (see their Table 2). The 200 CDT (central daylight time) radiosonde shows a LLJ of 12 m s^{-1} at 100 m. In the second (turbulent) night, a continuous LLJ with mean wind speed of 15.2 m s^{-1} and the LLJ altitude increased during the night. Mahrt and Vickers (2002) show that local friction velocity is obviously higher at 60 meters than near the ground. They qualify this SBL as an 'upside down' boundary layer and suggest advection and mesoscale circulations are important during this night (Section 3.4e). The last (radiative) night has a mean 10 meter wind speed of only 2.0 m s^{-1} and a mean LLJ speed of 3.8 m s^{-1}. The mean LLJ height is not well defined.

The surface sensible heat flux shows an intermittent character during the first night, is relatively constant and has a large magnitude during the second night, and vanishes during most of the last night. G is a relatively large component in the energy budget for all nights, with a clear maximum (in absolute sense) just after the day-night transition and a gradual increase during the night (Fig. 3.2).

3.4 Model description

The single-column model (SCM) used here is basically developed by Duynkerke (1991) to solve the governing equations for the atmosphere for an incompressible horizontal homogeneous flow (Stull, 1988; Garratt, 1992). The model combines the detailed calculation of turbulence, heat transfer by long-wave radiation, soil- and surface processes, and thus includes a detailed description of the main physical processes. For this study in particular the surface scheme is updated (Section c)

Table 3.1: Micrometeorological conditions for the three selected nights (23-24, 24-25 and 25-26 Oct) averaged over $0-6$ CDT.

Date (Oct 1999)	Type	u_* (m s^{-1})	U_{10} (m s^{-1})	T_{10} (K)	$Q*$ (W m^{-2})	H (W m^{-2})	$L_v E$ (W m^{-2})	G (W m^{-2})
23-24	Int.	0.069	2.9	275.02	-61.2	-9.1	0.5	-48.3
24-25	Turb.	0.300	6.28	282.11	-69.6	-43.4	3.9	-29.5
25-26	Rad.	0.023	2.02	285.29	-53.4	-2.9	-0.3	-39.6
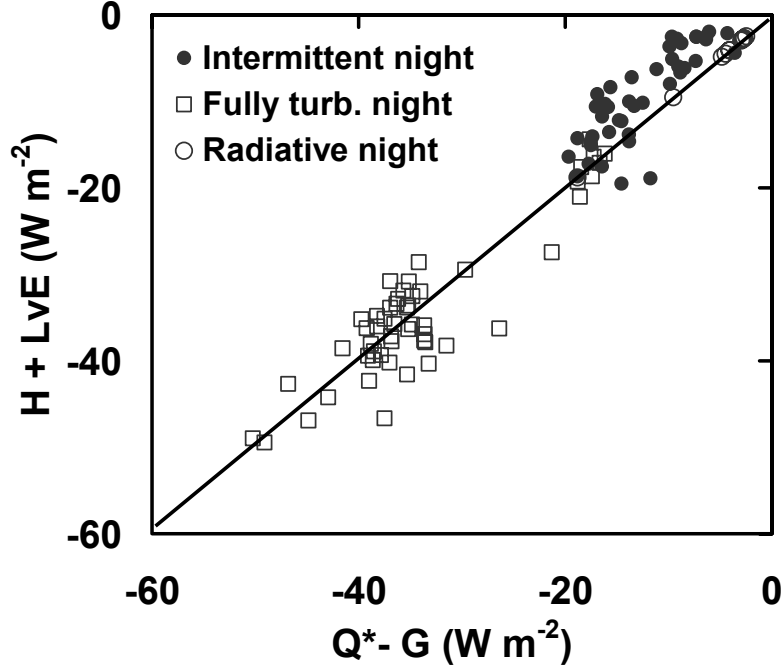
Figure 3.3: The closure of the observed surface energy balance for the night (0-6 CDT) for 23-24 (intermittent night), 24-25 (continuous turbulent night) and 25-26 (radiative night) October during CASES-99.

a) Turbulence

The turbulent mixing of momentum and heat is local (e.g. Duynkerke and De Roode, 2001):

$$\overline{w'X'} = -K_x \frac{\partial X}{\partial z} \tag{3.2}$$

where X is a mean quantity and X' is its fluctuating part. The eddy diffusivity K_x is given by first order closure (D91; Holtslag, 1998):

$$K_x = \frac{l^2}{\phi_m \phi_x} \left| \frac{\partial \vec{V}}{\partial z} \right| \qquad x \in \{m, h, q\} \tag{3.3}$$

with $l = k z$ and $x = m, h,$ and q for momentum, heat and humidity respectively and k is the Von Kármán constant (taken as 0.4). D91 proposes after reanalysis of Cabauw observations in Nieuwstadt (1984):

$$\phi_x(\zeta) = \frac{kz}{X_*} \frac{\partial \overline{X}}{\partial z} = 1 + \beta_x \zeta \left(1 + \frac{\beta_x}{\alpha_x} \zeta \right)^{\alpha_x - 1} \qquad x \in \{m, h, q\} \tag{3.4}$$

with $\zeta = z/\Lambda$, Λ the local Obukhov length, defined by $\Lambda = -\overline{\theta} u_{*L}^3 / (kg \overline{w'\theta'})$, with u_{*L} the local friction velocity. We use *a priori* $\beta_m = \beta_h = 5$ (Businger et al., 1971) and $\alpha_m = \alpha_h = 0.8$ (D91). This a priori choice gives reasonable agreement with CASES-99 observations, at least for $z/\Lambda < 2$. Fig. 3.4 shows the ϕ_x–functions inferred from analysis of mean profiles from CASES-99 (see Appendix) for momentum (*a*) and heat (*b*) together with proposals by Dyer

(1974) and Beljaars and Holtslag (1991). The ϕ_m agrees with the results of Klipp and Mahrt (2004) for CASES-99. Note that the uncertainty for ϕ_h is larger than that for ϕ_m (e.g. Andreas and Hicks, 2002) both increasing with stability. Note that we apply ϕ_h for humidity as well.

b) Radiation

Several studies show the relevance of radiative flux divergence on the structure and development of the SBL (GB81; André and Mahrt, 1982). We utilize the grey-body emissivity model by GB81 (and used by D91), which considers the absorbing effects of water vapor, CO_2 and liquid water. In this scheme, each specific layer emits radiation to other layers with a single emissivity that depends on the amount of absorber between the specific layer and the other layers.

Ha and Mahrt (2003) found the vertical resolution to be a key issue for the radiation transfer model performance. A fine grid spacing (approximately 1 m near the surface) is required to estimate the long-wave radiative divergence accurately. With a coarse resolution, radiative cooling near the ground is negligibly small or the model even predicts radiative warming.

Earlier studies (e.g. Tjemkes, 1988) showed that the output from several emissivity models can differ (approximately 10 Wm^{-2}) from those of line-by-line models near the surface (Gopalakrishnan et al., 1998), the latter giving the most accurate results. However, the grey-body approach is computationally more efficient. Therefore, we prefer the grey-body approach in this study.
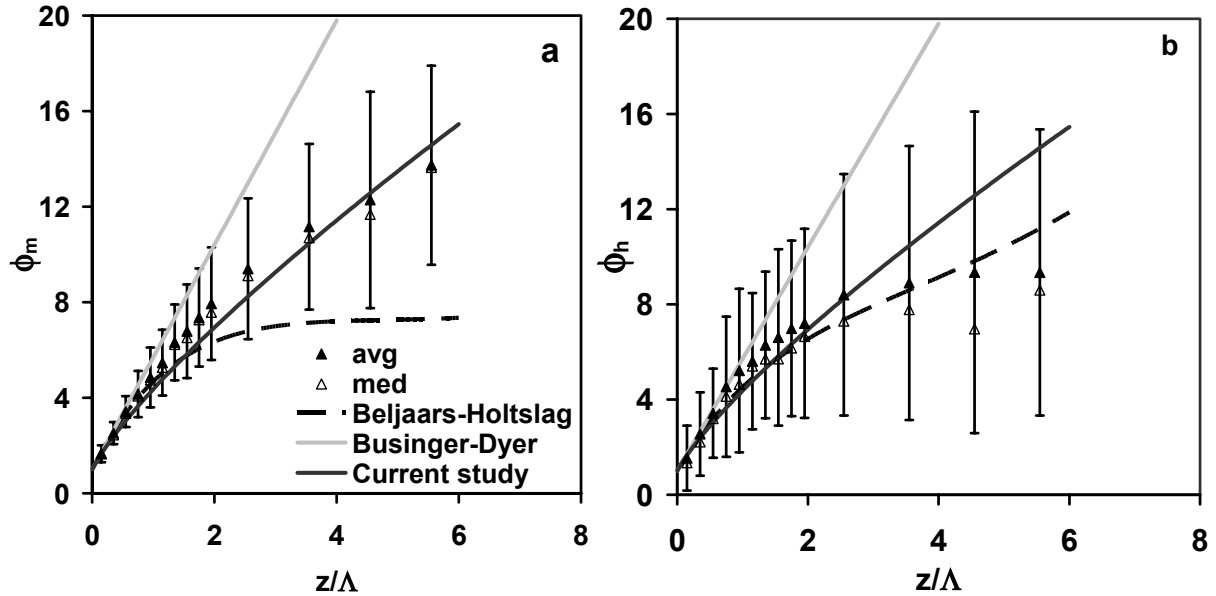
Figure 3.4: Observed dimensionless gradients of wind speed (a) and potential temperature (b) as function of local stability (*z/Λ*) for CASES-99. Filled triangles are mean values, open triangles are median values for the CASES-99 observations. Full lines are the proposals by Businger-Dyer (Dyer, 1974; grey line), Beljaars and Holtslag (1991) (long dashed) and the curve used in the current model (thick black line).

c) Soil and vegetation surface

Fig. 3.5 depicts the structure of the land-surface scheme and the definitions of the various temperatures. T_{veg} is the vegetation surface temperature, T_{s0}, the soil surface temperature just below the vegetation and T_d is the soil temperature 75 cm below the soil surface. $T_s(z)$ is the soil temperature at a level z below the surface.

The diffusion equation gives the evolution of the soil temperature (T_s):

$$\frac{\partial T_s}{\partial t} = \kappa \nabla^2 T_s ,$$ (3.5)

with κ the soil diffusivity for heat (m^2 s^{-1}). The soil heat flux, $G(z)$ is then given by

$$G(z) = -\lambda \frac{\partial T_s}{\partial z} ,$$ (3.6)

where λ is the soil conductivity ($\lambda = 0.6$ W m^{-1} K^{-1} estimated from the CASES-99 observations, W03). Note that λ and κ depend on the soil moisture content. However, the observed soil moisture content was relatively constant during three-day period we consider here, and therefore we use constant values for λ and κ. A conductance law parameterizes the soil heat flux at the surface, G_0:

$$G_0 - (1 - f_{veg})K^{\downarrow} = r_g \left(T_{veg} - T_{s0} \right),$$ (3.7)

where $K^{\downarrow}$ is the incoming shortwave radiation (W m^{-2}) at the surface, f_{veg} is the fraction of the soil surface covered by vegetation and r_g is the conductance for heat transport between the vegetation layer and the soil surface.

Fig. 3.6 shows the empirical conductance law of Eq. (3.7) for CASES-99 observations for both daytime and nighttime. With $f_{veg} = 0.9$, we estimate $r_g = 5.9$ W m^{-2} K^{-1} (from the slope in Fig. 3.6). Note the relatively large scatter due to the empirical character of Eq. (3.7). D91 found $r_g = 3.0$ W m^{-2} K^{-1} and Holtslag and De Bruin (1988) obtained $r_g = 5$ W m^{-2} K^{-1} for Cabauw. Thus, the current value is in reasonable agreement with other observations for grass. A better fit through the data is obtained by: $G_0 - (1 - f_{veg})K^{\downarrow} = \gamma \left(T_{veg} - T_{s0} \right) + \mu \left(T_{veg} - T_{s0} \right)^2$ with $\gamma = 5.4$ and $\mu = 0.11$. However, this more complex form only slightly improved the nighttime model results compared to Eq. (3.7).

The vegetation surface temperature (T_{veg}) follows from the surface energy budget:

$$C_v \frac{\partial T_{veg}}{\partial t} = Q * -G - H - L_v E$$ (3.8)

where C_v is the heat capacity of the vegetation per unit area, $Q*$ is the vegetation surface net radiation, L_vE the latent heat flux. D91 found $C_v = 2.10^4$ J m^{-2} K for Cabauw, while W03 used $C_v = 2000$ J m^{-2} K for CASES-99 (and is used here).

Measurements (Section 3.2) show that both T_{veg} and T_{s0} experience rapid changes, which indicate that relatively high temporal frequencies play a vital role in the soil heat dynamics (W03; Heusinkveld et al., 2004). The modeled G should be able to reproduce these fast dynamics and therefore the model requires fine vertical spatial resolution to resolve this.
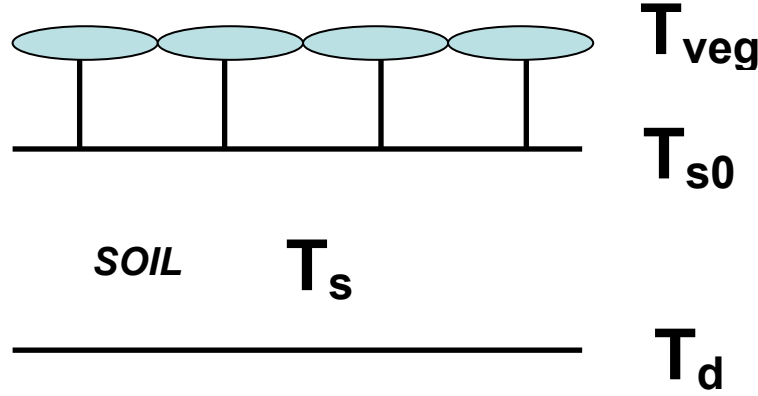
Figure 3.5: Illustration of the model set up of the vegetation and land surface. T_{veg} is the vegetation surface temperature, T_{s0} the soil surface temperature and T_d the deep soil temperature at 75 cm in the soil.
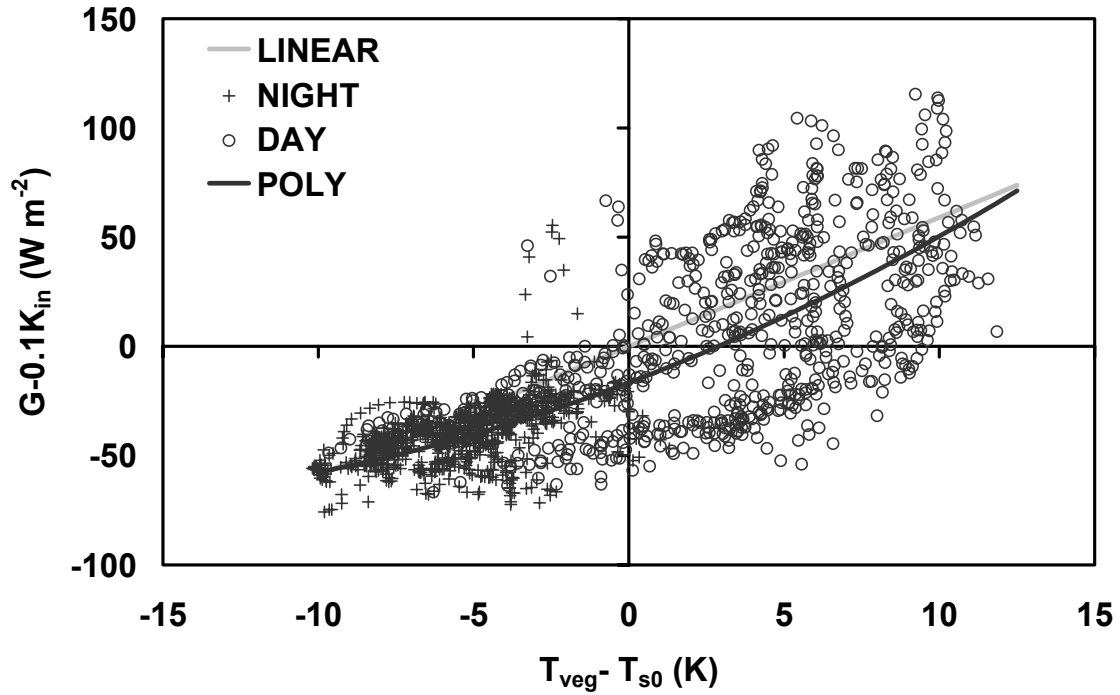
Figure 3.6: Observed relationship between the soil heat flux and the temperature difference between the vegetation surface temperature and the soil surface temperature. Open circles are data with daytime observations, plusses are nighttime observations (based on incoming solar radiation). The black thick line is a quadratic fit through the observations and the grey thick line is a linear regression through the observations (see text, Equation (3.7)). The slope of the curve indicates the bulk conductance.

Consequently, we add a homogenous soil of 0.75 m (150 layers with a vertical resolution of $\Delta z = 0.005$ m). Of course, in practice one could save computing time by using a logarithmic spacing near the surface. The soil diffusivity $\kappa = 0.155.10^{-6}$ m^2 s^{-1} (as found by W03), soil density 1850 kg m^{-3} and its heat capacity 2150 J kg^{-1}. We apply no explicit scheme for soil moisture.

d) Grid structure

To account for the large gradients of wind speed, temperature and humidity near the surface, we use a logarithmic grid spacing with $\Delta z \sim 0.5$ m close to the surface and $\Delta z \sim 60$ m at the model top (1800 m):

$$Z = \frac{z}{A} + \ln\left(\frac{z+B}{B}\right).$$

(3.9)

Here Z is the level of the grid points and z the actual height. We choose A = 200 m, B = 1 m. The first model level is located at 0.30 m. The model results are quite insensitive to the exact location of the first model level. A fine grid mesh is not specifically required for turbulent flux calculation (due to the compensating effects already indicated by Delage, 1988), but is necessary for the radiation transfer model (Ha and Mahrt, 2003).

e) Initial conditions

The initial profiles for wind speed, temperature and humidity are obtained from the radiosonde observations at the CASES-99 central site, 23 October 1999, 1400 CDT. At that time, the potential temperature in the convective boundary layer is constant up to 800 m.

The geostrophic wind $\mathbf{V_g}$ to force the model was derived from a series of radiosonde observations (usually available every 3 hours) at the CASES-99 central site at 800 m above ground level (Fig. 3.7). Based on the observations it is felt that the impact of baroclinicity was relatively small, so it is neglected and $\mathbf{V_g}$ is taken constant with height. Above $z = 1000$ m we prescribe the wind speed equal to $\mathbf{V_g}$.

From the CASES-99 observations we estimated $z_0 = 0.03$ m (W03; Sharan et al., 2003) and we apply $z_{0h} = z_0/10$ for the roughness length for heat (Garratt, 1992). For the calculation of the evapotranspiration, the canopy resistance was set constant at 1400 s m^{-1} to represent the very dry soil at the end of the growing season.

We used the observed values of initial vegetation surface temperature $T_{veg} = 296.1$ K, the initial soil surface temperature $T_{s0} = 292.6$ K and the deep soil temperature at $z = 0.75$ m in the soil $T_d = 286.6$ K. The initial soil temperature profile was imposed $T_s(z, t = 0) = \max$ (283.0, $T_{s0} - A\sqrt{z}$) K with $A = 16\,\mathrm{Km}^{-\frac{1}{2}}$. In this manner, the deep soil temperature matches the observed 288.0 K at 0.08 m and the T_s is uniform below 0.36 m. The lower boundary condition is a constant T_d of 283 K. The long-wave incoming radiation at the model top was taken from climatological values in Cerni and Parish (1984, their Fig. 3.5) and amounts 250 W m^{-2}.

f) Advection

The SCM approach requires prescription of advective tendencies. We determined the temperature advection rate from a mesoscale analysis of radiosondes in a network around the CASES-99 site. All sites are typically at 250 km distance from the CASES-99 site: Norman (Oklahoma, OUN), Dodge City (Kansas, DDC), Topeka (Kansas, TOP) and Springfield (Mis-

souri, SGF). We found 5.10^{-5} K s^{-1} for the temperature advection at the boundary-layer top for the period between 24 October 1400 CDT and 25 October 1400 CDT, and negligibly small advection for the rest of the period. From a mesoscale analysis with MM5, we found approximately the same value for temperature advection. This advection is prescribed to the whole model domain, except for the lowest 100 m where the advection decreases linearly to zero at the surface. Visual inspection of the inversion above the convective boundary layer from radiosondes provided the subsidence rate about $\sim 0.5.10^{-3}$ m s^{-1} during the first 48 hours and zero during the last 24 hours.
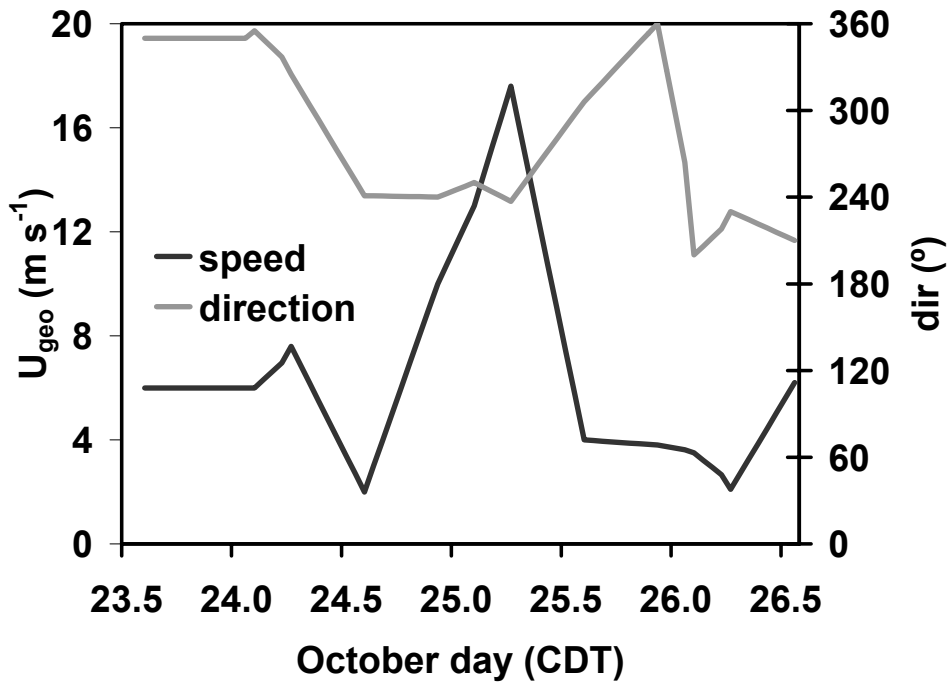
Figure 3.7: Graphical representation of the geostrophic wind speed (black line) and direction (grey line) obtained from radiosondes during CASES-99 for 23-26 October 1999. These observations are used to force the model.

3.5 Results and Discussion

This section provides model results in comparison with CASES-99 observations with a focus on surface fluxes, surface vegetation temperature, and vertical profiles of temperature and wind speed during nighttime. Note that the model is only initialized once and that the total run comprises three full days. Table 3.2 summarizes the bias, root-mean-square error (RMSE) and median of the error between model and observations for a number of surface variables.

a) Surface fluxes

The diurnal cycle of the modeled net radiation $Q*$ agrees with the observations (not shown). Net radiation amounts typically $Q* = 400$ W m^{-2} during daytime and $Q* = -70$ W m^{-2} during nighttime. For the second (turbulent) night and the second part of the third (radiative)

night, the magnitude of $Q*$ is somewhat underestimated (7.6 W m^{-2} on average). This is caused by the overestimated long-wave incoming radiation ($L^{\downarrow}$) (Fig. 3.8a). A first explanation for this overestimated $L^{\downarrow}$ is that the model is slightly too humid and too warm (next section), which increases the atmospheric emissivity and consequently $L^{\downarrow}$. A second possible explanation is that the real (unknown) $L^{\downarrow}$ at the model top can be larger than the imposed climatological value. The relative impact of radiative cooling is largest just during the day-night transition (not shown), which agrees with Funk (1960), Ha and Mahrt (2003) and Sun et al. (2003b). Outgoing long-wave radiation, $L^{\uparrow}$ is simulated correctly during the whole period, which implies an accurate simulation of the surface vegetation temperature (see Fig. 3.8e).

The evolution of the friction velocity (u_*) is shown in Fig. 3.8b. The friction velocity decrease during the sunset preceding the first (intermittent) night is simulated rather well, although the bias amounts 0.076 m s^{-1} over the whole night. The model lacks a clear turbulence collapse as observed during the first (intermittent) night. The cause of this overestimated u_* can either be due to the slightly underestimation of the fitted ϕ_m in the stability range of $1 < z/\Lambda < 3$ (Fig. 3.4a), or the imposed $\mathbf{V_g}$ is larger than the real $\mathbf{V_g}$. In the period 24 Oct., 700 CDT – 25 Oct., 1700 CDT the model performs well, while during the last (radiative) night u_* is slightly too high until midnight but follows the collapse at the end of the night. The overall bias amounts to 0.03 m s^{-1} for the last night. Sodar observations show much smaller wind speeds at 200 m AGL (which is above the SBL during this night) than the imposed $\mathbf{V_g}$. This may suggest that $\mathbf{V_g}$ was overestimated, and this consequently may explain the bias in u_*. In general it is known that models correctly predict u_* for strong winds, but overestimate u_* for weak winds (TD89, Sharan and Gopalakrishnan, 1997).

The maximum sensible heat flux amounts approximately 250 W m^{-2} during daytime (Fig. 3.8c) close to the observations. In the first (intermittent) night, the modeled $H = -14.1$ W m^{-2} on average, while -9.1 W m^{-2} was observed. However, the model does not simulate the observed intermittent character of the surface fluxes (Fig. 3.2). In contrast, the conceptual model by Van de Wiel et al. (2002a) was able to simulate and predict intermittent turbulence and was as such supported by observations. However, due to their highly simplified model, this can only be regarded more suggestive of intermittent SBL behavior than a rather definitive answer. Some models with more resolution (ReVelle, 1993; Welch et al., 1986) were also able to reproduce intermittent turbulence. On the other hand, the models by Sharan and Gopalakrishnan (1997) and Derbyshire (1999) did not show any intermittency. The current model is regarded as a more realistic physical model than the conceptual model by Van de Wiel et al. (2002a), with high resolution instead of a bulk scheme and with a more detailed soil and radiation scheme. A sensitivity study was performed (not shown) to investigate whether intermittency could be found in a certain part of the parameter space. A total collapse of the turbulence and even a small oscillation was found. However, this was not convincing evidence to state that the current model is able to represent intermittency, at least for the given case. This subject needs further investigation.

Just after the day-night transition to the intermittent night, the observed magnitude of *H* shows a clear maximum (see arrows in Fig. 3.8c), which is well reproduced by the model. This maximum is caused by a sudden reversal of the stratification near the surface due to long-wave radiation emission during the day-night transition, and is maintained by residual turbulence of the convective boundary layer. This is an often observed *realistic feature* (e.g. during 11 of the 30 nights for CASES-99 and in FIFE observations shown by Chen and Dudhia, 2001). However, most modeling studies rarely show these minima. The reproduction of this detailed feature emphasizes the realism of the model outcome.

During the turbulent night (24-25 Oct.), the predicted *H* follows the observations. The specific minimum during the day-night transition (24 Oct., 1900 CDT) is present here as well. Radiative flux divergence dominates the last (radiative) night and the observed *H* is approximately zero. The model slightly overestimates the magnitude of *H* (-2.9 W m^{-2}), mainly caused by an overestimation of u_*. This causes a weaker stratification and thus a larger magnitude of *H*. The second half of this night the model gives good results.

The actual latent heat flux was small, since the observed soil moisture content was low. The daytime Bowen ratio was ~ 5, which underlines the dry conditions. The latent heat flux shows a diurnal cycle with maxima of ~50 Wm^{-2} during daytime and negligibly small evapotranspiration during nighttime ($|L_vE| < 10$ W m^{-2}). The model satisfactorily simulates this (Table 3.2) with hardly any bias and small RMSE.

The model predicts G_0 accurately, except for a negative bias during noon (Fig. 3.8d). During nighttime, we find a bias of -0.2, -2.4 and -1.4 W m^{-2} for the three nights respectively. As mentioned above, G_0 is a dominant term in the surface energy budget (about −50 W m^{-2}) and has fast dynamics, i.e. a sharp maximum of the magnitude of G_0 is seen soon after the transition. TD89 also found this sharp maximum of the magnitude of G_0, although with a smaller frequency than found here. The fast dynamics are evidently important for the SBL development and are modeled correctly. This maximum occurs at the day-night transition, because the vegetation surface cools rapidly since the radiative forcing is largest at that moment. To compensate for the strong cooling, the magnitude of G_0 rapidly increases. Later on, the surface cooling rate is smaller because net radiative cooling diminishes (TD89; Poulos and Burns, 2003). As indicated above, the current model does not simulate intermittency in this case, thus no oscillations are present in the simulated G_0 either.

As mentioned in the introduction, a common problem for large-scale models is to provide a reliable prediction of T_{veg} (see also Section 3.2). Some models show unphysical decoupling of the atmosphere from the surface resulting in so-called "runaway cooling" of T_{veg} (Sorteberg, 2002). On the other hand, the pragmatic enhanced mixing approach that is commonly used for very stable conditions, leads to overestimation of T_{veg}. Fig. 3.8e shows the results for T_{veg} and Fig. 3.8f for T_{s0}, for the current study. For both day- and nighttime T_{veg} *is simulated in very good agreement with the data, despite the fact that we cover a broad range of stability.* Model bias amounts to -0.7, 1.1 and 0.0 K respectively for the three nights. This is a
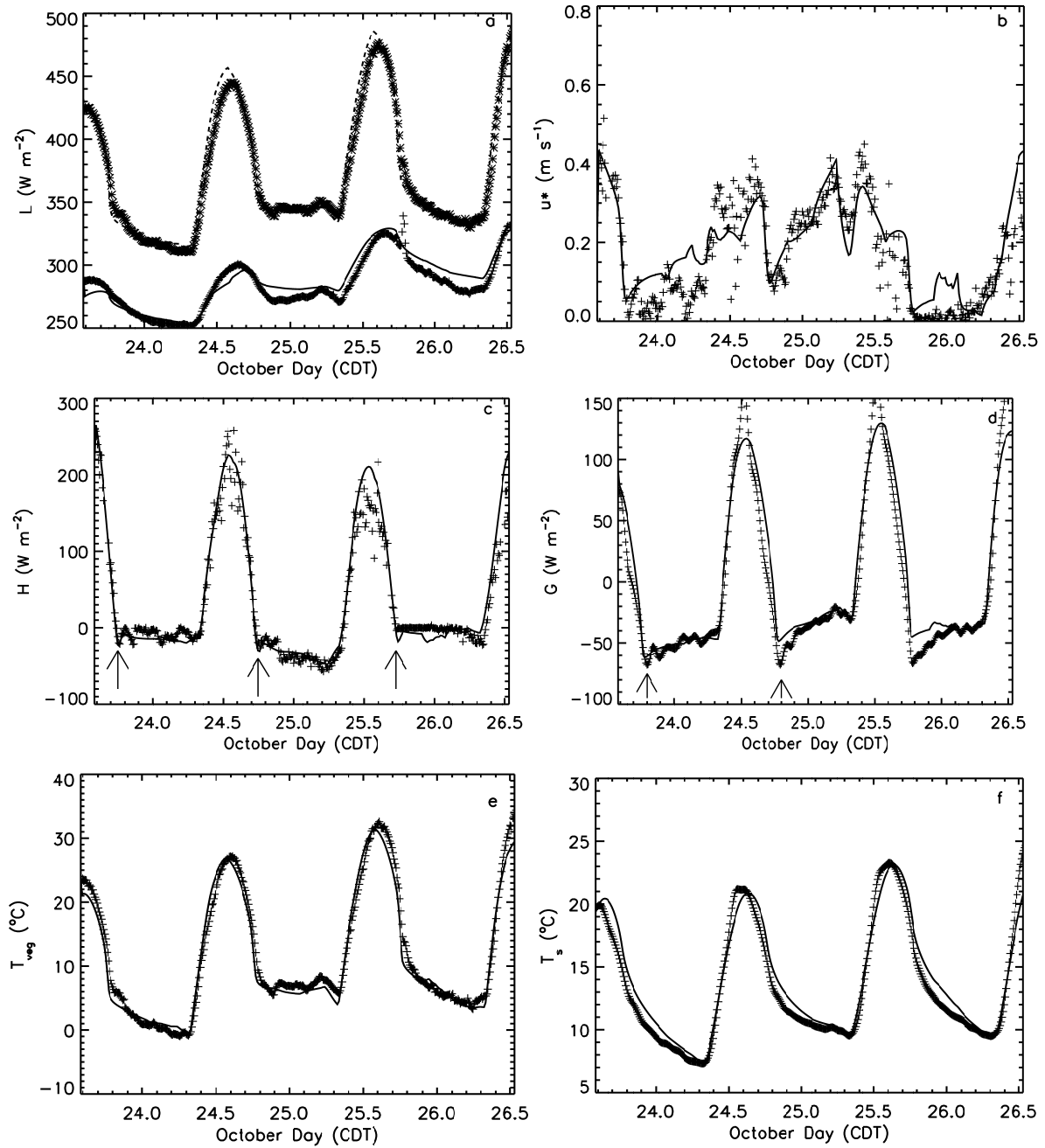
Figure 3.8: Time series of observed (+) and simulated (continuous line) downward long-wave radiation and observed (star) and simulated (dashed line) upward long-wave radiation at $z = 10$ m AGL (a), surface friction velocity (b), sensible heat flux (c), soil heat flux (d), vegetation surface temperature (e), and soil surface temperature (f), for the three nights during CASES-99.
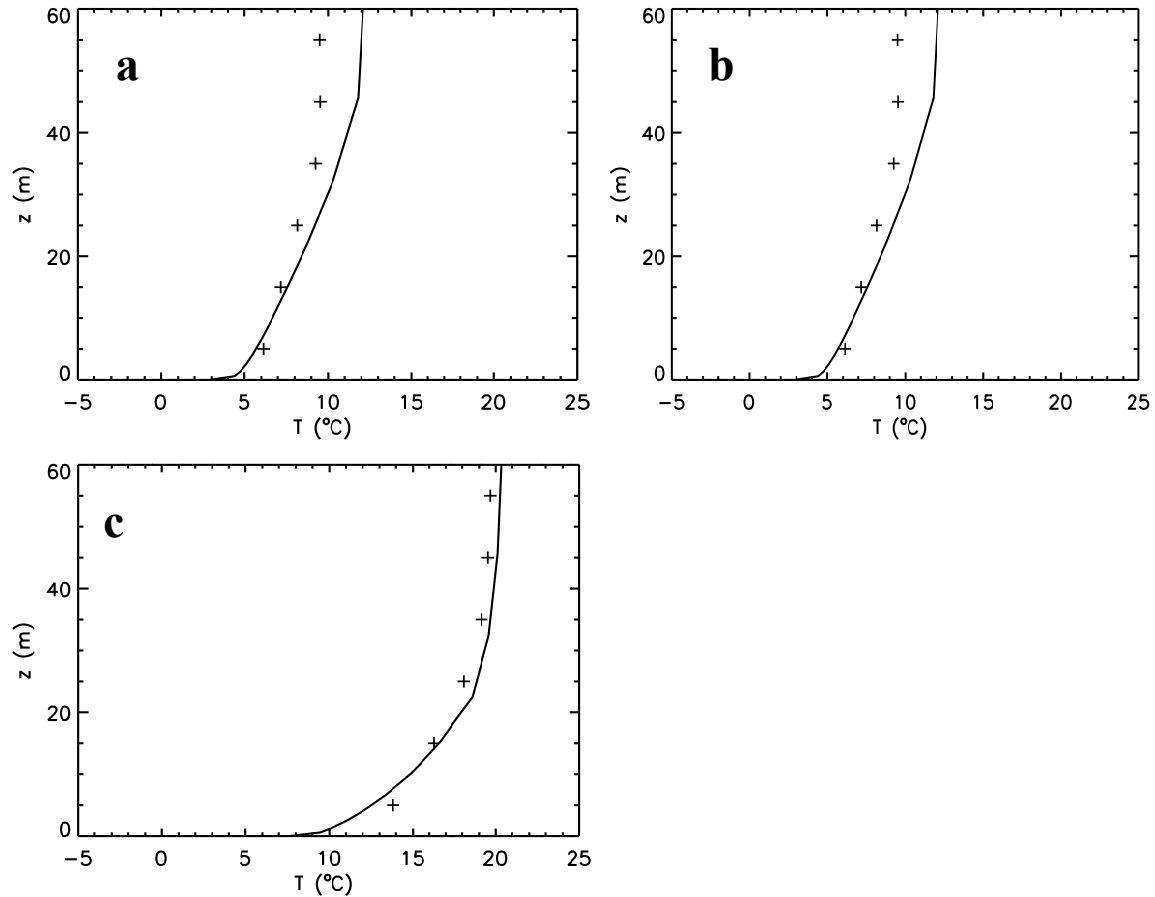
Figure 3.9: Observed (+) and simulated (line) temperature profiles for (a) 24 Oct, 100 CDT (intermittent night), (b) 25 Oct 100 CDT (continuous turbulent night) and (c) 25 Oct 2300 CDT (radiation night).

surprising result given the fact that T_{veg} is usually hard to predict, even with an off-line model (Best, 1998).

In summary, we conclude that the present model generates surface fluxes which are in good agreement with observations, because of the detail in the description of the surface scheme, the soil heat flux and radiation physics (with high resolution).

b) Vertical profiles

Figs. 3.9a-c show representative examples of observed and simulated instantaneous temperature profiles along the 60-m mast for the three nights. For the intermittent night (Fig. 3.9a), the agreement is reasonable, although the modeled curvature is less than observed. For the second (continuous turbulent) night (Fig. 3.9b) the temperature profile is represented very well. Both model results and observations show a strong curvature during the radiative night (Fig. 3.9c) with a surface inversion of about 13 K in the lowest 60 m. We can attribute satisfactory modeling to the radiation transport model, which takes over the heat transport in *a natural way* when turbulence vanishes. After the turbulence vanishes, the model does not show any kind of so-called runaway cooling. Negative feedbacks in Q^* (decreasing in response to surface cooling) as in G_0 (increasing magnitude in response to surface cooling)

compensate for absence of turbulence in a natural way. This clearly underlines the fact that a radiation transfer model is required, preferably with a high vertical resolution near the surface. The current model also satisfactorily reproduces the results of Estournel and Guedalia (1985) for $V_g = 3$ m s^{-1} (not shown).

Figs. 3.10a-c show measured (along the mast and from sodar) and modeled wind speed profiles. Sodar and mast observations agree well with each other, although they have been measured at a horizontal distance of approximately 2 km. During the first (intermittent) night (Fig. 3.10a), the modeled and observed wind speed profiles agree fairly well. During the fully turbulent night (Fig. 3.10b) with a wind speed of 9 m s^{-1} at 60 m, the wind profile estimate is in good agreement below $z = 60$ m. Above this level, the LLJ is clearly seen by sodar observations, but is underestimated in the model (see also Mailhot and Benoit, 1982). Lack of vertical resolution to resolve a LLJ cannot explain this deficiency here. Baroclinicity can play a role in the development or sharpening of the LLJ in reality (Stull, 1988) while we neglect baroclinicity in our SCM approach.

During the third (radiative) night, the observed wind is very weak. In the beginning of the night (before 200 CDT), the modeled wind speed is too large, probably related to the fact that our imposed V_g was larger than V_g in reality. In this period, the observed wind speed profile was decoupled from the surface over a ~20 m thick layer.

Table 3.2: Bias, root-mean-square error and median of the error between model results for the period (0 - 6 CDT) and observations, separated per night.

	BIAS			RMSE			Median		
	23-24	*24-25*	*25-26*	*23-24*	*24-25*	*25-26*	*23-24*	*24-25*	*25-26*
	INT	*TURB*	*RAD*	*INT*	*TURB*	*RAD*	*INT*	*TURB*	*RAD*
H (Wm^{-2})	5.0	-7.6	2.6	9.0	9.4	6.8	6.5	-7.8	2.4
L_vE (Wm^{-2})	-1.7	-1.1	-0.3	1.9	1.4	0.68	-1.9	-1.1	-0.15
G_0 (Wm^{-2})	-0.24	-2.4	-1.8	3.3	3.2	3.8	-0.07	-3.0	-1.26
T_{veg} (K)	-0.74	1.1	0.01	0.84	1.2	0.57	-0.74	1.1	0.16
u_* (ms^{-1})	-0.076	-0.015	-0.030	0.09	0.04	0.055	-0.07	-0.017	-0.019
RH(2m) (%)	2.4	-7.1	-18.3	2.3	7.8	19.8	2.3	8.0	-18.1
$Q*$ (Wm^{-2})	0.74	-7.6	-10.0	1.9	7.9	10.8	0.6	-6.8	-11.0
$L^{\downarrow}$ (Wm^{-2})	-2.8	-5.5	-10.8	2.9	5.9	11.2	-2.8	-6.1	-10.7
$L^{\uparrow}$ (Wm^{-2})	-3.6	2.1	-0.89	3.9	2.8	2.7	-3.6	2.3	0.0
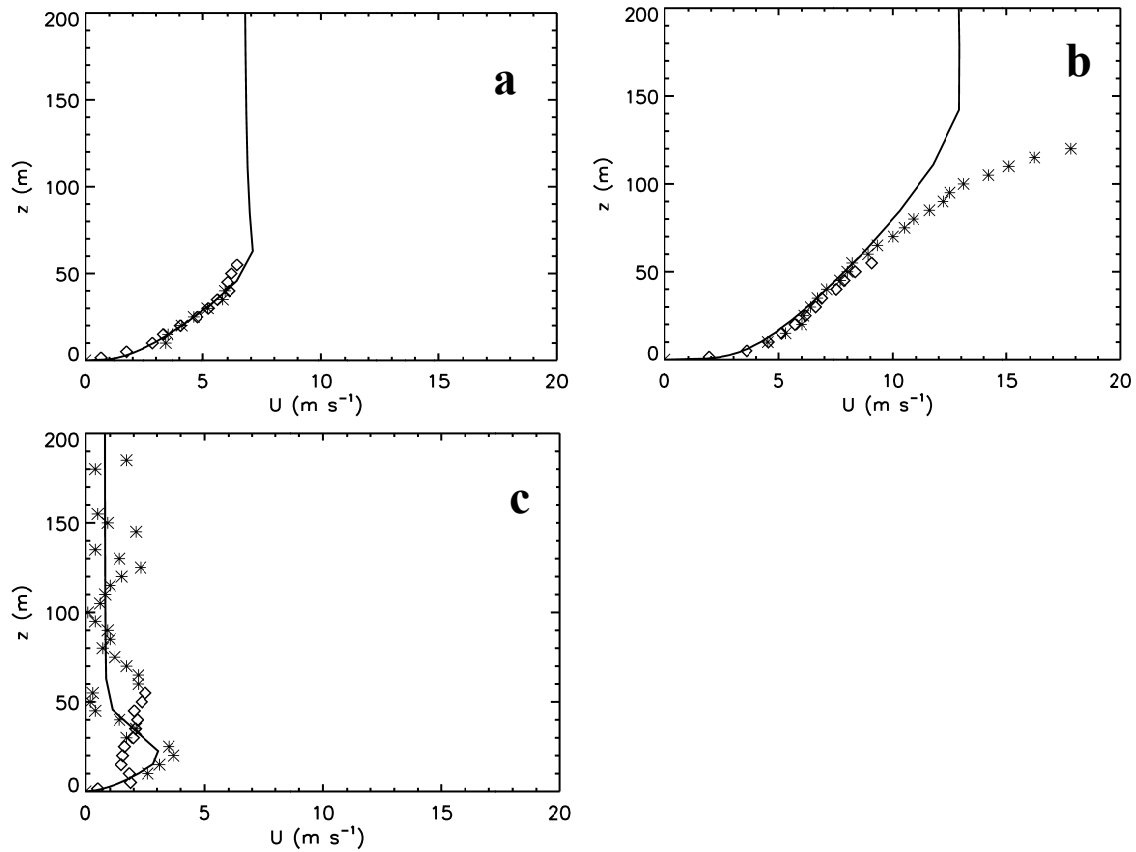
Figure 3.10: Same as figure 3.9, but for wind speed. Diamonds denote the mast observations and stars the sodar observations.

The model is not able to capture this decoupled boundary layer and overestimates the wind speed. Model results compare well with sodar observations for the shown profile, which is representative for the period 200 - 500 CDT. A weak LLJ (3.5 m s^{-1}, 25 m AGL) was observed, although the model underestimates its strength. Mast measurements clearly depart from sodar observations. With these weak winds, the SBL structure differs on small spatial scales. In addition, we approach the anemometer measurement accuracy. Specific humidity profiles show reasonable agreement (maximum bias 0.5 g kg^{-1}, not shown), except just before 26 Oct, 0000 CDT where a temporary accumulation of humidity appears (bias of +1.5 g kg^{-1}) and negative specific humidity gradient.

In general, the model is able to estimate temperature and wind profiles, except for the night that is purely driven by radiative cooling where the decoupled wind profiles could not be modeled correctly. In their intercomparison study, Sharan and Gopalakrishnan (1997) found that mean profiles become insensitive to the type of closure. The diffusion in these conditions is so small that differences in diffusion are hardly seen in the mean profiles. This underlines that processes other than turbulent diffusion become more important when the wind drops.

Figs. 3.11a-c show the characteristic calculated total cooling subdivided in the radiative cooling and the turbulent cooling as function of height for the three nights at 0200 CDT. Both turbulent and radiative cooling profiles are well defined for the first two nights, with strong

radiative cooling near the surface. Cooling profiles are comparable with those in TD89 who used a line-by-line radiation transfer model and with the results in Gopalakrishnan et al. (1998). For the last night we note that the cooling rates are large, especially considering the fact that the boundary layer is thin. Radiative cooling is less well defined with warming between $z = 10$ and 20 m, while the turbulent cooling is much stronger (large flux divergence despite small fluxes). The radiative warming is caused by the local accumulation of humidity in the lowest model levels (below $z = 50$ m) where $dq/dz < 0$. Below $z = 5$ m, dq/dz decreases and the radiation transfer model predicts cooling.

c) Sensitivity to initial conditions.

To examine the robustness of the results, we performed some sensitivity analysis on the initial conditions and model parameters. Disturbing the initial temperature (by 1 K), wind profiles (by 5%), soil temperature and vegetation temperature (both by 1 K) do not affect the results seriously. In addition, re-initialization the model every 24 hours (1400 CDT) with observed radiosonde information showed hardly any impact on the results (not shown).
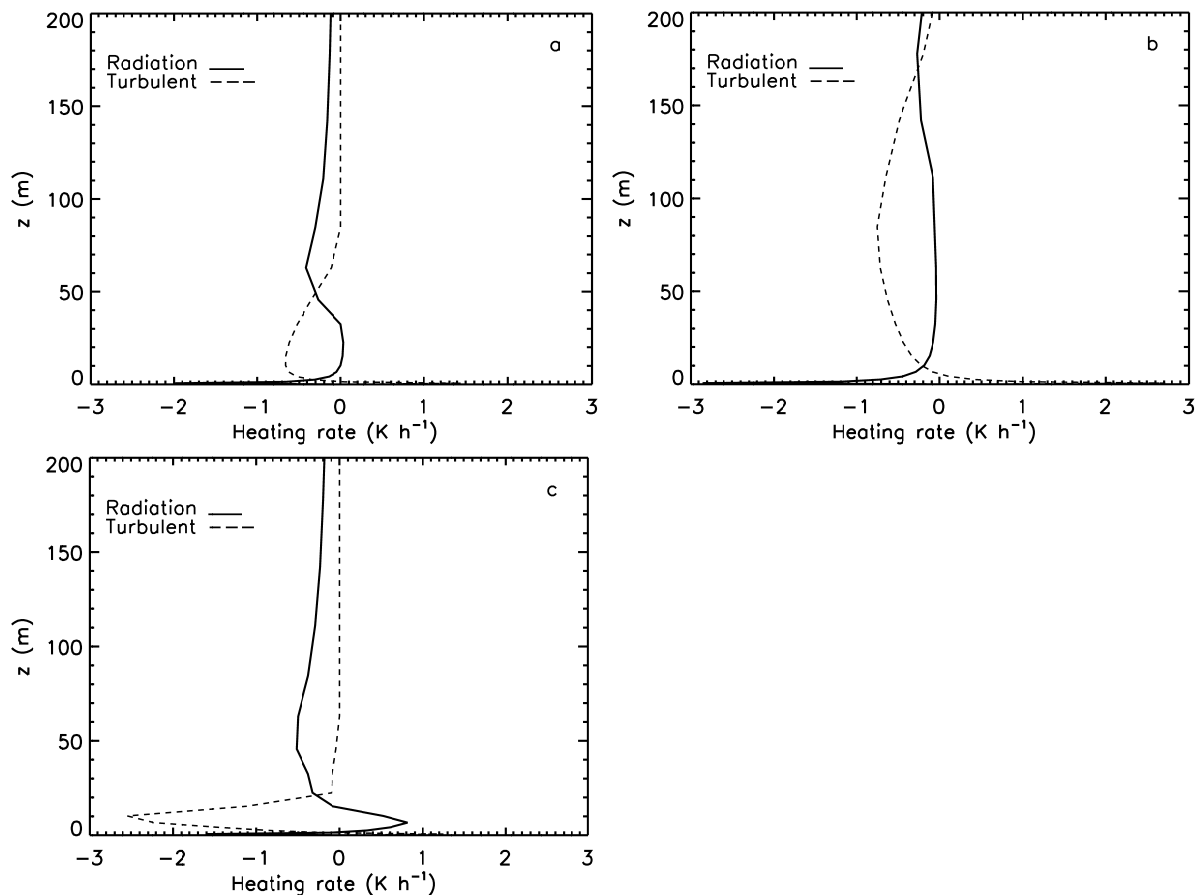
Figure 3.11: Vertical profiles of estimated turbulent (full line) and radiative cooling (dashed line) for (a) 24 Oct, 100 CDT (intermittent night), (b) 25 Oct 100 CDT (continuous turbulent night) and (c) 26 Oct 0200 CDT (radiation night).

3.6 Conclusions

The aim of the paper is to investigate whether the stable boundary layer can be satisfactorily modeled over a broad range of atmospheric stability with the current understanding of the stable boundary-layer physics. Therefore, we have studied the development of the atmospheric boundary layer over land for a three-day period including three different archetypes for stable conditions. These archetypes are a (i) fully turbulent night, an (ii) intermittently turbulent night and (iii) a radiation driven night. To ensure vertical resolution was not a limiting issue, we use very high resolution in both the atmosphere and the soil. We compare single-column model results with CASES-99 observations. Contrary to many former single-column models studies that prescribed the surface temperature, the current model solves the diffusion equation for heat in the soil and a detailed coupling between the soil and a vegetation layer. Furthermore, we use stability functions directly based on the local observations (which are well in agreement with previous ones).

We find that the vertical structure, the surface fluxes and the surface temperature in the stable boundary layer can be satisfactorily modeled (at least at a local scale) with our current understanding of the physics of the stable boundary layer for a broad stability range. This can be achieved by the use of a detailed coupling between the atmosphere and the underlying soil and vegetation, together with high resolution in both the atmosphere and the soil. These results are surprisingly good, certainly given the problematic feature regarding the parameterization of the stable boundary layer in large-scale models and the fact that in our case the model was initialized only once for the three-day period examined. Features that are not captured by the current model are the intermittent nature of the surface fluxes during the intermittent night and the sharp low-level jet in the turbulent night (the latter is related to the one-dimensional model character). Nevertheless, we have shown that a state-of-the-art boundary-layer model coupled to the vegetation and underlying soil, without limitations to the amount of vertical resolution in the soil and the atmosphere, is able to reproduce the CASES-99 observations. In a future study, we plan to explore the sensitivity of the model formulations to vertical resolution in more detail and to extend our findings for applications on a larger scale.

Appendix 3A: Estimating the flux-profile relationships for CASES-99

To cover the broad stability range in this study (Figs. 3.4a and 3.4b), the classical Businger-Dyer flux-profile relations (Businger et al., 1971) are extended from the weakly SBL ($z/\Lambda < 1$) to $z/\Lambda = 7$ with data from the CASES-99 experiment. Thermocouples and anemometers are located at z = 5, 15, 25, ..., 55 m and sonic anemometers at z = 1.5, 5, 10, 20, ..., 50 and 55 m and were considered with 5-min intervals. We estimate vertical gradients with an extension of the log-linear function (Nieuwstadt, 1984):

$$X = A + Bz + Cz^2 + D \ln z , \qquad (3.A1)$$

with $X = \theta$ or U. Alternatives for Eq. (3.A1) are given in e.g. Akima (1970), Oncley et al. (1996), Frenzen and Vogel (2001) or Johansson et al. (2001). The variability of the gradients from these methods is within 20% of the estimate for $z > 10$ m, but we found a factor 2 difference between methods near the surface. Only the log-linear profile and Eq. (3.A1) can capture large gradients near the surface. We restricted ourselves to data points with $d\theta/dz > 0.025$ K m^{-1}; $dU/dz > 0.025$ s^{-1}; $1.5 < z < 50$ m and $\overline{w'\theta'} < -0.005$ K m s^{-1}. Nights that were classified as radiative by W03 were excluded.

Appendix 3B: Model Sensitivity to Resolution in the Soil and Applicability in Operational Models

1. Introduction
The current paper shows the stable boundary layer can be satisfactorily modeled for a large range of atmospheric stability, if we know the boundary conditions (specifically geostrophic wind speed and soil and surface properties) accurately and use fine resolution in both the atmosphere and the soil. For operational large-scale models (e.g. ECMWF) such fine resolution is computationally too costly. Here we examine the applicability of the model results for coarse resolution and investigate what could be a suitable resolution.

2. Sensitivity to resolution in the soil
To examine the sensitivity of the model results to resolution in the soil, we rerun the case in Chapter 3 for resolution of 0.01 m, 0.05 m, 0.1 m, 0.15m, and 0.25 m in the soil. Fig. 3.A1 shows the difference of the predicted minimum vegetation surface temperature for the three nights compared to the run with Δz = 0.005 m. The minimum temperature strongly depends on the vertical resolution, but starts to converge around Δz = 0.07 m. For Δz = 0.07 m the difference with the default run is approximately 0.35 K, which is acceptable for operational forecasts. The sensitivity on resolution is stronger for the weak wind nights (1st and 3rd night).
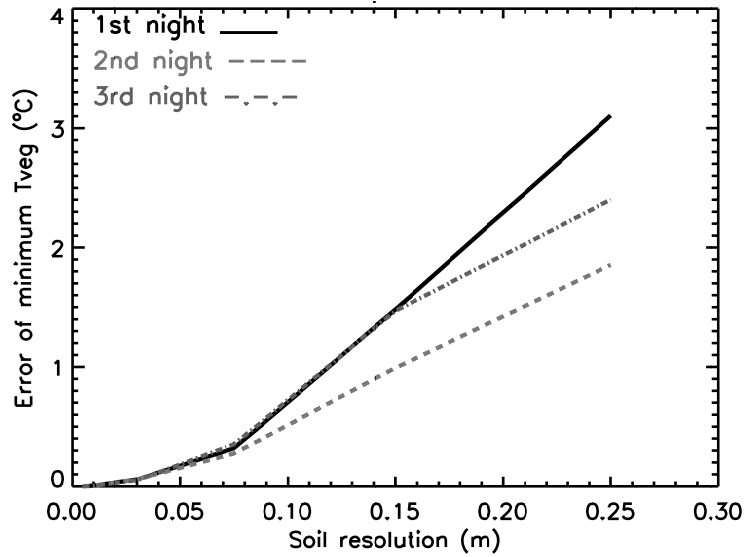
Figure 3.A1: Error in the predicted minimum temperature as function of the vertical resolution in the soil for each night. The error is calculated according to the run with the default resolution with $\Delta z = 0.005$ m.

3. Operational model set-up

To assess the model forecast quality for operational use, a logarithmically distributed grid mesh was built in (similarly as the TESSEL scheme in ECMWF). The model layers are 0.035 m, 0.14 m, 0.465 m and 1.26 m thick. Fig. 3.A2 shows a scatter plot of modeled vegetation surface temperature with fine (0.005 m) and operational resolution. Both simulations shows good correspondence.
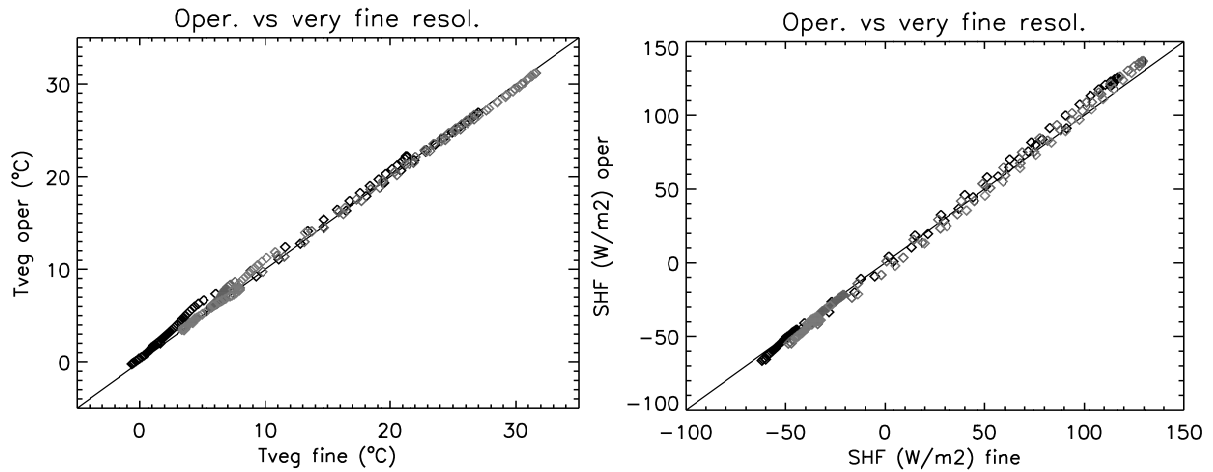
Figure 3.A2: Modelled surface vegetation temperature (a) and soil heat flux (b) for three different nights during CASES-99 as function of resolution in the soil.

4. Conclusion.

The model with operational resolution can predict the stable boundary-layer structure and surface accurately with the state-of-the-art resolution in the soil.

Chapter 4

Evaluation of limited area models for the representation of the diurnal cycle and contrasting nights in CASES-99

Abstract

This study evaluates the ability of three limited area models (notably MM5, COAMPS, and HIRLAM) to predict the diurnal cycle of the atmospheric boundary layer during the CASES-99 experimental campaign. We pay special attention to the stable boundary layer. Limited area model results for different boundary-layer parameterizations and different radiation transfer parameterizations are compared with the in situ observations. Model forecasts were found to be sensitive to the choice of the boundary-layer parameterization both during the day and at night. At night, forecasts are particularly sensitive to the radiation scheme. All three models underestimate the amplitude of the diurnal temperature cycle (DTR) and the near surface wind speed. Furthermore, they overestimate the stable boundary-layer height for windy conditions and underestimate the stratification of nighttime surface inversions. Favorable parameterizations for the stable boundary layer enable rapid surface cooling, and they have limited turbulent mixing. Additionally, we find that a relatively large model domain is required to model the Great Plains low-level jet. Finally, we implement a new scheme for the stable boundary layer in the medium range forecast model (MRF). This scheme introduces a vegetation layer, a new formulation for the soil heat flux, and turbulent mixing based on the local scaling hypothesis. The new scheme improves the representation of surface temperature (especially for weak winds) and the stable boundary-layer structure.

4.1 Introduction

Limited area models (LAM) such as MM5 (Dudhia and Bresch, 2002), COAMPS (Hodur, 1997) and HIRLAM (Undén et al., 2000) are used for operational short-range regional weather forecasting, to predict air pollution episodes (Hanna and Yang, 2001; hereafter HY01), to reconstruct regional budgets of several trace gases, e.g. CO_2 (Aalto et al., 2006), and for atmospheric research. It is important for many applications that LAMs predict correctly the profiles of potential temperature (θ), specific humidity (q), trace gases and wind speed and direction, as well as surface turbulent and radiation fluxes. To achieve this we need to include the relevant physical processes in the atmospheric boundary layer (ABL) within LAMs.

At mid-latitudes, the ABL undergoes a clear diurnal cycle (Betts, 2001). Daytime insolation heats the surface and a turbulent heat flux is directed towards the atmosphere. The ABL is well-mixed by convection which transport heat, moisture and scalars upward from the surface. ABL top entrainment also affects θ and q inside the ABL (e.g. Stull, 1988; Holtslag et al., 1995; Steeneveld et al., 2005). In contrast, at night, the ABL is not well-mixed and strong vertical gradients in wind speed and temperature are observed. Besides turbulent mixing, the impact of radiation divergence (e.g. Ha and Mahrt, 2003) and the feedback from the underlying soil and vegetation is also evident for stable conditions (Holtslag and De Bruin, 1988; Beljaars, 2001; Steeneveld et al., 2006b, hereafter S06). Moreover, a low-level jet (LLJ) can develop at night (e.g. Song et al., 2005), which can contribute to the ABL turbulent structure. In general, the structure of the stable boundary layer (SBL) is more complicated and more variable than the structure of the daytime ABL (Mahrt, 1998, 1999), making it more difficult to model.

Recent LAM evaluation studies have focused on specific topics such as complex terrain (Zhong and Fast, 2003; Berg and Zhong, 2005), Arctic (Tjernström et al., 2004) or Antarctic regions (e.g. King and Connolley, 1997), air pollution episodes (HY01), tropical cyclone formation (Braun and Tao, 2000), the American monsoon (Bright and Mullen, 2002) or the convective boundary layer (CBL, Vilà-Guerau de Arellano et al., 2001). Less attention has been paid to model representation of the diurnal cycle (Zhang and Zheng, 2004), although its representation in models is rather problematic (Beljaars, 2001; Holtslag, 2006). Moreover, the representation of the SBL in LAMs has not been comprehensively evaluated. Good representation of the diurnal cycle and the SBL is a key issue for Numerical Weather Prediction (NWP) and regional climate modeling, for air quality studies, wind energy engineering, and atmospheric research.

Considerable progress has been made in ABL parameterizations for NWP and climate modeling. However, the SBL is relatively poorly understood and modeled (Beljaars, 1995; King and Connolly, 1997; Savijärvi and Kauhanen, 2001; Cassano et al., 2001; Cuxart et al., 2006), since it is driven by two distinct physical processes: turbulence and radiative cooling. Additional processes such as gravity waves, intermittent turbulence, density currents, and

katabatic winds could play an important role, as well as the effects of land-surface heterogeneity. Consequently stationarity and homogeneity are usually absent at night, and parameterizations often fail (e.g. Holtslag, 2006).

This study extends previous work by evaluating three LAMs focusing on the representation of the diurnal cycle, and the SBL in particular. Due to the complexity of the SBL itself, we limit ourselves to three selected consecutive clear days, over relatively simple topography (CASES-99).

Previous studies mainly addressed the model sensitivity to turbulence schemes. Here we also discuss the sensitivity to the radiation scheme, because both processes play a key role in predicting the diurnal cycle. As such also the interplay between the turbulence, radiation and land-surface, is also considered through the surface vegetation temperature T_{veg} (Fig. 4.1). Since T_{veg} (together with the air temperature T_a) governs the atmospheric stability, it also governs the turbulence intensity. Moreover, the nighttime near surface clear air radiative cooling appears to be proportional to T_a- T_{veg}. Finally, the difference between T_{veg} and the soil temperature governs the soil heat flux (G). Thus, T_{veg} plays a key role for the surface energy budget and is therefore more critical than e.g. the 2m temperature.

Since many permutations of both the surface layer, ABL and land-surface schemes are considered in the current study, our strategy is to *a)* search for common deficiencies in all models, and *b)* to examine whether a certain model description is advantageous under certain atmospheric conditions. From this we can learn how to improve which perform less well in those conditions. Also LAMs other than those considered in our study may benefit from our findings. Finally, we implement an improved scheme for the SBL in MM5. This scheme introduces a vegetation layer to the land-surface scheme, a more realistic formulation for G, and local mixing at night. The new scheme provides a much better representation of T_{veg} and the SBL vertical structure (especially for weak winds).
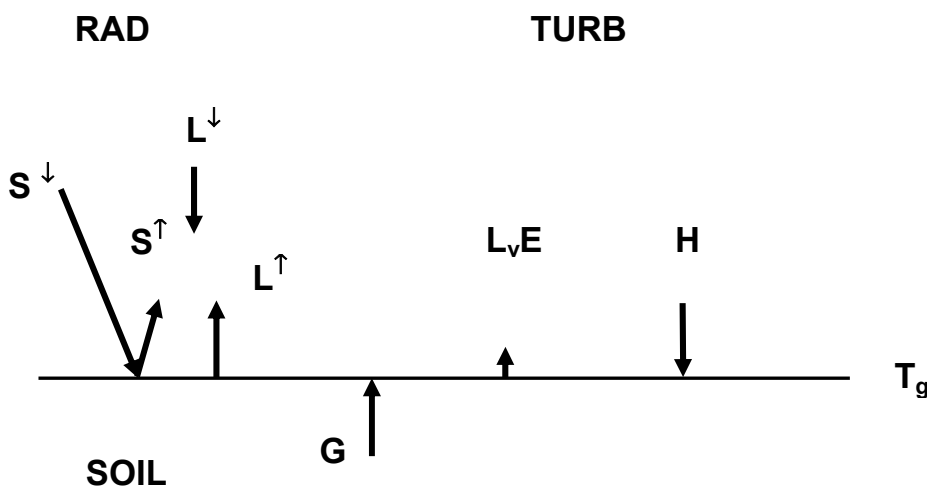
Figure 4.1: Illustration of the interaction between the energy fluxes by different physical processes in the SBL. The surface temperature T_g plays a central role in the SBL physics with its direct impact and feedbacks with the turbulence, radiative transport and the land-surface.

This study aims to examine whether ABL parameterizations in different LAMs, are able to forecast the mean thermodynamic profiles correctly, and consistently with the surface turbulent and radiation flux calculations (especially for the SBL). We compare widely used ABL schemes in MM5, COAMPS and the HIRLAM version operational at KNMI on three contrasting diurnal cycles during the CASES-99 campaign: calm, moderately windy and strong wind conditions (as in S06).

4.2 Observations and synoptic conditions

a) Observations

For this study we select the period 23-26 October 1999 during the CASES-99 campaign (Poulos et al., 2002), which has been analyzed before with a column model study in S06. This period has been chosen because the nights differ strongly in turbulence intensity. The first night is intermittently turbulent, the second is fully turbulent, and the third is hardly turbulent and mainly driven by radiative cooling (S06). The experiment has been conducted near Leon, Kansas, U.S.A. (37.65º N, 96.73º W, 436 m ASL). The area consists of gently rolling homogeneous terrain with a relatively dry soil, and lacks obstacles in the near surroundings. The area consists of prairie-grass, and has a roughness length for momentum (z_0) of 0.03 m.

Ground based observations consist of θ, q and wind profiles along a 60 m tower (mounted at 1.5, 5, 10,…, 55 m), and turbulent and radiative fluxes near the surface. The eddy-covariance measurements of the surface sensible heat flux, latent heat flux, and friction velocity were obtained at 2.6 m. G has been obtained as in Van de Wiel (2002). The surface energy budget closure is approximately 100% for these nights (S06). Additionally, sodar observations and irregularly launched radiosondes provided information on upper air characteristics and the ABL height (h), here taken arbitrarily as the height of 8 dB sodar signal reflection. Alternative h derived from turbulence observations along the 60 m tower are also used (Vickers and Mahrt, 2004). As such, this unique and extensive dataset is excellent evaluation material for the current study.

b) Synoptic conditions

The three selected nights have a moderate, strong and very weak synoptic forcing respectively (Fig. 4.2). During the first night the CASES-99 site is located under a high-pressure system with a geostrophic wind speed ~6 ms^{-1}. The near surface turbulence is of intermittent character during this night. During the second night a trough is west of the measurement site (Fig. 4.2b), which coincides with increasing geostrophic forcing in time and heat advection. At about 200 m AGL a typical Great Plains LLJ of 21 ms^{-1} was observed (Banta et al., 2002). A weak front passes at the end of the night, which was most clearly seen in the q increase from ~2.5 to ~6 g kg^{-1}, although no clouds were observed. In the last night, the site is under a high pressure area, and the geostrophic wind speed is about 4 ms^{-1}, and decreases at night. Advection is absent and radiative cooling plays an important role in the SBL during this night.
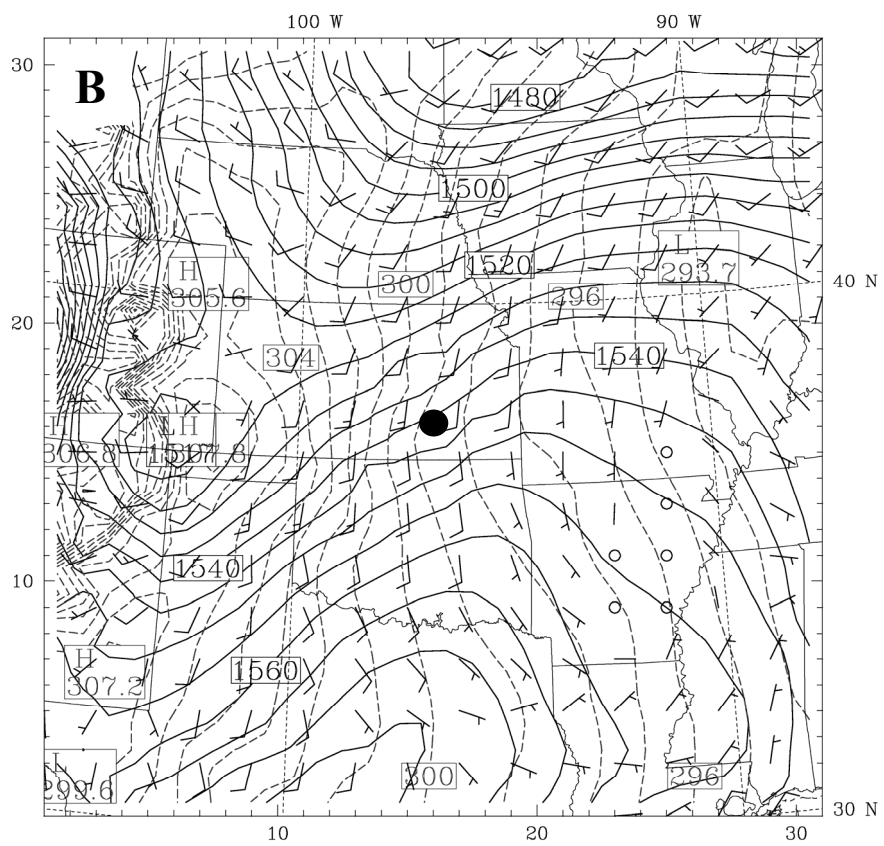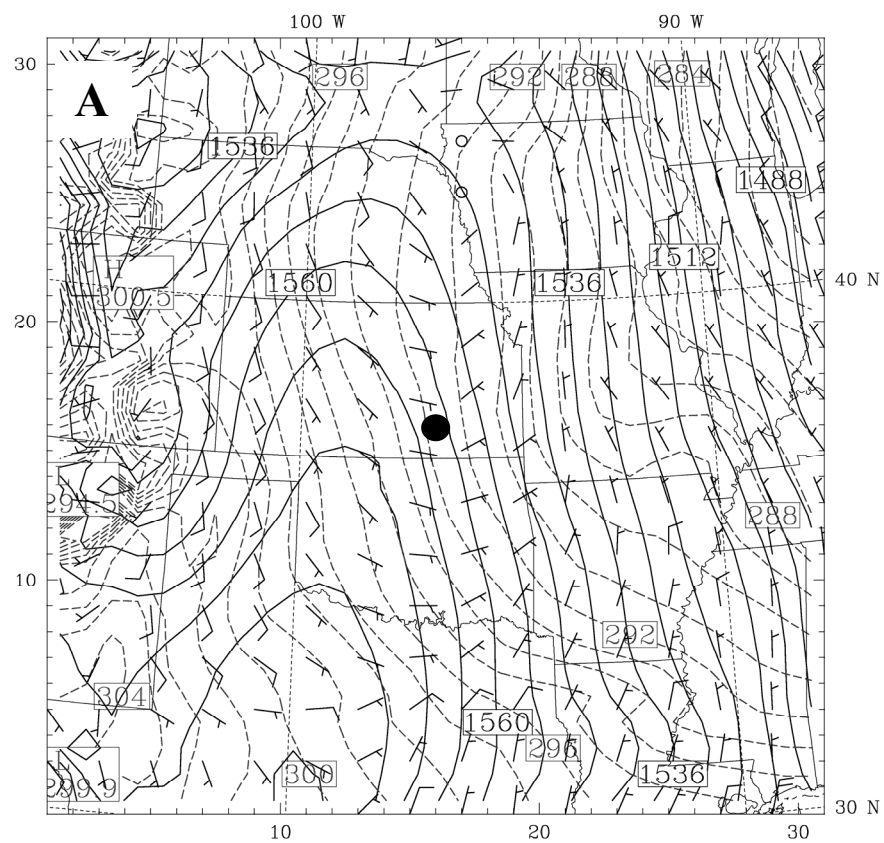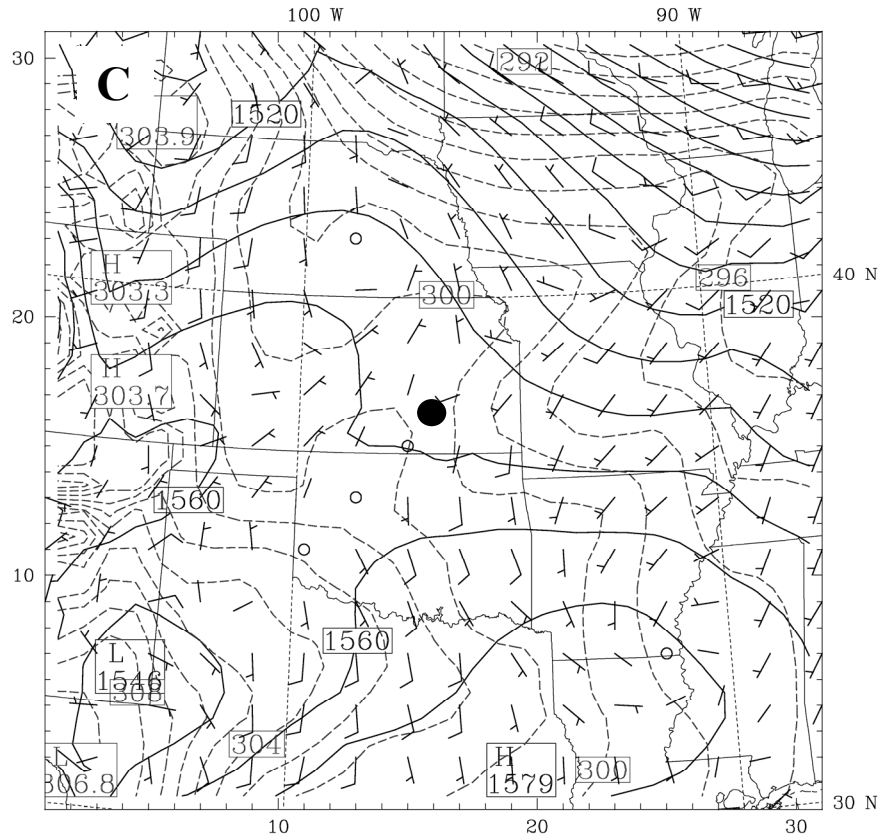
Figure 4.2: Synoptic overview at 0600 UTC (local midnight) for the three considered diurnal cycles: a) 24 Oct, b) 25 Oct, and c) 26 Oct. Plotted are 850 hPa geopotential height (black line), 850 hPa potential temperature (dashed line), and 10 m wind speed (vector) as forecasted by the MM5-MRF scheme. CASES-99 site is in the middle of the domain and marked with the block dot.

4.3 Model descriptions and configurations

4.3.1 Configuration

The LAMs are run for a 1620 km x 1620 km area over the central part of the U.S.A. (Fig. 4.3). MM5 and COAMPS use 31 x 31 grid points with a grid spacing in the outer domain of 54 and 49 km respectively. Three smaller domains (also 31 x 31 nodes) with a resolution of 18, 6 and 2 km are nested inside this domain to avoid model errors from coarse resolution. HIRLAM uses 10 km horizontal resolution without nesting in the whole domain, covering nearly the entire U.S.A. Although the three models do not have exactly the same horizontal resolution, they all use a very high resolution. Since land-surface properties are rather homogeneous in this region, significant improvement from increased resolution should not be expected. This was confirmed from coarse grid MM5 and COAMPS simulations, where the results from the 2 and 6 km nests are nearly identical.

The U.S. Geological Survey provides the land surface characteristics (Zehnder, 2002). We used the locally observed values for z_0 (0.03 m) and the soil moisture availability ($M = 0.08$), for the relevant land-use types. MM5 employed 36 terrain following σ_P-levels (22 layers are

71

in the lowest 2 km), COAMPS used 50 σ_z-levels, and HIRLAM 40 hybrid layers. Initial and boundary conditions for atmospheric variables are taken from the ECMWF (1º x 1º) operational analysis every 6 hours. No data-assimilation of surface and upper air observations has been performed during the simulations, and the models use a 24 h spin-up. We will analyze the period of 23 Oct 1800 UTC to 26 Oct 1800 UTC.

4.3.2 Model physics

The relevant model components to model the ABL are the surface-layer scheme, the ABL scheme, the radiation scheme, and the land-surface scheme. We briefly describe these model components (see Appendix for more details). With the current models we obtain the permutations summarized in Table 4.1. This study uses the PSU/NCAR MM5 (v3.6.1) model (Dudhia et al., 2000), COAMPS (v3.1.1), and HIRLAM (v7.0.1). In MM5, four ABL schemes were selected: Medium Range Forecast (MM5-MRF, Troen and Mahrt, 1986; Holtslag and Boville, 1993; Hong and Pan, 1996), the ETA-Mellor-Yamada scheme (MM5-ETA, Janjic, 1994), Blackadar (MM5-BLA) and Burk-Thompson (1989, MM5-BT). These schemes were selected because of their different physical assumptions and their common use in atmospheric models.

For completeness, we note that MM5 uses the Dudhia (1989) CLOUD radiation scheme,
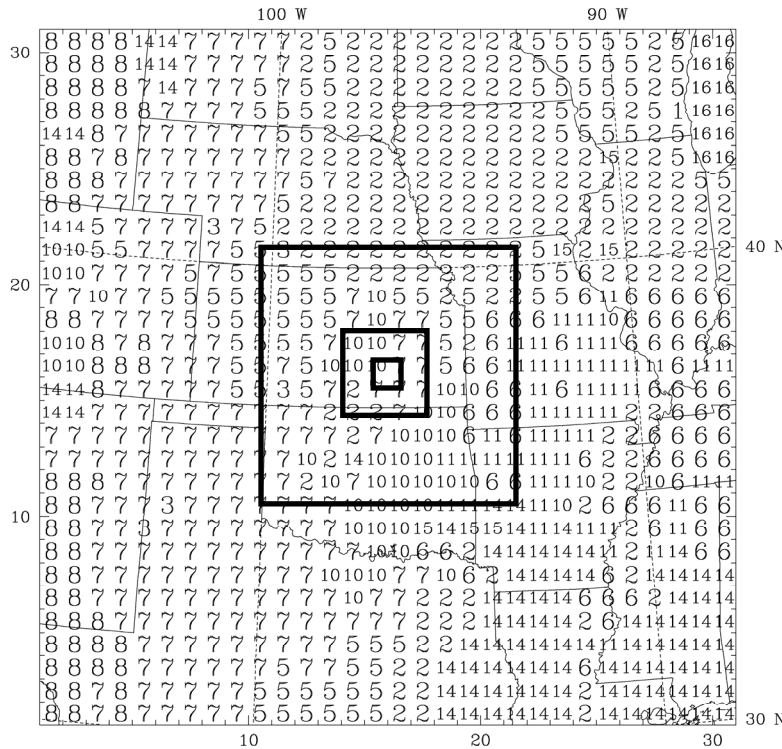
Figure 4.3: Model domain configuration (total size 1620 x 1620 km) and landuse (2 = Dryland Cropland and Pasture, 5 = Cropland/Grassland Mosaic, 6 = Cropland/Woodland Mosaic, 7 = Grassland, 8 = Schrubland, 10 = Savanna, 14 = Evergreen Needle leaf Forest, 16 = Water.

Table 4.1: Overview of model parameterizations in the surface layer, boundary layer and for the land surface in the current intercomparison.

Model	Surface-Layer	Boundary-Layer	Surface/ Vegetation
MM5-MRF	MO-short tail	*K* profile (non-local daytime)	5 soil layers – no veg. layer
MM5-BLA	MO-short tail	Local *K* theory (for stable) Non-local (for unstable)	5 soil layers – no veg. layer
MM5-ETA	MO-short tail	TKE-*l* $\quad l = \dfrac{kz}{1 + kz/l_\infty}$	5 soil layers – no veg. layer
MM5-BT	Louis	TKE-*l* $\quad l = \dfrac{kz}{1 + kz/l_\infty}$	Force restore + veg layer
HIRLAM	Louis	TKE-*l* (details Eq. 4.5-4.7) $\dfrac{1}{l} = \dfrac{1}{c_n kz} + \dfrac{1}{\sqrt{TKE}/N}$	ISBA, +veg layer, force restore
COAMPS	Louis	TKE-*l* $\quad l = \dfrac{kz}{1 + kz/l_\infty}$	SLAB model

while COAMPS and HIRLAM use the schemes by Harshvardhan et al. (1987) and Savijärvi (1990) respectively. MM5 and COAMPS use the Kain and Fritsch (1993) convection scheme, where HIRLAM uses the STRACO scheme (Undén et al., 2002).

4.3.2.1 Surface layer

All schemes calculate the surface fluxes of heat (*H*) and momentum (τ) according to:

$$H = -C_p C_\theta \rho_a U \left(\theta_{vg} - \theta_{va} \right), \tag{4.1}$$

and

$$\tau = C_D \rho_a U^2 . \tag{4.2}$$

Here C_p, ρ_a and *U* are the specific heat of air, the air density and near surface wind speed respectively. C_θ and C_D are the dimensionless stability dependent exchange coefficients for heat and momentum, and θ_{vg} and θ_{va} are the virtual potential temperatures at the surface and the air. We distinguish between two different formulations for C_θ and C_D. One type is based on Monin-Obukhov (MO) similarity theory (not allowing transfer if the Richardson number *Ri* is above its critical value Ri_{crit}, which is also referred to as a 'short tail' formulation), used by MM5-MRF, MM5-ETA and MRF-BLA. The other type is based on the Louis (1979)-approach (allowing for mixing for $Ri > Ri_{crit}$) which is used in COAMPS, HIRLAM, and MM5-BT.

4.3.2.2. Boundary Layer

Within the ABL schemes we can also distinguish between two types. In the first type the turbulent diffusion is based on non-local closure during the day, and the Louis scheme at

night. The non-local closure enhances the daytime mixing, which usually results in a better performance, compared to local schemes (Holtslag et al., 1995). As such, these schemes provide more realistic initial conditions for the night. At night non-local transport should be zero since large eddies are absent.

The second type is a 1.5 order (level 2.5 in the Mellor and Yamada (1974) hierarchy) closure model and solves the budget equation for turbulent kinetic energy (E), with the exchange coefficient K that depends on Ri via complicated algebraic functions:

$$K = l\sqrt{E} f(Ri) \tag{4.3}$$

The length-scale l specification plays a key role, and is usually given by:

$$l^{-1} = (kz)^{-1} + l_\infty^{-1}, \tag{4.4}$$

with k the Von Karman constant and l_∞ an asymptotic mixing length. HIRLAM uses an extra length-scale to account for stability, instead of correction via $f(Ri)$:

$$l^{-1} = (\max(l_{int}, l_{min}))^{-1} + l_s^{-1}, \tag{4.5}$$

with l_{int} and integral length-scale only used for the daytime, and

$$l_s = c_{m,h} \sqrt{E}\big/ N. \tag{4.6}$$

Here $c_h = 0.2$ and $c_m = 4\, c_h$, and N is the local Brunt-Vaisala frequency and,

$$l_{min}^{-1} = (c_n kz)^{-1} + l_{limit}^{-1}, \tag{4.7}$$

with $c_n = 0.5$ (Lenderink and Holtslag, 2004; Tijm, 2004). Within each approach $f(Ri)$ is based on either the Monin-Obukhov type or the Louis type.

4.3.2.3 Land surface

Within the land-surface schemes, we can generally distinguish between models that use the force-restore method (Deardorff, 1978) and those with a multi-layer scheme that solve the diffusion equation for heat. Secondly, the models use different heat capacities of the first soil-vegetation layer, some accounting for the small heat capacity of the vegetation. HIRLAM utilize the ISBA land-surface scheme, with vegetation layer (Noilhan and Mahfouf, 1996). MM5-BT is the only scheme that does not use the multi-layer scheme in MM5, but applies a force-restore method with a vegetation layer of small heat capacity on top. COAMPS also uses a force-restore method, but with a slower coupling with the atmosphere.

4.4 Surface Temperature and Fluxes

In this section we focus on the model results for turbulent and radiative surface fluxes. Table 4.2 provides an overview of statistical measures for model performance, i.e. bias, mean absolute error (*MAE*), root-mean-square error (*RMSE*), fractional bias (*FB*), correlation coefficient and the Index of Agreement (*IoA,* a modified correlation coefficient, that accounts for phase errors between modeled (MOD_i) and observed (OBS_i) time series, (Willmott, 1982)).

a) Surface radiation

Both COAMPS and MM5 (for all ABL schemes) overestimate the net surface solar radiation by 50 and 25 Wm^{-2}, respectively (not shown in table 4.2). This may be partly explained by a dry bias in the initial q field provided by ECMWF. An underestimation of q enhances shortwave downwelling radiation, and underestimates of downwelling long-wave radiation ($L^{\downarrow}$). The modeled long-wave net radiation (L^{*}, Fig. 4.4a) with MM5 is close to the observations (maximum bias 20 Wm^{-2} in the first night) with the best estimate by the BT scheme. MRF and BLA perform rather similar. However, during daytime L^{*} is underestimated due to underestimated T_{veg} and thus $L^{\uparrow}$ (Fig. 4.4f), except for COAMPS that forecasts a slightly higher T_{veg} than MM5. COAMPS and HIRLAM have negative L^{*} bias of ~30-40 Wm^{-2} and ~20 Wm^{-2} respectively, especially at night. In the radiative night (25-26 Oct.), MM5-BT slightly underestimates the magnitude of L^{*} while other MM5 schemes show good correspondence with observations. A closer look to both $L^{\downarrow}$ and outgoing long-wave fluxes ($L^{\uparrow}$) reveals that the bias of COAMPS in the net radiation is due to continuous underestimation of $L^{\downarrow}$ (~30 W m^{-2}, see Table 4.2), which is consistent with the dry bias aloft and cold ABL bias in COAMPS. MM5 estimates $L^{\downarrow}$ reasonably, except for 24 Oct during the day where MM5 overestimates $L^{\downarrow}$. This is probably caused by the q profile that differs strongly between MM5 and the observations (Fig. 4.6 below). MM5 is too humid compared to the radiosonde observations and predict the trough passage earlier than observed. Additionally, since the soil moisture content is low, both the observed and modeled L_vE at the surface are relatively small (50 Wm^{-2}). Therefore the relative contribution by entrainment of moist and warm air from the free atmosphere into the ABL can be large (e.g. Couvreux et al., 2005) and the entrainment process has a dominant impact on the q distribution in the ABL. In general MM5-MRF and MM5-BLA have a vigorous entrainment, and TKE models underestimate the entrainment. Note that HIRLAM is also too moist, but this because of overestimated L_vE. Except humidity, sources of the $L^{\downarrow}$ bias can also be due to the parameterization itself (nearly all radiation codes underestimate $L^{\downarrow}$ e.g. due to inaccurate treatment of the water vapor continuum) or they need more resolution than used here.

Note that $L^{\uparrow}$ is mainly governed by the surface temperature. MM5 underestimates $L^{\uparrow}$ during daytime, but overestimates $L^{\uparrow}$ at night. COAMPS shows a time delay with the observations of about 1 h at noon, due to the large response time of T_{veg} in the land-surface scheme. COAMPS has a larger diurnal cycle of $L^{\uparrow}$ than MM5, and performs well for $L^{\uparrow}$ (Table 4.2). Net radiation (Fig. 4.4b) is well estimated during daytime by COAMPS and by MM5 at night. COAMPS underestimates net radiation by ~50 Wm^{-2} (even more in the last night) which will have serious consequences for the SBL structure.

b) Turbulent surface fluxes

Friction velocity u_*, (see Fig. 4.4c), is well forecasted on 24 Oct. by ETA and BT and overestimated by MRF, BLA and COAMPS. In the following intermittently turbulent night

Table 4.2: Statistical model evaluation for the reference runs, based on the full time series. Bold numbers indicates the best score for a particular quantity and statistical measure.

	Model	Bias (m)	Mae (m)	Rmse (m)	FB (-)	Corr (-)	IoA (-)
T_{veg}	COAMPS	-1.37	**2.31**	**2.94**	-0.11	**0.980**	**0.981**
u_*	COAMPS	0.08	**0.09**	0.11	0.38	**0.854**	0.802
H	COAMPS	5.69	22.00	30.96	0.15	**0.982**	0.957
L_vE	COAMPS	**2.13**	**4.42**	**6.55**	**0.14**	**0.940**	**0.964**
$L^\downarrow$	COAMPS	-25.27	25.89	28.31	-0.09	0.834	0.625
$L^\uparrow$	COAMPS	3.40	**8.45**	**10.60**	0.01	**0.984**	**0.990**
T_{veg}	MM5-MRF	**0.63**	4.16	4.67	**0.05**	0.951	0.939
u_*	MM5-MRF	0.09	0.095	0.13	0.43	0.783	0.760
H	MM5-MRF	-5.51	15.95	23.91	-0.20	0.951	0.974
L_vE	MM5-MRF	3.94	6.96	9.70	0.29	0.876	0.907
$L^\downarrow$	MM5-MRF	6.31	10.14	11.95	0.02	0.863	0.906
$L^\uparrow$	MM5-MRF	**0.73**	17.58	20.44	**0.002**	0.959	0.951
T_{veg}	MM5-ETA	-0.69	4.01	4.87	-0.06	0.950	0.934
u_*	MM5-ETA	0.08	**0.09**	0.12	0.41	0.800	0.781
H	MM5-ETA	-3.47	15.61	22.83	-0.12	0.954	0.977
L_vE	MM5-ETA	8.55	10.92	15.89	0.53	0.873	0.750
$L^\downarrow$	MM5-ETA	**0.92**	**8.90**	11.54	**0.003**	0.817	0.912
$L^\uparrow$	MM5-ETA	-6.15	17.50	22.69	-0.017	0.957	0.939
T_{veg}	MM5-BLA	0.75	4.18	4.63	0.06	0.951	0.940
u_*	MM5-BLA	0.12	0.13	0.16	0.57	0.804	0.632
H	MM5-BLA	-7.60	17.69	26.24	-0.29	0.943	0.969
L_vE	MM5-BLA	5.20	8.32	11.03	0.36	0.846	0.880
$L^\downarrow$	MM5-BLA	6.15	9.41	11.44	0.02	**0.871**	0.914
$L^\uparrow$	MM5-BLA	1.34	17.61	20.09	0.004	0.959	0.952
T_{veg}	MM5-BT	-1.42	3.11	4.20	-0.13	0.970	0.950
u_*	MM5-BT	0.08	**0.09**	0.12	0.40	0.804	0.788
H	MM5-BT	**1.15**	**15.21**	23.09	**0.038**	0.957	0.976
L_vE	MM5-BT	7.43	10.15	16.38	0.48	0.885	0.734
$L^\downarrow$	MM5-BT	3.15	8.92	**11.00**	0.011	0.843	**0.920**
$L^\uparrow$	MM5-BT	-9.60	13.79	20.04	-0.026	0.974	0.953
T_{veg}	HIRLAM	-2.12	4.51	3.70	-0.19	0.956	0.937
u_*	HIRLAM	**-0.04**	**0.09**	**0.08**	**-0.29**	0.693	**0.842**
H	HIRLAM	-0.14	17.71	12.27	0.00	0.975	**0.986**
L_vE	HIRLAM	3.01	9.08	6.91	0.21	0.937	0.918
$L^\downarrow$	HIRLAM	-24.60	12.60	25.03	-0.09	0.800	0.565
$L^\uparrow$	HIRLAM	-14.28	21.30	18.52	-0.04	0.961	0.930
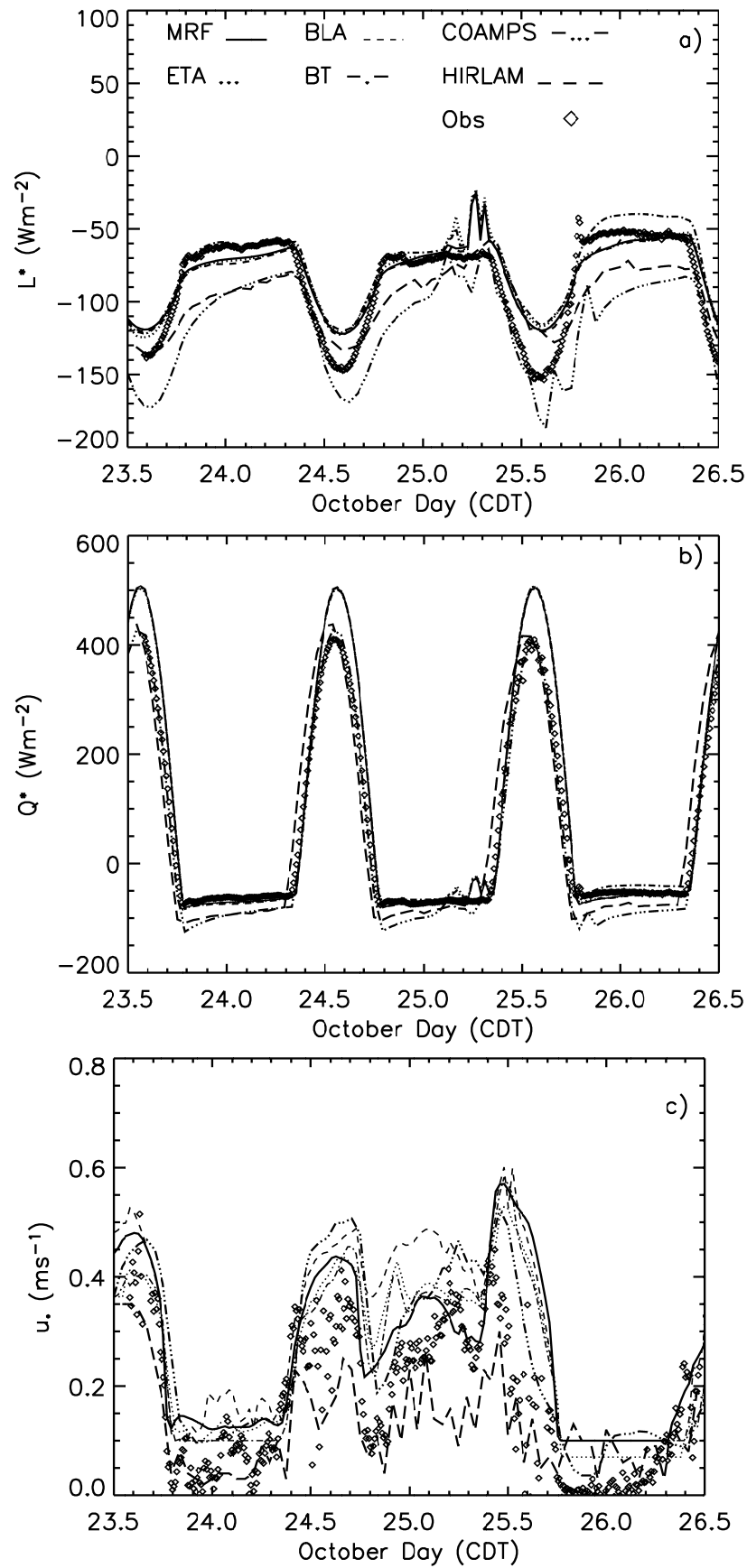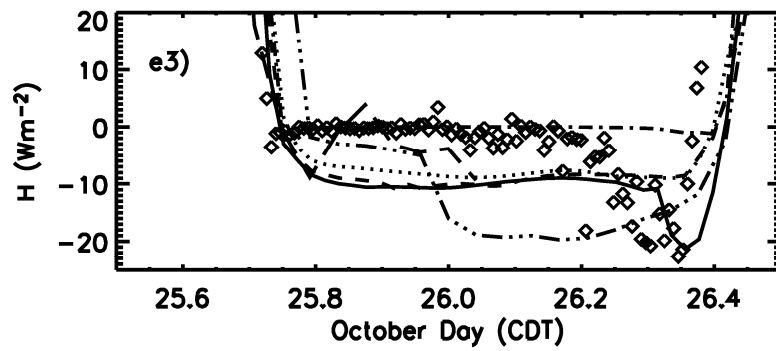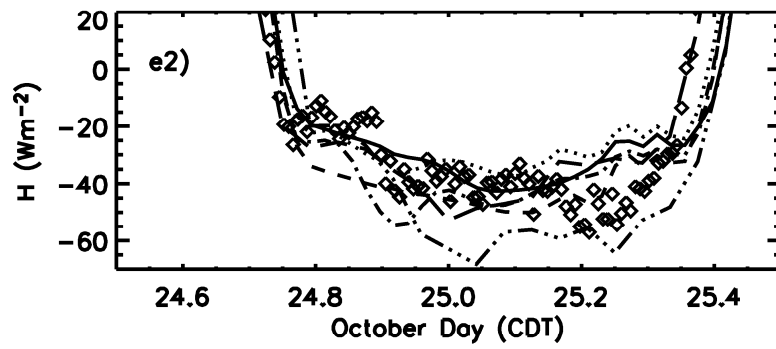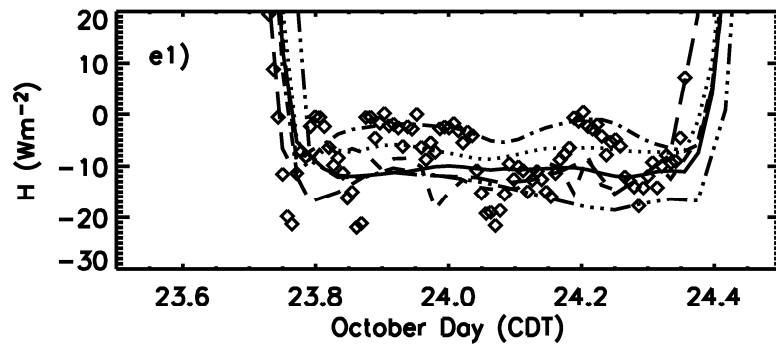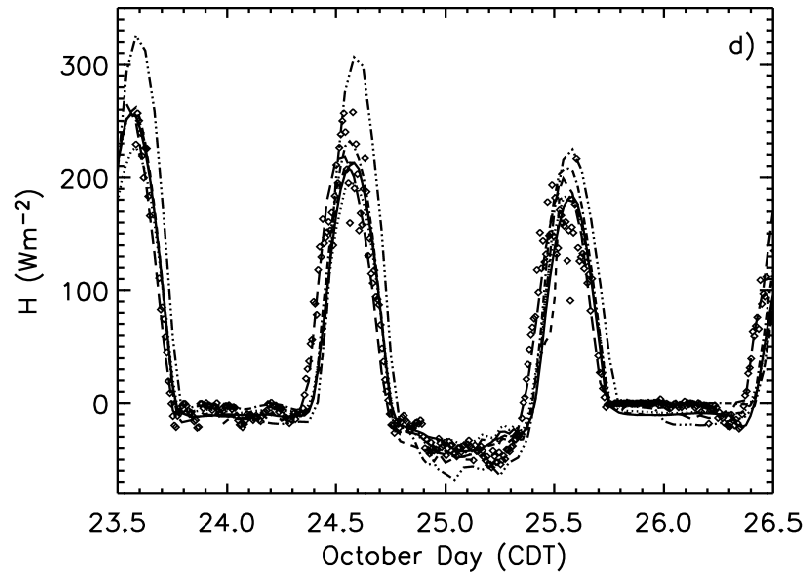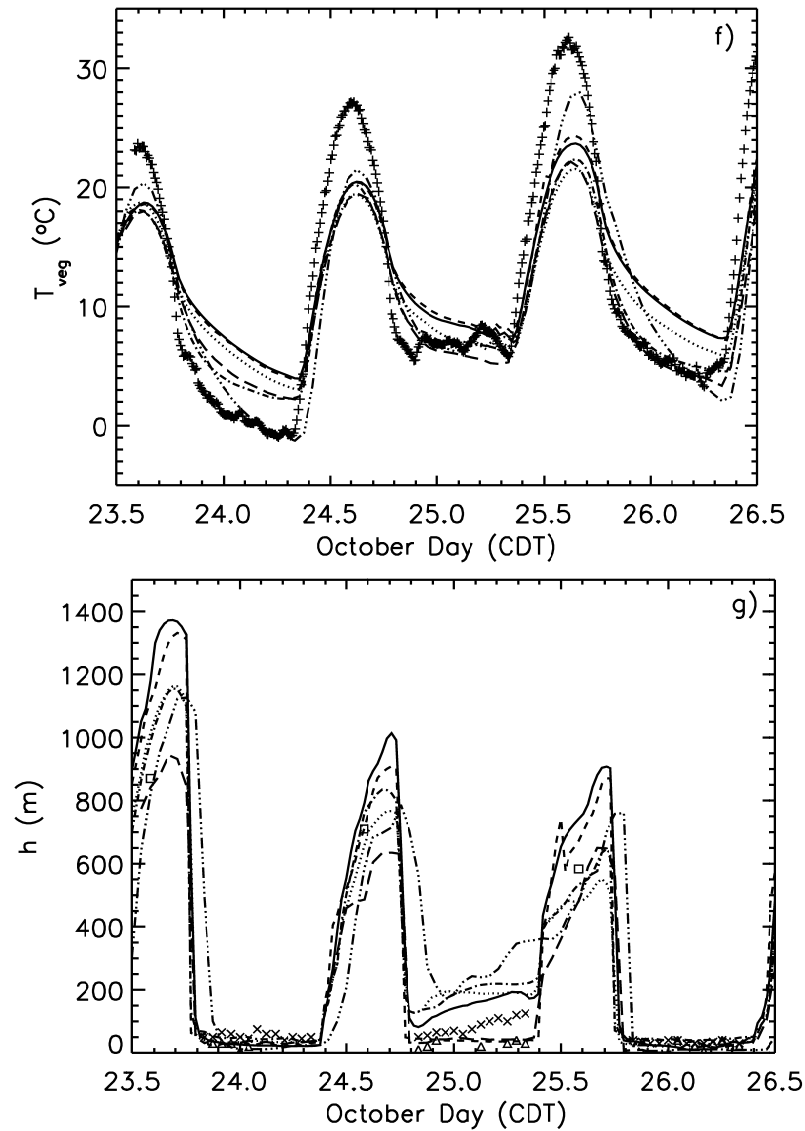
Figure 4.4: Time series of observed (+) and modeled net long-wave radiation (a), net radiation (b), friction velocity (c), sensible heat flux (d), nighttime sensible heat flux (e), surface vegetation temperature (f). Figure 4g: as a) but for boundary-layer height, □ are sounding observations, X are sodar observations, and Δ denote observations from Vickers and Mahrt (2004), based on u_* divergence along the 60 m mast.

(24-25 Oct.) all schemes tend to overestimate u_* slightly, and are unable to mimic the intermittent events. Most models fail to reduce u_* during the day-night transitions of 24-25 Oct. and u_* falls too late in the transition of 25-26 Oct. Finally, u_* is heavily affected by unphysical limiting values in MM5 for strong stability, and strongly overestimated by COAMPS, a common problem with the Louis (1979) scheme. The high u_* in COAMPS coincides with very steep U and θ profiles between the surface and the lowest model level (Fig. 4.7 below), which indicates the effect of an unphysical fix.

HIRLAM is the only model that is able to forecast small u_* in the first night (weak wind),

but underestimates u_* during daytime and during the windy night (24/25 Oct.). The small nighttime u_* contradicts with usual findings that the Louis scheme overestimates u_*. Scale analysis of the two terms in HIRLAMs length-scale formulation (Eqs. 4.5-4.7) showed that both terms are of same order of magnitude close to the ground in calm nights, and thus the second term considerably reduces l. Additionally, we show that MM5-BT and HIRLAM give stronger surface cooling at night than the other models, and also limit the turbulence and thus u_*. Therefore HIRLAM outperforms for u_* for most statistical parameters (Table 4.2).

The sensible heat flux (H, Fig. 4.4d,e) is best represented by MM5 and HIRLAM during daytime, where COAMPS overestimates H by 50 Wm^{-2} due to overestimated incoming solar radiation. During the night of 23-24 Oct. the TKE schemes calculate the smallest H, and all schemes are in the observed range (Fig. 4.4e). The intermittent character of the observed fluxes is absent in all model forecasts. In the night of 24-25 Oct, all models with the Louis scheme in the surface layer (COAMPS and MM5-BT) overestimate $|H|$, corresponding to earlier findings (Van den Hurk and Holtslag, 1997; Kot and Song, 1998). In the radiative driven night (25-26 Oct.) most models seriously overestimate $|H|$, except HIRLAM and BT. We will see below that those schemes permit the land surface to cool more rapidly, enhancing the stratification, which is beneficial to the forecasted H. Only MRF shows the flux increase before dawn. Based on the full diurnal cycle, HIRLAM gives the largest IoA (0.986).

Latent heat fluxes (L_vE) are only 50 Wm^{-2} at noon and well represented by MRF, BLA, and COAMPS (IoA = 0.964, Table 4.2). ETA, BT and HIRLAM overestimate L_vE by 25 Wm^{-2}. At night, both the modeled and observed fluxes are small (not shown).

T_{veg} is a peculiar but important quantity to predict, because of its central role in driving the schemes (Figs. 4.1 and 4.4f). All MM5 schemes overestimate the nighttime T_{veg} during weak winds (23-24 and 25-26 Oct.), although this warm bias is smaller for MM5-BT. HIRLAM also corresponds well with observations during these calm nights. Although Zhong and Fast (2003) indicate that the limited resolution might be responsible for the temperature bias, here we point to land-surface scheme design. Their remark that with increased resolution or different ABL schemes the surface inversion strength remains too small, implicitly shows that other issues than resolution and the ABL scheme might be responsible for the biased surface inversion strength (e.g. the land-surface scheme).

The BT scheme uses a force-restore method with vegetation layer, instead of the 5 soil layer model. The use of a vegetation layer is beneficial for the forecasted cooling rate. COAMPS forecasts the largest diurnal cycle amplitude, but reaches the minimum temperature too slowly, since the surface cools insufficiently fast. The *warm* bias in most schemes contradicts with the *cold* bias found by Zhong and Fast (2003), who attribute the vanishing of the modeled turbulence for this large cooling. However, the turbulence schemes provide several artificial fixes (e.g. minimum U, u_*, E, or maximum z/L) to maintain turbulence at strong stability such that a warm bias is expected. Moreover, the surface cooling responds on a long time-scale that is different from the time-scale of fluctuations of H (short time-scale). This

stresses that the surface properties (i.e. the soil equivalent depth) governs the surface cooling.

Zhang and Zheng (2004) also found an underestimation of the DTR, although in their case this was solely present during daytime, while here also the nighttime contribution is substantial. They also found that MM5-BT shows the smallest DTR, and in general a cold bias of typically 2 K at night, while here BT forecast the largest DTR within MM5. Note however that Zhang and Zheng (2004) do not report any verification of L_vE. If, in their case, the modeled daytime L_vE was too large, a DTR underestimation is consistent. A cool daytime bias can then persist at night. In the present study, the L_vE is in close agreement with the observations, and the bias for the CBL bulk temperature is small for the best models.

Zhang and Zheng (2004) report a systematic overestimation of the near surface wind speed at night and an underestimation during daytime, but this is not found here. The former study also reports substantial phase errors of the near surface wind. In the current study only MRF is some hours ahead from its daytime wind speed maximum.

Since all models use their own internal definition of the boundary-layer height (h), a clean comparison of h is not possible from direct model output. Therefore we initially calculated h from the modeled atmospheric profiles a posteriori, using the Troen and Mahrt (1986) with $Ri_{crit} = 0.25$. However, this method provides ABLs that are too deep for stable conditions, and is thus a less useful method for intercomparison. Therefore, for stable conditions we use the method in Vogelezang and Holtslag (1996) with $Ri_{crit} = 0.3$ to obtain h. During daytime h is typically 850 m for the last two days, but with a large spread, ranging between 650 m to 900 m between different schemes (Fig. 4.4g). MM5-MRF forecasts the deepest CBL. The single observation of h during daytime is insufficient to indicate which model is favorable. COAMPS exhibits a delay of the CBL collapse, caused by the relatively slow surface cooling in this model.

Surprisingly, all models predict h correctly at night during weak winds (23-24 and 25-26 Oct). This contradicts with earlier findings that h is typically overestimated by about a factor 2 by this type of models (HY01). For the second night (24-25 Oct), MRF, ETA, COAMPS and BT overestimate h with 75-150m, although dh/dt is reasonably estimated. The disagreement between findings for weak winds and those in HY01 might result from the chosen method to calculate h. We obtained similar conclusions as HY01 with the Troen and Mahrt (1986) method. However, the current method showed significantly more skill against Cabauw tower observations, and should therefore be preferred. Note that the estimate of h in this range could also be sensitive to the distribution of the model layers.

4.5 Atmospheric Profiles

Fig. 4.5 shows the temporal structure of modeled temperature and wind speed. Although the figure does not provide a direct test against observations, it provides a comparison between the outcome of the model approaches, which give a more complete picture than comparing some instantaneous profiles only. First, the incoming heat advection on 25 Oct. is easily seen following the 292 K isentrope, which reaches a lower altitude between October Day 24.7 and

A
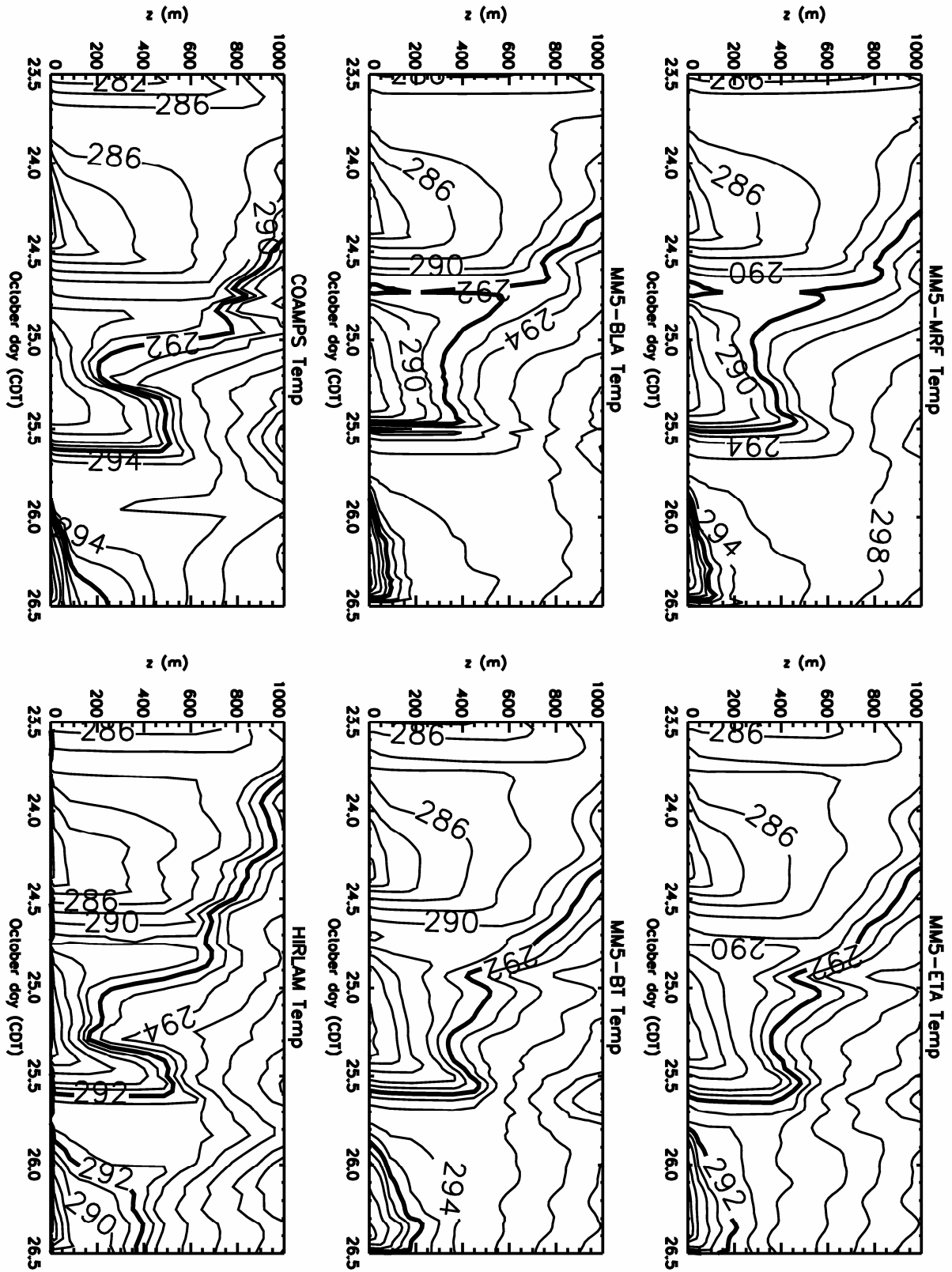
B
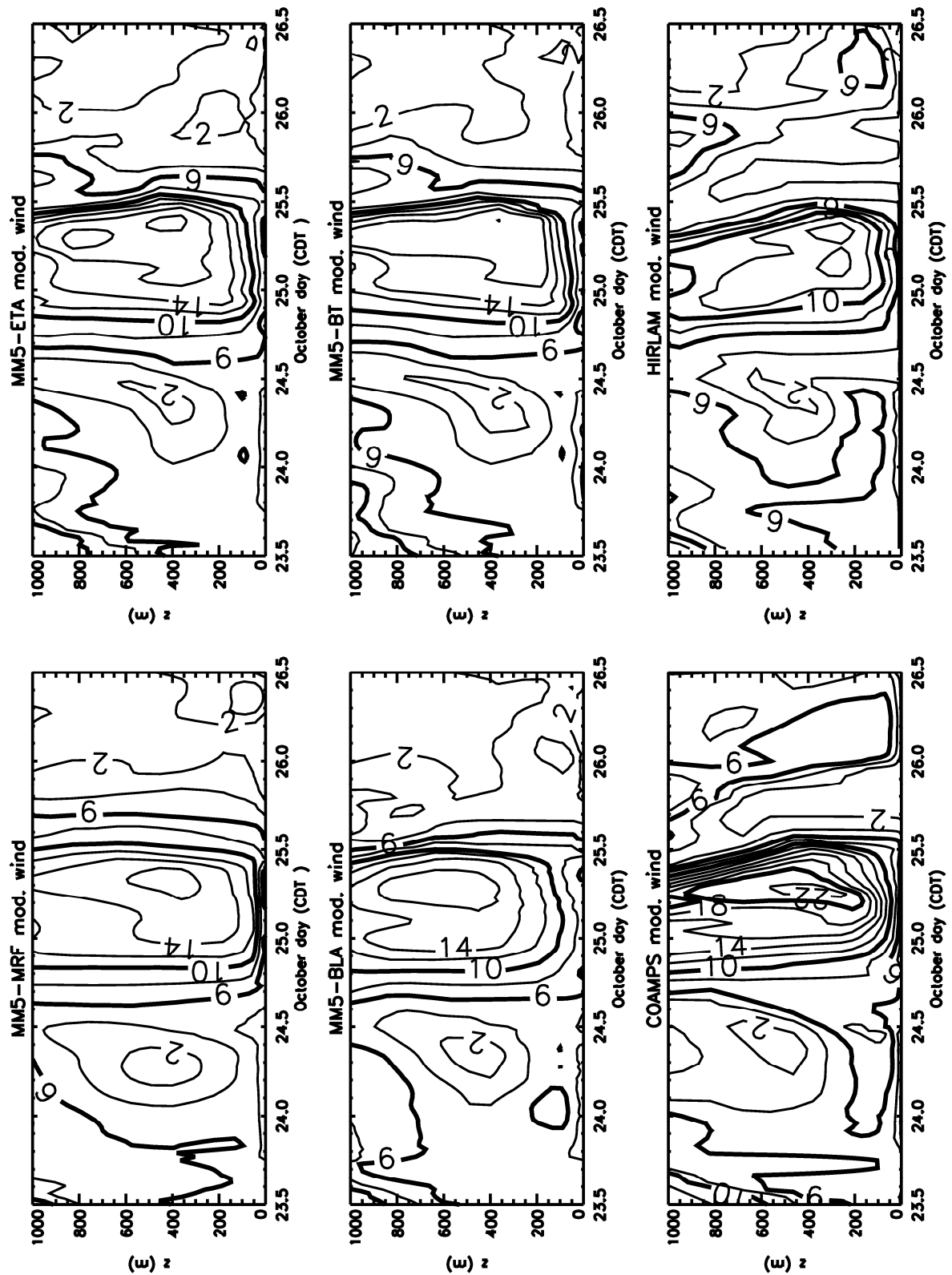
Figure 4.5: Contour plots of modeled potential temperature (a, contour interval 1 K for θ < 288 K, and 2K for θ > 288 K), and wind speed modulus (b) for 23 Oct, 1800 UTC- 26 Oct 1800 UTC.

25.0. HIRLAM and COAMPS show a corresponding advection rate over a deep layer, where in MM5 the advection is more slowly in time (the slope of the isentropes is smaller). MRF and BLA provide a rather similar temperature structure in the CBL with a very fast growth in the morning, and a deeper CBL than in other schemes. At night the TKE models mix the cool air at the ground over a shallower layer, especially during the weak wind nights. On the contrary, MRF and BLA mix the cold air over an unrealistically deep layer, and thus do not have a clear residual layer, while HIRLAM limits the cooling to a very shallow layer close to the surface.

A clear wind speed minimum at 500 m AGL is seen before dawn of 25 Oct. All schemes in MM5 produce a LLJ of about 16 ms^{-1} the second night (24-25 Oct). BLA has the jet typically at a higher altitude than MRF, and the TKE models produce a wind maximum over a deep layer, and a sharp wind speed maximum is only present in HIRLAM and COAMPS. During the last night (25-26 Oct) all MM5 schemes give a weak LLJ, although they differ in timing. Again, COAMPS provides a deep jet layer while HIRLAM lacks a LLJ.

Similar figures (not shown) for E revealed that the TKE models predict significant different E values in the ABL during daytime, ranging from ~0.9 J kg^{-1} for ETA and COAMPS to ~1.6-2 J kg^{-1} for HIRLAM and MM5-BT for 25 Oct. Next, we evaluate U and θ profiles against in-situ observations for the CBL and SBL respectively.

a) Convective boundary layer.

As an illustrative example (Fig. 4.6), we show the 700 m deep CBL of 24 Oct. 1900 UTC (which is after the initial effects of spin up and before strong advection). In correspondence with earlier verifications (e.g. Hong and Pan, 1996), the TKE closure models show a shallower and more humid ABL than the non-local schemes that forecast the CBL temperature well. MRF and BLA are 0.5 g kg^{-1} too humid due to excessive entrainment of moist air from the free atmosphere. HIRLAM is also 0.5 g kg^{-1} too humid, but because L_vE is overestimated (see FB in table 4.2). ETA and BT are too humid because L_vE (similar as in MRF and BLA) is mixed in a shallower ABL. Since L_vE is small, and thus convection is relatively strong, the CBL is forced by non-local mixing and thus the resulting q profiles strongly rely on CBL top entrainment (Beljaars and Viterbo, 1998). The MM5 schemes underestimate the stratification in the capping inversion, as found in HY01, while COAMPS and HIRLAM provide a sharper inversion. The length-scale formulation for stable stratification, that strongly reduces mixing, is likely responsible for this effect. This also explains why HIRLAM (although a TKE scheme) is not as moist as ETA and BT.

b) Stable boundary layer.

Recalling that our current understanding of the SBL is limited, we may expect more spread between model results at night than during the day. Observations in the intermittent night (23-24 Oct.) show a temperature inversion of 8 K near the surface, which is only clearly represented by COAMPS and BT near sunrise (not shown). The effect of the warmer CBL

remains at night in MM5-BLA and MM5-MRF with higher temperatures. In general the wind speed profiles are well represented, but a sharp 12 ms^{-1} LLJ at 24 Oct. 0700 UTC is predicted too late by all schemes, although COAMPS and BT, and at 1100 UTC also HIRLAM show slightly better performance than the other schemes.
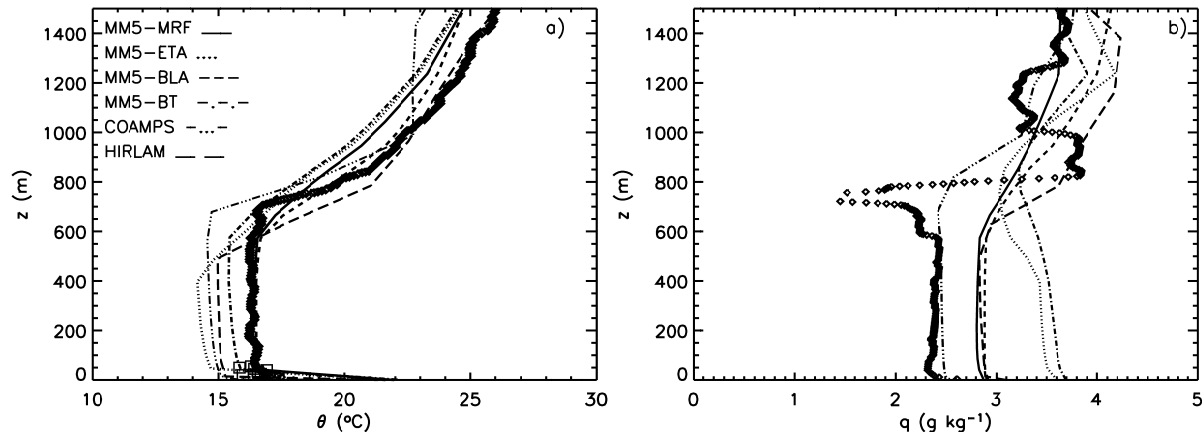
Figure 4.6: Profiles of observed (◊ = radiosonde observations, □ = tower observations) and simulated potential temperature (a) and specific humidity (b) for 24 Oct 1900 UTC.

The strength of the characteristic LLJ in the turbulent night (24-25 Oct.) is reasonably forecasted by COAMPS, although it overestimates the LLJ altitude and underestimates U in the residual layer (Fig. 4.7a). BT and ETA forecast a LLJ over a deep layer, although weaker than observed. BLA extensively mixes the LLJ over an even deeper layer. HIRLAM underestimates the LLJ speed. The wind direction is forecasted well, although BLA and MRF provide 10-20° less backing near the surface than observed (Fig. 4.7b). θ profiles are in reasonable agreement with the observations (not shown). Note that during the 25 Oct. 0700 UTC sounding, the spread of the modeled wind speed profiles was less than in the 1100 UTC sounding.

To examine the impact of resolution on the ability to resolve the LLJ, we performed a sensitivity study with MM5-BT in which we added 10 layers in the lowest 500 m. Unfortunately, this gave no improvement. The literature suggests several possible physical mechanisms for LLJ formation (Zhong et al., 1996). The explanation by Blackadar of an inertial oscillation after collapse of the turbulent friction at sunset is less probable here because u_* is large at night. Fast and McCorcle (1990) show that differences of evaporation rates along a slope can be an important LLJ forcing. However, in that case we would expect a stronger jet during the other nights as well. Finally, differential cooling between the slope and the adjacent air at constant height can generate a thermal wind V_T (Stull, 1988), in this case to the north. During the two first nights the horizontal temperature gradients are similar. However, during the first night the background wind speed is from the northeast, and thus opposes V_T. On the contrary, on the second night V_T adds to the southern background wind. Since this phenomenon is driven by the terrain slope, the modelling of the LLJ requires a sufficient representation of the model topography. In the radiative night (25-26 Oct), the underestimated surface cooling in
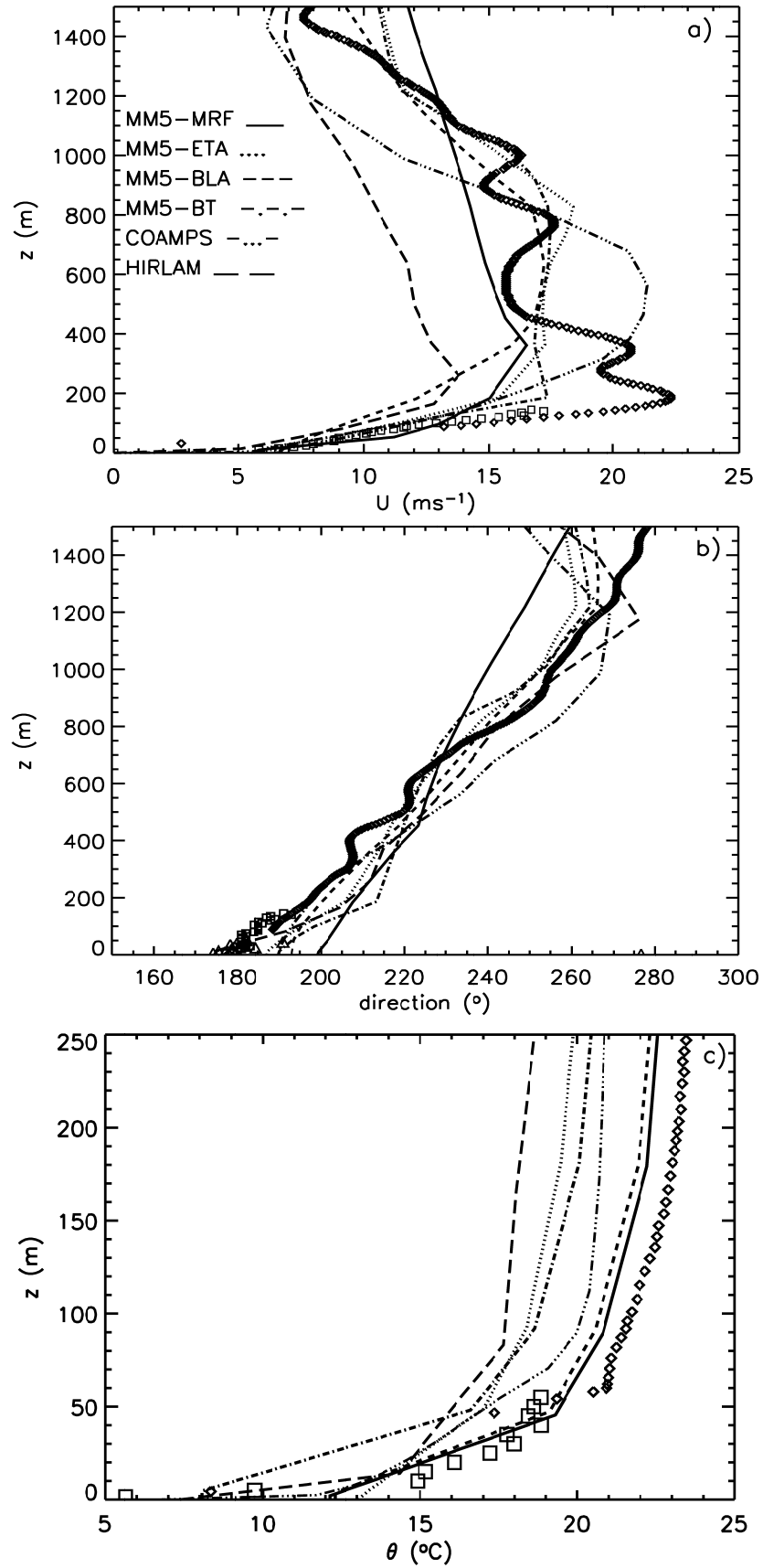
Figure 4.7: Modeled and observed ($\Diamond$ = sounding, $\square$ = minisodar, Δ = 60 m tower) modulus wind speed (a) and wind direction (b), 25 Oct, 1100 UTC. Figure 4.7c: Modeled and observed ($\Diamond$ = radiosonde observations, $\square$ = tower observations) potential temperature, 26 Oct, 0700 UTC.

MM5 is even more pronounced than during the intermittent night (24-25 Oct.), with an observed inversion strength of 16K over 100 m (Fig. 4.7c). ETA, BT and HIRLAM are too cold above 50 m AGL, the remnants of the cool CBL. COAMPS performs well in this night, with a curvature of the θ profile similar to the observed curvature, although somewhat weaker and more realistic. The θ jump between the surface and the first model level seems exaggerated.

c) Impact of domain size

Next we focus on the impact of the selected domain size on the LLJ representation. The Great Plains are slightly sloping towards the northwest direction. Rapid surface cooling on the slope causes a strong temperature gradient in the air at the same altitude. Accordingly, a LLJ develops according to the thermal wind relation. A sufficiently large area of this sloping terrain should be present in the model. Running the case with COAMPS and MM5 with finer resolution (27, 9, 3, 1 km), but a smaller domain (810 x 810 km) revealed a LLJ with at maximum 12 ms^{-1} instead of 17 ms^{-1} for all schemes. This is probably caused by the ECMWF boundary conditions, which showed a LLJ speed of only 11 ms^{-1}. With a small domain the LAMs are too much constrained by the boundaries. Note that normally the Great Plains Jet is a band of high wind speed, and thus a single radiosonde profile gives limited insight. It is therefore worth to note that a stronger LLJ was found elsewhere in the MM5 domain.

4.6 Sensitivity to radiation schemes

The previous section showed that model prediction of the near surface temperature at night is erroneous. Examining the sensitivity of the results to the choice of the radiation scheme is useful since radiation plays an important role in the surface cooling at night. To explore this sensitivity, the simulations with MM5-MRF and MM5-ETA have been repeated using the RRTM and CCM2 radiation transfer schemes in addition to the reference CLOUD scheme. The CLOUD scheme only considers the interaction of radiation with water vapor and CO_2, whereas RRTM represents a detailed absorption spectrum of CO_2, CH_4, NO_x and O_3. In CCM2 the long-wave radiative effects of the greenhouse gases CO_2, O_3, H_2O, CH_4, N_2O, CFC11, and CFC12 are treated using broadband approximations, and an 18-band δ-Eddington approximation is used for solar radiation. Details on the different radiation transfer schemes are beyond the scope of this paper but can be found in Dudhia (1989), Mlawer (1997) and Kiehl (1998) for the CLOUD, RRTM and CCM2 schemes respectively. As shown by Guichard et al. (2002), we expect the latter scheme to produce smaller $L^{\downarrow}$, permitting more nocturnal surface cooling under clear sky conditions.

Fig. 4.8 shows that the forecasted T_{veg} at night, using either MRF or ETA, depends strongly on the chosen radiation scheme. The CLOUD radiation scheme always predicts higher nighttime T_{veg}, while the CCM2 radiation scheme gives lower, and more realistic T_{veg}. The difference between the two schemes is 2.5, 2.5, and 5 K at maximum for the three nights respectively. The prediction of T_{veg} with ETA-CCM2 is rather good during the radiative night

(25-26 Oct.) and may be considered as an optimal parameterization for strongly SBLs. However, Table 4.3 reveals that the RRTM scheme and CCM2 scheme predict a cooler surface due to underestimation of $L^{\downarrow}$ and an overestimation of the magnitude of Q^*. This is a typical case of "getting the right answer for the wrong reason". Note that the forecasted T_{veg} is insensitive to the choice of the radiation scheme during daytime for both turbulence schemes. Thus, SBL modeling is not only very sensitive to the degree of turbulent mixing (e.g. Viterbo et al., 1999), the coupling between the atmosphere and the land surface (S06), but certainly it also depends on the radiation parameterization (Ha and Mahrt, 2003).
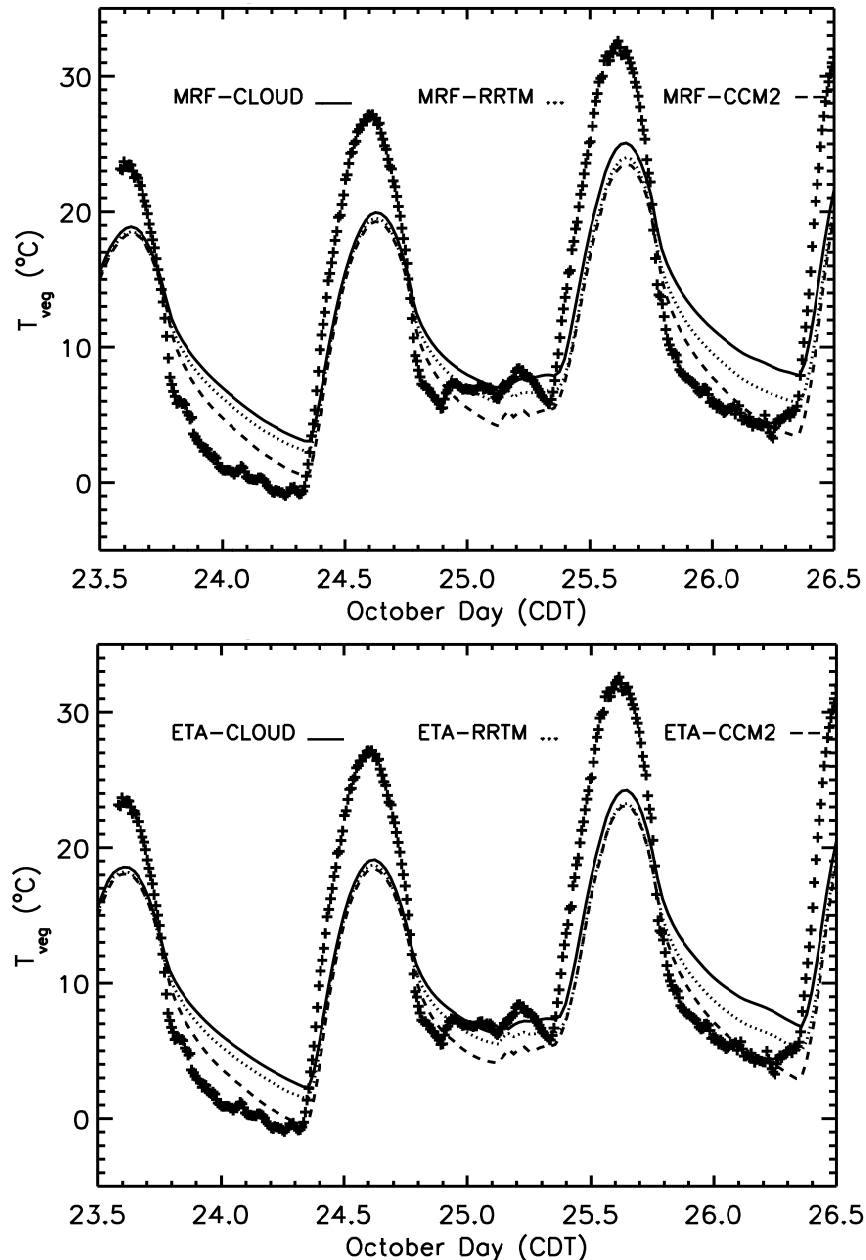
Figure 4.8: Modeled (MM5) and observed (+) surface vegetation temperature, as modeled with the CLOUD, RRTM and CCM2 radiation scheme in combination with the MRF (a) and ETA (b) boundary-layer scheme.

Table 4.3: Statistical model evaluation for the sensitivity to the radiation scheme.

	Model	bias (m)	mae (m)	rmse(m)	FB (-)	Corr (-)	IoA (-)
T_{veg}	MRF-cloud	0.35	4.65	5.34	0.03	0.88	0.92
u_*	MRF-cloud	0.06	0.09	0.11	0.32	0.68	0.80
H	MRF-cloud	-4.74	24.81	36.73	-0.18	0.87	0.94
L_vE	MRF-cloud	2.47	8.07	10.90	0.19	0.77	0.88
$L^{\downarrow}$	MRF-cloud	5.49	12.40	16.71	0.02	0.73	0.82
$L^{\uparrow}$	MRF-cloud	-0.67	20.34	24.28	0.00	0.89	0.93
T_{veg}	MRF-RRTM	-0.72	4.39	5.37	-0.06	0.87	0.92
u_*	MRF-RRTM	0.05	0.09	0.11	0.28	0.66	0.81
H	MRF-RRTM	-8.97	25.26	38.07	-0.37	0.86	0.93
L_vE	MRF-RRTM	0.94	7.55	10.53	0.08	0.77	0.89
$L^{\downarrow}$	MRF-RRTM	-9.44	14.72	17.97	-0.03	0.70	0.79
$L^{\uparrow}$	MRF-RRTM	-6.15	19.52	25.21	-0.02	0.88	0.93
T_{veg}	MRF-CCM2	-1.86	4.17	5.36	-0.18	0.88	0.92
u_*	MRF-CCM2	0.05	0.09	0.11	0.27	0.64	0.80
H	MRF-CCM2	-11.00	26.47	38.77	-0.47	0.86	0.93
L_vE	MRF-CCM2	0.21	7.29	10.61	0.02	0.76	0.88
$L^{\downarrow}$	MRF-CCM2	-35.38	37.48	39.80	-0.13	0.62	-0.01
$L^{\uparrow}$	MRF-CCM2	-11.71	19.16	26.06	-0.03	0.89	0.92
T_{veg}	ETA-cloud	-0.49	4.46	5.32	-0.04	0.88	0.92
u_*	ETA-cloud	0.05	0.08	0.10	0.30	0.78	0.86
H	ETA-cloud	-5.57	23.94	36.02	-0.21	0.87	0.94
L_vE	ETA-cloud	7.46	11.49	16.60	0.48	0.77	0.72
$L^{\downarrow}$	ETA-cloud	1.93	11.13	16.19	0.01	0.70	0.83
$L^{\uparrow}$	ETA-cloud	-4.99	19.70	24.71	-0.01	0.89	0.93
T_{veg}	ETA-RRTM	-1.50	4.29	5.49	-0.14	0.88	0.92
u_*	ETA-RRTM	0.05	0.07	0.09	0.27	0.78	0.86
H	ETA-RRTM	-9.10	24.25	37.27	-0.37	0.87	0.94
L_vE	ETA-RRTM	5.63	10.43	15.26	0.39	0.76	0.76
$L^{\downarrow}$	ETA-RRTM	-11.97	16.94	19.65	-0.04	0.68	0.75
$L^{\uparrow}$	ETA-RRTM	-10.14	19.42	26.37	-0.03	0.89	0.92
T_{veg}	ETA-CCM2	-2.55	4.09	5.53	-0.25	0.89	0.92
u_*	ETA-CCM2	0.04	0.07	0.09	0.25	0.77	0.87
H	ETA-CCM2	-11.04	24.35	37.58	-0.47	0.87	0.93
L_vE	ETA-CCM2	4.81	9.86	15.11	0.34	0.76	0.77
$L^{\downarrow}$	ETA-CCM2	-36.94	38.91	41.29	-0.14	0.60	-0.08
$L^{\uparrow}$	ETA-CCM2	-15.18	19.28	27.35	-0.04	0.90	0.91

4.7 Alternative land-surface scheme and turbulent mixing

Above we found that models with a vegetation layer and with limited turbulent mixing favor surface cooling in comparison with observations. Since the MM5-MRF model is computationally fast and has a good performance during daytime, we try to improve this model at night, and thus the model's representation of the full diurnal cycle. Two modifications are proposed:

a)   Several studies showed the importance of a correct representation of the atmosphere-land-interaction (Holtslag and De Bruin, 1988; Van de Wiel, 2002; S06). The latter study was able to predict T_{veg} and energy balance components satisfactorily for the same days as examined here. This was achieved by using a vegetation surface layer with small heat capacity, and to ensure that the soil was able to deliver heat to the surface sufficiently fast. This is especially important for quiet periods where turbulence vanishes and net radiation Q^* must equal the G. To improve the representation of the feedback with the soil in MM5-MRF, the original description of the G in MM5-MRF:

$$G = 1.18\Omega C_g \left(T_g - T_M\right) \tag{4.8}$$

has been replaced by

$$G = \Lambda\left(T_{veg} - T_g\right), \tag{4.9}$$

where T_g is the surface soil surface temperature, T_M the 24 h mean 2m air temperature used as the deep soil temperature, and Ω the Earth's angular velocity. This modification coincides with the implementation of a vegetation layer with a small heat capacity C_{veg}. We choose $C_{veg} = 2.10^3$ Jm^{-2}K^{-1} and surface resistance $\Lambda = 5.9$ Wm^{-2} K^{-1} as observed by S06 for CASES-99. Originally $C_g = 2.10^6$ Jm^{-2} K^{-1}, so this modification enables the modeled T_{veg} to react more quickly on a change of the net radiation. Fig. 4.9 summarizes the modified scheme conceptually.

b)   The original MM5-MRF scheme uses a prescribed K profile function form, where K depends on u_* and h. However, Nieuwstadt (1984) showed that turbulent mixing in the SBL is local and therefore K based on the surface friction seems to be less realistic (Mahrt and Vickers, 2003), especially when we realize that the model keeps surface u_* artificially large for calm conditions. Additionally, S06 found a very good performance for CASES-99 using a local turbulence scheme. Therefore, we replace the original scheme with a local ABL scheme. Herein $l = kz$, and flux-profile relation φ based on the local scaling hypothesis (Holtslag and Nieuwstadt, 1986; $\beta = 5$, $\alpha = 0.8$, $\zeta = z/\Lambda$, with Λ the local Obukhov length, Duynkerke, 1991):

$$\varphi(\zeta) = 1 + \beta\zeta\left(1 + \beta\zeta/\alpha\right)^{\alpha-1}, \tag{4.10}$$

for θ, U and q. This φ allows for some turbulent transport for $\zeta > 1$, but less than in large-

scale models (Viterbo et al., 1999). Moreover, in both simulations updates of the surface fluxes due to updated surface temperature were skipped since they were originally done with the T_g rather than with T_{veg}.
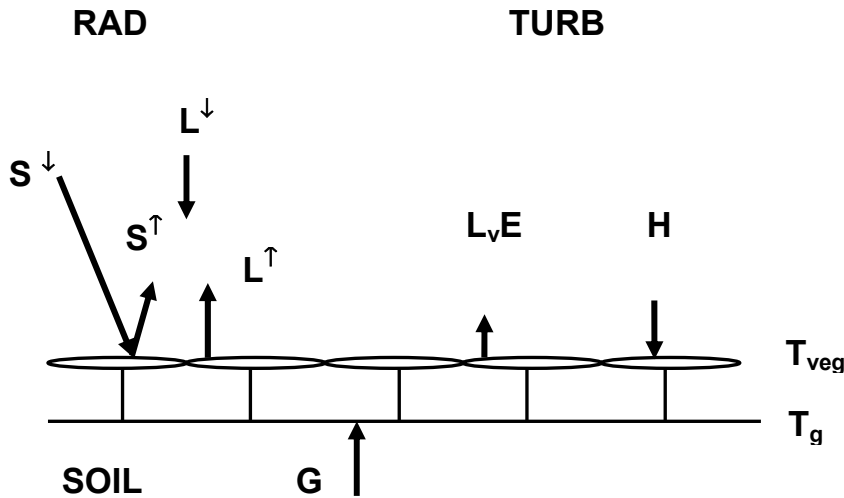
Figure 4.9: Illustration of the interaction between the energy fluxes by different physical processes in the SBL for the revised scheme in MM5-MRF, as extended with the surface *vegetation* temperature.

Fig. 4.10a shows the model results for T_{veg} for the modified scheme. At first, during all nights the modifications give a T_{veg} less than the reference scheme, and always better in agreement with the observations. Especially for the calm night, the cooling is 6 K stronger than for the reference run. T_{veg} also improves during daytime (~3 K), although the model is still too cold.

The friction velocity (Fig. 4.10b) with the modified schemes improves, especially after the day-night transition. During this stage of the diurnal cycle, the rapid surface cooling in the model enhances the stratification also rapidly, and consequently limits turbulent mixing. For the radiative night (25-26 Oct.), u_* improves strongly in the first half of the night compared to the reference run. Interestingly, the scheme for which only the vegetation layer has been altered shows a u_* increase at around 0100 CDT. The low u_* ensures a decoupling of the atmosphere from the surface. As such, the flow aloft accelerates, increasing the wind shear, and finally the flow recouples to the surface, and increases u_*. This effect is smaller when the local mixing scheme is also used. The strong and unrealistic revival of u_* might occur because the flow acceleration aloft starts at a different level than in reality, which might be due to limited resolution close to the surface. In general the addition of the local mixing scheme reduces the turbulence intensity compared to the simulation that only introduced the vegetation layer.

Fig. 4.10c shows that for the windy night (24-25 Oct.) the dynamical development of the SBL height agrees with the observations and increases with time. However, h is still overestimated, but less than for the reference runs. Unfortunately, the CBL deepens compared with the reference runs. This is because of an increased H during the day. The calculation of the CBL height in MM5-MRF might be reconsidered to circumvent too deep CBLs.
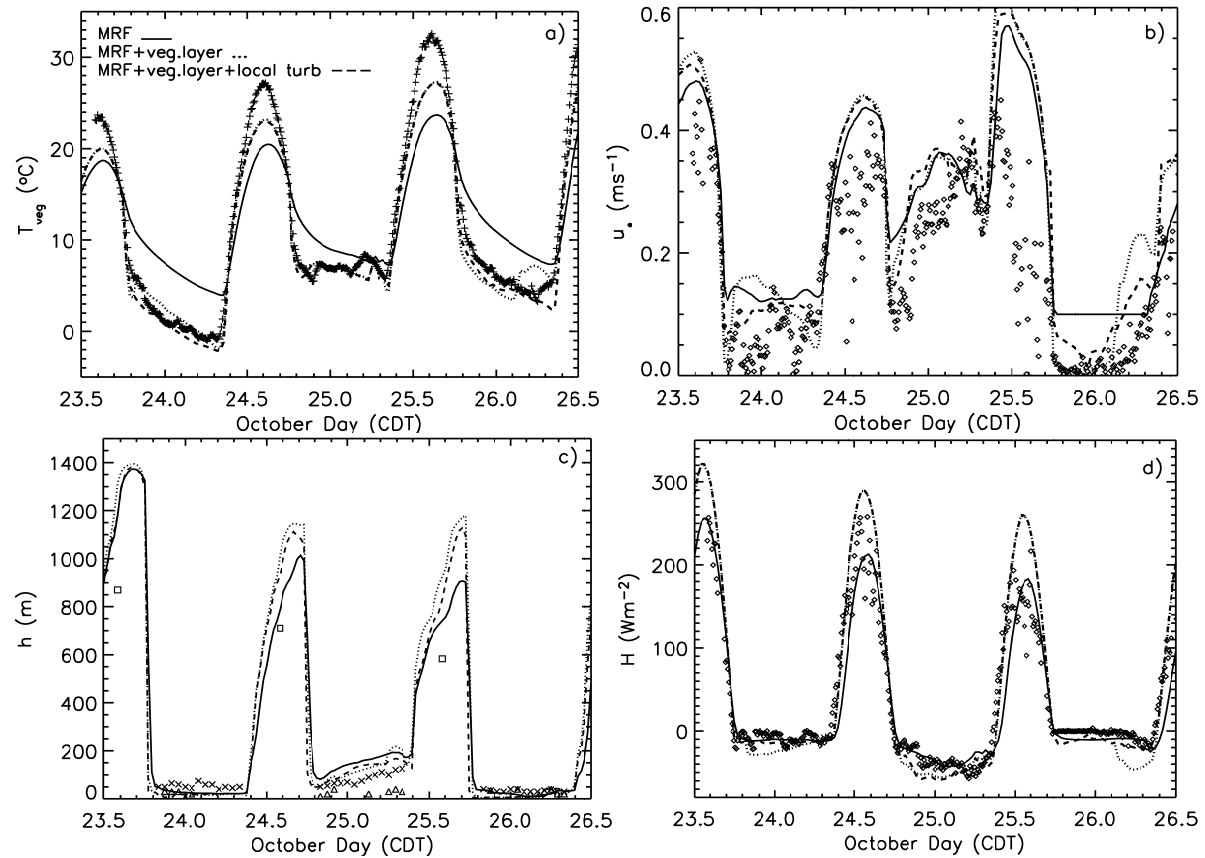
Figure 4.10: Modeled surface temperature (a), friction velocity (b) and boundary-layer height (c) and surface sensible heat flux (d) with the MM5-MRF scheme (full line), MM5-MRF updated with a vegetation layer (dotted line), and MM5-MRF updated with a vegetation layer + local mixing scheme (dashed line). Observations have been labeled as in Fig. 4.4.

Considering the θ and U profiles (Fig. 4.11), we find that improvements a) and b) provide realistic cooling during weak wind conditions (23-24 and 25-26 Oct.) and the LLJ is better represented. Unfortunately, the overestimated daytime heating provides warmer and deeper CBLs, and therefore the temperature profile is biased. However, the modeled and observed SBL *structure* corresponds rather well, especially when local mixing is utilized. The simulations with the Duynkerke (1991) turbulence scheme provide typically a shallower and more realistic SBL than with the K profile method. Additionally, the surface inversion is several degrees stronger than for the reference scheme (Fig. 4.11c). With the new schemes, also U is larger (Fig. 4.11b) in the residual layer due to enhanced daytime momentum mixing. The wind speed maximum is sharper, with a stronger wind speed, and at lower altitude.

Although the model results do not perfectly match the observations, the updated schemes show some clear and characteristic improvements for the modeled SBL profiles, and surface fluxes.
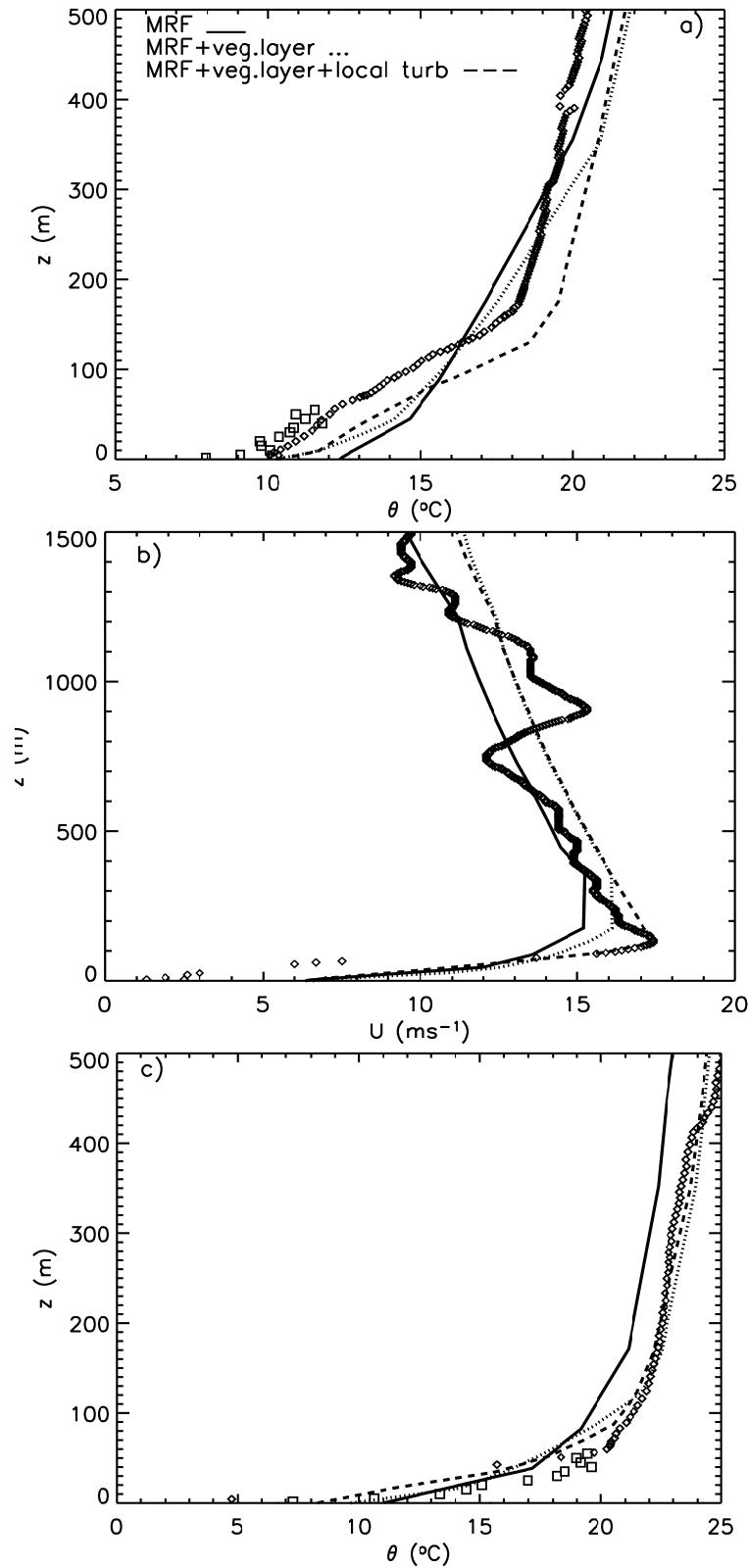
Figure 4.11: Modeled and observed potential temperature and wind speed for 25 Oct 0700 UTC (a and b), and modeled and observed potential temperature for 26 Oct 0700 UTC (c) for the reference MRF scheme (full line), MRF with a vegetation layer (dotted line) and MRF with vegetation layer + local mixing scheme by Duynkerke (1991) (dashed line).

4.8 Conclusions and recommendations

This study examines the performance of three limited area models (MM5, COAMPS and HIRLAM), for three diurnal cycles with contrasting stable boundary layers during the CASES-99 experimental campaign. The first night is classified as intermittently turbulent, the second continuously turbulent, and the last night weakly-turbulent. The strategy was to identify common deficiencies of these schemes and to identify conditions when certain schemes are beneficial.

All schemes underestimate the diurnal temperature cycle amplitude and the near surface stability at night. None of the parameterizations was able to represent the surface radiation and turbulent fluxes, the wind speed and temperature profiles, and the boundary-layer height correctly during the full diurnal cycle. Schemes with local mixing provide a more realistic representation of the nighttime boundary layer, especially for weak winds, and when the asymptotic length-scale is based on the flow properties. Moreover, the nighttime low-level jet is hard to reproduce, and we find a clear dependence on the chosen model domain size. Too small horizontal model domains provide a LLJ speed underestimation, because its generating mechanism (according to the thermal wind relation) is insufficiently resolved in that case. With a small domain, the modeled profiles depend too much on the boundary conditions by ECMWF, which underestimates the LLJ speed.

Additional sensitivity tests with different radiation schemes revealed large differences of the net cooling rate between these schemes and consequently to the forecasted surface temperature, especially for calm nights. This was mainly due to underestimated incoming longwave radiation.

Encouraged by earlier 1D results (Steeneveld et al., 2006) and to improve the current results, we implemented a new scheme for the stable boundary layer in MM5-MRF. The scheme introduces a vegetation layer with a small heat capacity, a realistic formulation for the soil heat flux, and a mixing scheme based on the local similarity hypothesis for stable conditions. The updated scheme improves the representation of the diurnal temperature range and the vertical structure of the forecasted profiles, especially for calm nights. This gives also more realistic shallow boundary layers with stronger inversions.

Appendix 4A: Model Description

a) Surface Layer. Surface fluxes of heat, momentum are calculated with Eq. (4.1) with the transfer coefficients specified below. z_a is the first atmospheric model level, k the Von karman constant, and ψ_m and ψ_h the stability corrections for momentum and heat.

MM5-MRF, MM5-ETA, MM5-BLA (Braun and Tao, 2000)**:**

$$C_\theta = k^2 \left(\ln(z/z_0) - \psi_m\right)^{-1}\left(\ln(z/z_0) - \psi_h\right)^{-1}; C_D = k^2\left(\ln(z/z_0) - \psi_m\right)^{-2} \tag{4.A1}$$

MM5-BT (with numerical coefficients $b = c = 5$)

$$C_\theta = \frac{k^2}{\ln^2(z/z_0)}\left[1 - \frac{3bRi_b}{1 + \frac{3bck^2}{\ln^2(z_a/z_0)}\sqrt{-\frac{z_a Ri}{z_0}}}\right]; C_D = \frac{k^2}{\ln^2(z/z_0)}\left[1 - \frac{2bRi_b}{1 + \frac{3bck^2}{\ln^2(z_a/z_0)}\sqrt{-\frac{z_a Ri}{z_0}}}\right]$$

$$\tag{4.A2}$$

COAMPS (Hodur, 1997)

$$C_D = \frac{k^2 f_m(z_a/z_0, Ri)}{\ln^2(z_a/z_0)}, \text{ and } C_\theta = \frac{k^2 f_h(z_a/z_0, Ri)}{R\ln^2(z/z_0)} \text{ with } R = 0.74. \tag{4.A3}$$

HIRLAM (Undén et al., 2000)

$$C_{m,h} = \frac{k^2}{\ln^2(z/z_0)}\left(1 + \frac{\ln(z_{0m}/z_{0h})}{\ln(z/z_{0m})}\right)^{-1} f_{m,h}\left(\frac{z}{z_0}, \frac{z}{z_{0h}}, Ri\right), \text{ with} \tag{4.A4}$$

$$f_m = 1 + \left(1 + \frac{10Ri}{\sqrt{1+Ri}}\right)^{-1}; f_h = 1 + \frac{1}{1 + 10Ri\sqrt{1+Ri}}\left(\frac{\ln(z/z_0)}{\ln(z/z_{0h})}\right) \tag{4.A5}$$

b) Boundary Layer. The ABL scheme is characterized by the specification of the eddy diffusion coefficient for momentum (K_m) and heat (K_h) as follows.

MM5-MRF

$$\overline{w\theta} = -K_h\left(\frac{\partial\theta}{\partial z} - \gamma_c\right); \gamma_c = \frac{7.8\overline{w\theta}_s}{w_s h} \text{ with } w_s \text{ an appropriate velocity scale, with } \gamma_c = 0 \text{ at}$$

night. $\tag{4.A6}$

Herein $K_h = kw_s z(1 - z/h)^2$ and $K_m = K_h \text{Pr} = K_h(\varphi_h/\varphi_m + 0.78k)$ with Prandtl number **Pr**.

MM5-ETA

$$K_{m,h} = S_{M,H}\left(Ri_{flux}\right)L_{MY}\sqrt{E}; \quad L_{MY} = kz/(1 + kz/l_\infty) \tag{4.A7}$$

MM5-BT

$$K_{m,h} = L_{MY}\sqrt{E}f_{m,h}; \qquad L_{MY} = kz/(1+kz/l_\infty) \tag{4.A8}$$

$$f_m = \frac{1}{1+2bRi(1+dRi)^{-\frac{1}{2}}}; \text{ and } f_h = \frac{1}{1+3bRi(1+dRi)^{-\frac{1}{2}}}, \text{ with } b = 5, d = 5. \tag{4.A9}$$

MM5-BLA

For CBL model layer j: $\overline{w\theta}_j = \overline{w\theta}_1 - \overline{m}\int_{z_1}^{z_j}[\theta_1 - \theta(z)]dz$ with $\overline{m} = \overline{w\theta_v}\Big/0.8\int_{z_1}^{z_m}\theta_1 - \theta(z)dz$,

For nocturnal $K_h = K_0 + |\partial U/\partial z|l^2 f(Ri)$; $f(Ri) = (1+10Ri(1+8Ri))^{-1}$ for $Ri > 0$, and K_0 is background diffusion.

COAMPS: as MM5-ETA**,** but $l_\infty = 0.1\int_0^h z\sqrt{E}dz\Big/\int_0^h \sqrt{E}dz$. \hfill (4.A10)

HIRLAM: $K_{m,h} = l\sqrt{E}$; with l as in Eqs. (4.5)-(4.9). \hfill (4.A11)

c) Surface scheme. All models solve the heat budget at the surface:
$$C_{surf}\,\partial T_{veg}\big/\partial t = Q^* - G - H - L_v E, \tag{4.A12}$$

but employ different C_{surf} values and different formulations for the soil heat flux (G).

MM5-MRF, MM5-ETA, MM5-BLA: $G = 1.18\Omega C_g(T_g - T_M)$. \hfill (4.A13)

MM5-BT: Deardorff, 1978

COAMPS: $G = 1.8.10^{-4}(T_g - T_M)$ \hfill (4.A14)

HIRLAM: ISBA scheme (Noilhan and Planton, 1989; Noilhan and Mahfouf, 1996).

$C_{surf} = \left(\dfrac{1-f_{veg}}{C_g} + \dfrac{f_{veg}}{C_{veg}}\right)^{-1}$ With $C_{veg} = 2.10^5$ Jm^{-1}K^{-1}. The scheme uses a force-restore method

in the deep soil, for which the coefficients are calibrated against a high resolution soil model.

Chapter 5

Exploring the possible role of small scale terrain drag on stable boundary layers over land

Abstract

Large-scale weather and climate models seem to need more drag in the stable atmospheric boundary layer than can be justified from turbulence field observations and Large-Eddy Simulations. This is necessary to obtain correct cyclone development, although it deteriorates the model performance in the stable boundary layer. A physical mechanism for the extra drag is currently missing. This paper illustrates the possible role of unresolved terrain drag in addition to turbulent drag on the development of the stable boundary layer. It appears that turbulent drag as estimated from field observations plus a first-order estimate for wave stress provides similar drag as the enhanced turbulent drag obtained with the so-called "long-tail" mixing function (currently in use in many operational schemes). Consequently, a simple parameterization of terrain drag divergence for use in large-scale models is proposed and tested in column mode. As an outcome, the cross-isobaric mass flow (a measure for cyclone filling) with the new scheme appears to be equal to what is found with the long tail scheme, but the new scheme produces a more realistic boundary-layer structure and height (less deep) at the same time.

5.1 Introduction

After sunset at clear skies, the land surface cools rapidly and potential temperature increases with height, and a stable boundary layer (SBL) develops. Generally, the dominant physical processes in the SBL are turbulent mixing, radiative cooling and the interaction with the land surface (e.g. Beljaars and Holtslag, 1991; André and Mahrt, 1982). Also, small-scale features such as gravity waves, katabatic flows, drainage flows and effects of land-surface heterogeneity can influence the SBL structure. The large variety of SBL physical processes, their nonlinearity and their interactions hampers our ability to understand and to model the SBL on a large spatial scale (e.g. in operational forecast models, Cuxart et al., 2006; Holtslag, 2006).

Despite the problems mentioned above, Steeneveld et al. (2006b) showed that the SBL can be satisfactorily modeled *on a local scale* for a broad stability range (i.e. on a specific site and for both clear calm and windy or cloudy nights). This can be achieved when forcings (geostrophic wind speed and advection) and the local characteristics of the soil and vegetation are well known. Also, the physical processes of turbulent mixing, radiation divergence and the soil heat flux should be accounted for in detail. Steeneveld et al. (2006) use a turbulent mixing scheme that agrees with tower observations and Large Eddy simulation results, and shows nearly vanishing turbulent mixing for $Ri > Ri_{crit}$ (e.g. Beljaars and Holtslag, 1991; Duynkerke, 1991). We will refer to this scheme as a "short tail" scheme.

Contrary to this local approach, large-scale models with a "short tail" formulation suffer from insufficient cyclone filling, i.e. low-pressure systems are forecasted too deep and their lifetime is longer than observed. Therefore large-scale models require more drag than is provided by the "short-tail" formulation. This is currently achieved by applying "enhanced turbulent mixing" or a non-physical "long tail" formulation, with nonzero turbulent mixing for $Ri > Ri_{crit}$. In addition, the long tail formulation also prevents models from unrealistic run-away surface cooling. Since there is no physical justification for the enhanced mixing approach, the current mixing formulations for both the surface layer and the stable boundary layer are strongly based on model performance and not on physical reality (Louis, 1979; Beljaars and Viterbo, 1998; Zilitinkevich et al., 2001). Although the enhanced mixing approach provides satisfying synoptic flow, a key drawback of this approach is the poor representation of some critical aspects of the stable boundary layer. First, the stable boundary layer becomes typically a factor 2-3 too deep, and the mean stratification is underestimated (Ek et al., 2003; Cuxart et al., 2006). This has clear consequences for forecasting the dispersion of pollutants. Second, the typical nocturnal wind maximum or low-level jet (LLJ) is forecasted at a too high altitude and is too weak (e.g. Steeneveld et al., 2007). This gives errors in the horizontal transport of e.g. humidity from the Mexican Gulf to the U.S. midwest (Cheinet et al., 2005). Also, the backing of the wind is insufficient in stable stratification, not only over land but also over sea (Brown et al., 2005). This mismatch of the SBL structure has significant impact on the ability to forecast fog, air quality and frost. Obviously, the present long tail parameterization is unsatisfactory from a physical point of view and improvement is needed.

The long tail formulation is often justified by means of mesoscale circulations due to land-surface heterogeneities smaller than the model grid cell. Asymmetric cooling on the subgrid scale can generate additional terms in the flux calculations due to spatial averaging of the non-linear flux-gradient relationship (Mahrt, 1987). However, McCabe and Brown (2006) show this effect cannot fully account for the requested additional mixing for their model and study area, but only contributes to the additional drag near the surface (first 10 m).

Hence, there is a need to examine other possible mechanisms that can account for the necessary drag. Therefore, we have to realize that drag is not necessarily only turbulent drag (with strong mixing), but can also be due to processes with less strong mixing properties. McCabe and Brown (2006) speculate that gravity wave drag or other forms of terrain drag might be possible candidates. This is supported by earlier studies in e.g. Chimonas and Nappo (1989). In this paper, we analyze the possible impact of gravity wave induced terrain drag on apparent flux-profile relationships from the CASES-99 field observations. Furthermore, we propose a *practical, quasi-empirical* method to account for terrain drag on the SBL, and we will show that this method provides both a realistic stable boundary-layer height and LLJ, and on the other hand also provides sufficient cyclone filling *at the same time*.

The paper is organized as follows: Section 5.2 gives some background material and Section 5.3 presents a brief theoretical background. Section 5.4 presents the observations and the impact of wave stress on local flux-profile relationships and in Section 5.5 a simple parameterization for wave stress in the SBL is proposed. Discussion and Conclusion are presented in Sections 5.6 and 5.7 respectively.

5.2 Background

There are few areas greater than a 2 or 3 square kilometers of the Earth's surface that are flat. Spatial variance of terrain height exists on all scales of atmospheric motions ranging from mountains and valleys on the global scale to hillocks and gullies on the PBL scale. On the global scale, the diurnal cycle has little influence on the atmospheric drags produced by the large-scale terrain features. However, as demonstrated by Nappo (1977), daytime convection tends to overwhelm the perturbations of the boundary-layer flow by small-scale terrain irregularities, but in the stable PBL these perturbations can be important. Examples of these types of perturbations include form drag, flow blocking, channeling, rotors, hydraulic jumps, vortex shedding, turbulent wakes, and buoyancy waves. These stresses are not considered in similarity theory, and their effects are not simulated in the treatments of the stable PBL in mesoscale models.

The integrated effects of terrain-height variance during convective conditions has been approached by the use of an 'effective' surface roughness parameter (e.g. Wood and Mason, 1993). However, such a parameter appears not to be accurate under stable conditions when gravity waves are excited. One reason for this is that the effective surface roughness is independent of the atmospheric flow and thermal stratification as is the case with the aerodynamic surface roughness, z_0.

In this study we explore the role of small-scale (amplitude O(10m) and horizontal scale O(1-10 km)) orographically generated wave stress and whether parameterization of its flux divergence in the SBL can circumvent the need for enhanced mixing. Wave stress divergence in the SBL may reduce the mean flow (analog to waves generated by large mountains), without the need for intensive turbulent mixing. Despite its potential impact, large-scale models currently do not specifically account for wave stress in the SBL.

As an example, Fig. 5.1 shows a 20 km North-South cross section of modeled horizontal and vertical wind speed by the mesoscale model MM5 at the end of a calm night during the CASES-99 field campaign (Steeneveld et al., 2007). Although the CASES-99 terrain is often referred to as relatively flat and homogeneous (Poulos et al., 2002), the U.S. Geological Survey (USGS) land-surface database (used for the land-surface properties in MM5) indicates that the terrain is gently undulating with a wavelength of about 10 km and an amplitude of about 15 m (see also Fig 5.3 below).

It is seen in Fig. 5.1 that the flow is seriously 'influenced' by the orography and the model produces standing waves that extends to 350 m above the main terrain height, and the wave crests tilt upstream (Nappo, 2002).

Figure 5.1: North-south cross section of modeled (MM5, 1x1 km horizontal resolution) boundary-layer flow over a small surface corrugation with a amplitude of ~15 m and a wave length of ~10 km for a calm night in the CASES-99 experimental campaign (23-24 Oct 1999, 1200 UTC (6 LT)). Full lines: vertical wind speed (cm s^{-1}), dashed line: wind component perpendicular to the orography (ms^{-1}).
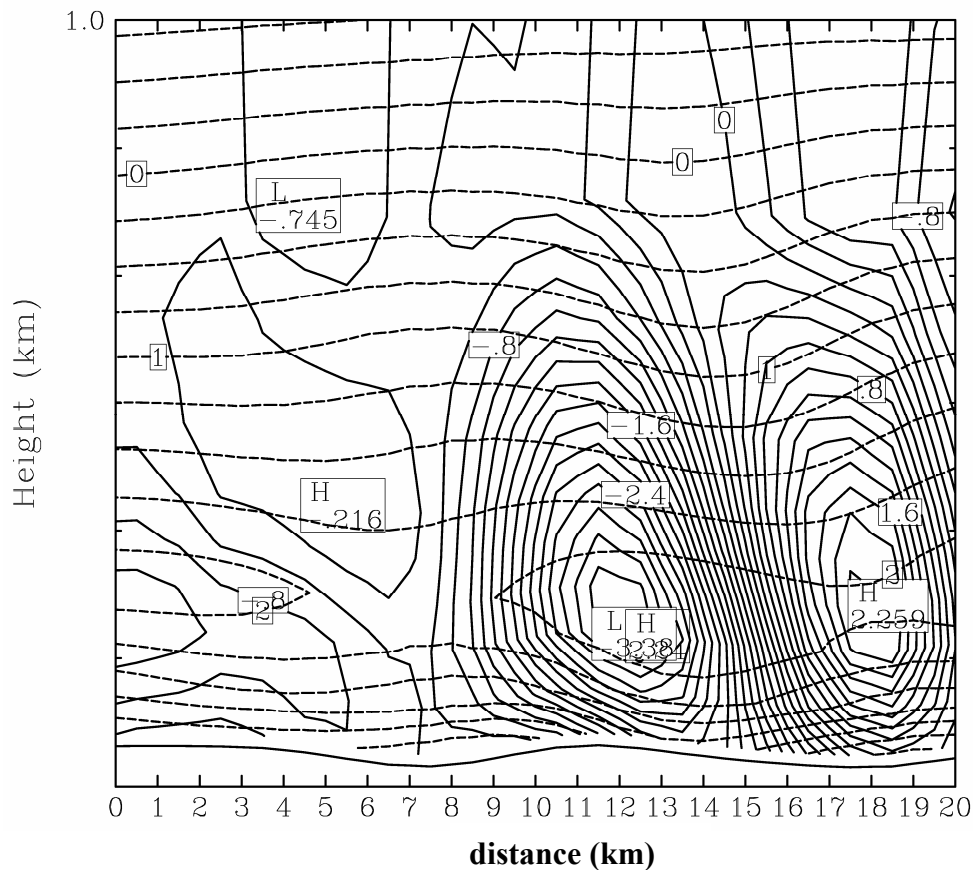
Thus, even for this relatively simple orography, complex flow structures are present, and it is only resolved in high resolution models, but not in large-scale models. Unfortunately, observing such structures in the field is also complicated. Tower measurements at a single station cannot reveal this 2D structure and obtaining an adequate sample size perpendicular to the wave phase lines with an aircraft might be a significant problem. Therefore, we have to rely here on model results to get an indication of the flow field.

Large-scale models deal with three effects to account for the impact of (mountain) orography on the flow (Lott and Miller, 1997):

- turbulent form drag due to pressure forces,

- gravity wave drag and

- flow blocking.

Turbulent form drag is currently often parameterized using an effective roughness length approach: the roughness length for momentum is increased if the amplitude of the underlying orography is sufficiently large, and the roughness length for scalars is decreased. An alternative approach is an explicit prescription of the turbulent flux enhancement with height (Brown and Wood, 2001; Rontu, 2006). Brown and Wood (2003) showed that the effective roughness length approach works satisfactorily in the SBL only in the case where gravity waves are not present, and therefore we will not consider this subject in more detail.

In a stably stratified medium mountains or ridges can generate stationary gravity waves. The role of propagating gravity waves in the ABL dynamics is actively discussed (e.g. Finnigan, 1999; Brown et al., 2003). Although specific knowledge of waves in the SBL is limited, there is sufficient observational (e.g. Kurzeja et al., 1991; Nappo, 1991; Sun et al., 2003; Cheng et al., 2005) and theoretical (Chimonas and Nappo, 1989; Nappo and Chimonas, 1992; Belcher and Wood, 1996) evidence to suggest that gravity waves are important. Since waves generate Reynolds stresses, they might play an important role on the dynamical evolution of the SBL (Einaudi and Finnigan, 1981; Finnigan, 1999).

Orographically generated waves propagate upward and the associated wave stress is in principle constant with height (i.e. under constant wind speed and stratification; Nappo, 2002). However, constant wind speed and stratification do not occur in the SBL. Also, when gravity waves are excited, the wave field can become convectively unstable at a certain level (i.e. overturning) and the waves will break. This will certainly happen when the waves approach a critical level (i.e. where wind speed $U = 0$). Consequently, a divergence of the wave stress can occur, and this will decelerate the flow. This mechanism is well understood for large mountain ridges. However, the SBL is shallow, and it can be expected that also small-scale orography can significantly influence the SBL flow through gravity wave propagation. Nappo (2002) and Chimonas and Nappo (1989) indeed theoretically showed that the magnitude of the SBL wave stress and turbulent stress are of the same order during weak winds.

Large-scale models account for mountain gravity waves resulting in forecast quality improvement (Palmer et al., 1986). However, normally *only orography on horizontal scales larger than 5 km.* (Beljaars et al., 2004) is considered. This may be correct for typical tropo-

spheric stratification, but is not a priori correct for the SBL, where smaller horizontal scales may impact on gravity wave generation.

Finally, flow blocking occurs when the vertical Froude number $Fr = U/(NH) < 1$ (U is the wind speed, N the Brunt-Vaisala frequency and H the amplitude of the hill). In that case, the stratification is so strong that the flow is unable to pass over the topography, and over a certain depth the flow becomes blocked. Hence, a force is directed from the orography to the air. Large-scale models account for flow blocking for the large scales (e.g. Lott and Miller, 1997). For moderate orography it is well known that flow blocking may be important (Grant, 1994; Holden et al., 2000), but is not accounted for in large-scale models. Flow blocking might be relevant for SBL modeling as well, but it will not be treated here.

In the next section we examine the wave contribution to the total drag in stable conditions, and compare with the required drag in large-scale models.

5.3 Theory

The turbulent mixing for the stable boundary layer is often calculated in large-scale models with an eddy diffusivity K_m. This can be written as (e.g. Duynkerke, 1991; Holtslag, 1998)

$$K_m = (\kappa z)^2 \left| \frac{\partial \vec{U}}{\partial z} \right| F_m(Ri) \tag{5.1}$$

where κ is the Von Karman constant (taken 0.4 here), z the height above the ground, $\vec{U}$ the modulus of the wind speed, Ri the gradient Richardson number.

The stability function for momentum F_m limits K_m for stronger stratification, and its form has been determined from many turbulent field observations (via the so-called flux-profile relationships), in particular for the surface layer (e.g. McVehil, 1964; Oke 1970; Businger et al., 1971; Skibin and Businger, 1985; Beljaars and Holtslag, 1991; Howell and Sun, 1997, Steeneveld et al., 2006; Baas et al., 2006) and from Large-Eddy Simulations (e.g. Beare et al., 2006). For weakly stable conditions there seems to be consensus on the log-linear form of the flux-profile relationship, established by field observations in Businger et al., (1971, henceforth B71):

$$\begin{cases} F_m = (1 - 5Ri)^2 & \text{for} & Ri < Ri_{crit} \\ F_m = 0 & \text{for} & Ri > Ri_{crit} \end{cases} \tag{5.2}$$

Note that for $1/6 < Ri < Ri_{crit}$, the functional form is uncertain and not confirmed by field observations (see Van de Wiel et al., 2007).

To estimate the wave drag (τ_{wave} (in Nm^{-2})), one may use linear theory. Then the wave drag for an (idealized sinusoidal) surface corrugation for constant wind speed and stratification is given by (Belcher and Wood, 1996; Nappo, 2002):

$$\tau_{wave} = \begin{cases} \frac{1}{2}\rho_0 k_s (UH)^2 \sqrt{\dfrac{N^2}{U^2} - k_s^2} \quad .....for \ \dfrac{N}{U} > k_s \\ \\ 0 ....for \ \dfrac{N}{U} \le k_s \end{cases} \qquad . \tag{5.3}$$

Here N is the Brunt-Vaisaila frequency, H and k_s the orography amplitude and the wave number respectively, ρ_0 the air density and U the background wind speed perpendicular to the orography. This reduces for weak winds to (Nappo, 2002):

$$\tau_{wave} = \frac{1}{2}\rho_0 k_s H^2 N U_0 \tag{5.4}$$

Note that this result can also be deduced from dimensional analysis realizing that N and U_0 are the relevant atmospheric variables and k_s and H the relevant terrain parameters.

Next, we investigate the possible role of wave stress on the form of the stability function. Therefore, we define an apparent stability function F_m^*

$$F_m^* = \frac{(\tau_{turb} + \tau_{wave})/\rho}{(\kappa z)^2 \left(\dfrac{\partial U}{\partial z}\right)^2} = \frac{\tau_{turb}/\rho}{\left(\kappa z \dfrac{\partial U}{\partial z}\right)^2} + \frac{\tau_{wave}/\rho}{\left(\kappa z \dfrac{\partial U}{\partial z}\right)^2}, \tag{5.5}$$

which results in (only for the lower part of the SBL: $H<<z<<h$, with h the SBL depth):

$$F_m^* = \frac{u_*^2}{\left(\kappa z \dfrac{\partial U}{\partial z}\right)^2} + \frac{k_s H^2 UN}{2\left(\kappa z \dfrac{\partial U}{\partial z}\right)^2} \tag{5.6}$$

Recalling that $\varphi_m = \dfrac{kz}{u_*}\dfrac{\partial U}{\partial z}$, $S = \dfrac{\partial U}{\partial z}$, and $Ri = \dfrac{N^2}{S^2}$, and approximating $U = \dfrac{\partial U}{\partial z}z$, we obtain

$$F_m^* = \frac{1}{\varphi_m^2} + \frac{k_s H^2 \sqrt{Ri}}{2\kappa^2 z} \tag{5.7}$$

Thus we see that the modified relationship includes an extra term to the original formulation by B71. This extra term is a function of Ri and indicates stronger impact for stronger stability.

Fig. 5.2 depicts Eq. (5.7) for small-scale orography ranging from $H = 5$-15 m and $L_x = 1000$ and 1500 m, together with the F_m-formulation in the current ECMWF model (also known as "LTG-revised" (LTGr); Beljaars and Viterbo, 1998). The LTGr scheme allows more (but only turbulent) drag for large Ri while with Eq. (5.2) mixing vanishes at $Ri_{crit} = 0.2$. The LTGr scheme has a strong departure from B71's turbulence field observations for $0.1 < Ri < 0.2$.
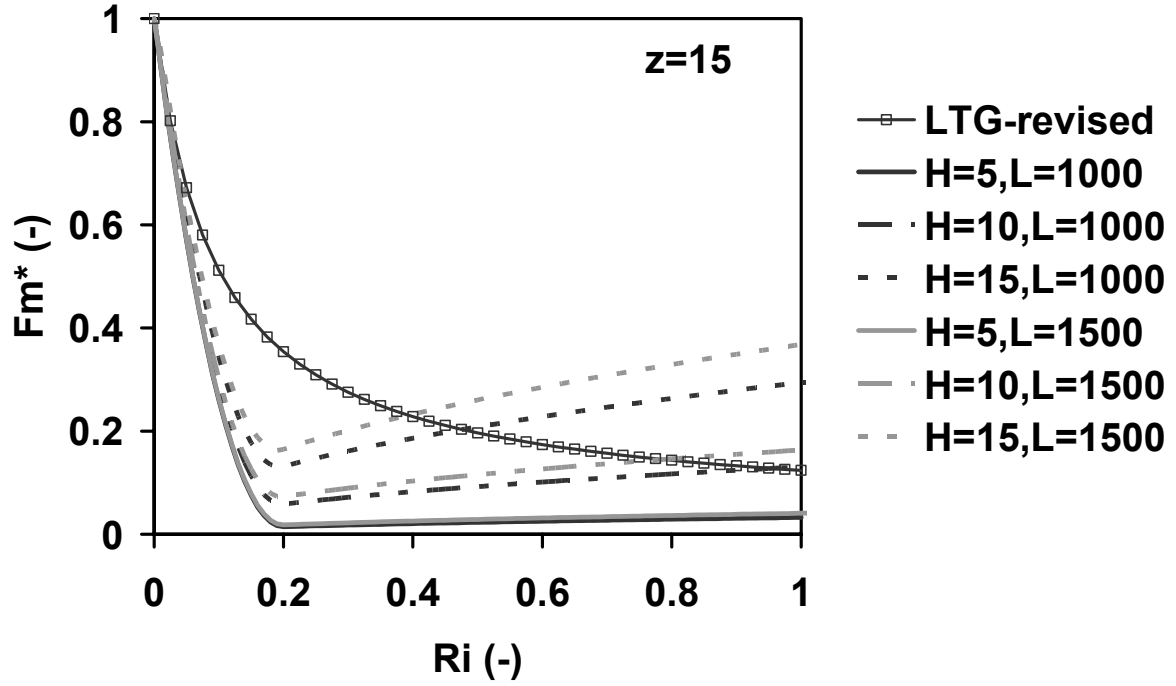
Figure 5.2: Apparent stability function F_m^* as function of gradient Richardson number for orography with amplitude of 5, 10 and 15 m and wavelength 1000 and 1500 m at 15 m height. The LTG line corresponds to the current formulation in the ECMWF model.

The formulation that accounts for terrain stress has some characteristic advantages compared to the LTGr scheme. First it satisfies the well-established B71 formulation (Eq. 5.2) for $Ri <$ 0.2 and is thus in closer agreement with field observations and LES for the weakly stable boundary layer (small Ri). Secondly, at the same time, F_m^* approaches the long tail formulation of LTGr for large Ri, but now based on the above consideration of terrain stress.

Note that Eq. (5.7) cannot be directly applied in practice in operational models. We present our results in this format only because the enhanced mixing problem is often presented in this format. Since the physical mechanism of turbulent mixing and wave stress are different, they should be treated separately in models, as will be done below. Note also that the parameterized wave drag does not include a companion transport of heat.

5.4 Evaluation with field observations

a) Observations and Site Description

We use CASES-99 observations, taken October 1-31, 1999 near Leon, Kansas, U.S.A. (37.6486° N, -96.7351° E, 430 m a.s.l.). CASES-99 was organized especially to study the relevant processes in the SBL (Poulos et al., 2002). The area is often referred to as relatively flat (on a local scale) prairie grassland and free of obstacles. However, on a somewhat larger scale, the topography is gently rolling with a wavelength of $L_x =$ 1600 m and an amplitude of $H =$ 15 m (obtained from orographic maps), especially in the north-south and east-west direc-

tion. Note that H/L_x is only of order 1%, so we consider small slopes.

Fig. 5.3 shows the mean spectral densities of the orography, calculated from the 0.33" USGS database (available at http://seamless.usgs.gov/) for about 40 x 40 km around the CASES-99 central mast. Note that for small scales the spectrum is subject to aliasing. We find that the variability in the orography (both in x and y direction) is the same over a broad range of scales, but more importantly, they are almost level between $k = 2.10^{-4}$ m^{-1} and 2.10^{-3} m^{-1}. So the clear cut-off of $k = 2.10^{-4}$ m^{-1} for the contributing scales in large-scale models is not a priori justified (at least for the current area). The variance of the orography amounts to 100 m^2, thus a typical amplitude of the surface corrugation of 15 m is reasonable. A similar spectral analysis for a 6 x 6 km area around Leon indeed revealed a spectral peak at approximately L_x = 1.6 km. Note that the orography is far from sinusoidal, and thus the amplitude and wavelength can only be estimated with considerable uncertainty, and as such L_x and H should be considered as effective values of the terrain wavelength and amplitude respectively.
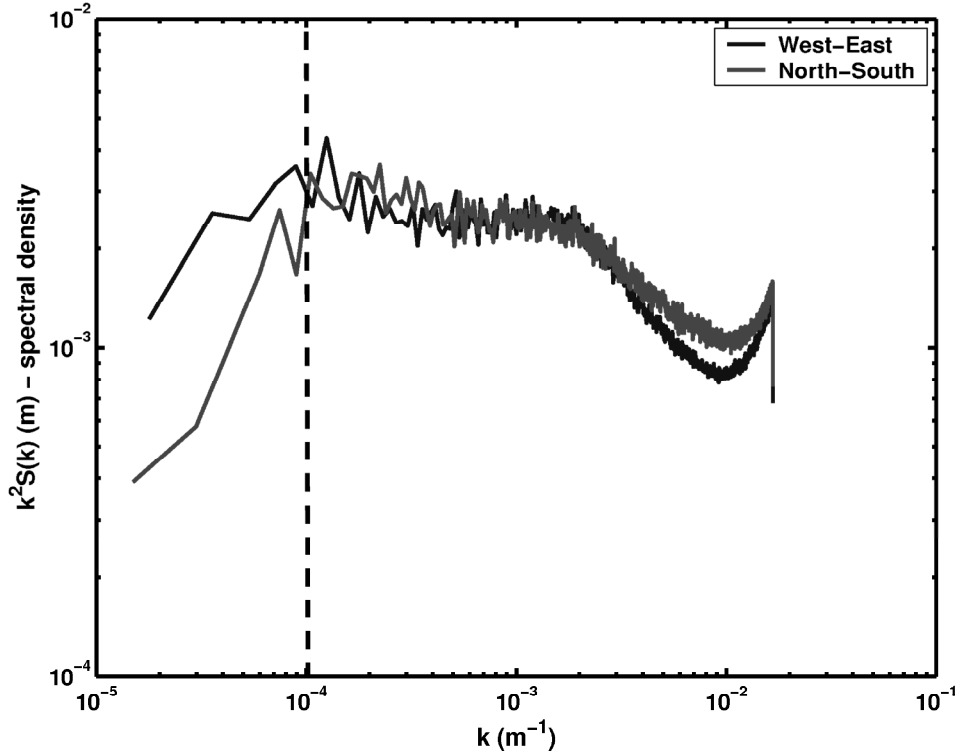
Figure 5.3: Spectrum of the orography in an area of 40 x 40 km around CASES-99 central site. The vertical dashed line indicates the cut-off wave number above which large-scale models neglect the effect of orographic wave stress.

To evaluate Eq. 5.4, the wind speed and temperature profiles along a 60 m mast are used. The surface turbulent momentum (τ_{turb}) is obtained with the eddy covariance technique at 2.6 m and temperature at the mast by thermocouples (10 minutes averages, Hartogensis and De Bruin, 2005). The observations have been selected for $u_* > 0.04$ ms^{-1} and $\overline{w\theta} < -2$ Wm^{-2}, because for small magnitudes of turbulent fluxes the accuracy becomes insufficient. Wind speed and potential temperature gradients were obtained by fitting a polynomial through the ob-

served profile:

$$X = A\ln^3(z) + B\ln^2(z) + C\ln(z) + c \tag{5.8}$$

and taking the derivatives. Observations from the 1.5 m and 55 m level have been disregarded since the quality of the fit at the edge of the mast is questionable (Akima, 1970). Data with a layer averaged mean wind speed larger than 5 ms^{-1} (terrain stress is relatively more important for weak winds) and observations with $\partial\theta/\partial z < 0.03$ Km^{-1} and $\partial U/\partial z < 0.03$ s^{-1} have been omitted because of their small accuracy. To estimate the terrain stress U and N are calculated as the averaged wind speed and stratification in the layer between 15 and 55 m. Because the orography follows the assumptions behind Eq. (5.4) (sinusoidal landscape) mostly in the North-South and East-West direction, we select only observations within a sector of 30º within these axes.

b) Results

We plot F_m^* vs Ri, although we know that this scaling is inappropriate for practical use, since turbulence and terrain stress should be separately scaled according to Eq. (5.2) and (5.3) respectively. However, to examine the combined effect of turbulence and terrain stress in the apparent formulation as function of stability with the LTGr scheme, we adopt Eq. (5.7). Data for small Ri follows B71 (not shown), as found by Baas et al. (2006). Fig. 5.4 shows that for the data based on turbulence only (diamonds) $F_m^* \rightarrow 0$ for large Ri. As such, we have confidence in the turbulence observations. When we include the estimate for the terrain drag (calculated with Eq. (5.4)), F_m^* is increased significantly for $0.2 < Ri < 0.3$. For $Ri > 0.6$, the data points with terrain stress included seem to follow the LTGr model. This result indicates that terrain stress generated by small-scale orography could indeed be an important candidate to describe the total SBL drag. In the next section we analyze the model impact on the SBL for a simple parameterization for the terrain stress.

5.5 Model impact of small-scale terrain drag

a)   Dynamics

Small-scale wave drag due to orography should be parameterized in large-scale models, since it is a subgrid process. Then, the prognostic equations for wind speed become:

$$\frac{\partial U}{\partial t} = -f(V - V_g) - \frac{\partial \overline{u'w'}}{\partial z} - \frac{1}{\rho}\frac{\partial \tau_{wave,u}}{\partial z}, \tag{5.9}$$

$$\frac{\partial V}{\partial t} = f(U - U_g) - \frac{\partial \overline{v'w'}}{\partial z} - \frac{1}{\rho}\frac{\partial \tau_{wave,v}}{\partial z}, \tag{5.10}$$

with U_g, V_g the x and y components of the geostrophic wind, f the Coriolis parameter, the second term on the RHS the turbulent flux divergence and the third term the divergence of the terrain stress.
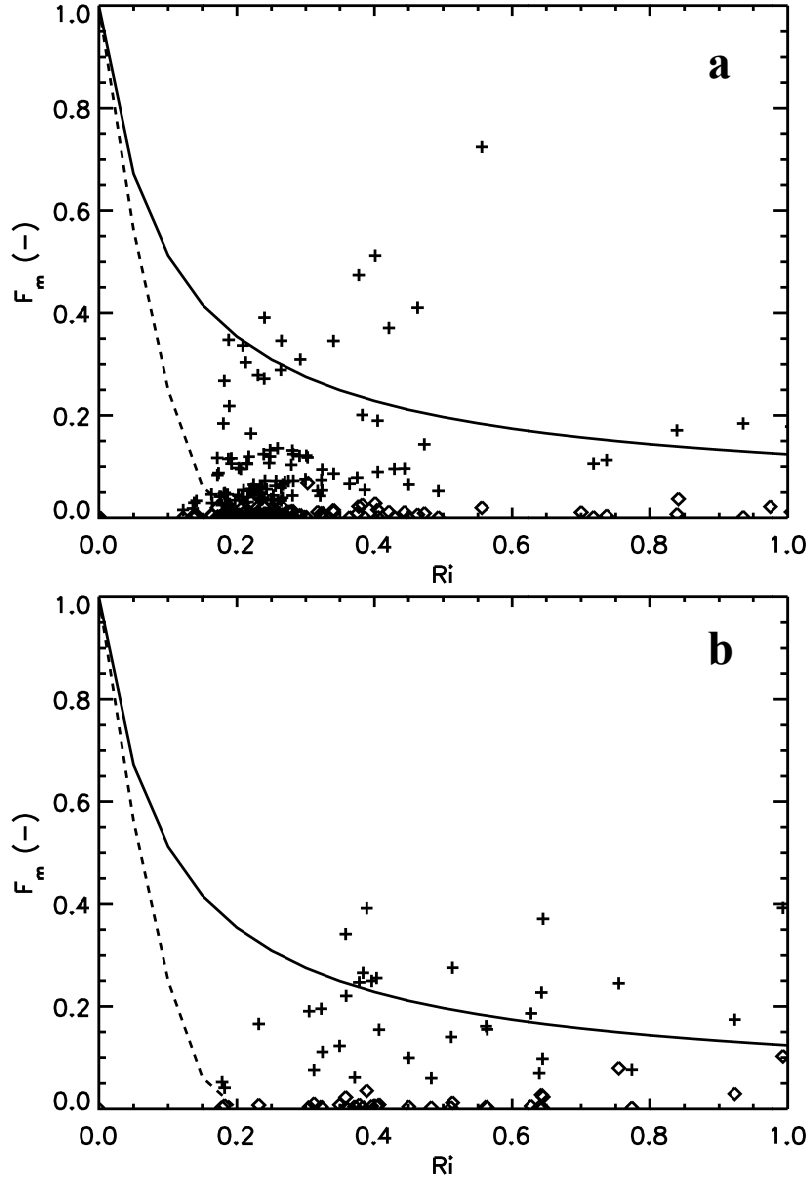
Figure 5.4: Stability function F_m as function of Ri for class $0.015 < N/U < 0.025$ m^{-1} and north-south direction (a, top panel) and east-west-direction (b, bottom panel). Diamonds: only turbulent drag included (not plotted for $Ri < 0.15$), +: both turbulent and wave drag included, Full line: LTGr mixing formulation; Dashed line: Businger (1971) model.

To account for the divergence of the wave drag, we assume that the terrain stress Eq. (5.3) is maximum at the surface and decreases parabolically (see discussion below) with height up to the scale depth of the stable PBL where it we assume it to be zero

$$\tau_{wave}(z) = \tau_{wave}(0)\left(1 - \frac{z}{h}\right)^2 , \qquad (5.11)$$

with h the SBL height, here defined as the height where the local u_* is 5% of its surface value and divided by 0.95 (Cuxart et al., 2006). In Eq. (5.11) $\tau_{wave}(0)$ is calculated with Eq. (5.4), with N and U obtained from the lowest half of the SBL. With the current formulation we rely on the correct formulation of the boundary-layer height. Note that the use of a linear depend-

ence of $\tau_{wave}/\tau_{wave}(0)$ with height would lead to similar model results. In addition, an arbitrarily chosen 10% of the terrain stress divergence is allowed to extend above the boundary-layer height. However, we found that altering the 10% criterion in the range between 1% and 5% does not modify the results significantly.

The functional form in Eq. (5.11) is supported by the form of the resolved wave drag in MM5 simulations (Fig. 5.5) for the case study presented in Fig. 5.1. For this simulation, MM5 was run in a 1600 x 1600 km area with 4 nested grids, with the inner nest at a 1 km horizontal resolution. Furthermore, ECMWF provided the initial and boundary conditions every 6 h. We used the MRF boundary-layer scheme and the cloud radiation scheme. Further details on those simulations can be found in Steeneveld et al. (2007). To calculate the resolved wave drag from forecasted MM5 fields, the u and w components along a transect have been detrended and the mean was subtracted, and the covariance was taken. Despite support from MM5 for the shape in Eq. (5.11), we note that in certain atmospheric conditions the functional form of the height dependence of the wave stress may be different and this height dependence does not necessarily scale with the boundary-layer depth. However, no other clearly definable height scale for this divergence is currently available; thus we use the SBL height as a working hypothesis for the vertical scale, as in Eq. (5.11).

Additional support for wave drag contributions to the SBL dynamics is given in Brown et al. (2003) who reasoned that orographically generated gravity waves propagate upward, but cannot pass the boundary-layer height. Since the nocturnal SBL develops against the background of a near neutral residual layer, waves cannot propagate (totally) into the free atmosphere (Zilitinkevich, 2002).
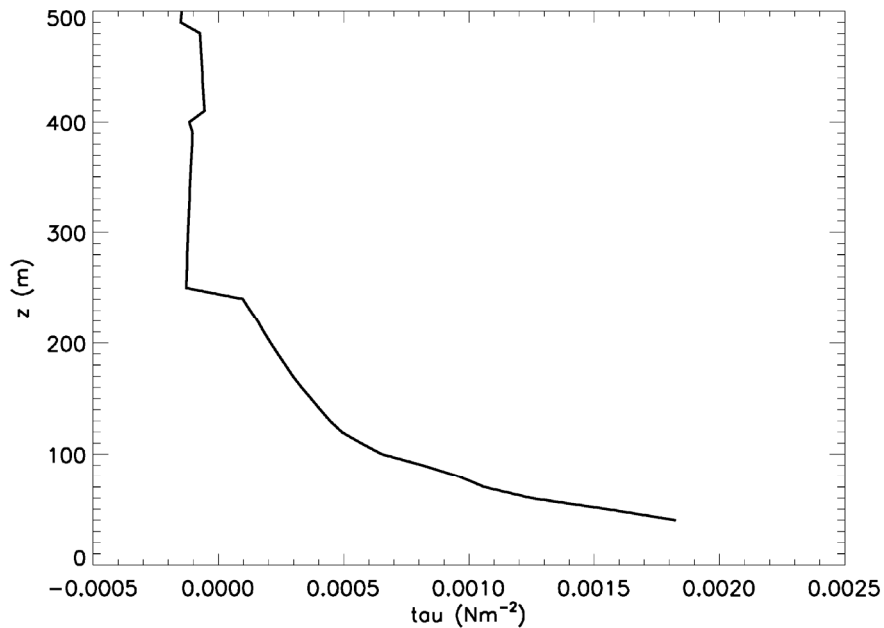
Figure 5.5: Vertical profile of resolved orographic wave drag in the MM5 simulation for the night of 23-24 Oct 1999, 1200 UTC (6 LT), in CASES-99 (see also Fig. 5.1).

Also, Grisogono (1994) and Jiang et al. (2006) found that in non-ideal conditions when turbulence is acting on the wave disturbances, the wave stress can be absorbed by the boundary layer. Consequently, a major part of the wave stress generated near the surface can be supported by momentum loss from the SBL and represented in the governing equations for the dynamics (Nappo, 2002).

b) Case study

To examine the behavior of the parameterization in a model, we start with a boundary layer with initial mean state by $\theta = 265$ K for $0 < z < 100$ m and 0.01 K m^{-1} increasing above $z > 100$ m, and the atmosphere is considered to be dry. The surface has a $z_0 = z_{0h} = 0.1$ m and we assume $H = 10$ m and $L_x = 1000$ m (with the corrugations parallel with *y*-axis) for illustrating the effect of accounting for terrain stress. The model integration is for 68 hours and for the current study we apply a 40-layer logarithmically spaced grid. This provides fine resolution near the surface ($\Delta z = 0.7$ m) and coarser near the model top (800 m). The geostrophic wind is $U_g = 6$ m s^{-1} and $V_g = 0$ m s^{-1} and $f = 1.39 \times 10^{-4}$ s^{-1} (equivalent with 73 °N). At the surface, we solve the energy budget to predict the surface temperature. Hence the surface turbulent heat flux is interdependent on the surface temperature and the ground heat flux (as in reality, Steeneveld et al., 2006b). The grey-body emissivity scheme of Garratt and Brost (1981) is utilized to account for radiative flux divergence.

The modelled wind speed and potential temperature profiles after 8 hours are shown in Fig. 5.6. We show results of three simulations: one using the B71 formulation (Eq. 5.2), one using the LTGr formulation and one using B71 + terrain stress (Eq. 5.11) included. After 10 hours the model reaches a stationary state (not shown). We see that some characteristic difference between the model formulations. Compared to the original B71 formulation, the LLJ with the new scheme is stronger, deeper and located at higher altitude (90 m with B71 and 140 m with the new scheme). The *v*-component is larger with the new scheme over a 200 m deep layer, with the strongest impact at 50 m height where the maximum speed changed from 2.1 ms^{-1} to 3.8 ms^{-1}, and the modulus of the LLJ speed from 6.5 to 7.5 ms^{-1}. Note that *h* is deeper than with the B71 formulation, although this seems to contradict with the extra removal of momentum from the mean flow. However, the current formulation removes most of the momentum near the surface, which means the shear over the total SBL increases and thus also the shear production, and the turbulent mixing, and consequently the SBL depth. The LLJ accelerates much slower compared with the case we use only B71, and we find an inflection point in the wind profile at *t* = 4 h (not shown). In reality this will provide a dynamically unstable profile.

More important is the comparison between the new scheme and the LTGr scheme results. The new scheme gives a LLJ of 7.5 ms^{-1} at 150 m, where the LTGr scheme lacks a clear LLJ. Also the wind speed gradient within the PBL is larger with the new scheme than with LTGr, and also the wind turning with height is much smaller with LTGr than with the new scheme. The thermal structure reveals a stronger stratification with terrain stress included at *t* = 4 (not

shown) and a more mixed structure after 8 hours. Furthermore, the thermal structure of the LTGr is less stable than both of the other simulations over a deep layer.

After $t = 4$ h the terrain stress is the main contributor to the total stress, and the turbulent stress is reduced compared to the run that uses the B71 formulation, although this counteracts cyclone filling required for more realistic model results. Note that the turbulent heat flux is hardly affected. The *Ri* number increases strongly with height and shows a sudden increase at 110 m for a run with Eq. (5.3) and at 200 m for the case with terrain stress included. The LTGr formulation shows a more gradual increase. The height-independent $\overline{v'w'}$ higher in the SBL corresponds to the modelled linear wind *v*-profile and a nearly height-independent *Ri* in that layer.

After 8 hours (Fig. 5.7) the turbulent stress $\overline{u'w'}$ is equal to the wave stress in the upper half of the SBL, and its magnitude is larger compared to the results with the B71 parameterization, but near the surface the wave stress dominates. The magnitude of the turbulent heat flux is slightly increased compared to the B71 parameterization, but both are about a factor 2 smaller than the LTGr formulation. Near the surface $\overline{u'w'}$ increases with height, caused by a reduced gradient of the near surface wind speed profile.
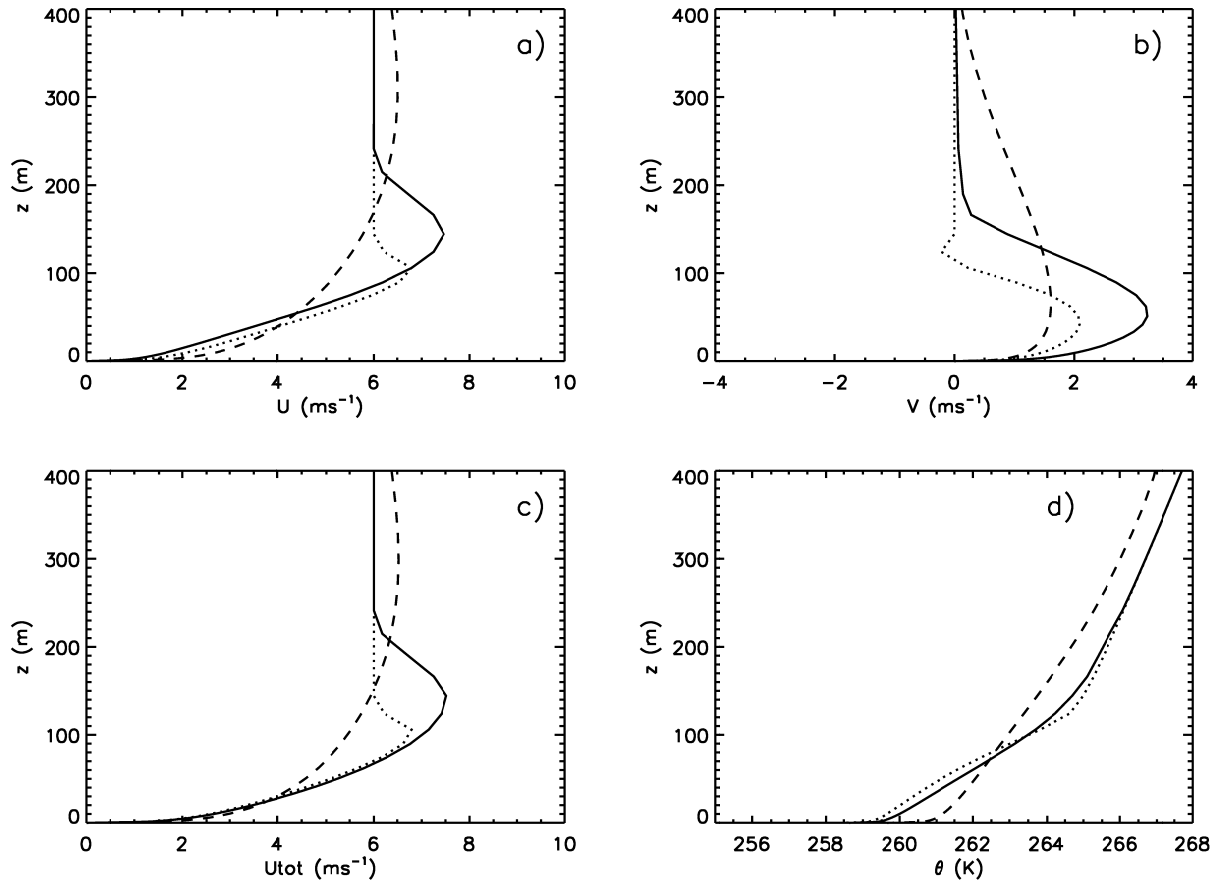
Figure 5.6: Modelled wind speed and potential temperature profiles after 8 hours simulation with the B71-formulation (dotted line), the LTGr formulation (dashed line) and the scheme with B71 + wave drag (full line).
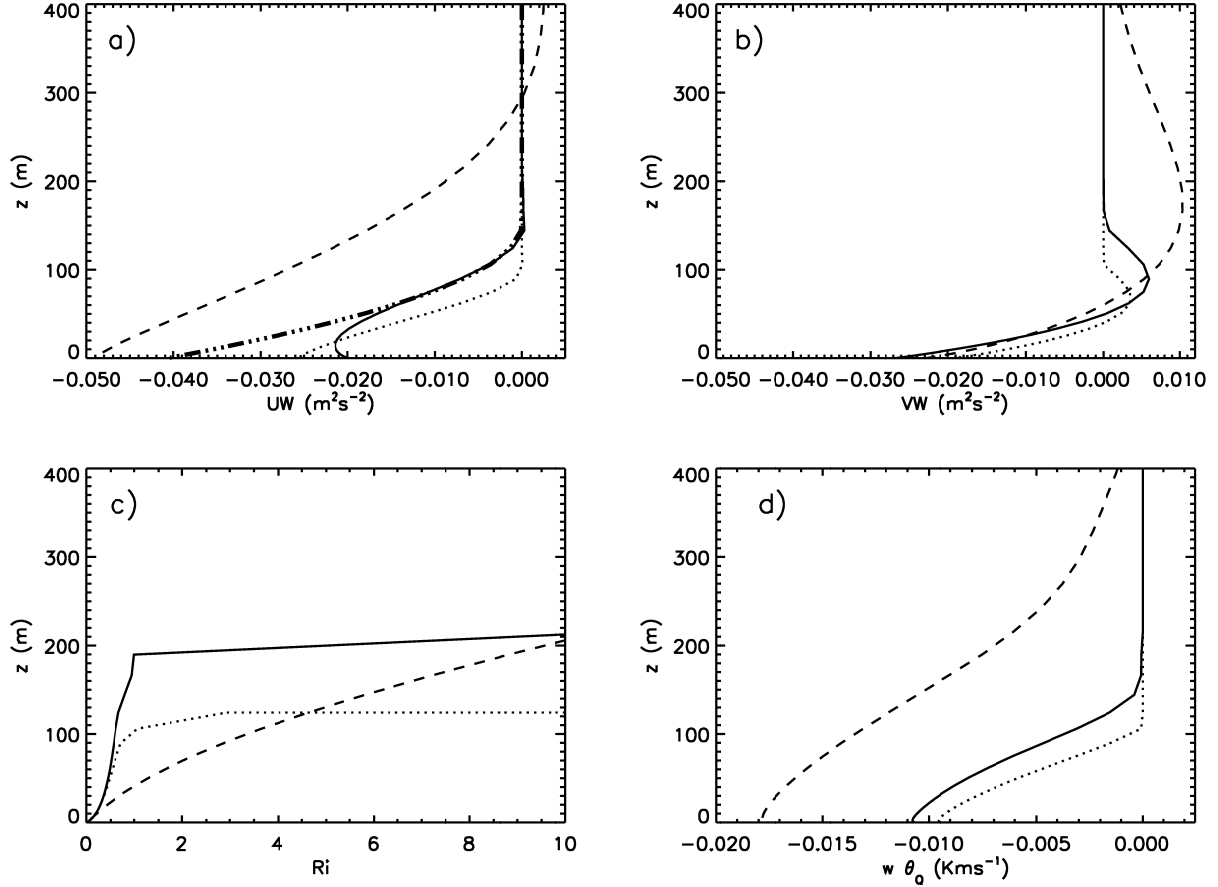
Figure 5.7: Modelled profiles of turbulent momentum fluxes ($\overline{uw}$ (a), $\overline{vw}$ (b)) gradient Richardson number (c), and turbulent sensible heat flux ($\overline{w\theta}$ (d) after 8 hours simulation for the Businger (1971) formulation (dotted line), the LTGr formulation (dashed line) and the new scheme with Businger (1971) + wavedrag (full line). In panel a) the thick dashed line is the forecasted wave stress profile.

c) Cyclone filling

As mentioned before, "long tails" (LTGr) play an obvious role to obtain sufficient cyclone filling. Fig. 5.8 shows cross isobaric mass flow (as a measure of cyclone filling), calculated as $f \int_{z=0}^{z=z_{TOP}} v(z)dz$ for a model integration of 68 hours, using the B71, LTGr and the presented alternative with terrain stress. There is a surprisingly good correspondence between cross-isobaric mass flow for the LTGr scheme and the current formulation that accounts for wave stress divergence. Hence the incorporation of the wave stress divergence gives similar cross-isobaric mass flow, and at the same time a smaller (more realistic) boundary-layer height, as well as a better representation of the LLJ.

Resolution dependence is an important issue for model parameterizations. We examined this sensitivity by re-running the case study for 30 and 25 layers instead of 40. At the same time we increase the height of the first model level. We found no major differences in the forecasted profiles, and in the cross-isobaric flow.
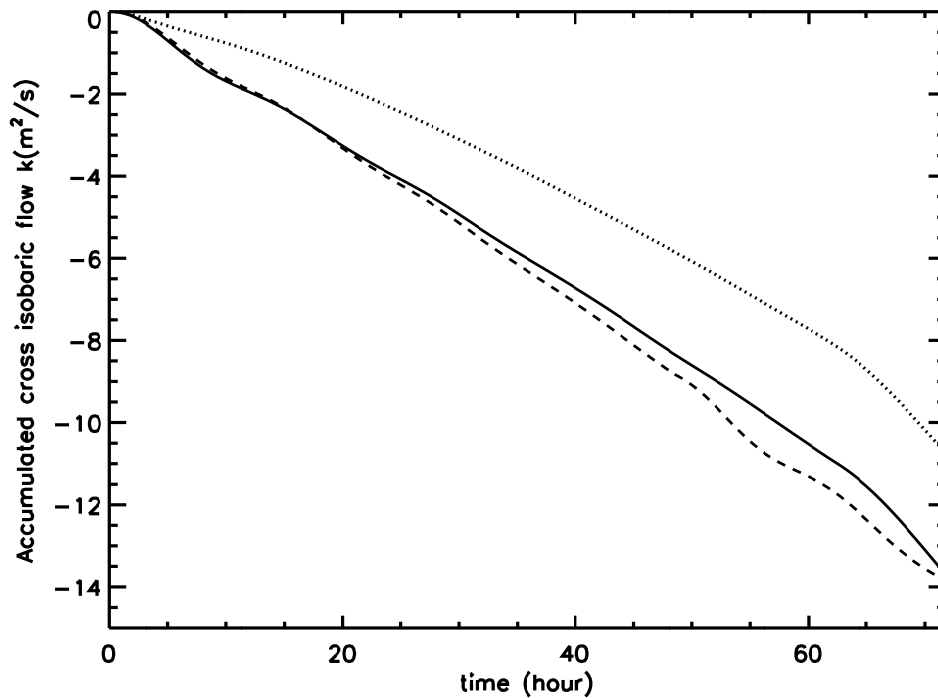
Figure 5.8: Modelled accumulated cross-isobaric mass flow for using "short tails" (i.e. Businger et al., 1971, **...**), Businger (1971) + wave stress according to Eq. (5.10) (full line), and the LTGr formulation (- - -).

An important advantage of the current proposal compared to the enhanced mixing approach, is first that wave stress is switched off in the case $N/U < k_s$, i.e. where gravity waves cannot propagate, instead of enhanced drag being active for all Ri. Thus it is more selective on physical grounds. Second, the scheme extracts mean momentum from the flow without making the boundary layer too deep, which will improve the forecast quality of minimum temperature, radiation fog and surface frost.

5.6 Discussion

The concept proposed in this paper is based on highly simplified physics of terrain stress in the SBL since we do not try to model the wave field itself, but only the net effect of gravity waves on the total drag on a large-scale. This is because the linear theory is based on a sufficiently slow variation of the wind speed and stratification with height (i.e. the WKB approximation). However, it is well known that the SBL is characterized by strong vertical gradients of wind speed and temperature (e.g. Balsey et al., 2003). Secondly, the majority of the theoretical work assumes a hyperbolic tangent wind speed profile in which a critical level is a priori present, although this is unrealistic for the major part of the SBL. Although these profiles can occur during very strong stratification (or above the LLJ), it is not the usually expected form. In addition, large-scale models lack the ability resolve this type of wind speed profiles (and critical levels as well). Therefore we have chosen to use this semi-empirical and practical approach.

We would like to remark that SBL terrain stress is just one process that might be responsible for the missing drag. An alternative mechanism that could add drag over a longer period of time could be due to non-local momentum mixing in the convective ABL (Frech and Mahrt, 1995; Brown and Grant, 1997; Beare, 2007), which is typically not accounted for in the current generation large-scale models. In the convective boundary layer, large eddies of the size of the whole ABL can transport momentum, scalars and heat through the whole ABL. Current operational models only account for non-local transport of heat at best (e.g. Holtslag and Boville, 1993).

Almost all previous studies of wave drag over orography used either monochromatic surface corrugation or idealized two- and three-dimensional obstacles. In these cases, the wave-stress calculations are essentially two-dimensional (see, for example, Kim and Mahrt, 1992; Nappo and Chimonas, 1992; Grisogono, 1995; Dörnbrack and Nappo, 1997; Nappo *et al*, 2004). Bretherton (1969), Hines (1988), and Shutts (1995) argued that the application of a two-dimensional wave-stress parameterization to realistic three-dimensional subgrid-scale terrain is an oversimplification of the problem. Thus, it is inaccurate to replace three-dimensional terrain with monochromatic surface corrugations. The results of such an approach is to overestimate the net wave stress. This is because a stably-stratified flow over real topography will have wind components passing over some obstacles. The magnitudes of these wind components are given by $u(\theta) = U \cos\theta$ where U is the surface wind speed and θ is the angle of the component. Because $u(\theta)$ decreases with increasing θ, the wave drag also decreases as $\theta \to \pi/2$. Accordingly, the average or net wave stress will be less than that estimated by assuming a uniform value of surface wind speed over all the terrain.

In the linear theory, each Fourier component of the surface terrain excites a wave response (Nappo, 2002). Thus, the spectrum of gravity waves is a linear function of the spectrum of the terrain disturbances. In the three-dimensional case, a two-dimensional Fourier transform of the surface topography is required. Bretherton (1969), Young and Pielke (1983), and Bannon and Yuhas (1990) used the meridional average of the Fourier transform of the zonal components of the real two-dimensional terrain. However, such a method implies an isotropy of the topography as does the use of an effective surface roughness parameter (see e.g. Masson, 1991; Georgelin et al., 1994; Taylor et al., 1998). Shutts (1995) recognized the directionality of the two-dimensional Fourier transform of terrain-height variance. Accordingly, Shutts (1995) converted the two-dimensional Fourier transform of the surface terrain into polar coordinates, and evaluated the wave stress in this coordinate system.

In consideration of these remarks, we see that the results presented in this paper represent an upper bound of the wave stress. However, considering the uncertainty of applying linear theory to real, non-linear flows, these estimates may not be unreasonably large. What is significant is the demonstration that the stress due to gravity waves in the stable PBL can be parameterized in a consistent and realistic way.

5.7 Conclusions

In this paper, we analyze the possible role of subgrid terrain stress in the momentum budget of the stable boundary layer, relative to the role of turbulent drag. This is done using the knowledge that Numerical Weather Prediction models need more drag ("long tails") to obtain good skill scores on the synoptic flow, than is justified with turbulence field observations. With adding a first order estimate of this terrain drag to the turbulent drag from CASES-99 field observations, we find good agreement between observed total drag and the "long tail" formulation. As such, the terrain stress may act as the bridge between "short tail" and "long tail" mixing functions.

In addition, we propose a practical and semi-empirical parameterization of the terrain stress divergence specifically in the stable boundary layer for use in large-scale models. Single-column model simulations revealed that the use of a "short tailed" parameterization for the turbulence (without mixing for $Ri > Ri_{crit}$), together with the new parameterization for terrain drag, gives cross-isobaric mass flow that corresponds with the mass flow with "long tailed" stability functions. With this new scheme, we obtain a much shallower (more realistic) boundary-layer with a sharper and stronger low-level jet compared with the "long tail" formulation. Finally, our results are in spite of the improved model performance, require additional validation against observations. We also recommend validation of the method in a full 3D forecast system.

Acknowledgements

Appendix 5A: Derivation of wave stress

Starting with the Taylor Goldstein Equation (see for derivation several standard books, e.g. Nappo 2002; Gossard and Hooke, 1974) that describes the behaviour of sine perturbations in the vertical direction ($\hat{w}$) as function of wind speed u_0 and stratification N:

$$\frac{\partial^2 \hat{w}}{\partial z^2} + \left[\frac{N^2}{(c-u_0)^2} + \frac{u_0^{''}}{c-u_0} - \frac{1}{H_s}\frac{u_0^{'}}{c-u_0} - \frac{1}{4H_s} - k^2 \right]\hat{w} = 0 \qquad (5A.1)$$

Here c is the phase speed (which is zero for standing waves). The first term within brackets is the buoyancy term, the second the curvature term, the third the shear term. H_s is the scale height of the atmosphere. The last term in brackets is the non-hydrostatic term. The plane wave solution of the Taylor Goldstein Equation (term within brackets is constant) reads for the vertical velocity perturbation, assuming no background wind:

$$w(x,z,t) = \tilde{w}e^{z/2H_s}e^{i(kx+mz-\omega t)} \tag{5A.2}$$

and equivalently for the horizontal direction

$$u(x,z,t) = \tilde{u}e^{z/2H_s}e^{i(kx+mz-\omega t)} \tag{5A.3}$$

Note that $\tilde{w} = \hat{w}e^{z/2H_s}$ and $\tilde{u} = \hat{u}e^{z/2H_s}$ are the scaled perturbations. Then it follows from the continuity equation:

$$\tilde{u} = \left(-\frac{m}{k} + \frac{i}{2kH_s}\right)\tilde{w} = 0 \tag{5A.4}$$

The wave stress averaged over one wavelength is:

$$\tau(z) = -\frac{1}{\lambda_x}\int_0^{\lambda_x}\rho_0\,\mathrm{Re}(u)\,\mathrm{Re}(w)dx = -0.5\,\mathrm{Re}(\rho_0 uw^*) \tag{5A.5}$$

Nappo (2002) shows that over a surface corrugation the perturbation velocity w_1,

$$w_1(x,z) = -iu_0 Hk_s e^{-i(kx+mz)} \tag{5A.6}$$

and

$$u_1(x,z) = -iu_0 Hm_s e^{-i(k_s x+m_s z)} \tag{5A.7}$$

and using $k = k_s$, and

$$m = \left(\frac{N^2}{u_0^2} - k_s^2\right)^{1/2} \tag{5A.8}$$

Using this in (5A.6) we obtain:

$$\tau = \begin{cases} 0.5\rho_0(u_0 H)^2 k_s\left[\dfrac{N^2}{u_0^2} - k_s^2\right]^{1/2} & \text{for } \dfrac{N}{u_0} > k_s \\[4mm] 0 & \text{for } \dfrac{N}{u_0} \le k_s \end{cases} \tag{5A.9}$$

Chapter 6

On land surface temperature trends in calm and windy nights

Abstract

Long-term surface observations over land have shown a temperature increase during the last century, especially during nighttime. Observations presented by Parker (2004) show similar trends for calm and windy conditions at night, and as such it was suggested that possible disturbances by urban heat effects are apparently small. On the other hand, a model study of Pielke and Matsui (2005) suggests that at night the temperature trends over land should be influenced by wind speed, even in undisturbed conditions. In this paper we return to this issue and we use a validated column model to explore the night time boundary layer over land. On basis of our study we find that the temperature increase is indeed constant for a rather broad range of geostrophic wind speeds. As such we confirm the results by Parker (2004). We also note that the model study by Pielke and Matsui overlooks important land-atmospheric feedbacks, which mostly explains their different findings.

6.1 Introduction

Long-term air temperature increase at screen height (normally 2 m) is dominantly observed at night over land (Folland and Karl, 2001). Parker (2004, 2006) examined whether the trend differs between windy and calm nights. Globally averaged screen level temperature increase over land appeared to be quantitatively the same for windy and calm nights (0.19 K/decade). Following this analysis, it was concluded that global temperature increase is not obscured by urban heat island effects because otherwise the temperature increase is expected to be smaller for stronger winds.

Pielke and Matsui (2005, from now on PM05) question the findings by Parker (2004). Based on a rather simple boundary-layer model, PM05 find that an increase in surface heat flux of 1 Wm^{-2} (from -50 Wm^{-2} to -49 Wm^{-2}) gives a screen level temperature increase of 0.29 K for 10 ms^{-1} and of 1.7 K at 1 ms^{-1} wind speed, respectively. Thus, PM05 state that temperature increase should depend on wind speed, and thus Parker's finding need further analysis before urban heat effects can be excluded definitely.

In this paper we return to the above issue. First we show that the combination of wind speed and surface cooling for which PM05 make their statement, is not supported by field observations. Secondly, we discuss the validity of the model used by PM05's. As an alternative, we use a high resolution, well validated, column model for the boundary layer to examine the vertical structure of the temperature increase by forcing the model with increased carbon dioxide and we assess whether this temperature increase differs for different geostrophic wind speeds (V_g). It turns out that our approach supports the conclusions of Parker's (2004) for at least his range of observed wind speeds.

6.2 Background

The atmospheric boundary layer (ABL) is the lowest part of the atmosphere over land where the influence of the diurnal cycle is felt. At clear nights, the temperature at the land surface falls rapidly and the air becomes cooler close to the ground than aloft, i.e. the ABL is stably stratified. Apart from the large-scale dynamics (i.e. pressure gradient and Coriolis force), the physics that govern the structure of wind speed and temperature profiles is complex and involves several processes with many feedbacks (both positive and negative). These physical processes are turbulent mixing, radiative heat transport and heat supply from the underlying soil towards the surface. In addition, small scale and less well understood processes as propagating gravity waves (e.g. Finnigan and Einaudi, 1981), drainage flows (Monti et al., 2002), low-level jets and intermittent turbulence (e.g. Van de Wiel et al., 2003, Holtslag, 2006) may be relevant.

Turbulent mixing by eddies of different scales in the SBL is produced by wind shear and dissipated by molecular viscosity and buoyancy destruction. The main result of turbulence is mixing (and thus smoothing) of atmospheric profiles and 'removal' of momentum. However, turbulent mixing in the SBL is a highly non-linear process. Concerning the turbulent sensible

heat flux (F_H (Wm^{-2})), we can at least distinguish two different regimes (e.g. Van de Wiel et al., 2002). In the first regime increased stratification results in an increased magnitude of F_H, since F_H is proportional to the stratification in this regime. This negative feedback dominates during windy nights. Contrary, in the second regime, increased stratification inhibits turbulent mixing so strongly that the magnitude F_H decreases with increased stratification, and in the extreme case turbulence vanishes. This regime is dominant during calm nights (e.g. Delage et al., 2002; Van de Wiel et al., 2003).

Radiative heat transport is a complex process of absorption and emission of thermal radiation (by absorbers) in the atmospheric layers to each other, and to and from the surface. The net effect close to the surface is a cooling of the atmosphere and a smoothing of the temperature profile, but the quantitative contribution depends on the time dependent (curvature of the) temperature and (slope of the) humidity profiles (Ha and Mahrt, 2003).

Finally, land surface cooling is the process that increases gradients of the atmospheric temperature profile. A strong and direct feedback between the surface vegetation and the underlying soil (Van de Wiel et al., 2003) is present. Increased long-wave cooling leads to a stronger compensating heat flux from the soil to the surface. In the case of inhibited F_H, the net radiation and the soil heat flux are the dominating contributors to the surface energy budget.

The sketch above clearly illustrates that the SBL cooling and resulting temperature profile at night is highly non-linear and a subtle balance of processes. Nevertheless, PM05 use a rather simple model to describe the temperature profile at night which was original proposed by Stull (1983, 2000). In the latter approach the potential temperature profile $\theta(z)$ is described as function of height z and a stable boundary-layer height scale H_e by using:

$$\theta(z) = \Delta\theta_s e^{-\frac{z}{H_e}} = \frac{\int F_H dt}{\rho C_p H_e} e^{-\frac{z}{H_e}}. \tag{6.1}$$

Here $\Delta\theta_s$ is the temperature difference between the surface and the residual layer, which can be expressed in terms of the sensible heat flux and the scale height as shown at the right hand side. Furthermore, the scale height is given by:

$$H_e = aV_{RL}^{\,3/4}\sqrt{t}, \tag{6.2}$$

where V_{RL} the residual layer wind speed, t the time since the day-night transition, and $a = 0.15$ m$^{1/4}$s$^{1/4}$ is a numerical constant (taken from Stull, 2000).

It is important to note that in the analysis by PM05, F_H is prescribed *independently* from the wind speed and the temperature profile. This is, however, very unrealistic, since in reality the sensible heat flux F_H depends interactively on both the wind speed and the stratification (Derbyshire, 1999). This point is further illustrated in Fig. 6.1, which shows the observed nighttime sensible heat flux versus the 10 m wind speed from the CASES-99 experimental campaign over a prairie grassland (Poulos et al., 2002; Hartogensis and De Bruin, 2005). It is immediately clear that nature only allows a certain sensible heat flux for a small range of

wind speeds (given clear sky conditions).

Additionally, two regimes are found, one where the magnitude of F_H increases with wind speed, and one where it decreases with wind speed (see also previous works by Holtslag and De Bruin, 1988; and Van de Wiel et al., 2002). Thus the case discussed by PM05 (their Table 6.1) with a prescribed sensible heat flux of -50 Wm^{-2} for wind speeds of 1 ms^{-1} and 10 ms^{-1} cannot be realized in nature. In addition, the above model lacks feedbacks with the land surface, and does not account for radiation divergence, although both were shown to be important for SBL modeling, especially for calm conditions, Steeneveld et al. (2006, henceforth S06) and references therein.
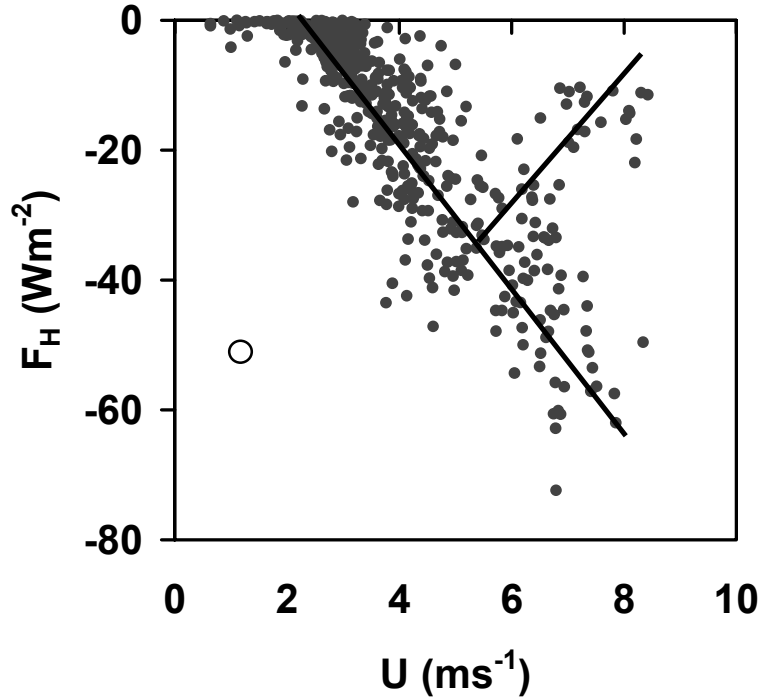
Figure 6.1: Observed sensible heat flux *H* as function of wind speed *U* (10 m) during the CASES-99 experiment. Observations have been selected for 22-7 local time and surface net radiation smaller than -50 Wm^{-2} (to exclude clouds). The open circle is the estimate by Eq. (6.1) and the bold lines indicate the different regimes.

6.3 Model and experimental set-up

To study the vertical structure of the temperature increase during clear nights, we use a high resolution atmospheric column model which accounts for turbulent mixing, long-wave flux divergence and a full coupling with the land surface and soil.

a)   Model description

To calculate the temperature increase for enhanced radiative forcing, we utilize the single column model by Duynkerke (1991). This model has been validated by S06 for a series of contrasting nights (both calm and windy) for the CASES-99 experiment. In this model the magnitude of the turbulent mixing is described by local gradients of wind speed and θ, which has been proven a suitable method in the SBL (Nieuwstadt, 1984, 2005). Heat transport by long-

wave radiation is calculated by a broadband grey body emissivity scheme that accounts for the absorbing properties of water vapour, liquid water and CO_2. In the soil (75 cm at high vertical resolution) the model solves the diffusion equation. Finally, the surface temperature is modeled by solving the surface energy budget interactively with the other model components. For more detailed description of the model, we refer to Duynkerke (1991) and S06. We utilize 100 logarithmically distributed model layers in a vertical domain of 10 km and a time step of 60 s.

b)   Experimental set-up

In our model study we use information of the clear night of 23-24 Oct. 1999 during the CASES-99 campaign. For this night we run the model and analyze the structure of the near surface temperature increase as function of the geostrophic wind V_g, The required thermal properties of the soil and the land surface were taken from observations (see S06). The initial profile was adopted from the radiosonde of 23 Oct 1900 UTC, with an approximately constant potential temperature (θ) profile of (284 K) from the surface to $z = 800$ m, and an inversion aloft. Specific humidity was taken constant (1.0 g kg^{-1}) in the whole model domain for the default experiment. The initial wind speed was constant with height and equal to the geostrophic wind speed, but matching a logarithmic profile close to the surface.

All model runs are first done for a uniform tropospheric CO_2 concentration of 330 ppm and then repeated for increased values for the tropospheric CO_2 concentration of 10, 20, 30 and 40% (note that a 40% increase was observed in the last century).

The land-surface coupling coefficient (Λ) that strongly determines the heat flux from the soil to the vegetation, was set to 5.0 $Wm^{-2}K^{-1}$ (as observed in Cabauw, The Netherlands, and which is consistent with CASES-99). We also examine the sensitivity of our results for the value of Λ, since it plays an important role in the coupled land surface-atmosphere system (S06).

6.4 Results and discussion

Fig. 6.2 shows the modeled potential temperature profile of θ at the end of the night for a geostrophic wind V_g of 2 and 9 ms^{-1}, and for various values of CO_2 concentrations. For the calm night, we note the typical strong negative curvature over the whole ABL depth consistent with Eq. (6.1), while for the windy night the profile is only negatively curved close to the surface and positively curved aloft (see also Estournel and Guedalia, 1985; Vogelezang and Holtslag, 1996; Edwards et al., 2006). The shape of the profile in each wind class is similar for all increased CO_2 concentrations. Furthermore, we see that the potential temperature increase for enhanced CO_2 concentrations decreases with height (particularly for low winds).

Fig. 6.3a shows the modeled θ increase due to a 40% CO_2 concentration increase, at the end of the night (6 LT, after 16 simulation hours) for all V_g and as function of height (until 300 m) and until 50 m in Fig. 6.3b. First, we observe that the additional heating is distributed

over a deeper layer for larger V_g. This is the effect of a deeper turbulent boundary layer in case of stronger wind speed. Especially for the larger V_g the near surface temperature increase is smaller than for low V_g. The near surface temperature increase is largest for $3 < V_g < 7$ ms^{-1}. In this regime the turbulent intensity is small, and additional heating cannot be efficiently transported upward, and thus the degree of atmosphere-land surface coupling and radiative transfer determine the heating rate. In addition, the near surface temperature increase is approximately constant in this V_g range, which corresponds to the findings in Parker (2004). Note that in our model calculations the difference in 2m temperature increase is only 0.1 K if we vary the geostrophic wind speed between 1 and 10 ms^{-1}. PM05 find 1.3 K difference with their approach, which is erroneous due to the lack of atmosphere-land feedback.
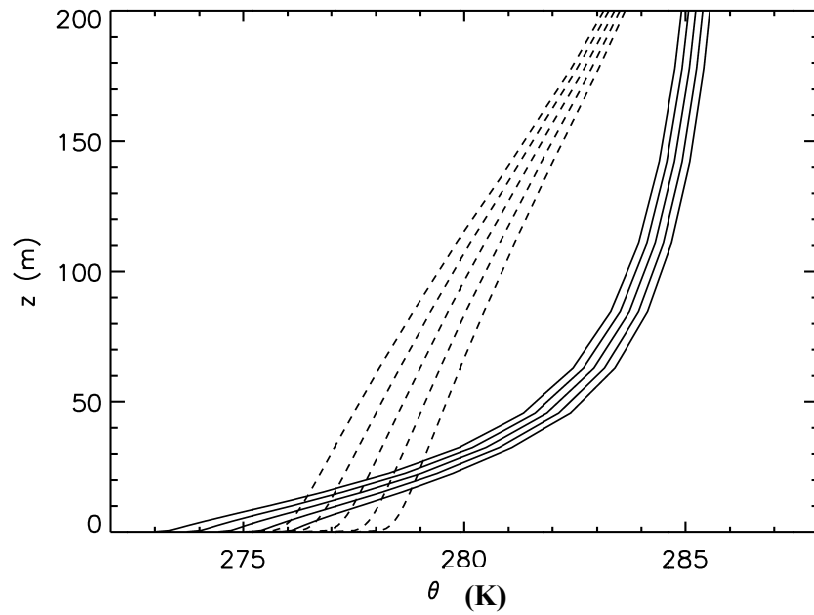
Figure 6.2: Potential temperature profiles after 18 simulation hours (8 LT) for $V_g = 2$ m s^{-1} (full lines) and $V_g = 9$ m s^{-1} (dashed lines) for reference runs and for increased long-wave forcing by 10, 20, 30 and 40 % CO_2 increase respectively (from left to right).
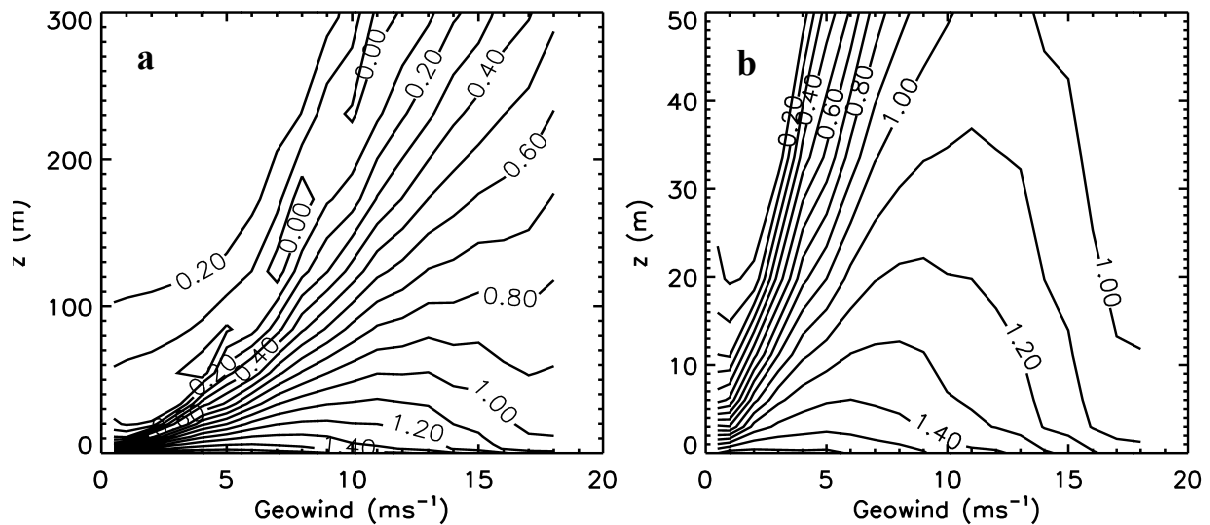
Figure 6.3: Modeled vertical distribution of potential temperature increase after 16 simulation hours (6 h local time) and land surface coupling coefficient 5.0 Wm^{-2}K^{-1}, for 0-300m (a) and 0-50 m (b).

Fig. 6.4 shows the sensitivity of the temperature increase to the land surface coupling. For all cases the temperature increase close to the surface does not depend on wind speed for $2 < V_g < 7$ ms^{-1}, and thus confirms the result for the reference case. However, for a smaller Λ the atmospheric heating near the surface increases. We would like to stress that the quantitative findings here are not representative for the global scale, because the temperature increase for the global scale is found by integrating the model on a global scale for a long time, for feedbacks with clouds, the land surface and vegetation. We also would like to remark that Parker (2004) based his classification on near surface wind speed. The near surface wind speed, in principle, depends on the SBL stability itself, and is calculated in the model. So it might be that if the SBL stability changes due to different long wave forcing, the wind speed is also altered. Increased forcing might result in reduced stability and increased near surface wind speed, so that some nights may jump from the calm night class to the windy night class. However, the model simulations above revealed a very small sensitivity change of the wind speed (<0.1 ms^{-1}, not shown) for increased CO_2, so Parkers classification appears to be useful.
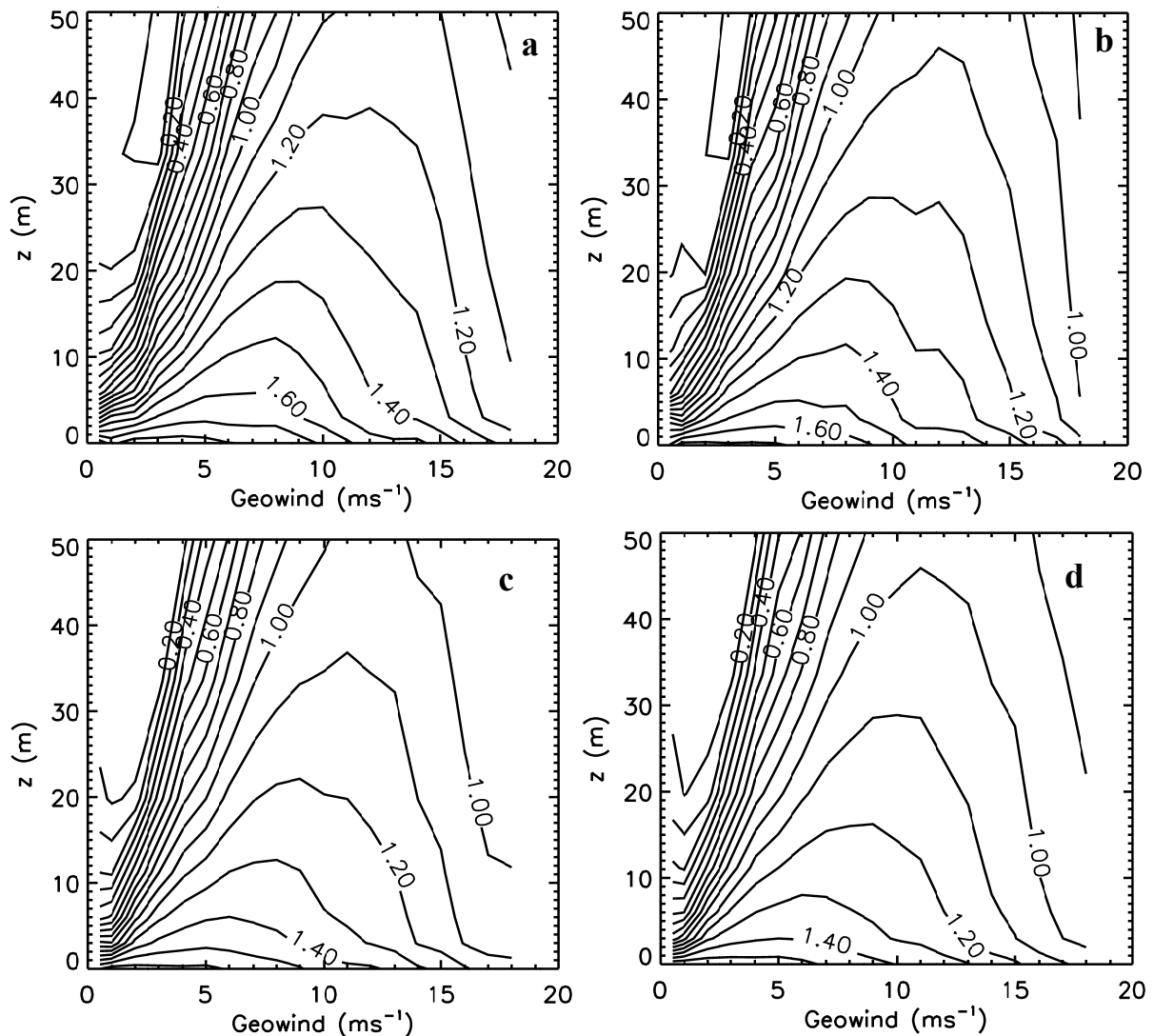
Figure 6.4: Sensitivity of vertical distribution of temperature increase for degree of land surface coupling a) $\Lambda = 3.0$, b) $\Lambda = 4.0$, c) $\Lambda = 5.0$ and d) $\Lambda = 6.0$ Wm^{-2}K^{-1}.

PM05 may have a good point when they raise the question whether screen level observations are a good measure for assessing long-term temperature increase. Perhaps an integral measure over the SBL (as in S06) might be more suitable. Note that radiosondes often lack the vertical resolution close to the surface to resolve the structure in the SBL as sketched above.

6.5 Conclusion

Pielke and Matsui (2005) recently argued that the nighttime 2m temperature increase due to long-wave forcing strongly depends on wind speed. Here we argue that their model is not sufficient for such an analysis because of the limitations in the descriptions of the dynamics. Instead, we use a well-validated high resolution column model that accounts for turbulent mixing, radiative heat transport and heat flux from the soil to assess the question whether the observed long term near surface temperature increase differs between calm and windy nights. We find that the temperature increase close to the surface is much less sensitive to wind speed than suggested by Pielke and Matsui (2005). This supports the earlier findings by Parker (2004) who found that the temperature increase from observations is independent from wind speed. In addition, the forecasted temperature increase does depend on the degree of atmosphere land coupling. This illustrates that climate models should properly account for this interaction to provide reliable results.

Chapter 7

Diagnostic equations for the stable boundary-layer height: evaluation and dimensional analysis

Abstract

The performance of diagnostic equations for the stable boundary-layer height (h) is evaluated with four observational datasets that represent a broad range of latitudes, land-use and surface roughness. In addition, Large-Eddy Simulation results are used. Special care is given to data quality selection. The diagnostic equations evaluated are so-called multi-limit equations as derived by Zilitinkevich and co-workers in a number of papers. It appears that these equations show a serious negative bias especially for $h < 100$ m and it was found that the parameters involved could not be determined uniquely with calibration. As an alternative, we use dimensional analysis to derive a formulation for h that is more robust. The formulation depends on the surface friction velocity (u_*), surface buoyancy flux (B_s), Coriolis parameter and the free flow stability (N). We also discuss the relevance of the Coriolis parameter for the boundary-layer height estimation in practice. If the Coriolis parameter is ignored, we find two major regimes, namely: $h \sim u_*/N$ for weakly stable conditions and $h \sim \sqrt{B_s/N^3}$ for moderate to very stable conditions.

7.1 Introduction

The stable boundary-layer (SBL) height (h) is an important quantity to describe the relevant processes that govern the SBL development and its vertical structure (Holtslag and Nieuwstadt, 1986). Clearly, the stable boundary-layer height has an impact on the mixing properties of the SBL. Also model formulations that use an explicit prescription of the vertical profile of an eddy diffusion coefficient K, require an explicit expression for the SBL height (e.g. Troen and Mahrt, 1986; Holtslag and Boville, 1993).

Furthermore, the dispersion of pollutants during stable stratification is strongly affected by h (e.g. Salmond and McKendry, 2005). Release of pollutants below h during periods of weak winds and consequently weak vertical mixing, may result in very high concentrations of primary and secondary pollutants, causing serious consequences for human health. Therefore, h is a critical quantity to estimate for meteorological preprocessors in air quality models (Venkatram, 1980; Gryning et al, 1987; Lena and Desiato, 1999; Seibert et al., 2000; Karppinen et al., 2001).

In contrast to the daytime convective boundary layer, where the height can be obtained relatively simply from profile observations (e.g. Vogelezang and Holtslag, 1996, henceforth VH96), observing the SBL height (h_{obs}) is less straightforward. This is because turbulence is gradually suppressed during stable conditions and it may also show intermittent behavior (e.g. Holtslag and Nieuwstadt, 1986). Vickers and Mahrt (2004, VM04 from now on) found a classical SBL with well-defined surface based turbulence for only 22% of the time for the CASES-99 field campaign. In addition to turbulence, other processes as radiation divergence (Anfossi et al., 1976; Garratt and Brost, 1981), gravity waves, wave breaking (Newsom and Banta, 2003) and baroclinicity (Zilitinkevich and Esau, 2003) influence the SBL structure for very stable conditions. In that case, problems occur in measuring h_{obs}, in absence of a universal relationship between the profiles of temperature, wind speed and turbulence variables. The interpretation of wind speed and temperature profiles is not straightforward in that case, and it is therefore not surprising that several definitions for h are in use nowadays (VM04, Beyrich, 1994).

Despite the uncertainties mentioned above, much work has been devoted to modeling (scaling) the SBL height (h_{mod}, see Section 7.2) from profile information or from turbulent variables at the surface. However, many of these models have been validated for a limited range of boundary-layer heights or for a single data set. Zilitinkevich and Mironov (1996, henceforth ZM96) presented a framework paper in which they summarize classical material on the subject. They derive two diagnostic multi-limit equations for the SBL equilibrium height by inverse interpolation of relevant SBL height scales. The first aim of the current paper is to evaluate the performance of these two multi-limit equations against four observational datasets at different latitudes and against Large-Eddy Simulation (LES) results. The second aim is to present an alternative, robust and practical formulation for h based on the same variables as the multi-limit equations, *but based on formal dimensional analysis instead*

of inverse interpolation. Finally, we discuss and assess the relevance of the Coriolis parameter in practical estimates for *h*.

In Section 7.2 we present background information on defining and modeling *h*. Section 7.3 describes the observational datasets and the LES data, then in Section 7.4 the two multi-limit equations are evaluated and re-calibrated. In section 7.5, we use dimensional analysis to obtain an alternative formulation and concluding remarks are made in Section 7.6.

7.2 Background

The subject of defining and modeling the stable boundary-layer height has a long history. Well-known definitions for *h* are (e.g. VM04):

a) a fraction of the layer through which turbulence exists (Lenschow et al., 1988),

b) the top of the downward turbulent sensible heat flux (Caughey et al., 1979),

c) the lowest maximum of the wind speed (often referred to as the Low-Level Jet, LLJ, Melgarejo and Deardorff, 1974), and

d) the top of the temperature inversion or the first discontinuity in the potential temperature profile (Yamada, 1979).

Some other definitions are given in Stull (1988). Seibert et al. (2000) state that no final answer is received to the question what is the most suitable height scale to characterize the vertical mixing in the SBL. The first two definitions focus on the turbulent structure of the SBL near the surface, while the latter two are based on profile information from radiosondes, tethered balloons or remote sensing methods.

It is obvious that different values are found by using different definitions. For example, the LLJ (definition c) is also influenced by other processes in the boundary layer than the actual turbulence intensity (e.g. inertial and baroclinicity effects, Stull, 1988). Therefore, the LLJ is perhaps a better measure for the history of the boundary layer than of the actual SBL structure (Mahrt et al., 1982). On the other hand, shear below and above the LLJ will generate turbulence, and thus affects the turbulence intensity over the whole boundary layer (Cuxart and Jiménez, 2007). In addition, definition c) is hard to apply when a LLJ is absent, which occurs in reality. For definition d) we should realize that besides the effect of turbulent fluxes, the temperature profile is also strongly influenced by radiative cooling (André and Mahrt, 1982) and by heat release of breaking waves at the SBL top. Surprisingly Kosovic and Curry (2000) indicate, based on their LES simulations that under ideal conditions definitions a), c) and also d) are equivalent. In this study we will mainly apply the last two definitions (Section 7.3), because turbulent flux profile data are often absent aloft, and radiosondes provide information concerning *h* aloft. In this manner, observations biased towards smaller values of *h* are circumvented.

In principle also subsidence and baroclinicity determine the value of *h* (Zilitinkevich and Baklanov, 2002; Zilitinkevich and Esau, 2003). However, routine observations of subsidence and baroclinicity are usually unavailable and are therefore not taken into account in this study.

Note that the technique of dimensional analysis we use in the second part of the paper is also applicable to other definitions of *h*.

Apart from defining *h*, Seibert et al. (2000) and Beyrich (1997) review methods to observe the SBL height. Traditional methods use sodar or other remote sensing methods (e.g. Van Pul et al., 1994), or employ parcel methods on atmospheric profiles (VH96). Beyrich (1997) states that automated detection of *h* works unsatisfactorily at this moment, and that visual inspection of vertical profiles by experts is still recommended. Therefore in this study an approach with visual inspection is followed. In any case, the uncertainty of h_{obs} is typically 30-40%.

From the modeling perspective, several parameterizations for h_{mod} have been proposed. These can in general be subdivided into prognostic equations (e.g. Nieuwstadt, 1980a; Nieuwstadt and Tennekes, 1981; Mahrt, 1981; Gassmann and Mazzeo, 2001) and diagnostic equations based on surface parameters (e.g. Zilitinkevich, 1972; Arya, 1981; Estournel and Guedalia, 1990). Nieuwstadt and Tennekes (1981) conclude that from a fundamental point of view prognostic equations should be preferred. However, their performance depends strongly on the initial conditions because the inter-nocturnal variation of *h* is larger than the intra-nocturnal variation (André, 1983). In contrast, Yu (1978) concludes that diagnostic models perform better than prognostic models.

ZM96 proposed a framework and identified rotation, surface buoyancy flux and free flow stability to be the key physical processes that govern *h*. A formula for the equilibrium value of *h* was derived by ZM96, considering the steady state turbulent kinetic energy equation and parameterizing the vertical mixing in the SBL due to these three processes. The formula uses the surface friction velocity (u_*), surface buoyancy flux ($B_s = (g/\theta)\overline{w\theta_s}$), Earth's rotation given by the Coriolis parameter (*f*) and free flow stability (represented by the Brunt-Väisälä frequency $N = \sqrt{(g/\theta)\nabla_z \theta}$) (*g* is the gravity acceleration, θ the potential temperature and *z* the height above ground level). The equilibrium height *h* is then given by:

$$\left(\frac{fh}{C_n u_*}\right)^2 + \frac{h}{C_s L^*} + \frac{Nh}{C_i u_*} = 1, \tag{7.1}$$

where L^* is the (modified) Obukhov length, given by $L^* = -u_*^3/B_s$ (as defined without the Von Kármán constant, following ZM96) and C_n, C_s and C_i are constants of proportionality. As such, this is effectively a diagnostic method. The three terms represents the impact of rotation, the surface buoyancy flux and free flow stability respectively. The main advantage of Eq. (7.1) is its multi-limit behavior, i.e. both for $f \to 0$, or $N \to 0$ or $L^* \to \infty$, the value of *h* by Eq. (7.1) remains defined. Note that many earlier proposals by e.g. Zilitinkevich (1972) and Nieuwstadt (1980b) are undefined for $f \to 0$.

Based on Zilitinkevich (1972) and Pollard et al. (1973), ZM96 add (using inverse interpolation, i.e. geometric averaging) two additional terms to Eq. (7.1) to "include the cross interac-

tions" between rotation, the buoyancy flux and free flow stability. This results finally in a multi-limit equation for h:

$$\left(\frac{fh}{C_n u_*}\right)^2 + \frac{h}{C_s L^*} + \frac{Nh}{C_i u_*} + \frac{\sqrt{|fB_s|}h}{C_{sr}u_*^2} + \frac{\sqrt{|fN|}h}{C_{ir}u_*} = 1, \qquad (7.2)$$

with $C_n = 0.5$, $C_s = 10$, $C_i = 20$, $C_{sr} = 1$, $C_{ir} = 1.7$. Recently, Joffre et al. (2001) re-evaluated these coefficients and found $C_n = 0.2$, $C_s = 2.5$, $C_i = 10$, $C_{sr} = 0.4$, $C_{ir} = 1.2$ from Sodankylä tower observations, while VM04 propose $C_n = 0.04$, $C_s = 6$, $C_i = 15$, $C_{sr} = 0.7$, $C_{ir} = 0.8$ based on observations from CASES-99, CBLAST and FLOSS experiments.

The difference between these three sets of coefficients for Eq. (7.2) is relatively large, which indicates that these (many) coefficients are hard to obtain with a sufficient degree of confidence. For example, C_n ranges from 0.045 to 0.6 in the literature (Benkley and Schulman, 1979; Mason and Thomson, 1987; Beyrich and Kotroni, 1993; Kosovic and Lundquist, 2004) and C_s ranges from 1.2-100 (ZM96). This subject will be addressed in more detail in Section 7.4. Furthermore, VM04 found a stability dependence of C_s and C_{sr}, which questions the uniqueness of the constants. We have seen that several of these coefficients have a large range in literature.

Finally, Kosovic and Curry (2000) remark that Eq. (7.2) uses five dimensionless groups, while only three can be justified according to Buckingham Π theory. Based on the five relevant quantities and only two basic dimensions (namely meters and seconds), three dimensionless groups should be sufficient to describe the datasets. As such, Eq. (7.2) has redundancy. Inspired by this comment and by the fact that the coefficients do not seem to be robust, we decided to start with formal application of the Π-theorem without prescribing some particular shape (such as with inverse interpolation). In this way we will also show that bias for small values of h disappear so that the result is applicable to high stability cases. Note that the Π-theorem is semi-empirical and only applicable in the range of available observations (see Section 7.5).

7.3 Observations

Many model formulations for the SBL height have been proposed based on a single dataset or on datasets biased towards shallow boundary layers (VM04), and thus universality is not a priori guaranteed for these models. Contrary, the analysis in this paper is based on four observational data sets over different terrain types according to their surface roughness and land use. We also use LES results of the GEWEX Atmospheric Boundary Layer Study (GABLS) (Beare et al., 2006) for model verification. The latter reflects a moderately stable case. We do not use LES for more stratified cases because of the many uncertainties which still exist in LES for stratified conditions.

Below we describe the observational sites, the data processing and the method we used to obtain *h* from profile observations. Table 7.1 provides the number of data points per dataset and the observed range of the relevant quantities.

a) CASES-99

This measurement campaign was held October 1-31, 1999 near Leon, east of Wichita, Kansas, U.S.A. (37.6486º N, -96.7351º E, 430 m a.s.l). The objective was to study the relevant processes in the SBL (Poulos et al., 2002). The area is relatively flat prairie grassland, free of obstacles, with an estimated roughness length $z_0 = 0.03$ m (Van de Wiel et al., 2003). During CASES-99 126 radiosondes were launched from the central site at night (defined here as the period 0100-1300 UTC). Soundings were launched every six hours and hourly during Intensive Observation Periods (IOP) (see Poulos et al., 2002 for an overview of the IOPs). The quality of the validation and calibration of SBL height models strongly depends on the data quality, data range (Table 7.1) and careful data selection and processing. Because many variables are used and we want to have reliable estimates for all of them, we have to reduce the data strictly. Similar to Van de Wiel et al. (2003), nights that are subject to rapidly changing synoptic conditions are disregarded (those were classified as "Non" in that paper). Consequently, we determined the SBL height for the remaining 101 profiles using the method in Joffre et al. (2001). They identified the SBL height subjectively by inspecting simultaneously the wind speed, potential temperature and Richardson number profiles for clear changes below the inversion height that would indicate a change in the structure of the lower atmosphere. This is illustrated in Fig. 7.1 for 0700 UTC 23 Oct 1999. The SBL height was based on (1) the LLJ height and (h_{LLJ}) and (2) the height of the first discontinuity in the potential temperature profile (h_θ), from curved to linear in Fig. 7.1a. Fig. 7.1b illustrates the first peak in the gradient Richardson number at that level. If h_{LLJ} and h_θ differ more than 60 m, the data points were rejected, which left 58 data points. In addition, we selected data for $N > 0.015$ s^{-1}, since weaker *N* could not be determined accurately, and 48 data points remained. The reliability of eddy covariance measurements (10 min. averages) for weak turbulence is questionable, and therefore we disregarded data with friction velocity $u_* < 0.04$ m s^{-1} and sensible heat flux $H > -2$ Wm^{-2}. Because all nights in CASES-99 are well described in the literature, we checked the literature to see whether the remaining data were probably subject to "events" (e.g. the density current of 18 Oct.). During such events the boundary layer will not behave like a classical boundary layer, and therefore these data should be disregarded. After this selection only 32 data points remained.

Table 7.1: Overview of observations (per station) during stable stratification, before and after data reduction.

	Sodankylä	**CASES-99**	**Cabauw**	**SHEBA**
#data points be- fore reduction	34	126	189	338
#data points after reduction	30	32	149	20
Range h (m)	100-490	75-325	60-540	103-146
Range H (W m^{-2})	-53.0 to -6.6	-58.9 to -7.6	-96.2 to -6.4	-18.0 to -6.7
Range u_* (m s^{-1})	0.149-0.879	0.06-0.49	0.06-0.77	0.10-0.22
Range N (s^{-1})	0.015-0.035	0.016-0.060	0.016-0.037	0.016-0.046
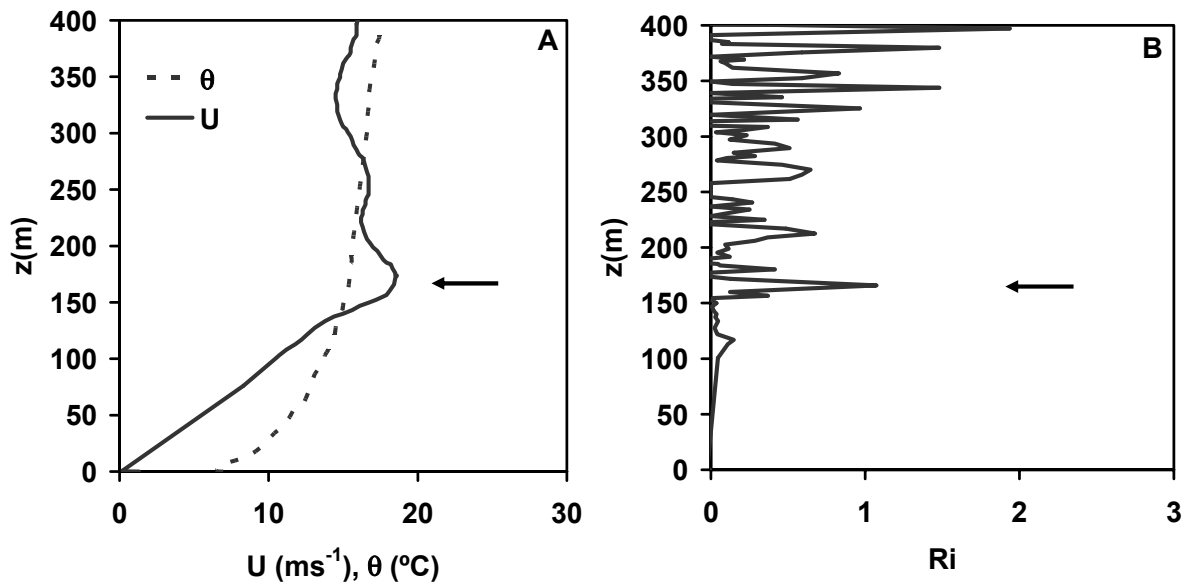
Figure 7.1: Profiles of potential temperature, wind speed (a) and gradient Richardson number (b) for 23 October 0700 UTC during CASES-99. The arrow indicates the stable boundary-layer height.

b) Sodankylä

The dataset (34 data points during stable stratification) is based on an intensive campaign of radiosondes performed during the international NOPEX/WINTEX program at the observatory of Sodankylä, Finland (67.4° N, 26.7° E, 180 m a.s.l.) between 10-21 March 1997 (Halldin, 1999). The terrain topography around the site is mostly flat, characterized by isolated gently rolling hills (altitude differences 50-150 m). This area of Lapland is covered by sparse forest (mean tree height of ~8 m around the site). The immediate vicinity of the mast was character-ized by semi-open pine forest with a mean height $H_r \approx 8$ m for the trees around the mast. By assuming a displacement height of $d \approx 0.66 H_r = 5.3$ m, neutral profiles yielded $z_0 \approx 1.4$ m (Joffre and Kangas, 2002). The data were already carefully selected by Joffre et al. (2001). After applying selection criteria on u_* H and N similarly as for CASES-99, 30 data points remained.

c) Cabauw

The current dataset (189 data points) has been obtained in the period 1977-1979 at Cabauw, The Netherlands (51.971 ºN, 4.927 ºE; -0.7 m a.s.l.), by Nieuwstadt (1980b). For boundary-layer heights, VH96 made an extensive study with these data and later on the data were also used by Zilitinkevich and Baklanov (2002). The data were carefully selected (e.g. filtered for gravity waves) before in VH96. The additional restriction we made $u_* < 0.04$ m s^{-1}, sensible heat flux $H > -2$ Wm^{-2} and $N > 0.015$ s^{-1} and the rejection of Type I boundary layers (dominantly driven by radiation divergence and low winds, as defined in VH96).

The Cabauw area is flat and covered with grass with an overall roughness length of 0.20 m (mesoscale effects are included, De Rooy and Holtslag, 1999). A more extensive description of this site can be found in Van Ulden and Wieringa (1996). The SBL height was observed with a sodar with an uncertainty of about 40% (VH96). This method differs from the one used at the two previously mentioned. However, Arya (1981) states that h_{LLJ} is probably a suitable alternative to represent the observed boundary-layer height with a sodar. In addition, Hicks et al. (1977) found no systematic differences between sodar observations and the nocturnal surface inversion, based on temperature profile information. We therefore assume the two methods (h_{LLJ} and sodar) to be "equivalent", although it is not necessarily true (See Section 7.4).

The free flow stability was obtained from the 160 m and 200 m levels of the tower for cases that h was less than 200 m. When h was larger than 200 m, we estimated N above the SBL by a statistical relationship obtained from the CASES-99 (section *a*) observations: $N = 0.015 + 0.51 N_{BL}$, in which N_{BL} is N from measurements made between the surface and the 200 m level. This method certainly introduces an additional uncertainty for N, but meanwhile offers a possibility to increase the number of available data points in this dataset.

d) SHEBA

The SHEBA (Surface Heat Budget of the Arctic) dataset (338 data points with stable stratification) was obtained over the Arctic ice pack north of Alaska between October 1997 and October 1998. During this period, Ice Station SHEBA drifted from approximately 75°N, 144°W to 80°N, 166°W. Visual inspection of the profiles left 47 data points, the other data were rejected because of insufficient wind speed observations in the lowest part of the sounding or because of fog conditions (particularly in wintertime). Especially the latter caused large reduction of useful data. For this site, h_{LLJ} was taken as the SBL height as observed from radiosondes (as discussed for the CASES-99 dataset), taking into account that this height should also be supported by a 'discontinuity' in the θ profile. 41 data points were not saturated near the surface. After applying the same criteria for surface fluxes and free flow stability as for CASES-99, 20 data points remained.

e)   GABLS LES

Next to datasets from measurement campaigns we also used ensemble mean LES results from the GABLS intercomparison study (Beare et al., 2006) to verify our model. The LES case-study was based on simulation of an Arctic SBL over an ice surface during nine hours, with 0.25 K h^{-1} of prescribed surface cooling, and for a geostrophic wind speed of 8 m s^{-1}. After nine hours a moderate SBL of about 180 m height developed. The advantage of LES is that the free flow stability is prescribed (N = 0.019 s^{-1}) without any uncertainty, while in the observations N is relatively uncertain. The most relevant disadvantage is that the current LES data set consists of only one "surface stability point".

f)   Data considerations

We would like to stress that although these datasets cover a broad range of stabilities, surface roughnesses and latitudes, they differ in averaging time of the surface fluxes. Different averaging times can affect the surface fluxes, and consequently h_{mod}. Furthermore, we should be aware that the friction velocity at a local scale used in this study is not a priori the amount of friction that is felt by the whole boundary layer on a larger horizontal scale (Beyrich and Kotroni, 1993). Mesoscale circulations are often reported in SBL studies (e.g. Mahrt and Vickers, 2002) and these circulations can contribute considerably to the surface fluxes (VM04). Garratt (1982) found that in studies that compare modeled and observed SBL heights, the largest uncertainty is associated with the uncertainty of surface fluxes, which act as input variables for the model calculations.

7.4 Evaluation and parameter estimation

a) Evaluation

Next we evaluate the performance of Eqs. (7.1) and (7.2) with the coefficients given in ZM96 and Zilitinkevich and Baklanov (2002) (Section 7.2). Furthermore, we also evaluate the simple estimate by Koracin and Berckowicz (1988), written as $h = 700 u_*$. Note that a timescale is implicitly included in the numerical constant.

Table 7.2 summarizes model performance given by several statistical quantities: the mean absolute error (mae), the root-mean-square error (rmse), subdivided in a systematic (rmse-s) and an unsystematic (rmse-u) part, the median of the absolute errors (meae), the fractional bias (FB) and the Index of Agreement (IoA, Willmott, 1982). Note that the correlation coefficient r is not a reliable parameter for model quality (in the case of strong bias, see below) and is omitted here. Good model performance will result in IoA = 1, a small mae, meae and in the ideal case the rmse-s is close to zero and rmse-u is equal to the total rmse. To avoid that too much weight is given to the larger datasets, we present the statistics per dataset separately. Apart from these statistical measures, scientific evaluation can be enhanced by examination of graphical data display (Willmott, 1982).

The performance of the three-term multi-limit formula, Eq. (7.1) is shown in Fig. 7.2. For the Sodankylä data, h is estimated reasonably well for thick SBLs, although the number of data points is limited in that range. In contrast, for shallow SBL heights, we find a clear off-set: h_{mod} is only several meters where h_{obs} = 50-80 m. Similar results were found for Cabauw. For SHEBA, h_{obs} is relatively shallow and underestimated by Eq. (7.1) despite the high correlation between h_{mod} and h_{obs}. The IoA ranges from 0.62 to 0.82 for this Equation (Table 7.2). For CASES-99, h_{mod} is nearly always smaller than h_{obs}, even for thick SBLs (FB = -0.91). This agrees with the results of VM04, who found a bias of -68% with Eq. (7.1) for CASES-99. They conclude that the introduction of the free flow stability does not improve model performance (in contrast to our results in Section 7.4), even in the case of marine boundary layers (CBLAST campaign) with a relatively strong free flow stability aloft. For the LES model results, Eq. (7.1) gives h_{mod} = 218 m, while h_{LES} = 180 m. Based on the rmse, Eq. (7.1) with coefficients from Joffre et al. (2001) results in similar performance as with the ZM96 coefficients. With the coefficients in VM04 also a clear negative bias is found. This difference is perhaps also due to the different definitions used here and in VM04. Note that in the current analysis, the impact of subsidence was not taken into account.

Fig. 7.3 depicts the modeled and observed h for the five-term multi-limit model, Eq. (7.2). For Sodankylä, h_{mod} is systematically smaller than h_{obs} for both deep and shallow boundary layers. Table 7.2 demonstrates that a large part of the rmse is of systematic nature in this case, and the FB < -0.48. For the LES case h_{mod} = 90 m while h_{LES} = 180 m. Except for Sodankylä the IoA is smaller for Eq. (7.2) than for Eq. (7.1). The off-set for shallow SBLs as with Eq. (7.1) persists in Eq. (7.2). In general, Eq. (7.2) underestimates h_{obs} by a factor 2, in agreement with VM04 who found a bias of and -78% with Eq. (7.2). This was also found for other observational sites and for the LES data. In fact, the addition of the two terms that should account for the interaction between f, N and L, deteriorates the model performance! It seems that too much weight is given to the added (shortest) length scales with the inverse interpolation method. Especially for Eq. (7.2) the use of parameters with values given in Joffre et al. (2001) gave poor results. For example, the mean meae increased from 94.6 m with the coefficients in ZM96 to 137.3 m with the use of coefficients of Joffre et al. (2001).

Our conclusion is that the current parameter set in Eqs. (7.1) and (7.2) cannot properly predict the observed boundary layer heights. Consequently, we will undertake a re-calibration of the coefficients in Eq. (7.1). Note that we also found a negative bias for shallow SBLs and no unique parameter set could be obtained for Eq. (10) in Zilitinkevich and Esau (2003, not shown), which is an improved version of (7.1) and (7.2).

Before we proceed we note that the simple empirical estimate of $h = 700u_*$ performs well overall.
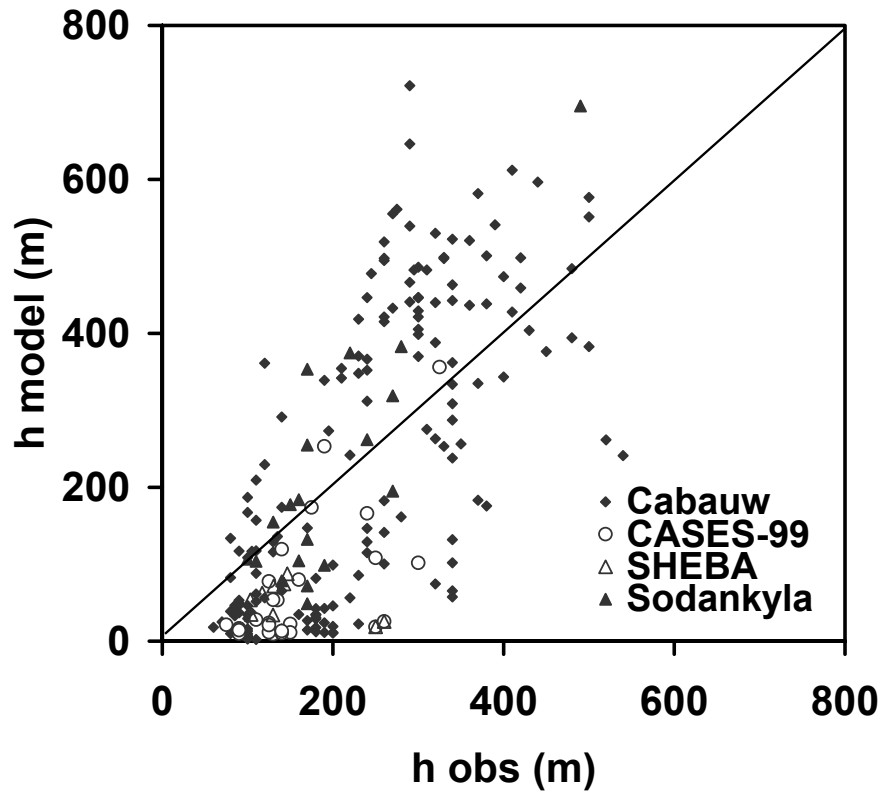
Figure 7.2: Observed and estimated stable boundary-layer height using Eq. (7.1) for Sodankylä, Cabauw, CASES-99 and SHEBA.
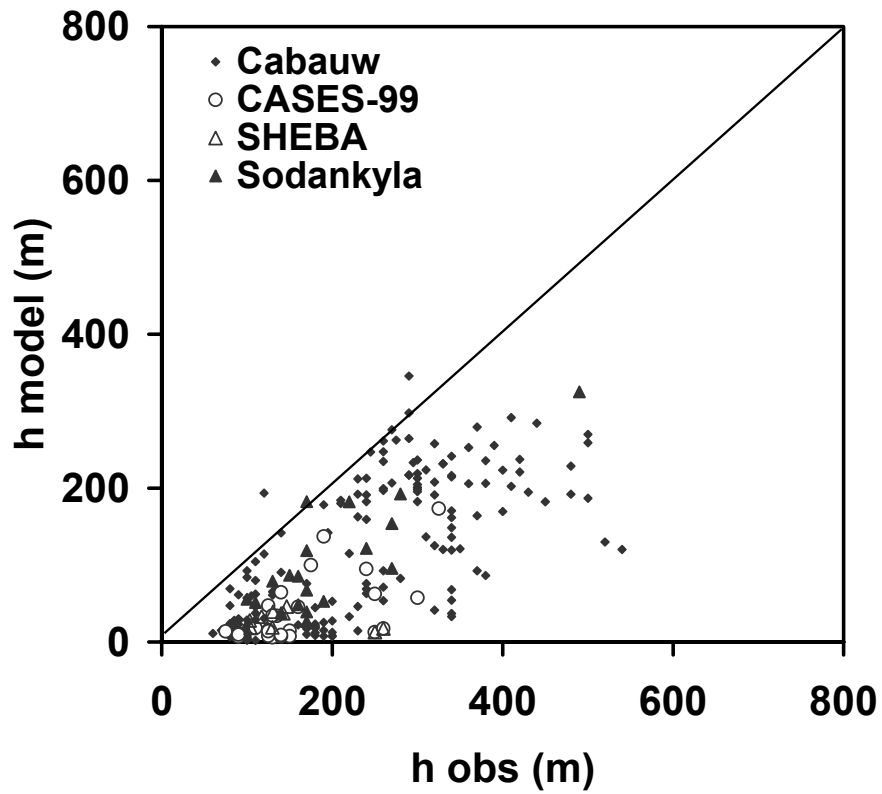
Figure 7.3: Observed and estimated stable boundary-layer height using Eq. (7.2) for Sodankylä, Cabauw, CASES-99 and SHEBA.

b) Calibration

With the available dataset at hand it is tempting to recalibrate the coefficients in Eqs. (7.1) and (7.2). Note that Zilitinkevich and Baklanov (2002) determined the numerical values of the coefficients among others on the same Cabauw dataset as in the current study. However, they limited themselves to $h < 200$ m, and therefore the obtained coefficients can only be representative for a small subset of the total dataset. Especially for $h < 200$ m this Cabauw dataset contains a relatively large scatter compared to the scatter for $h > 200$ m. The use of this data subsection may hamper robust parameter estimation.

The calibration of coefficient C_n, which represents the constant of proportionality for a truly neutral boundary layer ($B_s = 0$ and $N = 0$), from atmospheric observations is difficult since due to radiation divergence, subsidence etc, truly neutral boundary layers are generally absent in the atmosphere. Therefore, we prefer to determine C_n from LES studies performed earlier by e.g. Mason and Thomson (1987). The same strategy was followed by ZM96. They find $C_n = 0.6$ and we will use this value from now on. Note that the precise value of C_n does not seem to be very important in the atmosphere where truly neutral boundary layers hardly exist. From a scale analysis of the different terms of Eq. (7.1), using typical values for $f = 1.10^{-4}$ s^{-1}, $\overline{w\theta}_s = -0.024$ K m s^{-1}, $u_* = 0.3$ m s^{-1} and $N = 0.03$ s^{-1}, we find that the three terms from left to right contribute for 3%, 25% and 72% of the sum of the three terms, respectively.

The remaining coefficients in Eq. (7.1) (C_s and C_i) are calibrated with the Sodankylä dataset with a Monte Carlo approach (e.g. Franks et al., 1997). Several statistical quantities can be used as a measure for model quality. Due to the relatively large uncertainty in the observations, we prefer the median of the absolute error (meae) to prevent outliers to dominate the statistical quality parameter too much. Fig. 7.4 shows a surface plot of the meae for parameters ranges $C_i \in [5,20]$ and $C_s \in [0,100]$. The meae has a minimum for $C_i = 11$. These results are supported by calibration on the whole dataset. Our findings agree with the results of Van Pul et al. (1994), and Kitaigorodskii and Joffre (1988), VH96 (who found $C_i = 7$-13), and Joffre et al. (2001) who found $C_i = 10$. VM04 proposed $C_i = 15$. Note that the variability in C_i may strongly depend on the wind shear across the SBL, as discussed in VH96.

However, no clear minimum is found in the contour plot along the C_s axis. That means that the model performance is insensitive for C_s for $C_s > 40$. This also explains the large range of proposed values for C_s. Similar results were found using other statistical quality measures. Note that also no unique parameter combination for C_i and C_s was found with $0.1 < C_n < 0.7$ (not shown).

To summarize, the multi-limit equations show a clear bias against observations and their parameters cannot be determined uniquely. We will derive an alternative formulation using formal dimensional analysis instead of using inverse interpolation.
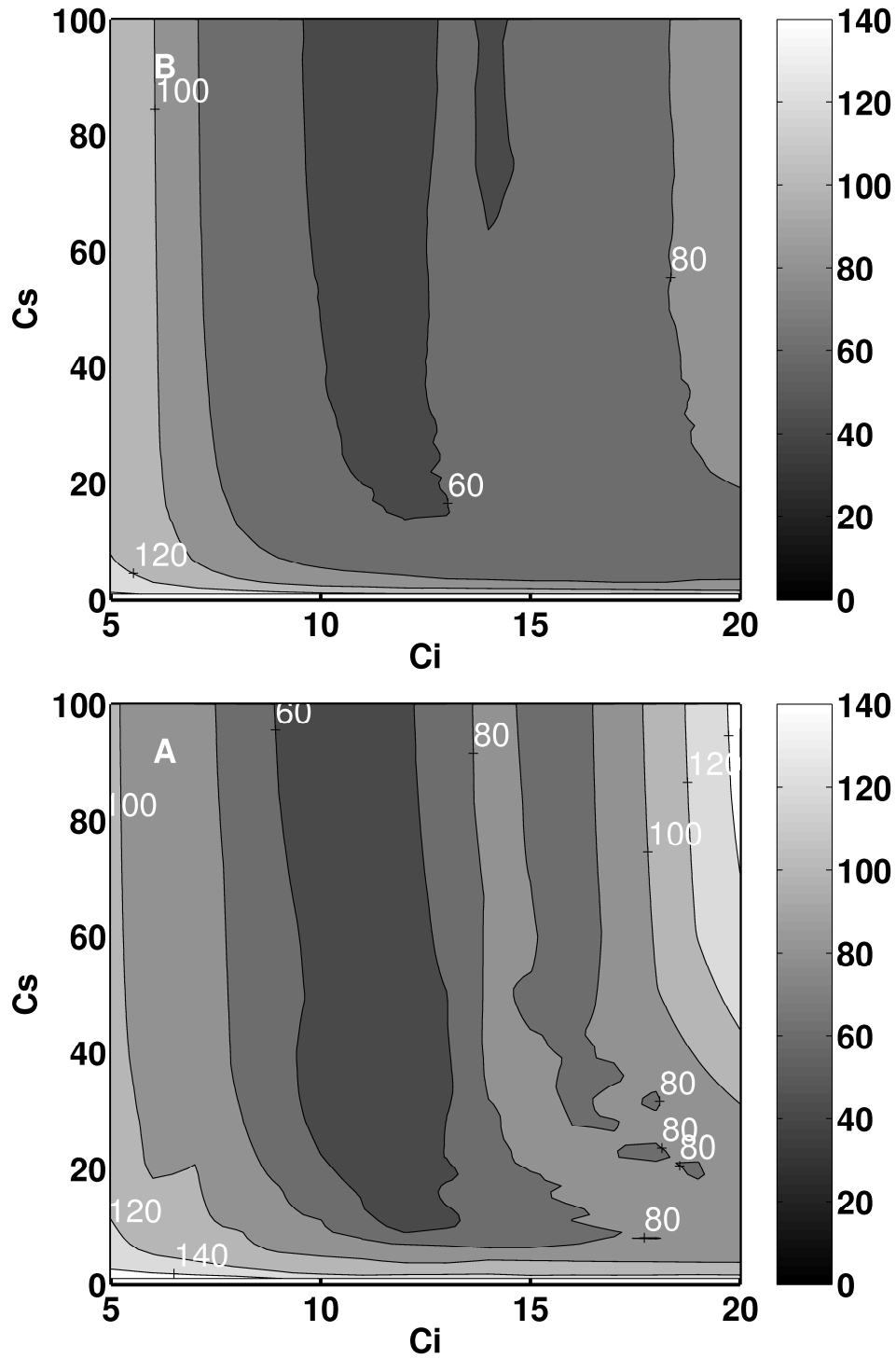
Figure 7.4: Contour plot of the median of absolute error (MEAE in m) for a range of C_i and C_s for Sodankylä (a) and the total dataset (b). For both figures we used $C_n = 0.6$.

7.5 Alternative formulation using dimensional analysis

a) Three dimensionless groups

On the basis of the earlier works, we identify that the relevant quantities to describe h are u_*, f, B_s and N. Using the Buckingham Π theory (e.g. Langhaar, 1951) we find three dimensionless groups:

$$\Pi_1 = \frac{|B_s|}{hfu_*N}, \quad \Pi_2 = \frac{kh|B_s|}{u_*^3} = \frac{h}{L}, \text{ and } \quad \Pi_3 = \frac{N}{f}.$$

Consequently we may determine the functional form of the surface that describes the relationship between Π_1, Π_2 and Π_3 from observations. This should be a universal relationship if all relevant quantities are included.

Fig. 7.5a shows Π_1 versus Π_2 on a linear scale for different classes of Π_3 using Sodankylä observations. Despite the small number of data per class, Π_2 clearly increases with Π_1, but levels off at different values for different classes of *N/f*. This relevance of *N/f* was already mentioned by Kitaigorodskii and Joffre (1988). Note that no data are available for *N/f* < 50 and *N/f* > 300. Furthermore we remark that the plotted dimensionless groups in Fig. 7.5 have common terms, and the risk of spurious correlation exists (e.g. Baas et al., 2006). However, it turns out that by randomizing the current datasets the scatter increases. Moreover, below we also use dimensional plots to confirm the performance.

On a log-log scale (Fig. 7.5b), we can determine the different slopes for different classes of *N/f*. We propose to fit the data according to $\Pi_1 = \alpha\Pi_2^{\beta_1-\beta_2\Pi_3}$. Applying this result and after some re-arrangement we find for h:

$$h = L\left(\frac{\left|\frac{g}{\theta}\overline{w\theta_s}\right|}{\alpha u_* fNL}\right)^{\lambda} \tag{7.3}$$

with $\alpha = 3$, $\lambda = \left(C_1 - 0.001 N/f\right)^{-1}$, and $C_1 = 1.8$. The calibration for α and C_1 is discussed in detail below, L is the classical Obukhov length (thus including the Von Kármán constant). Note that the innovative aspect of this equation is that the exponent is not constant, but it depends on one of the dimensionless groups. The numerical value 0.001 in λ was found by plotting the slopes in Fig. 7.5b for different classes of *N/f* (not shown). In addition, the obtained coefficients (based on Sodankylä observations) were confirmed by using each half of every dataset for calibration and the other halves for validation.

Considering the applicability range of Eq. (7.3), we have to realize that the denominator in the exponent should be positive, hence *N/f* < 1800. With the maximum free flow stability in the dataset (N=0.076 s^{-1}), this corresponds to a latitude $|\phi| > 16°$. In addition, both N and L need to be larger than zero.
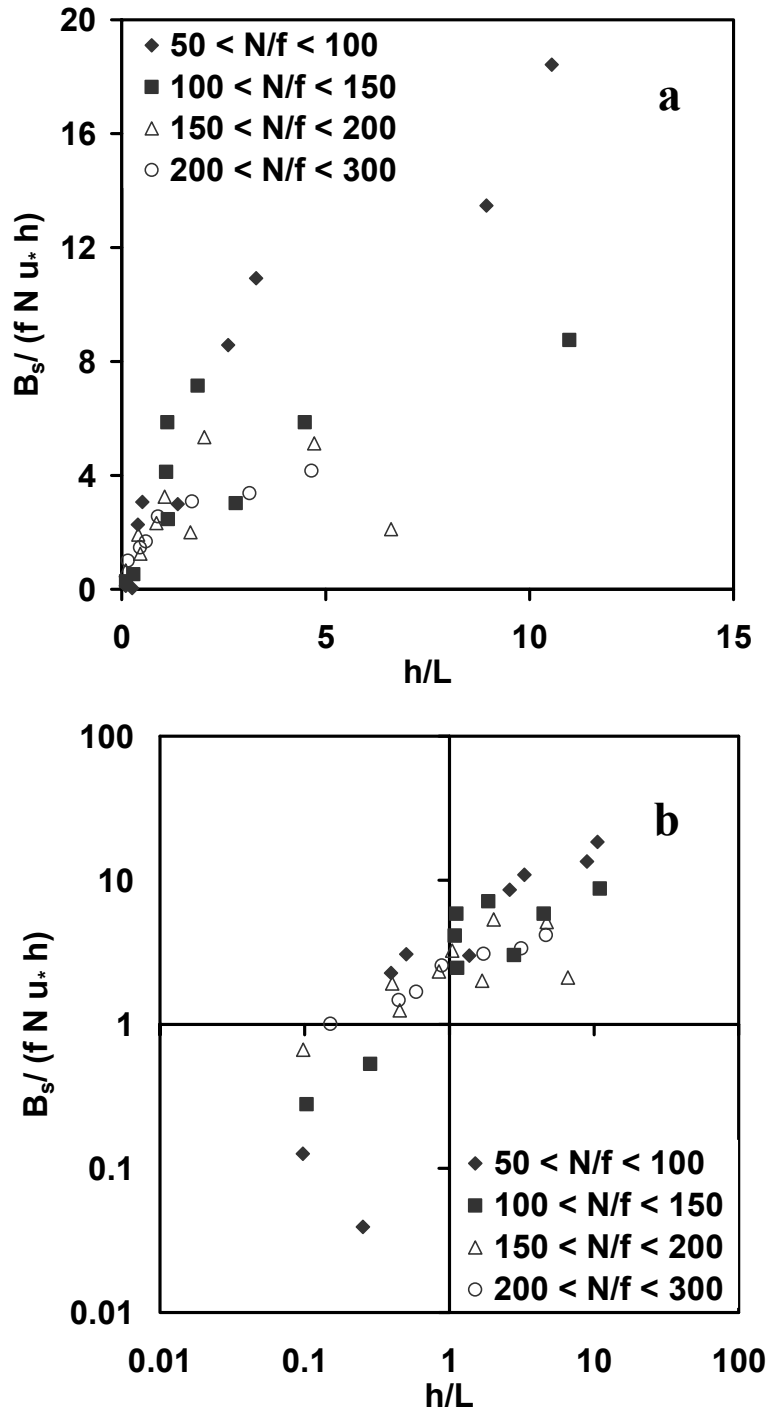
Figure 7.5: Dependence of observed dimensionless groups $B_s / (u_* fNh)$ versus h/L for different classes of *N/f* on a linear (a) and logarithmic scale (b).

A Monte-Carlo strategy, similar to the one in the previous section, was followed to estimate α and C_1 (on Sodankylä (Fig. 7.6a) and on the whole dataset (Fig. 7.6b)). In this case, a clear minimum in the meae is found in the contour plots with $C_1 = 1.8$ and $\alpha = 3$ as optimal estimates and is confirmed using the other statistical quality measures (not shown). So in contrast to Eqs. (7.1) and (7.2), the parameters in Eq. (7.3) can be determined with good confidence.
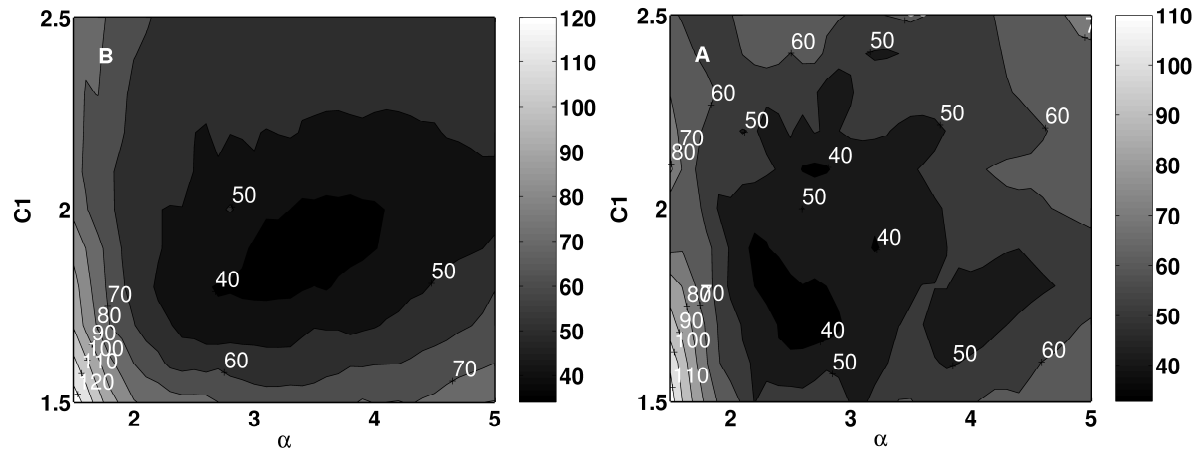
Figure 7.6: Contour plot of the median of absolute error (MEAE in m) for a range of C_1 and α for So-dankylä (a) and the total dataset (b).

Table 7.2: Overview of statistical measure for the evaluated proposals for the stable bound-ary-layer height.

Site	*mae* (m)	*rmse* (m)	*rmse-s* (m)	*rmse-s* (m)	*meae* (m)	*FB*	*IoA*
Eq. (7.1)							
Cabauw	128.3	155.6	36.9	151.1	118.3	0.076	0.746
Sodankylä	136.6	200.2	153.2	128.9	84.5	0.290	0.823
CASES-99	94.1	106.9	90.1	57.5	79.9	-0.911	0.621
SHEBA	63.3	69.1	48.1	48.8	62.4	-0.439	0.620
Eq. (7.2)							
Cabauw	115.5	140.1	118.3	75.1	95.7	-0.608	0.677
Sodankylä	101.7	117.2	103.0	55.8	100.1	-0.4754	0.858
CASES-99	111.4	122.3	118.7	29.5	95.5	-1.295	0.488
SHEBA	85.3	89.9	85.9	17.12	86.9	-1.068	0.417
KB88: 700 u_*							
Cabauw	89.9	111.3	29.9	107.2	71.2	0.117	0.808
Sodankylä	79.0	105.3	44.0	95.6	60.0	0.092	0.880
CASES-99	60.7	72.4	35.3	63.2	51.8	-0.274	0.767
SHEBA	22.9	27.3	16.9	21.4	23.5	-0.147	0.853

b) Verification

In this Section we will *verify* the performance of Eq. (7.3) against the independent data from Cabauw, CASES-99, SHEBA (Fig. 7.7b-d, Table 7.3) and a cross validation for Sodankylä (Fig. 7.7a). The good performance for Sodankylä is obvious, since these are the same data as used for the calibration. Nevertheless, it seems that the data collapse onto a *single* curve. This is not trivial and it gives confidence in the method and the variables that we selected. The model agrees well with the CASES-99 (rmse = 53.6 m, but is largely unsystematic) and Cabauw observations (rmse = 80.3 m with rmse-u = 62.6 m), although the scatter is larger for the Cabauw dataset than for the other datasets. This relatively large scatter is probably inherent to the sodar based observations for Cabauw instead of radiosondes profiles for the other datasets (Section 7.3). For SHEBA the model performance is good (rmse = 40.3 m of which 37.6 m is unsystematic), although the model seems to underestimate the observations slightly (Fig. 7.5d). Overall, the magnitude of FB < 0.15, which is not achieved for any of the other proposals, and IoA is larger than for Eqs. (7.1) and (7.2). In general, the alternative proposal is superior to Eq. (7.1) and (7.2) (see Table 7.2), where the main improvement by Eq. (7.3) is achieved for shallow boundary layers. For the LES model, Eq. (7.3) predicts $h = 173$ m which is close to $h_{LES} = 180$ m. Given the typical uncertainties of h_{obs} (typically 30%), the model performs rather well, which gives us good confidence in the applied method.

c) On the relevance of the Coriolis parameter f: two dimensionless groups only.

The recent literature discusses the variables that govern h (Kosovic and Curry, 2000; Kosovic and Lundquist, 2004). Although f should theoretically play a role in governing h based on it presence in the Ekman equations (at least for neutral boundary layers), we can discuss the relevance of f as compared with N in practical application for the SBL as mentioned in VH96 and Zilitinkevich and Baklanov (2002).

Since free flow stability is always present in the atmosphere and is of order $O(10^{-2})$ while f is typically $O(10^{-4})$, VH96 suggest that the impact of f can be neglected in practice. Mahrt and Heald (1979) and VM04 also argue that the Coriolis parameter is of minor importance since the SBL development is governed by an inertial oscillation. In that case, a pure Ekman boundary layer does not exist and thus the use of f is doubtful.

In addition, if we analyze sodar observations during so-called intermittent nights (e.g. during CASES-99, Van de Wiel et al., 2003), we find that the boundary-layer turbulence and also the boundary-layer height responds quickly (< 10 min) to a change of the near surface turbulence intensity if decoupling from the surface occurs. This suggests that the SBL can react on a timescale much shorter than f^{-1} which is believed to be the governing timescale for the SBL (Nieuwstadt and Duynkerke, 1996). This implies that f^{-1} is not a priori the most dominant timescale for the SBL growth, but that timescales that originate from the interaction with the surface may be more important. Estournel and Guedalia (1990) and VM04 suggest that the roughness length for momentum (z_0) is a relevant quantity. Consequently, the relevance of f and z_0 will be examined below.
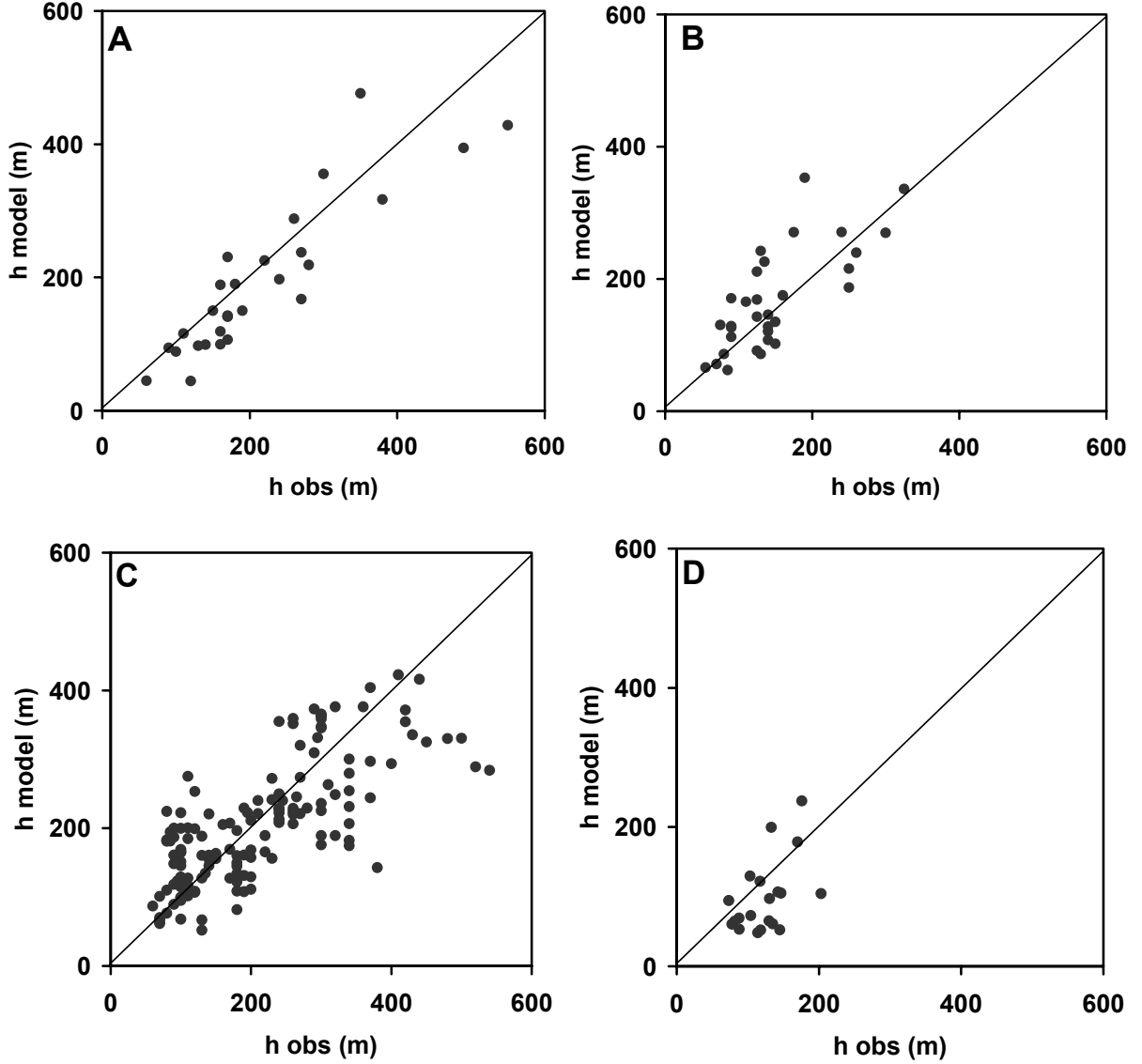
Figure 7.7: Observed and modeled stable boundary-layer height using Eq. (7.3) for Sodankylä (a), CASES-99 (b), Cabauw (c) and SHEBA (d).

Due to the variable nature of h, it is useful to adopt statistical techniques to gain insight into the relevant quantities that govern h. In this section, we perform a principal component analysis (PCA) on h_{obs} from all datasets to obtain information about the relative impact of the different variables on h_{obs}. Recall that PCA is a statistical technique in which the total variance of a dataset is decomposed along orthogonal vectors by determining the eigenvalues and eigenvectors of the covariance matrix between the variables. These eigenvectors are sorted in descending order according to the eigenvalues. The eigenvector associated with the largest eigenvalue is called the first principal component (FPC), the second large is called second principal component (SPC), etc. Finally, the data are transformed back into real space, and correlated to the original variables.

Table 7.3: Overview of statistical measure for the new proposals for the stable boundary-layer height.

Equation(7.3)	mae (m)	rmse (m)	rmse-s (m)	rmse-s (m)	meae (m)	FB	IoA
Cabauw	61.5	80.3	50.3	62.6	49.9	-0.108	0.843
Sodankylä	71.1	109.7	77.1	78.1	45.5	-0.146	0.831
CASES-99	41.1	53.6	19.0	50.1	33.5	0.114	0.855
SHEBA	35.2	40.3	16.0	37.6	39.8	-0.137	0.746
Equation (7.4)							
Cabauw	65.1	86.7	57.4	65.0	46.4	0.042	0.795
Sodankylä	166.4	271.9	123.3	242.4	61.8	0.390	0.606
CASES-99	55.7	74.3	20.7	71.4	40.4	-0.125	0.753
SHEBA	225.0	349.2	193.2	290.9	86.5	0.857	0.135

Table 7.4 shows the absolute values of the correlation coefficients between the observed u_*, N, $\overline{w\theta_s}$, f and z_0 and the FPC. The FPC explained 99.9% of the variance, so the higher principal components can be neglected safely. It appears that the correlation coefficient between u_* and the FPC is large compared to the other coefficients. The quantities $\overline{w\theta_s}$ and N show a considerable smaller correlation but are still relevant. The Coriolis parameter and z_0 have a correlation coefficient of only 0.15 and 0.16 with the FPC respectively. Therefore, the latter quantities are *in practice* relatively unimportant for h estimation (at least for these datasets). Note that the dominance of u_* gives support to the simple estimate by Koracin and Berkowicz (1988).

Table 7.4: Correlation coefficient r between the relevant quantities and the First Principal Component.

Parameter	u_*	N	$\overline{w\theta_s}$	f	z_0
r	0.75	0.47	0.37	0.15	0.16

Given the discussion above, we may exclude f and z_0 from the list of relevant variables, at least for estimation of h in practical applications. Then only two dimensionless groups remain, namely hN/u_* and h/L^* (Fig. 7.8a, all data are used). Two regimes can be clearly distinguished. For $h/L^* < 1$ (towards the near neutral limit) $h \propto u_*/N$, in accordance with Kitaigorodskii and Joffre (1988), Van Pul et al., (1994), and VH96.

For $h/L^* > 1$ (towards the very stable limit) the two groups are linearly related on the log-log scale. This means that $h \propto \sqrt{|B_s|/N^3}$. Although, it seems that h is independent of u_* in this regime, this is not really the case. The dependence of u_* comes in via B_s, because in the very

stable regime the turbulent temperature scale θ_* is linearly dependent on u_* (Holtslag and De Bruin, 1988; Van de Wiel, 2002). Thus making B_s quadratically dependent on u_* means that h is again proportional to u_*, but now with a different factor depending on N. Thus our diagnostic equation for h based on the current analysis reads as:

$$h = \begin{cases} 10 u_* / N & \text{for} \quad u_*^2 N / |B_s| > 10 \\ 32 \sqrt{|B_s|/N^3} & \text{for} \quad u_*^2 N / |B_s| < 10 \end{cases} \tag{7.4}$$

Obviously the application of Eqs. (7.3) and (7.4) is limited to cases where $N>0$. Eq. (7.4) is well supported by Fig. 7.8a. Fig. 7.8a also shows Eq. (7.1), neglecting the small contribution from the term $\dfrac{fh}{C_n u_*}$, for the parameter set proposed by ZM96 and Joffre et al. (2001). For strong stability (i.e. large h/L^*) Eq. (7.1) does *not* correspond to the observations. Interestingly, the dimensional analysis (ignoring f) corresponds to the same dimensionless groups as in Eq. (7.1) if the f-group is neglected in the latter case! However, as before the important difference lies in the particular functional relationship between the group (Fig. 7.8a). In our case it has a power law (instead of a geometric average).

For stable conditions the length scale $\sqrt{|B_s|/N^3}$ in Eq. (7.4) has an equivalent form as the classical Ozmidov length scale ($l_{OZ} = \sqrt{\varepsilon/N^3}$, with ε the TKE dissipation rate), above which eddies are deformed by stratification. Both scales represent the destruction of TKE during stable conditions. The final result in terms of Eq. (7.4) is given in Fig. 7.8b. Table 7.3 demonstrates that Eq. (7.4) performs well for CASES-99 and Cabauw (FB < 0.15 and IoA > 0.75). For Sodankylä the rmse increases (although rmse-s < rmse-u) and for SHEBA the performance degrades even more (IoA = 0.13). Thus Eq. (7.3) performs better and seems to be more general although Eq. (7.4) is physically more appealing.

7.6 Conclusions

This paper evaluates two so-called multi-limit (diagnostic) equations for the stable boundary-layer height (h) proposed by Zilitinkevich and Mironov (1996) against four observational datasets and large-eddy model simulation. These equations are based on inverse interpolation of characteristic length scales that account for rotation, surface buoyancy flux and free flow stability respectively.
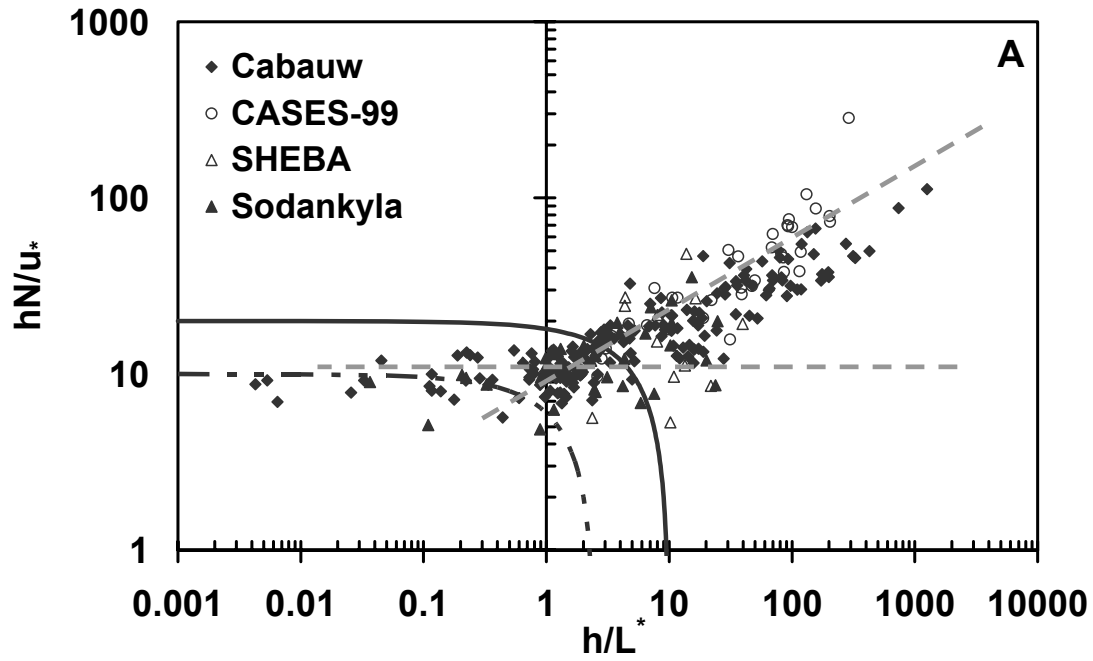
Figure 7.8a: Relationship between dimensionless groups hN/u_* and h/L^*. The two straight grey lines represent the limiting regimes in Eq. (7.4). Black line: Eq (7.1) with $C_s = 10$, $C_i = 20$; dotted black line: Eq (7.1) with $C_s = 2.5$ and $C_i = 10$.
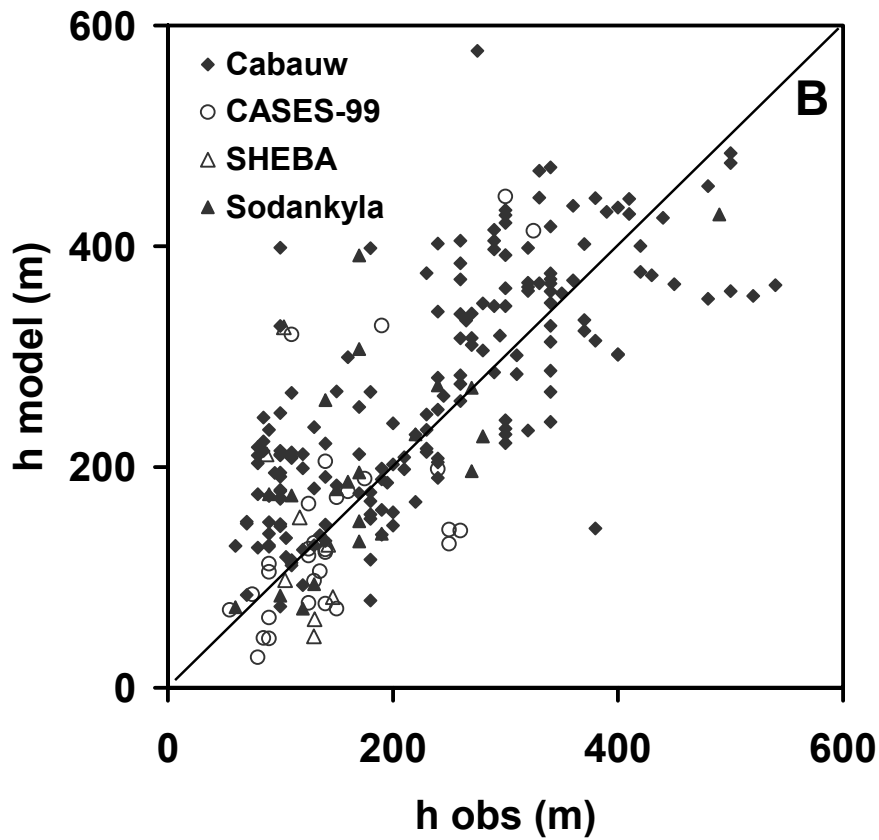
Figure 7.8b: Modeled and observed boundary-layer heights for Equation (7.4).

We found that the multi-limit equations underestimate the stable boundary-layer height, especially for shallow boundary layers. This is undesirable since shallow boundary layers will result in high pollutant concentration during episodes and a proper estimate is required. In an attempt to recalibrate the parameters, we found that no unique parameter set for these multi-limit equations could be determined.

To circumvent the difficulties with the multi-limit equations, an alternative formulation is developed with formal dimensional analysis with the same quantities as in the multi-limit equations. The proposed formulation is robust and appears to reduce a significant model bias for shallow boundary-layer heights in comparison with the existing formulations. As such, the proposed formulation appears applicable also for high stability conditions in contrast to existing formulations that primary are derived for weakly stable cases. Contrary to the multi-limit equations, a unique parameter set was found for this new formulation.

Finally, we discuss whether the Coriolis force and the surface roughness length z_{0m} are relevant parameters for estimating the stable boundary-layer height in practice. Omitting the Coriolis parameter f, the data reveal a division in two regimes. For moderately stable conditions the boundary-layer height is proportional to u_*/N and for stronger stable conditions it appears that the boundary-layer height is proportional to the length scale $\sqrt{|B_s|/N^3}$. Overall, our analysis shows that the strongest relation of h exists with u_* (and B_s in the very stable limit), in addition to N while f and z_{0m} are less relevant for the data utilized!

Acknowledgements

Appendix 7A: Dimensional analysis for the stable boundary-layer height formula.

$$\Pi = h^{\alpha} u_*^{\beta} B_s^{\gamma} N^{\varepsilon} f^{\delta}$$

The number of variables $m = 5$, the number of basic units $n = 2$, so we can construct $r = 3$ dimensionless groups.

We get a system of equations:

$$\begin{cases} \alpha + \beta + 2\gamma = 0 \\ -\beta - 3\gamma - \delta - \varepsilon = 0 \end{cases}$$

To obtain 3 dimensionless groups, we have to choose 3 parameters.

I. $\gamma = 1; \delta = -1, \varepsilon = -1$

$$\begin{cases} \alpha + \beta + 2 = 0 \\ -\beta - 3 + 1 + 1 = 0 \end{cases}$$

Consequently $\beta = -1$ and $\alpha = -1$, and thus $\Pi_1 = h^{-1} u_*^{-1} B_s^1 N^{-1} f^{-1} \Rightarrow \Pi_1 = \dfrac{B_s}{fNu_*h}$

II. $\alpha = 1; \delta = 0, \varepsilon = 0$

$$\begin{cases} 1 + \beta + 2 = 0 \\ -\beta - 3\gamma = 0 \end{cases}$$

Consequently $\beta = -3$ and $\gamma = 1$, and thus $\Pi_2 = h^1 u_*^{-3} B_s^1 N^0 f^0 \Rightarrow \Pi_2 = \dfrac{hB_s}{u_*^3} = \dfrac{h}{L}$

III. $\alpha = 0; \delta = 1, \varepsilon = -1$

$$\begin{cases} \beta + 2\gamma = 0 \\ -\beta - 3\gamma + 1 - 1 = 0 \end{cases}$$

This can only be true if $\gamma = 0$ and $\beta = 0$, and thus $\Pi_3 = h^0 u_*^0 B_s^0 N^1 f^{-1} \Rightarrow \Pi_3 = \dfrac{N}{f}$

Chapter 8

Comments on deriving the equilibrium height of the stable boundary layer

Abstract

Recently, the equilibrium height of the stable boundary layer received much attention in a series of papers by Zilitinkevich and co-workers. In these studies the stable boundary-layer height is derived in terms of inverse interpolation of different boundary-layer height scales, each representing a prototype boundary layer. As an alternative, we propose an inverse interpolation of the eddy-diffusivities for each prototype before applying the definition of the Ekman layer depth. The new equation for the stable boundary-layer height improves performance in a comparison against four observational datasets.

8.1 Introduction

The equilibrium height of the stable boundary-layer h_E, and its relevance for predicting the stable boundary-layer (SBL) structure and for air quality modelling has been discussed intensively (among others Zilitinkevich and Esau, 2003, henceforth ZE03; Steeneveld et al., 2007). Recently, several papers (Zilitinkevich and Mironov, 1996; Zilitinkevich and Calanca, 2002; Zilitinkevich and Baklanov, 2002; ZE03) discuss the relevant processes that govern the stable boundary-layer height in equilibrium conditions. In these studies, the basic variables governing h_E are the surface friction velocity u_*, the surface buoyancy flux $B_s = \frac{g}{\theta}\overline{w\theta}_s$, the Coriolis parameter f and the free flow stability N. Based on these variables, ZE03 identified three boundary-layer prototypes: the truly neutral ($B_s = 0$ and $N = 0$), the conventionally neutral ($N \neq 0$ and $B_s = 0$) and the nocturnal boundary-layer ($N=0$ and $B_s \neq 0$).

   In the papers by Zilitinkevich and co-workers the coupling of these prototypes is done by interpolation of associated boundary-layer height scales. In this paper we propose an approach directly related to the bulk eddy diffusivity of the prototypes. We will show that the new alternative improves the predictive skill.

8.2 Background

Following the reasoning by ZE03, the stable boundary-layer depth is defined as the Ekman layer depth (h_*), which is given by the eddy diffusivity K_M and the absolute value of the Coriolis parameter f (e.g. Stull, 1988):

$$h_* = \sqrt{\frac{K_M}{f}} \qquad (8.1)$$

For the eddy viscosity K_M ZE03 distinguish between three different boundary layer types, and for each type a characteristic velocity scale u_T and length scale l_T:

Truly neutral $\qquad\qquad K_M = u_T l_T = u_* h_* \qquad\qquad (8.2)$

Conventionally neutral

$$K_M = u_T l_T = \frac{u_*^2}{N} \qquad (8.3)$$

Nocturnal

$$K_M = u_T l_T = u_* L \qquad (8.4)$$

with $L = -u_*^3/B_s$ the Obukhov length (note the Von Karman constant is not included here). ZE03 obtain an equilibrium height for the boundary layer for each boundary layer type:

Truly neutral

$$h_{E,TN} = C_R \frac{u_*}{f} \qquad (8.5)$$

Conventionally neutral

$$h_{E,CN} = \frac{C_S}{C_{uN}^{1/2}} \frac{u_*}{\sqrt{|fN|}} \qquad (8.6)$$

Nocturnal

$$h_{E,Noct} = C_S \frac{u_*^2}{\sqrt{|fF_{bs}|}} \qquad (8.7)$$

To obtain an equilibrium height that accounts for all three combined prototypes, the equilibrium heights of the individual prototypes are interpolated as follows:

$$\frac{1}{h_E^2} = \frac{1}{h_{E,TN}^2} + \frac{1}{h_{E,CN}^2} + \frac{1}{h_{E,Noct}^2} \qquad (8.8)$$

Then

$$h_E = C_R \frac{u_*}{f} \left(1 + \frac{C_R^2 C_{uN}}{C_S^2} \frac{N}{f} + \frac{C_R^2}{C_S^2} \frac{u_*}{fL} \right)^{-1/2} \qquad (8.9)$$

with $C_R = 0.5$; $C_{uN}/C_S^2 = 0.56$ and $C_S = 1.0$.

If the relevant eddy diffusivities are indeed represented by Eqs. (8.2)-(8.4) we note that the bulk diffusivity K_M can directly be written as:

$$\frac{1}{K_M} = \frac{1}{u_* h_*} + \frac{1}{u_*^2/N} + \frac{1}{u_* L}, \qquad (8.10)$$

Here the proportionality constants are taken 1 for convenience.

Consequently,

$$K_M = \frac{u_*^2 h_* L / N}{u_* h_* / N + h_* L + u_* L / N}$$
(8.11)

Combining Eq. (8.11) in Eq. (8.1), solving for $h_* = h_E$ and choosing the physical solution in the quadratic equation, we obtain:

$$h_* = \alpha \frac{u_*}{N},$$
(8.12)

where

$$\alpha = \frac{-1 + \sqrt{1 + 4\left(\dfrac{u_*}{fL} + \dfrac{N}{f}\right)}}{2\left(\dfrac{u_*}{NL} + 1\right)}$$
(8.13)

Also Eq. (8.9) can be written in the format of Eq. (8.12). Then α is given by:

$$\alpha = \frac{C_R \, N/f}{\sqrt{1 + \dfrac{C_R^2 C_{uN}}{C_S^2} \dfrac{N}{f} + \dfrac{C_R^2}{C_S^2} \dfrac{u_*}{fL}}},$$
(8.14)

which is clearly different from Eq. (8.13).

The format of Eq. (8.12) was already found earlier in many studies. Vogelezang and Holtslag (1996) found α to be a function of the shear and Richardson number across the SBL, while Steeneveld et al. (2007) derived Eq. (8.12) with α solely depending on the free-flow stability. In any case, Eqs. (8.13) and (8.14) show that α is related to the traditional parameter groups $u_*/(fL)$ (the Monin-Kazanski parameter) and N/f (Kitaigordskii and Joffre, 1988). The numerical value of α is typically 7-13 (e.g. Vogelezang and Holtslag, 1996).

8.3 Observations and Results

In order to validate Eq. (8.12) with Eq. (8.13), and to compare its performance with Eq. (8.9), we use the data set described in Steeneveld et al. (2007). The dataset consists of observed SBL heights, turbulent surface fluxes (eddy covariance) and free flow stability over a wide range of latitude, surface roughness (z_0) and landuse. Data are available from Cabauw (149 data points, $z_0 = 0.20$ m, grassland, 51ºN, The Netherlands), Sodankylä (30 data points, $z_0 = 1.4$ m, boreal forest, 67ºN, Finland), CASES-99 (32 data points, $z_0 = 0.03$ m, prairie grassland,

37ºN, U.S.A.) and SHEBA (20 data points, $z_0 = 1.10^{-4}$, sea ice, 75ºN). The SBL height was obtained from soundings using the method in Joffre et al. (2001), except for Cabauw where *h* was obtained from sodar measurements. The observations have been selected for $u_* > 0.04$ ms^{-1}, $\overline{w\theta}_s < -0.0016$ Kms^{-1} and $N > 0.015$ s^{-1} to ensure a reliable data set. For more details see Steeneveld et al. (2007).

Results obtained with Eq. (8.9) and Eq. (8.12) with Eq. (8.13) are shown in Figs. 8.1 and 8.2, respectively. Table 8.1 summarizes some statistical quantities for model performance, i.e. mean absolute error (MAE), Systematic RMSE (RMSE-S), median of the mean absolute error (MEAE) and the index of agreement (IoA, Willmott, 1982. The IoA equals 1 for a perfect model performance). Equation (8.12) gives a substantial reduction of the RMSE-S, and an increased IoA compared to Eq. (8.9). Note that for shallow SBLs, mesoscale effects may become important and these may contribute to the bias, since mesoscale effects are not incorporated in the current model. Unfortunately the proposed interpolation method cannot avoid the negative bias for shallow SBLs.

As an alternative, Steeneveld et al. (2007) applied a formal dimensional analysis on *h*, u_*, *N*, and B_s, not taking into account *f*. See Steeneveld et al. (2007) for discussion of the relevance of this parameter. This gives the dimensionless groups $\Pi_1 = hN/u_*$, $\Pi_2 = h/L$.

Then it is found that the equilibrium SBL height is given by:

$$
h_E = \begin{cases} 10\dfrac{u_*}{N} & \dfrac{u_*^2 N}{|B_s|} > 10 \\[2em] 32\sqrt{\dfrac{|B_s|}{N^3}} & \dfrac{u_*^2 N}{|B_s|} < 10 \end{cases}
\tag{8.15}
$$

Fig. 8.3 shows that the negative bias for a shallow SBL is not present with Eqs. (8.15), in particular due to the impact of Eq. (8.15b) for (very) stable conditions. For moderately stable and near neutral conditions, Eq. (8.15a) does also well, even with a constant value of the coefficient (here 10). Thus a satisfactory prediction of the SBL height can be obtained without taking into account *f* explicitly (see also discussion in Vogelezang and Holtslag, 1996). Note that this formula is only valid for the range of the variables for which it has been derived. Nevertheless it is worthwhile considering its applicability beyond this range, i.e. its limit behaviour. The formula behaves properly for $B_s \to 0$, since in this case the upper branch should be utilized. For $N \to 0$, Eq. (8.15) seems not a priori approach a proper limit. Formally speaking, Eq. (8.15) would lead to unrealistically deep SBLs. However, in practice, this limit is hardly ever found in the atmosphere due to radiation divergence, which depends on the temperature profile rather than on the potential temperature profile. Finally, we note that Eq. (8.9) has a proper limit behaviour for $N \to 0$ and $B_s \to 0$, but this in turn leads to an infinite SBL depth for $f \to 0$ (equatorial case).

We realize that the evaluation of the above equations for the equilibrium depth with field data may be troublesome, due to the complexity of making observations in stable conditions and due to the fact that in reality conditions cannot be controlled. Alternatively, we may consider to explore Large Eddy Simulation results for more controlled testing (as in Esau, 2004). In that case however, we must be aware of the fact that especially in very stable conditions, LES results (profiles of mean and turbulent quantities) are strongly dependent on the model resolution (Beare and MacVean, 2004). Also long-wave radiation divergence plays an important role, which is usually not taken into account by LES. Note that the field data used in this study cover a wide range of conditions, including non-turbulent effects such as radiation divergence (e.g. André and Mahrt, 1982).
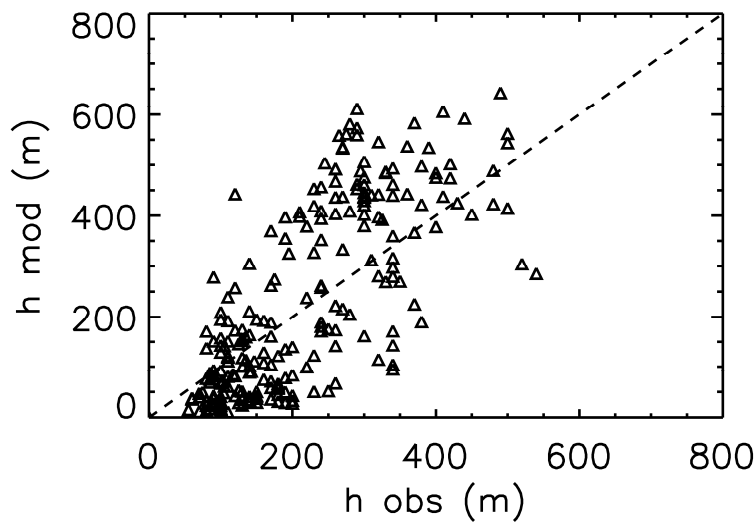
Figure 8.1: Modelled (Eq. 8.9) vs. observed stable boundary-layer height.
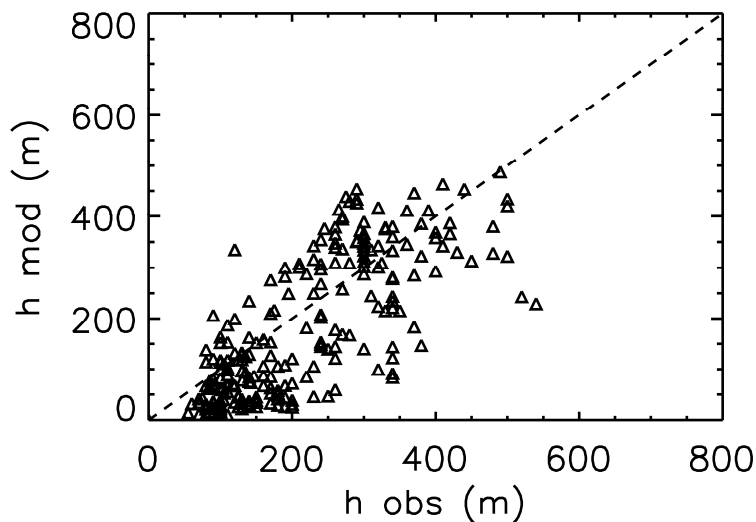
Figure 8.2: Modelled (Eq. 8.12) vs. observed stable boundary-layer height.

Table 8.1: Statistical Evaluation of SBL height proposals

Model	*MAE (m)*	*RMSE-S (m)*	*MEAE (m)*	*IoA (-)*
Eq. (8.9)	100.9	99.3	83.0	0.80
Eq. (8.12)	78.7	62.9	67.9	0.84
Eq. (8.15)	65.2	41.5	49.7	0.84
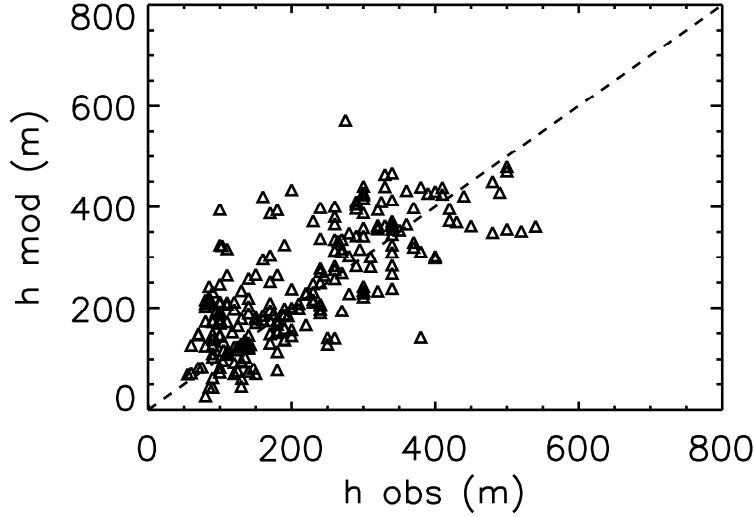
Figure 8.3: Modelled (Eq. 8.15) vs. observed stable boundary-layer height.

8.4 Conclusions

We propose an alternative method to derive a formula for the stable boundary-layer height when more than one stable boundary-layer prototype contributes to the final boundary-layer height. Instead of interpolating the height scales for each prototype, we directly interpolate the eddy diffusivities of each prototype. The alternative formulation performs well, and reduces the bias of the predicted stable boundary-layer height compared to the original formulation. Furthermore, a second alternative based on formal dimensional analysis shows improved skill, especially for shallow stable boundary layers. Further improvements are possible by following the full approach in Steeneveld et al. (2007).

Chapter 9

Summary, reflections and recommendations

9.1 Summary

In this thesis the understanding and prediction of the stable boundary layer over land is studied. A stable boundary layer occurs when the potential temperature increases with height, which is observed predominantly at night, and in polar regions in winter. This study was motivated by the fact that weather forecast models and climate models show significant and systematic errors of unknown cause under stable conditions. An important cause for this poor representation of the stable boundary layer lies in the fact that many physical processes play a role in stable conditions (in contrast to the daytime where convection is the dominant process). The most important processes are turbulent mixing, radiative transport, the coupling with the land surface and the underlying soil, gravity waves, and aspects of heterogeneous land use, baroclinicity, the nocturnal wind maximum and possibly fog. All those processes should be well described in models to obtain a reliable forecast.

Weather Prediction and Climate models use more turbulent mixing than can be justified from field observations. The most important reason for models to apply enhanced mixing is to obtain sufficient cyclone filling. In addition, the models show a strong sensitivity for small modifications in the amount of turbulent mixing. Because the stable boundary layer is a shallow layer (typically 100-200 m deep, or even less in calm conditions), and weather forecast models only have a limited vertical resolution, the resolving capacity of such models is limited for the stable boundary layer. Together, this provides strong uncertainties for operational weather forecasts for minimum temperatures, fog and night frost, but also for future climate projections and applications in dispersion models.

To improve our understanding and ability to model the stable boundary layer, we point out the following questions in this thesis:

1. To what extent is the stable boundary layer influenced by the coupling to the land surface?
2. Can the stable boundary layer be satisfactorily modelled at the local scale when all relevant processes are taken into account?
3. Can orographic drag possibly explain the required additional drag for cyclone filling in large-scale models?
4. Is it possible to obtain an improved formulation for the stable boundary-layer height?

Loosely speaking the thesis follows three paths. The first path considers the aspects of modelling the SBL in column mode. The second part investigates 3D aspects of SBL modelling, and the final part consists of the evaluation and improvement of robust formulations for the stable boundary-layer height.

Chapter 2 extends the first GABLS intercomparison case study, in which model results were compared for a moderately stable boundary layer with prescribed surface temperature (see also Introduction). However, a prescribed surface temperature is not a realistic boundary

condition for the SBL. In reality, the boundary layer should be directly coupled to the land surface, so the heat flux from the soil can be accounted for. A sensitivity study shows that the structure, depth and integrated cooling strongly depend on the degree of atmosphere-land surface coupling. Consequently, the question can be raised how sensitive the results are for the chosen model resolution, in both the atmosphere and in the soil, and to which process the available computation capacity is best allocated for. The modelled SBL appears to be very sensitive to the chosen model resolution in the soil. Too coarse resolution can be partly, but not fully, compensated by adding turbulent mixing to obtain realistic mean wind and temperature profiles.

Chapter 2 also addresses the length scale formulation for turbulent mixing, as compared with Large Eddy Simulation results. The SBL structure is forecasted more satisfactorily when, next to the height z, a dynamic length scale based on the local properties of the turbulent flow is accounted for, confirming earlier work (Nieuwstadt, 1984).

Chapter 3 presents a process-study in which three diurnal cycles with different mechanical forcing (i.e. geostrophic wind speed) are modelled with a high-resolution column model that accounts for land surface coupling. The nights are intermittently turbulent, fully turbulent and non-turbulent respectively. They have been selected from the CASES-99 experimental campaign over prairie grassland in Kansas (U.S.A.), also because of the availability of high quality observations. The aim of the study is to examine whether we can model the SBL satisfactorily on a local scale (thus given the locally observed surface roughness, soil and vegetation thermal properties, geostrophic wind speed and advection), when we do not restrict vertical resolution, but when we do account for all physical processes (such as turbulent mixing, radiation divergence, and land surface coupling). It appears that both the vertical structure and the surface fluxes can be modelled accurately. Aspects that were erroneously modelled were the intermittent behaviour of the turbulent fluxes and the vertical structure of the nighttime wind maximum. The work in Chapter 3 was later used for the set-up of the second GABLS intercomparison study (Svensson and Holtslag, 2006).

In Chapter 4, we apply the knowledge gained in Chapter 3 to a number of 3D models for the same case study. In addition we study whether 3D models are able to correctly model the low-level jet. Also, the work within the GABLS context is extended here to 3D models. Frequently used mesoscale models such as MM5, HIRLAM (KNMI), and COAMPS are compared with in-situ observations for different types of nights. Moreover, we look for common deficiencies in these models, and for what type of atmospheric conditions they occur. In general, these models share an underestimation of (rapid) surface cooling and the diurnal cycle of wind speed and temperature, and an overestimation of the boundary-layer depth during strong winds. The representation of the low-level jet is also problematic in all models. A sufficiently large model domain is required for a proper representation of baroclinicity, and the associated nighttime wind maximum. Surface-layer schemes with a vegetation layer are advantageous in forecasting the minimum temperature. A sensitivity study with several radiation transfer schemes showed up to 6 K difference in minimum temperature for calm nights. Finally, we

show that a considerable improvement of forecasted minimum temperature is obtained when we introduce a) a realistic formulation of the soil heat flux, b) a vegetation layer, c) turbulent mixing based on a local scaling approach.

Chapter 5 considers the drag on the SBL caused by small-scale orography. Chapter 3 showed that the SBL can be modelled satisfactorily on a local scale for a broad wind regime. Thus, the question remains why large-scale weather forecast models require additional drag compared to the turbulent drag as found for local field observations. The modelled low-pressure systems are too intensive and deep without this additional drag. Here we explore the potential role of orographically induced drag on the SBL. Until now, large-scale model only account for effects by large mountain ridges. First order estimates of the orographic drag (based on scaling arguments) appeared to explain the difference between the required and justified drag for the CASES-99 terrain. The inclusion of the divergence of this drag over the SBL in a column model provided an improved wind speed profile. Moreover, cyclone filling (estimated from the cross-isobaric flow) was in agreement with the required cyclone filling in large-scale models.

Chapter 6 examines the response of the stable boundary layer, and especially the 2m temperature) on a 40% CO_2 concentration increase. This research contributes to a scientific debate whether urban effects affect the 2m temperature rise as observed in the last 50 years. Worldwide observations showed the same temperature rise for windy and calm conditions, which is counterintuitive because the SBL structure differs strongly between these circumstances. Climate skeptics use this argument to doubt the reliability of the 2m temperature record. Our model study shows that indeed the 2m temperature rise is similar for calm and windy conditions.

The following two chapters consider the forecasting of the stable boundary-layer height. Numerous applications (especially for dispersion modelling for air quality) need a robust expression of the SBL depth, without the need for expensive measurement devices. In Chapter 7, we evaluate a number of formulas for the SBL against field observations over a broad range of land use, land roughness and latitudes. Many of these proposals (although based on theory) show large errors, specifically for shallow boundary layers (with high potential concentrations of pollutants). In the current study, we use dimensional analysis and obtain three dimensionless groups that are relevant for the stable boundary-layer height. This provided a formula for the stable boundary-layer height that is robust for a broad range of observations. In addition, the relevance of the Coriolis parameter for the SBL has been examined. Both dimensional analysis and a principal component analysis indicate that the Coriolis parameter is not a required variable to describe the SBL height in practical applications.

Chapter 8 considers the derivation of a formula for the equilibrium height of the SBL. Previous work proposed to calculate the equilibrium height of the SBL as a weighted interpolation of height of three prototype boundary layers, i.e. the nocturnal boundary layer, the truly neutral boundary layer, and the conventionally neutral boundary layer. In this chapter, we comment on this work, and we state that if these prototypes act together, it is better to interpo-

late the bulk eddy-diffusivities of the prototypes than their heights. This provides an alternative formulation for the SBL height that improves the predictive skill compared to field observations.

To summarize, this thesis confirms that the SBL development is a subtle balance between turbulent mixing, radiative cooling and the interaction with the land surface. It was found that the stable boundary layer can be satisfactorily modelled on the local scale when all these processes are taken into account and the forcings are well known. The stable boundary layer is strongly influenced by the coupling to the land surface. Some evidence was found that small-scale gravity wave drag due to the presence of small-scale orography might contribute significantly to the momentum budget of the stable boundary layer. This also impacts on the cyclone filling on the synoptic scale. Finally, a new formula for the stable boundary-layer depth was derived. Despite these encouraging results above, further research is necessary in the field of modelling, observations and fundamental concepts.

9.2 Recommendations for further research

9.2.1 Intermittent turbulence and periodic oscillations in observations

The first fundamental question that needs further understanding is the so-called global intermittency in the SBL. This refers to periods of turbulence which alternate with quiet periods in which the turbulence disappears for a time period of an order of an hour. Those periods are regularly observed during stable stratification (e.g. Hartogensis and De Bruin, 2005). Here we present a case study of observed global intermittency in the Netherlands and examine its horizontal extent based on routine observations. Next, we reflect on five open issues in the stable boundary layer and we provide recommendations for future work.

During conditions of light winds and a reasonable amount of radiative cooling during stable stratification, the exchange of heat and momentum may occur in so-called "bursts", i.e. short episodes of increased turbulence and mixing (e.g. Kondo 1978; Weber and Kurzeja, 1991; Van de Wiel, 2002). Several different physical mechanisms have been suggested to explain the observed oscillations. At first, large shear stress at the low-level jet (LLJ) causes locally increased turbulence that can be transported downwards (Mahrt, 1999). Secondly, gravity waves that are launched in stratification can be responsible (Duynkerke, 1991; Nappo, 1991). Thirdly, Businger (1973) and Van de Wiel (2002) explain the oscillations by decoupling of air when stratification is so strong that momentum fluxes are suppressed. Subsequently the acting pressure force accelerates the flow and recouples the flow with the surface.

Beyond the exact mechanism, little is known about the horizontal extent of this phenomenon, although it is important for flux calculations in atmospheric models. This is because these intermittent patches can be present in only a part of a grid cell (Mahrt, 1987). Then, the grid averaged wind speed and temperature gradients are not uniquely related to the mean surface fluxes.

We consider the night of 15/16 November 2002 in The Netherlands. In that night, The Netherlands were situated between four weak low-pressure areas, and experienced weak winds (typically 2-3 ms^{-1}) from the southeast. A series of radiosondes showed that advection was weak and can be safely neglected. A weak frontal zone entered The Netherlands from the east during the night and reached the eastern part of The Netherlands around 2100 UTC, while the western part remained clear till 0000 UTC the next day. Before the clouds arrived, the clear sky gave rise to strong radiative cooling. At screen level (1.5 m AGL) the air temperature dropped from 9 ℃ at 1700 UTC to 4 ℃ when the clouds arrived and the Cabauw mast reported an inversion strength of 6 K between the 140 m and 2 m levels. The relative humidity increased from 85% in the afternoon to 95% at night. At some nearby stations, especially later in the night some fog was reported. These are excellent circumstances in which oscillations can occur because both wind (so turbulence) and radiative cooling are present as 'forcings'.

a) Single station observations: The Wageningen field

Fig. 9.1 shows 10 min. averaged observations at the Wageningen University observational field (Jacobs et al., 2003). At 1830 UTC, the temperature at screen level drops sharply (from 7 to 2.5 ℃), and then after about one hour increases again to 7℃, although the long wave incoming radiation (LWD) does not change. Long-wave outgoing radiation follows these temperature oscillations. Note the amplitude is about 3.5 K at 10 cm and 2.5 K at 1.5 m. At 2100 UTC, another temperature decrease was observed of the same magnitude. Striking is that the temperature decrease occurs while the clouds are coming in, as can be seen in the LWD. After 2200 UTC, the temperatures at 10 cm and screen level are the same. Temperature oscillations coincide with oscillations in wind speed, soil heat flux and wind direction (not shown): high temperatures coincide with a temporary wind speed increase. The surface ground heat flux is less negative during a burst (period of increased turbulence) than during calm conditions. Wind direction shows a small veering when a temperature is increased. Both fluxes of momentum, sensible heat and latent heat are strongly reduced when low temperatures are observed. This global picture seems to be typical for the Businger (1973) mechanism.

Because little is known whether this phenomenon is locally driven or is present on a larger scale, we use the routine weather observations in The Netherlands (a 300 x 400 km area) from the locations to examine the horizontal scale of these events. Observations from coastal station were discarded because they may be influenced by the sea-land transition.

b) Spatial development

To investigate the horizontal extent of the observed oscillations, the 10 min. averaged temperature signal from the 32 automatic weather stations were moving average (MA) filtered with a 2 hour window to remove high frequency fluctuations. Next, we applied a 30 min MA filter. The resulting signal is used to determine the amplitude, period and number of oscillations at various stations. Fig. 9.2 shows the 2m temperature as observed in Wageningen,

Soesterberg and De Bilt (see Fig. 9.2d for the locations). Although the different stations are located far apart, and also located over different landscapes and landuse, we find a surprising correspondence of the frequency and amplitude of the temperature oscillation.
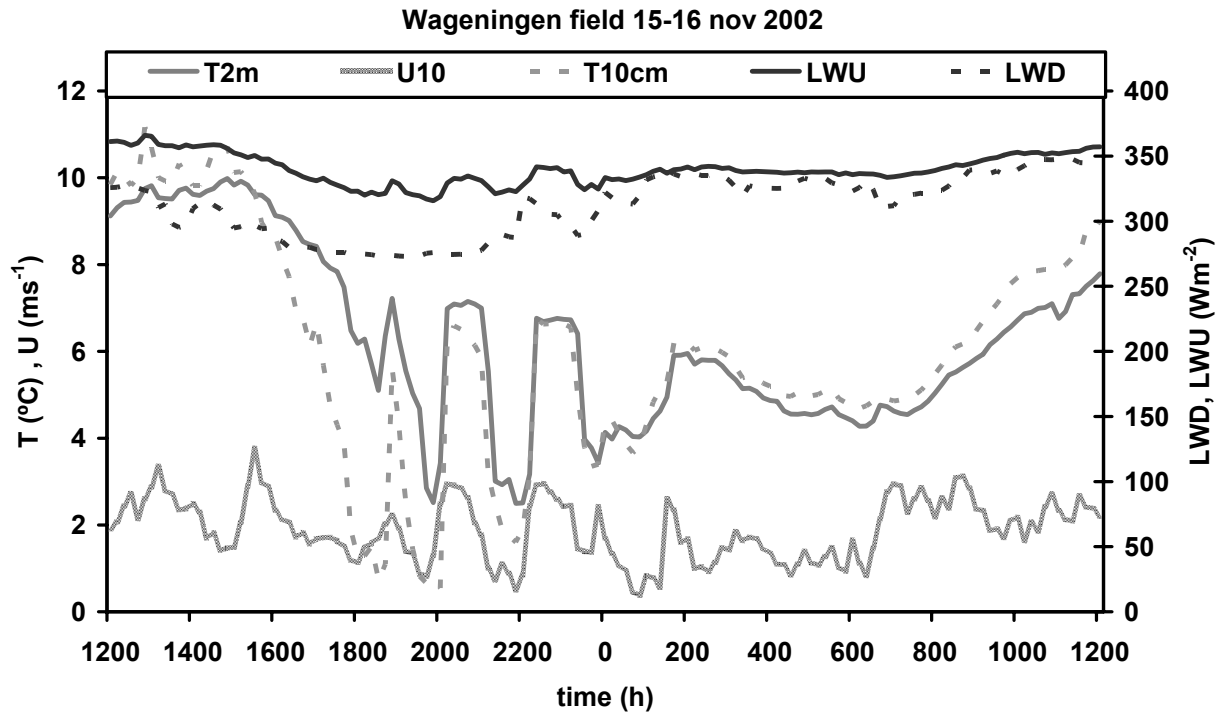
Figure 9.1: Observations of screen level wind speed, temperature (and at 10 cm.), long-wave radiation components at the Wageningen field.

For each station, we count the number of observed oscillations (here arbitrarily defined as burst with a maximum temperature anomaly $\delta T"_{max} > 0.8$ K. Although this is a subjective measure, a sensitivity test and visual inspection of the temperature record showed that a higher threshold value was too strict, and a smaller threshold value gave high frequency oscillations as well. Future studies should focus on the development of a robust formulation of an 'intermittency measure'. Fig. 9.3a shows the spatial distribution of oscillation intensity by means of $\delta T"_{max}$. The oscillations are seen in a large part of The Netherlands, about 100 x 100 km. For stations where oscillations are present, the observed averaged period is shown in Fig. 9.3b. The period is about 110 minutes at all stations. The strongest oscillations are found at the Wageningen field.
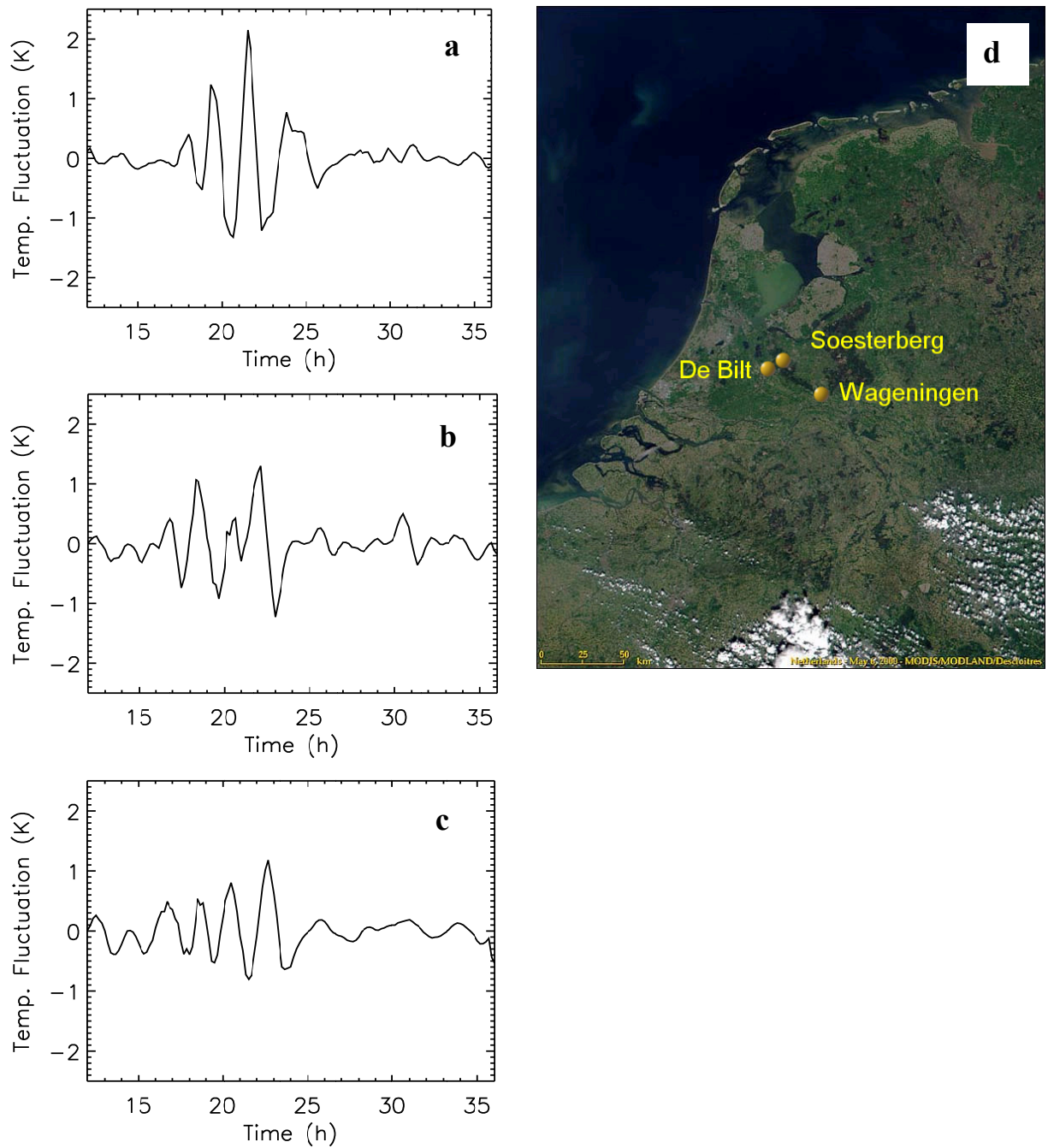
Figure 9.2: MA filtered temperature signal in Wageningen (a), Soesterberg (b) and De Bilt (c) for the night of 15-16 November 2002. d) Map of The Netherlands.
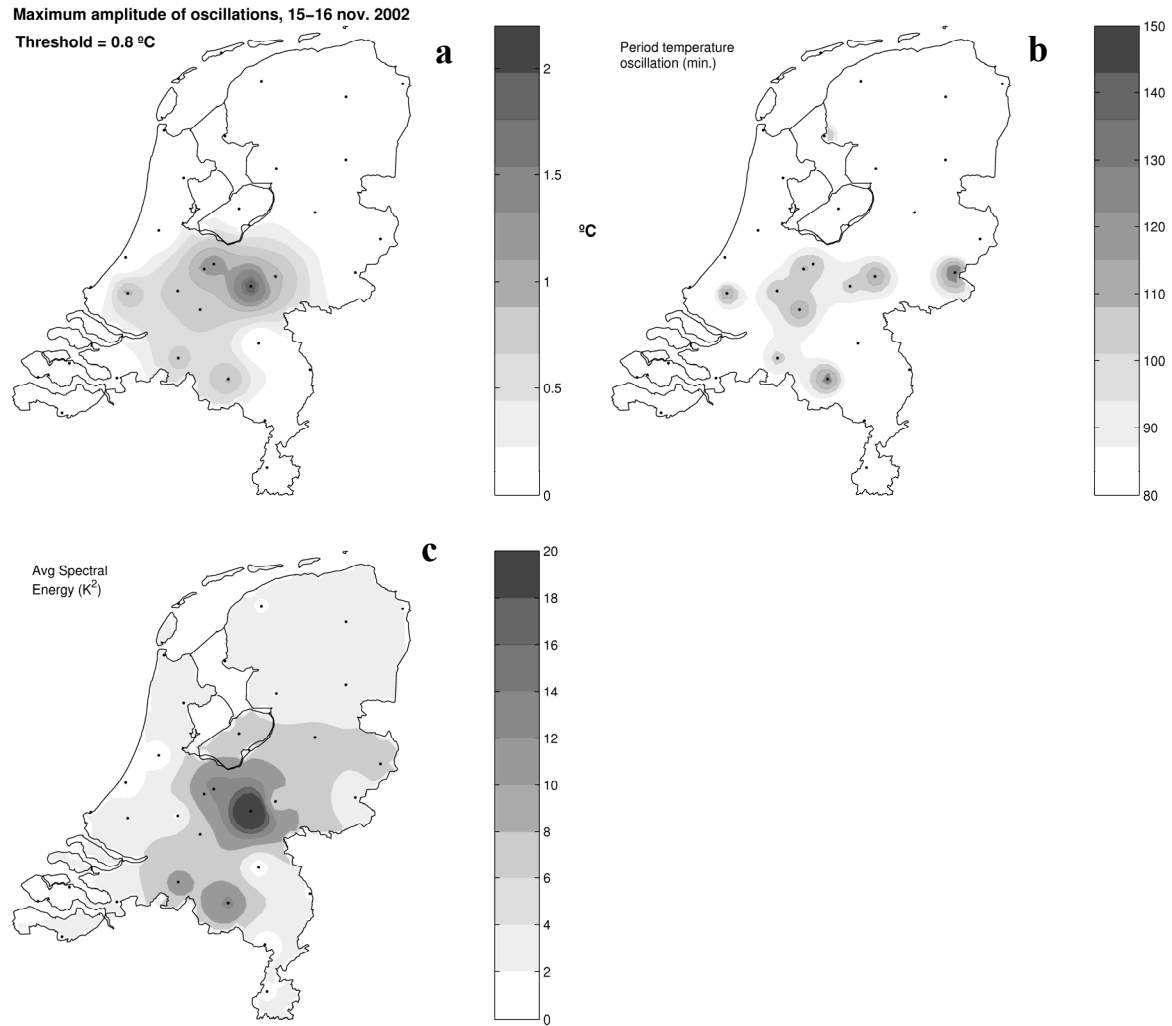
Figure 9.3: Contour plots of number of observed oscillations per station with 0.8 K as threshold anomaly (a), spectral energy (b) and wave period (c).

c) Wavelet analysis

To analyze the results in section b) with a more objective measure, we applied a Morlet wavelet analysis on the temperature observations (Torrence and Compo, 1998). To summarize the information stored in the observed variance, Fig. 9.3c shows the integrated variance between 1800 UTC and 2200 UTC over the time scales between 0 and 160 minutes (nearly 3 hours) for each stations. In this manner, we dismiss the high frequent transition form day to night and the high frequent temperature change due to incoming clouds. The spatial development of the time integrated temperature variance clearly shows that this method confirms the results from section b). In this case, intermittency is seen in a larger area than by Kurzeja and Weber (1991) who found intermittency in an at least 30 x 30 km area.

To summarize, global intermittency can occur over large spatial scales (here at least 100 x 100 km). Unfortunately, we cannot identify the physical source of the oscillations. Local observations at the Wageningen field indicate the Businger mechanism as a possible mechanism. However, because we can translate the oscillation to De Bilt and Soesterberg, and because we also found that the phenomenon travels (phase speed about 10 ms^{-1}, not shown) faster than the

typical wind speed (2 ms^{-1}), we also have strong indication that a wave motion may initiates the oscillations. This is supported by the scintillometer signal at the Wageningen field: during cold period the scintillometer shows enhanced signal, indicating 'noise' in the atmosphere, while we expect a weak signal due to weak turbulence according to the Businger mechanism. Mesoscale model calculations also indicate oscillations, concentrated at about 200 m AGL, but not at the surface.

9.2.2 Intermittency and oscillations in column models

Apart from the observational aspect of intermittent turbulence, the modeling part is also interesting. Van de Wiel et al., 2002 built a bulk model for the SBL that showed periodic oscillations of surface temperature, and turbulent fluxes. In addition, they were able to predict periodic oscillations of the wind speed and temperature. Because the model is a highly simplified representation of the real stable boundary layer, it is tempting to test whether the sophisticated column model in Chapters 2 and 3 is able to reproduce this intermittency, with similar periodicity, amplitude and for similar parameter range. It is expected that the column model with more vertical resolution will give a more realistic representation of stable boundary layer.

As an illustration, we have run a case study as inspired in Van de Wiel et al. (2002) for an initially neutrally stratified boundary layer. This boundary layer is cooled at the surface due to net outgoing long-wave radiation (parameterized similarly as in van de Wiel et al., 2002). Fig. 9.4a shows the modeled time series of surface vegetation temperature, for different vertical resolution in the atmosphere. It is clear that coarse model resolution supports the occurrence of oscillations in the model. For finer model resolution, the amplitude of the oscillations decreases and the frequency increases. Note that the model results were approximately similar in the case radiation divergence was applied (not shown). Fig. 9.4b also shows that the degree of intermittency depends on the resolution in the soil and roughness length. The current findings illustrate that column models are able to produce intermittency. However, its strong dependency on resolution raises the question whether this is a physical or a numerical issue. It is clear that intermittency is still an unresolved problem. On the other hand, the presented analysis with a 1D model does not necessarily invalidate the hypothesized mechanism (Businger, 1973, Van de Wiel, 2002) itself, because the 1-D model is not a true turbulence model. Moreover, it is well possible that the simple description of the turbulence by a gradient approach (in both van de Wiel et al., 2002 and the current model) is not able to capture the full dynamics of the turbulence collapse and consequent recoupling.
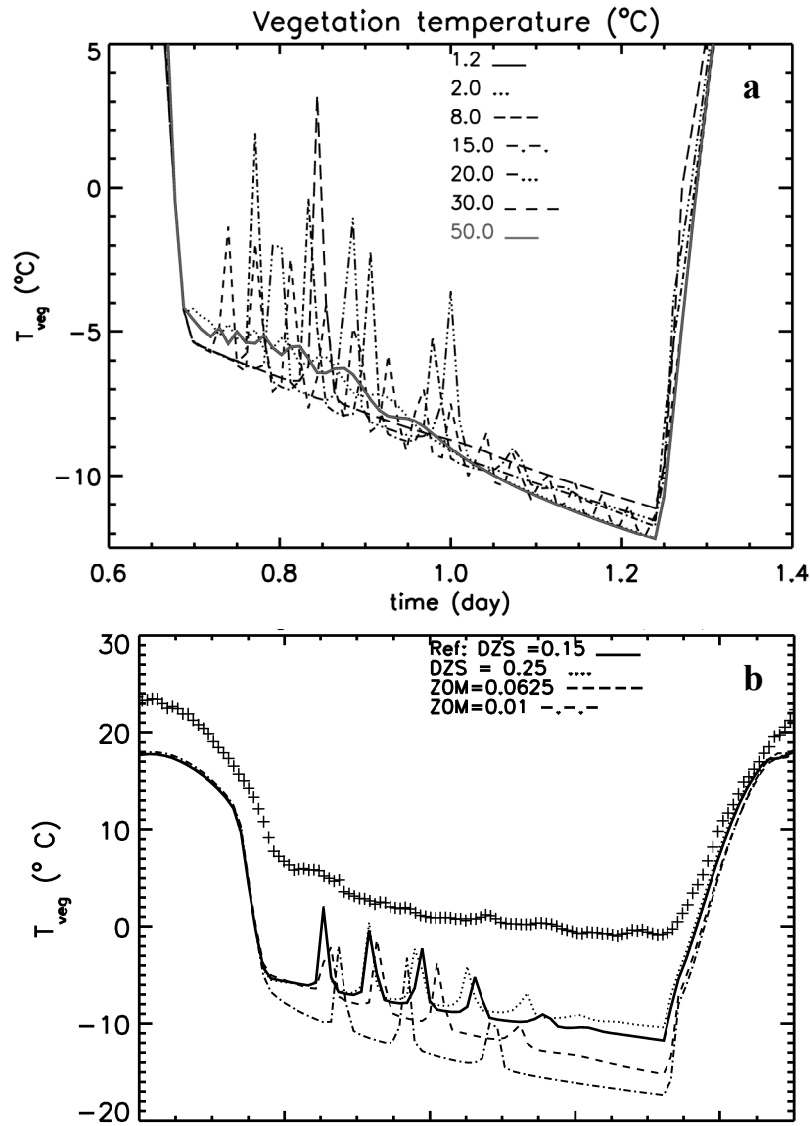
Figure 9.4: Time series of modelled vegetation surface temperature, as function of atmospheric resolution in cm. (a), roughness length ($Z0_M$) and resolution in the soil (*DZS*) (b).

9.2.3 Collapse of turbulence

Turbulence intensity of flows are generally supported by wind shear, and inhibited by rotation and stratification. As stratification increases, the buoyancy destruction of turbulence enlarges and reduces the turbulent kinetic energy. In the end, the turbulence can die out totally. Both from a physical point of view, and for practical considerations, it is highly interesting to be able to predict this collapse of the turbulence. Recently, van de Wiel et al. (2007) derived a criterion that predicts the collapse of turbulence for an irrotational idealized laboratory flow. The criterion depends on z_0/h and h/L, which is new with respect to the current proposals in the literature. The next step is to translate those findings from an idealized flow to the atmospheric boundary layer, and test its applicability on field observations (Van de Wiel et al., 2007).

169

9.2.4 Transition periods

Since the representation of the diurnal cycle in weather forecast and climate models is rather poor at the moment, it gets more and more attention in recent studies. The transitions hours are an important period for the diurnal cycle since it governs the die-out and start of turbulence intensity. From several model intercomparison studies, it became clear the day night transition and the night-day transition are both not very well captured by the models. In addition, only a small amount of papers report on those transitions appeared in the literature (Angevine et al., 2001 and Lapworth, 2006; Pino et al., 2006). Those studies found a predominant effect of entrainment for the boundary-layer development in the early morning.

9.2.5 Model intercomparison: How to proceed?

In the recent years, many stable boundary-layer mixing formulations have been tested and compared against Large Eddy Simulation models in the GEWEX-Atmospheric Boundary Layer Study (Beare et al., 2006; Cuxart et al. 2006, Svensson and Holtslag, 2006). From these studies, we learn that operational models mix the boundary layer over a too deep layer. This mixing is caused by the requirements at the large scale: filling of cyclones is too small. Furthermore, we learn that model output strongly diverges even with the most simple (nearly academic) case description as in the first intercomparison.

LES models in general reproduce local scaling as observed in a series of field studies (Beare et al., 2006). In addition, even for the weakly SBL LES models are sensitive to model resolution (at least 2 m is necessary) and subgrid closure type (Beare and MacVean, 2004). Especially the second GABLS study reveals a strong anomalous behaviour of models during the transitions hours between day and night (and v.v.). See also Edwards et al. (2006), and the observational studies by Angevine et al. (2000) and Lapworth (2006).

An important aspect for future intercomparison studies is the specification of the boundary conditions. Until now, boundary conditions (surface temperature and geostrophic wind speed) in the referred studies were chosen independently (for simplicity). However, Holtslag et al. (2007) illustrate that the variability of the forecasted boundary layer mean profiles in an intercomparison study *not only* depends on the parameterization. They showed spurious variability can occur if the specification of the surface temperature and geostrophic wind speed are not consistent. In reality the only external forcing parameters for the SBL are the net long-wave cooling and the geostrophic wind. The use of a surface energy budget equation prevents that models enter a regime where the surface temperature and the geostrophic wind do not physically match.

Future model intercomparison studies might consider the following aspects of the SBL. At first, a new case study based on much stronger inversion could be proposed, e.g. a so-called long-lived boundary layer (Zilitinkevich et al., 2002). It is well known that for this SBL type, large-scale models encounter evident problems for the surface temperature forecast (e.g. the Nordic Temperature Problem in HIRLAM). In addition, turbulence is not the dominant physi-

cal process for such a case. This requires understanding of these additional physical processes, and their representation in models. Valid measurement stations for these boundary layers are located in Halley (Antarctica), and Sodankylä (Finland, Joffre et al., 2001).

Since radiative transfer is important for very stable boundary layers, an intercomparison study for radiative transfer models would be a fruitful second track. The intercomparisons on this type of models and calibrations currently focus on the atmospheric cooling rates in the lowest 20 km of the atmosphere. From this point of view the shallow SBL can be easily overlooked, whereas radiative cooling can be the dominant process for calm nights.

A third future track is the further intercomparison of 3D models, e.g. mesoscale models such as MM5, WRF, HIRLAM, RAMS, ARPS, MESO-NH. This track can be fruitful since the main problem occurs typically for 3D models, and not for LES nor single-column models. Steeneveld et al. (2007, Chapter 4) addresses this subject by comparing different turbulence and radiation schemes in the mesoscale model MM5 for a case study on CASES-99 observations. An additional advantage of this approach is that the boundary conditions for the SBL are independently calculated by each mesoscale model, and thus always met the conditions discussed in Holtslag et al. (2007). Finally, this approach is beneficial to understand how the different parameterization schemes (i.e. for turbulence, land-surface, radiation, gravity waves) act together.

References

Aalto, T., J. Hatakka, U. Karstens, M. Aurela, T. Thum, and A. Lohila, 2006: Modeling atmospheric CO_2 concentration profiles and fluxes above sloping terrain at a boreal site. *Atmos. Chem. Phys.*, **6**, 303-314.

Acevedo, O. C., and D. R. Fitzjarrald, 2001: The early evening surface layer transition: temporal and spatial variability. *J. Atmos. Sci.*, **58**, 2650-2667.

Akima, H., 1970: A New method of Interpolation and Smooth Curve Fitting Based on Local Procedures. *J. Assc. Comp. Mach.*, **17**, 589-602.

André, J.C., 1983: On the variability of the nocturnal boundary-layer height. *J. Atmos. Sci.*, **40**, 2309-2311.

André J.C., and L. Mahrt, 1982: The nocturnal surface inversion and influence of clear-air radiative cooling. *J. Atmos. Sci.*, **39**, 864-878.

Andreas, E.L., 2002: Parameterizing scalar transfer over snow and ice: a review. *J. Hydrometeor.*, **3**, 417-432.

Andreas, E.L., and B.B. Hicks, 2002: Comments on "Critical Test of the Validity of Monin-Obukhov Similarity during Convective Conditions". *J. Atmos. Sci.*, **59**, 2605-2607.

Anfossi, D., P. Bacci, and A. Longhetto, 1976: Forecasting of vertical temperature profiles in the atmosphere during nocturnal radiation inversions form air temperature trend at screen height. *Quart. J. Roy. Meteor. Soc.*, **102**, 173-180.

Angevine, W.M., H. Klein Baltink, and F.C. Bosveld, 2001: Observations of the morning transition of the convective boundary layer. *Bound.-Layer Meteor.*, **101**, 209-227.

Arya, S.P.S., 1981: Parameterizing the height of the stable atmospheric boundary layer. *J. Appl. Meteor.*, **20**, 1192-1202.

Baas, P., G.J. Steeneveld, B.J.H. van de Wiel, and A.A.M. Holtslag, 2006: Exploring Self-correlation in Flux-Gradient Relationships for Stably Stratified Conditions. *J. Atmos. Sci.*, **63**, 3045-3054.

Balsey, B., R.G. Frehlich, M.L. Jensen, Y. Meilleir, and A. Muschinski, 2003: Extreme gradients in the nocturnal boundary layer: Structure, Evolution and Potential Causes. *J. Atmos. Sci.*, **60**, 2496-2508.

Bannon, P.R, and J.A. Yuhas, 1990: On Mountain Wave drag over Complex Terrain. *Meteor. Atmos. Phys.*, **43**,155-162.

Banta, R.M., R.K. Newsom, J.K. Lundquist, Y.L. Pichugina, R.L. Coulter, and L. Mahrt, 2002: Nocturnal Low-level Jet Characteristics over Kansas during CASES-99. *Bound.-Layer Meteor.*, **105**, 221-252.

Basu, S., and N. Raghavan, 1986: Prediction of inversion strengths and heights from a 1-D nocturnal boundary layer model. *Bound.-Layer Meteor.*, **35**, 193-204.

Beare, R.J., and M.K. MacVean, 2004: Resolution sensitivity and scaling of large-eddy simulations of the stable boundary-layer. *Bound.-Layer Meteor.*, **112**, 257-281.

Beare, R.J., M.K. MacVean, A.A.M. Holtslag, J. Cuxart, I. Esau, J.C. Golaz, M.A. Jiménez, M. Khairoutdinov, B. Kosovic, D. Lewellen, T.S. Lund, J.K. Lundquist, A. McCabe, A.F. Moene, Y. Noh, S. Raasch, and P.P. Sullivan, 2006: An intercomparison of Large-eddy simulations in the stable boundary-layer. *Bound.-Layer Meteor.,* **118**, 247-272.

Belcher, S.E., and N. Wood, 1996: Form and wave drag due to stably stratified flow over low ridges. *Quart. J. Roy. Meteor. Soc.*, **122**, 863-902.

Beljaars, A.C.M., 1995: The impact of some aspects of the boundary layer scheme in the ECMWF model. Parameterization of sub-grid scale physical processes, Seminar proceedings 5-9 September at ECMWF, 125-161.

Beljaars, A., 2001: Issues in boundary layer parameterization for large scale models, *Seminar on Key issues in the parametrization of subgrid physical processes*, 3-7 September 2001, ECMWF, Reading, United Kingdom, p71-87.

Beljaars, A.C.M., and P. Viterbo, 1998: Role of the boundary layer in a numerical weather prediction model, in *Clear and Cloudy boundary layers*, A.A.M. Holtslag and P.G. Duynkerke Eds, Royal Netherlands Academy of Arts and Sciences, Amsterdam, 372pp.

Beljaars, A.C.M., and A.A.M. Holtslag, 1991: Flux parameterization over land surfaces for atmospheric models. *J. Appl. Meteor.*, **30**, 327-341.

Beljaars, A.C.M., and F.C. Bosveld, 1997: Cabauw Data for Validation of Land Surface Parametrization Schemes. *J. Climate*, **10**, 1172-1193.

Beljaars, A.C.M., and P. Viterbo, 1998: Role of the boundary layer in a numerical weather prediction model, in *Clear and Cloudy boundary layers*, A.A.M. Holtslag and P.G. Duynkerke Eds., Royal Netherlands Academy of Arts and Sciences, Amsterdam, 372 pp.

Beljaars, A.C.M., A.R. Brown, and N. Wood, 2004: A new parameterization of turbulent orographic form drag. *Quart. J. Roy. Meteor. Soc.,* **130**, 1327-1347.

Benkley, C.W., and L.L. Schulman, 1979: Estimating Hourly Mixing Depths from Historical Meteorological Data. *J. Appl. Meteor.*, **18**, 772-780.

Berg, L.K., and S. Zhong, 2005: Sensitivity of MM5 Simulated Boundary-Layer Characteristics to Turbulence Parameterization. *J. Appl. Meteor.*, **44**, 1467-1483.

Best, M.J., 1998: A model to predict surface temperatures. *Bound.-Layer Meteor.* **88**, 279-306.

Betts, A.K., 2001: The diurnal cycle over land, *Seminar on Key issues in the parametrization of subgrid physical processes*, 3-7 September 2001, ECMWF, Reading, United Kingdom, p289-304.

Betts, A.K., P. Viterbo, and A.C.M. Beljaars, 1998: Comparison of the Land-Surface Interaction in the ECMWF Reanalysis Model with the 1987 FIFE Data. *Mon. Wea. Rev.*, **126**, 186-198.

Beyrich, F., 1994: Sodar observations of the stable boundary-layer height in relation to the nocturnal low-level jet. *Meteor. Z.*, **3**, 29-34.

Beyrich, F., 1997: Mixing height estimation from sodar data- a critical discussion. *Atmos. Environ.*, **31**, 3941-3953.

Beyrich, F., and V. Kotroni, 1993: Estimation of Surface Stress over a Forest from Sodar measurements and its use to parameterize the stable boundary layer height. *Bound.-Layer Meteor.*, **66**, 93-103.

Beyrich, F., H. A. R. De Bruin, W. M. L. Meijninger, J. W. Schipper, and H. Lohse, 2002: Results from One-Year Continuous Operation of a Large Aperture Scintillometer over a Heterogeneous Land Surface. *Bound.-Layer Meteor.,* **105**, 85-97.

Bony, S. and co-authors, 2006: How well do we understand and evaluate climate change feedback processes? *J. Climate*, **19**, 3445-3482.

Braun, S.A., and W.K. Tao, 2000: Sensitivity of high-resolution simulations of hurricane Bob (1991) to planetary boundary layer parameterizations. *Mon.Wea.Rev.*, **128**, 3941-3961.

Bretherton, F.P., 1969: Waves and turbulence in stably stratified fluids, *Radio. Sci.*, **4**, 1279-1287.

Bright, D.R., and S.L. Mullen, 2002: The Sensitivity of the Numerical of the Southwest Monsoon Boundary Layer to the Choice of PBL Turbulence Parameterization in MM5. *Wea. Forecasting*, **17**, 99-114.

Bromwich, D.H., J.J. Cassano, T. Klein, G. Heinemann, K.M. Hines, K. Steffen, and J.E. Box, 2001: Mesoscale modeling of katabatic winds over Greenland with polar MM5. *Mon. Wea. Rev.*, **129**, 2290-2309.

Brost, R.A., and Wyngaard, J.C., 1978: A Model Study of the Stably Stratified Planetary Boundary layer. *J. Atmos. Sci.* **35**, 1427-1440.

Brown, A.R., and A.L.M. Grant, 1997: Non-Local Mixing of Momentum in the Convective Boundary Layer. *Bound.-Layer Meteor.*, **84**, 1-22.

Brown, A.R, and N. Wood, 2001: Turbulent form drag on anisotropic three-dimensional orography. *Bound.-Layer Meteor.*, **101**, 229-241.

Brown, A.R, and N. Wood, 2003: Properties and Parameterization of the Stable Boundary Layer over Moderate Topography. *J. Atmos. Sci.*, **60**, 2797-2808.

Brown, A.R., M. Athanassiadou, and N. Wood, 2003: Topographically induced waves within the stable boundary layer. *Quart. J. Roy. Meteor. Soc.,* **129**, 3357-3370.

Brown, A.R., A.C.M. Beljaars, H. Hersbach, A. Hollingsworth, M. Miller, and D. Vasiljevic, 2005: Wind turning across the marine atmospheric boundary layer. *Quart. J. Roy. Meteor. Soc.,* **131**, 1233-1250.

Bruin, H.A.R. de, 1994: Analytic solutions of the equations governing the temperature fluctuation method. *Bound.-Layer Meteor.,* **68**, 427-432.

Burk, S. D., and W. T. Thompson, 1989: Vertically nested regional numerical weather prediction model with second-order closure physics. *Mon. Wea. Rev.*, **117**, 2305-2324.

Businger, J.A., J.C. Wyngaard, Y. Izumi, and E.F. Bradley, 1971: Flux profile Relationships in the Atmospheric Surface Layer. *J. Atmos. Sci*, **28**, 181-189.

Carlson, M., and R.B. Stull, 1986: Subsidence in the Nocturnal Boundary layer. *J. Clim. Appl. Meteor.*, **25**, 1088-1099.

Carson, D.J., and P.J.R. Richards, 1978: Modelling surface turbulent fluxes in stable conditions. *Bound.-Layer Meteor.*, **14**, 67-81.

Cassano, J. J., T.R. Parish, and J.C. King, 2001: Evaluation of Turbulent Surface Flux Parameterizations for the Stable Surface Layer over Halley, Antarctica. *Mon. Wea. Rev*, **129**, 26-46.

Caughey, S.J., J.C. Wyngaard, and J.C. Kaimal, 1979: Turbulence in the evolving stable boundary layer. *J. Atmos. Sci.*, **36**, 1041-1052.

Cheinet, S., A. Beljaars, M. Kohler, J-J. Morcrette, and P. Viterbo, 2005: *Assessing Physical processes in the ECMWF Model Forecasts using the ARM SCP Observations*, ECMWF-ARM Report Series, ECMWF Tech. Memo. No 1, 25pp.

Cerni, T.A., and T.R. Parish, 1984: A Radiative Model of the Stable Nocturnal Boundary Layer with Application to the Polar Night. *J. Clim. Appl. Meteor.*, **23**, 1563-1572.

Chen, F., and J. Dudhia, 2001: Coupling an Advanced Land Surface–Hydrology Model with the Penn State–NCAR MM5 Modeling System. Part II: Preliminary Model Validation. *Mon Wea Rev.*, **129**, 587–604.

Chen, Y., F. L. Ludwig, and R. L. Street, 2004: Stably Stratified Flows near a Notched Transverse Ridge across the Salt Lake Valley. *J. Appl. Meteor.*, **43**, 1308–1328.

Cheng, W., M.B. Parlange, and W. Brutsaert, 2005: Pathology of Monin-Obukhov similarity in the stable boundary layer. *J. Geophys. Res.*, **110**, D06101, doi:10.129/2004JD004923

Chimonas, G., and C.J. Nappo, 1989: Wave drag in the planetary boundary layer over complex terrain. *Bound.-Layer Meteor.*, **47**, 217-232.

Coulter, R.L., and J.C. Doran, 2002: Spatial and temporal occurrences of intermittent turbulence during CASES-99. *Bound.-Layer Meteor.,* **105**, 329-349.

Couvreux, F., F. Guichard, J.-L. Redelsperger, C. Kiemle, V. Masson, J.-P. Lafore, and C. Flamant, 2005: Water-vapour variability within a convective boundary-layer assessed by large-eddy simulations and IHOP-2002 observations. *Quart. J. Roy. Meteor. Soc.*, **131**, 2665-2693.

Cuxart, J., and M.A. Jiménez, 2007: Mixing Proceses in a Nocturnal Low-Level Jet, an LES study. *J. Atmos. Sci.*, **64**, 1666-1679.

Cuxart, J., C. Yagüe, G. Morales, E. Terradellas, J. Orbe, J. Calvo, A. Fernández, M.R. Soler, C. Infante, P. Buenestado, A. Espinalt, H.E. Joergensen, J.M. Rees, J. Vilà, J.M. Redondo, I.R. Cantalapiedra, and L. Conangla, 2000: Stable Atmospheric Boundary-Layer Experiment in Spain (SABLES 98): A Report. *Bound.-Layer Meteor.,* **96**, 337-370.

Cuxart, J., A.A.M. Holtslag, R.J. Beare, E. Bazile, A.C.M. Beljaars, A. Cheng, L. Conangla, M. Ek, F. Freedman, R. Hamdi, A. Kerstein, H. Kitagawa, G. Lenderink, D. Lewellen, J. Mailhot, T. Mauritsen, V. Perov, G. Schayes, G.J. Steeneveld, G. Svensson, P.A. Taylor, W. Weng, S. Wunsch, and K-M. Xu, 2006: A single-column model intercomparison for a stably stratified atmospheric boundary layer. *Bound.-Layer Meteor.,* **118**, 273-303.

Deardorff, J.W, 1978: Efficient Prediction of Ground Surface Temperature and Moisture with Inclusion of a Layer of Vegetation. *J. Geophys. Res.*, **83**, 1889-1903.

Delage, Y., 1974: A Numerical Study of the Nocturnal Atmospheric Boundary Layer. *Quart. J. Roy. Meteor. Soc.,* **100**, 351-364.

Delage, Y., 1988: A Parameterization of the Stable Atmospheric Boundary Layer. *Bound.-Layer Meteor.*, **43**, 365-381.

Delage, Y., 1997: Parameterising sub-grid scale vertical transport in atmospheric models under statically stable conditions. *Bound.-Layer Meteor.* **82**, 23-48.

Delage, Y., P.A. Barlett, and J.H. McCauchy, 2002: Study of 'soft' night time surface layer decoupling over forest canopies in a land-surface model. *Bound.-LayerMeteor.*, **103**, 253-276.

Derbyshire, S.H., 1995: Stable boundary-layer modelling: established approaches and beyond. *Bound.-Layer Meteor.*, **90**, 423-446.

Derbyshire, S.H., 1999: Boundary-layer decoupling over cold surfaces as a physical boundary instability. *Bound.-Layer Meteor.* **90**, 297-325.

Dudhia J., 1989: Numerical study of convection observed during the winter monsoon experiment using a mesoscale two-dimensional model. *J. Atmos. Sci.*, **46**, 3077-3107.

Dudhia, J., and J. F. Bresch, 2002: A global version of the PSU-NCAR mesoscale model. *Mon. Wea. Rev.*, **130**, 2989-3007.

Dudhia, J., D. Gill, Y.R. Guo, K. Manning, W. Wang, and J. Chiszar, 2000: PSU/NCAR Mesoscale Modelling System Tutorial Class Notes and User's Guide: MM5 Modelling System Version 3. Tech. Rep., National Center for Atmospheric Research Boulder, CO, 138 pp. http://www.mmm.ucar.edu/mm5/documents/.

Duynkerke, P.G., 1991: Radiation fog: A comparison of model simulation with detailed observations. *Mon. Wea. Rev.* **119**, 324-341.

Duynkerke, P.G., 1999: Turbulence, radiation and fog in Dutch stable boundary-layers. *Bound.-Layer Meteor.* **90**, 447-477.

Duynkerke, P.G., and S. de Roode, 2001: Surface energy balance and turbulence characteristics observed at the SHEBA Ice Camp during FIRE III. *J. Geophys. Res.*, **106**, D4, 15313-15322.

Dyer, A.J., 1974: A Review of Flux-Profile Relationships. *Bound.-Layer Meteor.*, **7**, 363-372.

Edwards, J.M., R.J. Beare, and A.J. Lapworth, 2006: Simulation of the observed evening transition and nocturnal boundary layers: Single Column Modelling. *Quart. J. Roy. Meteor. Soc.,* **132**, 61-80.

Einaudi, F., and J.J. Finnigan, 1981: The interaction between an internal gravity waves and the planetary boundary layer. Part I: The linear analysis, *Quart. J. Roy. Meteor. Soc.*, **107**, 793-806.

Einaudi, F., D.P. Lalas, and G.E. Perona, 1978: The Role of Gravity Waves in Troposheric Processes. *Pure and Applied Geophysics*, **117**, 627-663.

Ek, M.B., K.E. Mitchell, Y. Lin, E. Rogers, P. Grunmann, V. Koren, G. Gayno, and J.D. Tarpley, 2003, Implementation of the Noah land surface model advances in the National Cen-

ters for Environmental Prediction operational mesoscale Eta model. *J. Geophys. Res*, **108** (D22), 8851, doi:10.1029/2002JD003296.

Esau, I., 2004: Simulation of Ekman boundary layers by large eddy model with dynamic mixed sub-filter closure. *Env. Fluid Mech.*, **4**, 273-303.

Estournel, C., and D. Guedalia, 1985: Influence of geostrophic wind on atmospheric nocturnal cooling. *J. Atmos. Sci.*, **42**, 2695-2698.

Estournel, C., and D. Guedalia, 1987: A new parameterization of eddy diffusivities for nocturnal boundary-layer modeling. *Bound.-Layer Meteor.*, **39**, 191-203.

Estournel, C., and D. Guedalia, 1990: Improving the diagnostic relation for the nocturnal boundary layer height. *Bound.-Layer Meteor.*, **53**, 191-198.

Fast, J.D., and M. D. McCorcle, 1990: A two-dimensional numerical sensitivity study of the Great Plains low-level jet. *Mon. Wea. Rev.*, **118**, 151-163.

Finnigan, J., 1999: A note on the wave-turbulence interaction and the possibility of scaling the very stable boundary layer. *Bound.-Layer Meteor.*, **90**, 529-539.

Folland, C.K., Karl, T.R., Christy, J.R., Clarke, R.A., Gruza, G.V., Jouzel, J., Mann, M.E., Oerlemans, J., Salinger, M.J. and Wang, S.-W., 2001b: *Observed Climate Variability and Change*. pp. 99-181 In: Climate Change 2001: The Scientific Basis. Contribution of Working Group I to the Third Assessment Report of the Intergovernmental Panel on Climate Change (Houghton, J.T., Ding, Y., Griggs, D.J., Noguer, M., van der Linden, P.J., Dai, X., Maskell, K. and Johnson, C.A. Eds.). Cambridge Univ. Press, Cambridge, UK, 881pp.

Franks, S.W., K.J. Beven, P.F. Quinn, and I.R. Wright, 1997: On the sensitivity of soil-vegetation-atmosphere transfer (SVAT) schemes: equifinality and the problem of robust calibration. *Agric. For. Meteor.*, **86**, 63-75.

Frech, M., and L. Mahrt, 1995: A two-scale mixing formulation for the atmospheric boundary layer. *Bound.-Layer Meteor.*, **73**, 91-104.

Frenzen P., and A.G. Vogel, 2001: Further studies of atmospheric turbulence in layers near the surface: scaling the TKE budget above the roughness sublayer. *Bound.-Layer Meteor.*, **99**, 173-206.

Funk, J.P., 1960: Measured radiative flux divergence near the ground at night. *Quart. J. Roy. Meteor. Soc*, **86**, 382-389.

Galmarini, S., C. Beets, P.G. Duynkerke, and J. Vilà-Guerau de Arellano, 1998: Stable nocturnal boundary-layers: a comparison of one-dimensional and large-eddy simulation models. *Bound.-Layer Meteor.* **88**, 181-210.

Garratt, J.R., 1982: Surface fluxes and the nocturnal boundary layer height. *J. Appl. Meteor.*, **21**, 725-729.

Garratt, J.R., 1985: The Inland Boundary Layer at Low Latitudes, I. The Nocturnal Jet, *Bound.-Layer Meteor.*, **32**, 307-327.

Garratt, J.R., 1992: *The Atmospheric Boundary Layer*, Cambridge Univ. Press, 316 pp.

Garratt, J.R., and R.A. Brost, 1981: Radiative Cooling effects within and above the nocturnal boundary-layer. *J. Atmos. Sci.* **38**, 2730-2746.

Gassmann, M.I., and N.A. Mazzeo, 2001: Nocturnal stable boundary layer height model and its application. *Atmos. Res.*, **57**, 247-259.

Georgelin, M., E. Richard, M. Petitdidier, and A. Druilhet, 1994: Impact of subgrid scale orography parameterization on the simulation of orographic flows. *Mon. Wea. Rev.,* **122,** 1509-1522.

Gopalakrishnan, S.G., M. Sharan, R. T. McNider, and M. P. Singh, 1998: Study of radiative and turbulent processes in the stable boundary layer under weak wind conditions. *J. Atmos. Sci.*, **55**, 954-960.

Gossard, E. E., and W.M. Hooke: 1974, *Waves in the Atmosphere*, Elsevier Sci. Publ. Co., New York.

Grant, A.L.M., 1994: Wind profiles in the stable boundary layer, and the effect of low relief. *Quart. J. Roy. Meteor. Soc.,* **120,** 27-46.

Grisogono, B., 1994: Dissipation of Wave Drag in the Atmospheric Boundary Layer. *J. Atmos. Sci.*, **51**, 1237-1243.

Gryning, S.E., A. A. M. Holtslag, J. S. Irwin, and B. Siversten, 1987: Applied dispersion modelling based on meteorological scaling parameters. *Atmos. Environ.,* **21,** 79-89.

Guichard, F., D.B. Parsons, J. Dudhia, and J. Bresh, 2002: Evaluating mesoscale model prediction of clouds and radiation with SGP ARM data over a seasonal timescale. *Mon. Wea. Rev.*, **131**, 926-944.

Ha, K.J., and L. Mahrt, 2003: Radiative and turbulent fluxes in the nocturnal boundary-layer. *Tellus* **55A**, 317-327.

Halldin (ed.), 1999: *Final Report for WINTEX*, NOPEX Technical Report No. 29,70 pp. (Available from: NOPEX Central Office, Institute of Earth Sciences, Uppsala University, Norbyvägen 18B, SE-75236 Uppsala, Sweden).

Hanna, S.R., and R. Yang, 2001: Evaluation of meso scale models' simulations of near-surface winds, temperature gradients, and mixing depths. *J. Appl. Meteor.*, **40**, 1095-1104.

Harshvardhan, R. Davies, D. Randall, and T. Corsetti, 1987: A fast radiation parameterization for atmospheric circulation models. *J. Geophys. Res.*, **92**, 1009-1016.

Hartogensis, O. K., and H. A. R. de Bruin, 2005: Monin-Obukhov similarity functions of the structure parameter of temperature and turbulent kinetic energy dissipation rate in the stable boundary layer. *Bound.-Layer Meteor.*, **116**, 253-276.

Heusinkveld, B.G., A.F.G. Jacobs, A.A.M. Holtslag, and S.M. Berkowicz, 2003: Surface Energy balance Closure in an Arid Region: Role of Soil Heat Flux. *Agr. For. Meteor.*, **122**, 21-37.

Hicks, R.B., D. Smith, P.J. Irwin, and T. Mathews, 1977: Preliminary studies of atmospheric acoustic sounding at Calgary. *Bound.-Layer Meteor.*, **12**, 201-212.

Hodur, R.M., 1997: The Naval Research Laboratory coupled ocean/atmosphere mesoscale prediction system. *Mon. Wea. Rev.*, **125**, 1414-1430.

Holden, J.J., S.H. Derbyshire, and S.E. Belcher, 2000: Tethered balloon observations of the nocturnal stable boundary layer in a valley. *Bound.-Layer Meteor.*, **97**, 1-24.

Holtslag, A.A.M, 1998: Modeling of atmospheric boundary layers, in *Clear and Cloudy boundary layers*, A.A.M. Holtslag and P.G. Duynkerke Eds., Royal Netherlands Academy of Arts and Sciences, Amsterdam, 372 pp.

Holtslag, A. A. M., 2003: GABLS initiates intercomparison for stable boundary layer case. *GEWEX News*, **13** (2), 7-8.

Holtslag, A.A.M., 2006: Special issue for boundary-layer meteorology: GEWEX Atmospheric Boundary-Layer Study (GABLS) on stable boundary layers. *Bound.-Layer Meteor.*, **118**, 243-246.

Holtslag, A.A.M., and B.A. Boville, 1993: Local Versus Nonlocal Boundary-Layer Diffusion in a Global Climate Model. *J. Climate* **6**, 1825-1842.

Holtslag A.A.M., and F.T.M. Nieuwstadt, 1986: Scaling the Atmospheric Boundary Layer. *ound.-Layer Meteor.*, **36**, 201-209.

Holtslag, A.A.M., and Bruin, H.A.R. de, 1988: Applied modelling of the nighttime surface energy balance over land. *J. Appl. Meteor.* **27**, 689-704.

Holtslag, A. A. M., R. J. Beare, and J. Cuxart Rodamillans, 2003: GABLS workshop on stable boundary layers. *GEWEX News*, **13** (4), 11-13.

Holtslag, A.A.M., E. van Meijgaard, and W.C. de Rooy, 1995: A comparison of boundary layer diffusion schemes in unstable conditions over land. *Bound.-Layer Meteor.*, **76**, 69-95.

Holtslag, A.A.M., G.J. Steeneveld, and B.J.H. van de Wiel, 2007: Role of land-surface feedback on model performance for the stable boundary layer, *Bound.-Layer. Meteor.*, in press.

Hong, S.Y., and H.L. Pan, 1996: Nonlocal boundary layer vertical diffusion in a Medium-Range Forecast model. *Mon. Wea. Rev.*, **124**, 2322-2339.

Howell, J.F., and J. Sun, 1999: Surface-Layer Fluxes in Stable Conditions. *Bound.-Layer Meteor.*, **90**, 495-520.

Hunt, J.C.R., J.C. Kaimal, and J.E. Gaynor, 1985: Some observations of turbulence structure in stable layers. *Quart. J. Roy. Meteor. Soc.*, **111**, 793-815.

Jacobs, A.F.G., B.G. Heusinkveld, and A.A.M. Holtslag, 2003: Carbon dioxide and water vapour flux densities over a grassland area in the Netherlands, *Int. J. Clim.*, **23**, 1663-1675.

Janjić, Z.I., 1990: The step-mountain Coordinate: Physical Package. *Mon. Wea. Rev.*, **118**, 1429-1443.

Jiang, Q., J.D. Doyle, and Ronald, B. Smith, 2006: Interaction between Trapped Waves and Boundary Layers, *J. Atmos. Sci.*, **63**, 617-633.

Joffre, S.M., M. Kangas, M. Heikinheimo, and S.A. Kitaigorodskii, 2001: Variability of the stable and unstable boundary layer height and its scales over a boreal forest. *Bound.-Layer Meteor.*, **99**, 429-450.

Joffre S., and M. Kangas, 2002: Determination and scaling of the atmospheric boundary layer height under various stability conditions over a rough surface. In: Rotach M., Fisher B., Piringer M. (Eds.), COST *Action 715 Workshop on Urban Boundary Layer Parameterisations*, Zurich, 24-25 May 2001. Office for Official Publications of the European Communities, EUR 20355, pp. 111-118.

Johansson, C, A. Smedman, U. Högström, J.G. Brasseur and S. Khanna, 2001: Critical Test of the Validity of Monin-Obukhov Similarity during Convective Conditions. *J. Atmos. Sci*, **58**, 1549-1566.

Kain J. S., and J. M. Fritsch, 1993: Convective parameterization for mesoscale models: The Kain–Fritsch scheme. The Representation of Cumulus Convection in Numerical Models. *Meteor. Monogr.*, **24**, Amer. Meteor. Soc., 165-170.

Karppinen, A., S. Joffre, J. Kukkonen, and P. Bremer, 2001: Evaluation of inversion strengths and mixing heights during extremely stable atmospheric stratification. *Int. J. Environment and Pollution*, **16**, No 1-6, 1-11.

Kiehl, J.T, J. J. Hack, G. B. Bonan, B. A. Boville, D. L. Williamson, and P. J. Rasch, 1998: The National Center for Atmospheric Research Community Climate Model: CCM3. *J. Climate*, **11**, 1131-1149.

Kim, J., and L. Mahrt, 1992: Momentum transport by gravity waves. *J. Atmos. Sci.*, **49**, 735-748.

King, J.C., and W.M. Connolley, 1997: Validation of the surface energy balance over the Arctic Ice sheets in the U.K. Meteorological Office unified climate model. *J. Climate*, **10**, 1273-1287.

King, J.C., W.M. Connolley, and S.H. Derbyshire, 2001: Sensitivity of modelled Antarctic climate to surface flux and boundary-layer flux parameterizations. *Quart. J. Roy. Meteor. Soc.,* **127**, 779-794.

King, J.C., A. Jrrar, and W.M. Connolly, 2007: Sensitivity of modelled atmospheric circulation to the representation of the stable boundary layer processes. *Geophys. Res. Lett.*, **34**, L06708, doi: 10.1029/2006/GL028563.

Kitaigorodskii, S.A., and S. Joffre, 1988: In search of a simple scaling for the height of the stratified atmospheric boundary layer. *Tellus,* **40A**, 419-433.

Klipp, C.L., and L. Mahrt, 2004: Flux-gradient relationship, self-correlation and intermittency in the stable boundary layer. *Quart. J.Roy. Meteor. Soc.,* **130**, 2087-2103.

Koivusalo, H., Heikinheimo, M., and Karvonen, T., 2001: Test of a simple two-layer parameterisation to simulate the energy balance and temperature of a snow pack. *Theor. Appl. Climatol.* **70**, 65-79.

Kondo, J., O. Kanechika, and N. Yasuda: 1978, Heat and Momentum Transfers under Strong Stability in the Atmospheric Surface Layer. *J. Atmos. Sci.*, **35**, 1012-1021.

Koracin, D., and R. Berkowicz, 1988: Nocturnal boundary-layer height: observations by acoustic sounders and prediction in terms of surface-layer parameters. *Bound.-Layer Meteor.*, **43**, 65-83.

Kosovic, B., and J.A. Curry, 2000: A Large Eddy Simulation study of a quasi-steady, stably stratified atmospheric boundary-layer. *J. Atmos. Sci.*, **57**, 1052-1068.

Kosovic, B., and J.K. Lundquist, 2004: Influences on the height of the stable boundary layer, *16th Symposium on Boundary-layer and Turbulence*, Portland, Maine, U.S.A., 9-13 Aug. 2004, Amer. Meteorol. Soc., Boston, p. 4.20.

Kot, S.C., and Y. Song, 1998: An improvement of the Louis scheme for the surface layer in an atmospheric modeling system. *Bound.-Layer Meteor.*, **88**, 239-254.

Kurzeja, R.J., S. Berman, and A.H. Weber, 1991: A climatological study of the nocturnal planetary boundary layer. *Bound.-Layer Meteor.*, **105**, 105-128.

Langhaar, H.L., 1951: *Dimensional Analysis and Theory of Models*, Wiley, New York, 166p.

Lapworth, A., 2006: The morning transition of the nocturnal boundary layer. *Bound.-Layer Meteor.*, **119**, 501-526.

Lena, F., and F. Desiato, 1999: Intercomparison of nocturnal mixing height estimate methods for urban air pollution modeling. *Atmos. Environ.* **33**, 2385-2393.

Lenderink, G., and A.A.M. Holtslag, 2004: An updated length-scale formulation for turbulent mixing in clear and cloudy boundary layers. *Quart. J. Roy. Meteor. Soc.*, **130**, 3405-3428.

Lenderink, G., B. Van den Hurk, E. van Meijgaard, A. van Ulden, and H. Cuijpers, 2003: *Simulation of present day climate in RACMO2: First results and model developments*. KNMI Technical report TR-252, 24 p.

Lenschow, D.H., X. S. Li, C.J. Zhu, and B.B. Stankov, 1988: The stably stratified boundary layer over the great plains, I. Mean and Turbulent structure. *Bound.-Layer Meteor.*, **42**, 95-121.

Lott, F., and M.J. Miller, 1997: A new subgrid-scale orographic drag parameterization: Its formulation and testing. *Quart. J. Roy. Meteor. Soc.,* **123**, 101-127.

Louis, J.F., 1979: A parametric model of vertical eddy fluxes in the atmosphere. *Bound.-Layer Meteor.* **17**, 187-202.

Mahrt, L., 1981: Modelling the height of the stable boundary-layer. *Bound.-Layer Meteor.*, **21**, 3-19.

Mahrt, L., 1987: Grid-averaged surface fluxes. *Mon. Wea. Rev.* **115**, 1550-1560.

Mahrt, L., 1998: Stratified atmospheric boundary layers and breakdown of models. *Theo. Comp. Fluid. Phys.*, **11**, 263-279.

Mahrt, L., 1999: Stratified atmospheric boundary layers. *Bound.-Layer Meteor.*, **90**, 375-396.

Mahrt, L., and R.C. Heald, 1979: Comments on "Determining Height of the Nocturnal Boundary Layer". *J. Appl. Meteor.*, **18**, 383.

Mahrt, L., and D. Vickers, 2002: Contrasting vertical structures of nocturnal boundary layers. *Bound.-Layer Meteor.*, **105**, 351-363.

Mahrt, L., J.C. André, and R.C. Heald, 1982: On the height of the nocturnal boundary layer. *J. Appl. Meteor.*, **21**, 90-92.

Mahrt, L., J. Sun, W. Blumen, T. Delany, and S. Oncley, 1998: Nocturnal Boundary-layer re-gimes. *Bound.-Layer Meteor.*, **88**, 255-278.

Mailhot, J., and R. Benoit, 1982: A Finite-Element Model of the Atmospheric Boundary layer Suitable for Use with Numerical Weather Prediction Models. *J. Atmos. Sci.*, **39**, 2249-2266.

Mason, P. J.: 1988, The Formation of Areally-Averaged Roughness Lengths, *Quart. J. Roy. Meteor. Soc.* **114**, 399-420.

Mason P.J., and D.J. Thomson, 1987: Large-eddy simulations of the neutral-static-stability planetary boundary layer. *Quart. J. Roy. Meteor. Soc.,* **113**, 413-443.

McCabe, A., and A.R. Brown, 2006: The role of surface heterogeneity in modelling the stable boundary layer. *Bound.-Layer Meteor.*, **122**, 517-534.

McVehil, G.E, 1964: Wind and Temperature Profiles near the Ground in Stable Stratification. *Quart. J. Roy. Meteor. Soc*, **90**, 136-146.

Melgarejo, J.W., and J.W. Deardorff, 1974: Stability Functions for the Boundary-Layer Resistance Laws Based upon Observed Boundary-Layer Heights. *J. Atmos. Sci.*, **31**, 1324-1333.

Mellor, G.L., and T. Yamada, 1974: A Hierarchy of Turbulence Closure Models for Planetary Boundary Layers. *J. Atmos. Sci.*, **31**, 1791-1806.

Mlawer, E. J., S. J. Taubman, P. D. Brown, M. J. Iacono, and S. A. Clough, 1997: Radiative transfer for inhomogeneous atmospheres: RRTM, a validated correlated-k model for the longwave. *J. Geophys. Res.*, **102** (D14), 16663-16682.

Monti, P., H.J.S. Fernando, M. Princevac, W.C. Chan, T.A. Kowalewski, and E.R. Pardyjak, 2002: Observations of Flow and Turbulence in the Nocturnal Boundary layer over a Slope. *J. Atmos. Sci.*, **59**, 2513-2534.

Musson-Genon, L., 1987: Numerical simulation of a fog event with a one-dimensional boundary layer model. *Mon. Wea. Rev.*, **115**, 592-607.

Nakamura, R., and L. Mahrt, 2006: Vertically integrated sensible-heat budgets for stable nocturnal boundary layers, *Quart. J. Roy. Meteor. Soc.*, **132**, 383-403.

Nappo, C.J., 1991: Sporadic breakdowns of stability in the PBL over simple and complex terrain. *Bound.-Layer Meteor*., **54**, 69-87.

Nappo, C.J., 2002: *An Introduction to Atmospheric Gravity Waves*, Academic Press, London, 276 pp.

Nappo, C.J., and G. Chimonas, 1992: Wave Exchange between the Ground Surface and a Boundary-Layer Critical Level. *J. Atmos. Sci.*, **49**, 1075-1091.

Nappo, C. J., and P.-E. Johansson, 1999: Summary of the Lövånger international workshop on turbulence and diffusion in the stable planetary boundary layer. *Bound.-Layer Meteor.*, **90**, 345-374.

Nappo, C.J., H-Y Chun, and H.J. Lee, 2004: A parameterization of wave stress in the planetary boundary layer for use in mesoscale models. *Atmos. Environ.,* **38**, 2665-2675.

Neu, U., 1995: A parameterisation of the nocturnal ozone reduction in the residual layer by vertical downward mixing during summer smog situations using sodar data. *Bound.-Layer Meteor.*, **73**, 189-193.

Newsom, R.K., and R.M. Banta, 2003: Shear-flow instability in the stable nocturnal boundary layer as observed by Doppler lidar during CASES-99. *J. Atmos. Sci.*, **60**, 16-33.

Nieuwstadt, F.T.M, 1980a: A rate equation for the inversion height in a nocturnal boundary layer. *J. Appl. Meteor.*, **19**, 1445-1447.

Nieuwstadt, F.T.M., 1980b: Some aspects of the turbulent stable boundary layer. *Bound.-Layer Meteor.*, **30**, 31-55.

Nieuwstadt, F.T.M., 1984: The turbulent structure of the stable, nocturnal boundary-layer. *J. Atmos. Sci.* **41**, 2202-2216.

Nieuwstadt, F.T.M., 2005: Direct Numerical Simulations of Stable Channel Flow at Large Stability. *Bound.-Layer Meteor.*, **116**, 277-299.

Nieuwstadt, F.T.M., and A.G.M. Driedonks, 1979: The nocturnal boundary-layer: a case study compared with model calculations. *J. Appl. Meteor.* **18**, 1397-1405.

Nieuwstadt, F. T. M., and H. Tennekes, 1981: A rate equation for the nocturnal boundary-layer height. *J. Atmos. Sci.*, **38**, 1418-1429.

Nieuwstadt, F.T.M., and P.G. Duynkerke, 1996: Turbulence in the atmospheric boundary layer. *Atmos. Res.*, **40**, 111-142.

Nkemdirim, L., 1978: A Comparison of Radiative and Actual Nocturnal Cooling Rates over Grass and Snow. *J. Appl. Meteor.*, **17**, 1643-1646.

Nkemdirim, L., 1988: Nighttime Surface-Layer Temperature Tendencies with and Without Chinooks. *J. Appl. Meteor.*, **27**, 482-489.

Noilhan, J., and S. Planton, 1989: A simple parameterization of land surface processes for meteorological models. *Mon. Wea. Rev.,* **117,** 536-549.

Noilhan, J., and J. F. Mahfouf, 1996: The ISBA land surface parameterisation scheme. *Global and Planetary Change*, **13**, 145-159.

Oke, T.R., 1970: Turbulent Transport Near the Ground in Stable Conditions. *J. Appl. Meteor.*, **9**, 778-786.

Oke, T. R., 1978: *Boundary-layer Climates.* Methuen & Co., London, United Kingdom, 372p.

Oncley, S.P., C.A. Friehe, J.C. Larue, J.A. Businger, E.C. Itsweire, and S.S. Chang, 1996: Surface-Layer Fluxes, Profiles, and Turbulence Measurements over Uniform Terrain under Near Neutral Conditions. *J. Atmos. Sci.*, **53**, 1029-1044.

Palmer, T. N., G. J. Shutts, and R. Swinbank, 1986: Alleviation of a systematic westerly bias in general circulation and numerical weather prediction models through an orographic gravity-wave drag parameterization. *Quart. J. Roy. Meteor. Soc.*, **112**, 1001-1039.

Panofsky, H.A., H. Tennekes, D.H. Lenschow, and J.C. Wyngaard, 1977: The characteristics of turbulent velocity components in the surface layer under convective conditions. *Bound.-Layer Meteor.*, **11**, 355-361.

Parker, D.E., 2004: Large Scale warming is not urban, *Nature*, **432**, 290.

Parker, D.E., 2006: A demonstration that Large-Scale Warming is not Urban, *J. Climate*, **19**, 2882-2894.

Pattantyús-Ábrahám, M., and I.M. Jánosi, 2004: What determines the nocturnal cooling time-scale at 2m? *Geophys. Res. Lett.*, **31**, L05109, doi:10.1029/2003GL019137.

Pattey, E., I.B. Strachan, R.L. Desjardins, and J. Massheder, 2002: Measuring nighttime CO_2 flux over terrestrial ecosystems using eddy covariance and nocturnal boundary layer methods. *Agr. For. Meteor.*, **113**, 145-158.

Pielke, R.A. Sr., and T. Matsui, 2005: Should light wind and windy nights have the same temperature trends at individual levels even if the boundary layer averaged heat content change is the same?, *Geophys. Res. Lett.*, **32**, L21813, doi:10.1029/2005GL024407.

Pino, D., H.J.J. Jonker, and J. Vila-Guerau de Arellano, 2006: Role of shear and the inversion strength during sunset turbulence over land: characteristic length scales, *Bound.-Layer. Meteor.*, **121**, 537-556.

Pollard, R. T., P. B. Rhines, and R.O.R.Y. Thompson, 1973: The deepening of the wind-mixed layer. *Geophys. Fluid Dyn.* **3**, 381-404.

Poulos, G.S., and co-authors, 2002: CASES-99: A comprehensive Investigation of the stable nocturnal boundary layer. *Bull. Am. Met. Soc.*, **83**, 555-581.

Poulos, G.S., and S.P. Burns, 2003: An evaluation of Bulk Ri-Based Surface Layer Flux Formulas for Stable and Very Stable Conditions with Intermittent Turbulence. *J. Atmos. Sci*, **60**, 2523-2537.

Pul, W.A.J. van, A.A.M. Holtslag, and D.P.J. Swart, 1994: A Comparison of ABL heights inferred routinely from LIDAR and radiosondes at noon. *Bound.-Layer Meteor.*, **68**, 173-191.

Rama Krishna, T.V.B.P.S., M. Sharan, and Aditi, 2003: Mean structure of the Nocturnal Boundary-layer under Strong and Weak Wind Conditions: EPRI Case Study. *J. Appl. Meteor.* **42**, 952-969.

ReVelle, D.O., 1993: Chaos and "bursting" in the planetary boundary-layer. *J. Appl. Meteor.* **32**, 1169-1180.

Rodgers, C.D., 1967: The use of emissivity in atmospheric radiation calculation. *Quart. J. Roy. Meteor. Soc.*, **93**, 43-54.

Ronda, R.J., and H.A.R de Bruin, 1999: A Note on the Concept of 'Effective' Bulk Exchange Coefficients for Determination of Surface Flux Densities, *Bound.-Layer Meteor.*, **93**, 155-162.

Rontu, L., 2006: A study on parameterization of orography-related momentum fluxes in a synoptic-scale NWP model. *Tellus*, **58A**, 69-81.

Rooy, W.C. de, and A.A.M. Holtslag, 1999: Estimation of surface radiation and energy flux densities from single-level weather data. *J. Appl. Meteor.*, **38**, 526-540.

Salmond, J.A., and I.G. McKendry, 2005: A review of turbulence in the very stable boundary layer and its implications for air quality. *Progress in Phys. Geography*, **29**, 171-188.

Savijärvi, 1990: Fast radiation parameterization schemes for mesoscale and short-range forecast models. *J. Appl. Meteor.*, **29**, 437-447.

Savijärvi H., and J. Kauhanen, 2001: High resolution numerical simulations of temporal and vertical variability in the stable wintertime boreal boundary layer: a case study. *Theor. and Appl. Clim.*, **70**, 97-1003.

Seibert, P., F. Beyrich, S.E. Gryning, S. Joffre, A. Rasmussen, and P. Tercier, 2000: Review and intercomparison of operational methods for the determination of the mixing height. *Atmos. Environ.*, **34**, 1001-1027.

Sharan, M., and S.G. Gopalakrishnan, 1997: Comparative Evaluation of Eddy Exchange coefficients for strong and weak wind stable boundary layer modeling. *J. Appl. Meteor.*, **36**, 545-559.

Sharan, M., T.V.B.P.S Rama Krishna, and Aditi, 2003: Surface-Layer characteristics in the stable boundary layer with strong and weak winds. *Bound.-Layer Meteor.*, **108**, 257-288.

Shutts, G. J., 1995: Gravity-wave parameterization over complex terrain: The effect of critical level absorption in directional wind shear. *Quart. J. Roy. Meteor. Soc.*, **121**, 1005-1021.

Skibin, D., and J.A. Businger, 1985: The vertical extent of the log-linear wind profile under stable stratification. *Atmos. Environ.*, **19**, 27-30.

Song, J., K. Liao, R.L. Coulter, and B. M. Lesht, 2005: Climatology of the Low-Level Jet at the Southern Great Plains Atmospheric Boundary Layer Experiments Site. *J. Appl. Meteor.*, **44**, 1593-1606.

Sorteberg, A., 2002: *The sensitivity of inversion strength to the formulation of the non-dimensional momentum and heat profiles*, Norwegian Meteorological Institute, Oslo, Norway, 61 pp.

Steeneveld, G.J., B.J.H. van de Wiel, and A.A.M. Holtslag, 2004: Modelling the evolution of the nocturnal boundary-layer for three different nights in CASES-99, *16th Symposium on Boundary-layer and Turbulence*, Portland, Maine, U.S.A., 9-13 Aug. 2004, Amer. Meteorol. Soc., Boston, p 4.3

Steeneveld, G.J., A.A.M. Holtslag, and H.A.R. de Bruin, 2005: Fluxes and gradients in the convective surface layer and the possible role of boundary-layer depth and entrainment flux. *Bound.-Layer Meteor.*, **116**, 237-252.

Steeneveld, G.J., B.J.H. van de Wiel, and A.A.M. Holtslag, 2006a: Modelling the Arctic nocturnal stable boundary layer and its coupling to the surface. *Bound.-Layer Meteor.*, **118**, 357-378.

Steeneveld, G.J., B.J.H. van de Wiel, and A.A.M. Holtslag, 2006b: Modeling the evolution of the atmospheric boundary layer for three contrasting nights in CASES-99. *J. Atmos. Sci.*, **63**, 920-935.

Steeneveld, G.J., B.J.H. van de Wiel, and A.A.M. Holtslag, 2007: Diagnostic Equations for the stable boundary layer height: evaluation and dimensional analysis, *J. Appl. Meteor. Clim.,* **46**, 212-225.

Stull, R.B., 1983: A heat-flux history length scale for the nocturnal boundary layer, *Tellus*, **35A**, 219-230.

Stull, R.B, 1988: *An Introduction to Boundary-layer Meteorology*, Kluwer Academic Publishers, Dordrecht, 666 pp.

Stull, R.B, 2000: Meteorology for Scientists and Engineers, 2nd Edition, *Brooks/Cole Thomson*, Pacific Grove, USA, 502 pp.

Sun, J., D.H. Lenschow, S.P. Burns, R.M. Banta, R.K. Newsom, R. Coulter, S. Frasier, T. Ince, C. Nappo, B.B. Balsey, M. Jensen, L. Mahrt, D. Millar, and B. Skelly, 2003a: At-

mospheric disturbances that generate intermittent turbulence in nocturnal boundary layers. *Bound.-Layer Meteor.*, **110**, 255-279.

Sun, J., S.P. Burns, A.C. Delany, S.P Oncley, T.W. Horst, and D. H. Lenschow, 2003b: Heat balance in the nocturnal boundary layer during CASES-99. *J. Appl. Meteor.*, **42**, 1649-1666.

Svensson, G., and A.A.M. Holtslag, 2006: Single column modeling of the diurnal cycle based on CASES99 data - GABLS second intercomparison project, *17th Symposium of Boundary layers and Turbulence*, 22-25 may 2006, San Diego, U.S.A. American Meteor. Soc. Boston, P8.1.

Teixeira, J., and P.M.A. Miranda, 2001: Fog prediction at Lisbon Airport using a one-dimensional boundary layer model. *Meteor. Appl.*, **8**, 497-505.

Tijm, A.B.C., 2004: Tuning CBR. *HIRLAM newsletter,* **46**, 18-28.

Tjemkes, S.A., 1988: *Radiative Cooling in the Nocturnal Boundary Layer*, PhD thesis, Wageningen University, Wageningen, The Netherlands, 107 pp.

Tjemkes, S.A., and P.G. Duynkerke, 1989: The nocturnal boundary layer: model calculations compared with observations. *J. Appl. Meteor.*, **28**, 161-175.

Tjernstrom, M., M. Zagar, and G. Svensson, 2004: Model simulations of the arctic atmospheric boundary layer from the SHEBA year. *Ambio: A Journal of the Human Environment*, **33**, 221-227.

Troen, I.B., and L. Mahrt, 1986: A simple model of the atmospheric boundary layer; sensitivity to surface evaporation. *Bound.-Layer Meteor.*, **37**, 129-148.

Ulden, A. P. van, and J. Wieringa, 1996: Atmospheric boundary layer research at Cabauw. *Bound.-Layer Meteor.*, **78**, 39-69.

Undén, P., and many co-authors., 2002: *HIRLAM-5 Scientific Documentation*, HIRLAM-5 Project, c/o Per Unden SMHI, S 601 76 Norrkoping, Sweden.

Venkatram, A., 1980: Estimating the Monin-Obukhov length in the stable boundary layer for dispersion calculations. *Bound.-Layer Meteor.* **19**, 481-485.

Vickers, D., and L. Mahrt, 2004: Evaluating formulations of the stable boundary layer height. *J. Appl. Meteor.*, **43**, 1736-1749.

Vilà-Guerau de Arellano, J., Vellinga, O.S., Holtslag, A.A.M., Bosveld, F.C., and H. Klein Baltink, 2001: Observational evaluation of PBL parameterization modeled by MM5, *11th PSU/NCAR Mesoscale Model Workshop Users's workshop, 25-27 June Boulder, Colorado,* 102-104.

Viterbo, P., and A.C.M. Beljaars, 1995: An improved land surface parameterization in the ECMWF model and its validation. *J. Climate*, **8,** 2716-2748.

Viterbo, P., Beljaars, A., Mahfouf, J.F., and Teixeira, J., 1999: The representation of soil moisture freezing and its impact on the stable boundary-layer. *Quart. J. Roy. Meteor. Soc.,* **125**, 2401-2426.

Vogelezang, D.H.P., and A.A.M. Holtslag, 1996: Evaluation and model impacts of alternative boundary-layer height formulations. *Bound.-Layer Meteor.*, **81**, 245-269.

Welch, R.M., M.G. Ravichandran, and S.K. Cox, 1986: Prediction of quasi-periodic oscilla-tions in radiation fogs. Part I: Comparison of simple similarity approaches. *J. Atmos. Sci.* **43**, 633-651.

Wiel, B.J.H van de, 2002: Intermittent turbulence and oscillations in the stable boundary layer over land, PhD thesis, Wageningen University, Wageningen, 129p.

Wiel, B.J.H. van de, A.F. Moene, and G.J. Steeneveld, 2004: Stable Boundary Layer Decoup-ling: Towards a Linear Stability Analysis, *16th Symposium on Boundary-layer and Turbu-lence*, Portland, Maine, U.S.A., 9-13 Aug. 2004, Amer. Meteorol. Soc., Boston, p. 4.18.

Wiel, B.J.H. van de, R.J. Ronda, A.F. Moene, H.A.R. de Bruin, and A.A.M. Holtslag, 2002a: Intermittent turbulence and oscillations in the stable boundary-layer over land. Part I: A bulk model, *J. Atmos. Sci.* **59**, 942-958.

Wiel, B.J.H. van de, A.F. Moene, R.J. Ronda, H.A.R. de Bruin, and A.A.M. Holtslag, 2002b: Intermittent turbulence and oscillations in the stable boundary-layer over land. Part II: A system dynamics approach. *J. Atmos. Sci.*, **59**, 2567-2581.

Wiel, B.J.H. van de, A.F. Moene, O.K. Hartogensis, H.A.R. de Bruin, and A.A.M. Holtslag, 2003: Intermittent turbulence and oscillations in the stable boundary-layer over land. Part III: a classification for observations during CASES99. *J. Atmos. Sci.*, **60,** 2509-2522.

Wiel, B.J.H van de, A.F. Moene, G.J. Steeneveld, O.K. Hartogensis, and A.A.M. Holtslag, 2007: Predicting the Collapse of Turbulence in Stably Stratified Boundary Layers. *Flow Turb. Comb.*, accepted.

Wijk, W. R. van, and D. A. de Vries, 1963: Periodic temperature variations. *Physics of Plant Environment,* W. R. van Wijk, Ed., Interscience, pp. 133-138.

Willmott, C.J., 1982: Some Comments on the Evaluation of Model Performance. *Bull. Amer. Meteor. Soc.*, **63**, 1309-1313.

Wood, N., and P.J. Mason, 1993: The pressure force induced by neutral, turbulent flow over hills. *Quart. J. Roy. Meteor. Soc.*, **119**, 1233-1267.

Wyngaard, J., 1985: Structure of the Planetary Boundary Layer and Implications for its Mod-eling. *J. Clim. Appl. Meteor.*, **24**, 1131-1142.

Yagüe, C., and J.M. Redondo, 1995: A case study of turbulent parameters during the Antarc-tic winter. *Antarctic Sci.*, **7**, 421-433.

Yamada, T., 1979: Prediction of the nocturnal surface inversion height. *J. Appl. Meteor.*, **18**, 526-531.

Young, G. S., and R. A. Pielke, 1983: Application of Terrain Height Variance Spectra to Mesoscale Modeling, *J. Atmos. Sci.*, **40**, 2555-2560.

Yu, T.W., 1978: Determining height of the Nocturnal Boundary Layer. *J. Appl. Meteor.*, **17**, 28-33.

Zehnder, J.A., 2002: Simple modifications to improve fifth-generation Pennsylvania state university-national center for atmospheric research mesoscale model performance for the Phoenix, Arizona, metropolitan area. *J. Appl. Meteor.*, **41**, 971-979.

Zhang, D.L., and W.Z. Zheng, 2004: Diurnal Cycles of Surface Winds and Temperatures as Simulated by Five Boundary Layer Parameterizations. *J. Appl. Meteor.*, **43**, 157-169.

Zhong, S., J. D. Fast, and X. Bian, 1996: A case study of the Great Plains low-level jet using wind profiler network data and a high-resolution mesoscale model. *Mon. Wea. Rev.*, **124**, 785-806.

Zhong, S., and J. D. Fast, 2003: An evaluation of MM5, RAMS, and Meso Eta at sub-kilometer resolution using the VTMX field campaign data in the Salt Lake Valley. *Mon. Wea. Rev.*, **131**, 1301-1322.

Zilitinkevich, S.S., 1972: On the determination of the height of the Ekman Boundary Layer. *Bound.-Layer Meteor.*, **3**, 141-145.

Zilitinkevich, 2002: Third-order transport due to internal waves and non-local turbulence in the stably stratified surface layer. *Quart. J. Roy. Meteor. Soc.*, **128**, 913-925.

Zilitinkevich S.S., and D.V. Mironov, 1996: A multi-limit formulation for the equilibrium height of a stably stratified boundary layer. *Bound.-Layer Meteor.*, **81**, 325-351.

Zilitinkevitch, S.S., and P. Calanca, 2000: An extended similarity theory for the stably stratified atmospheric surface layer. *Quart. J. R. Met. Soc.*, **126**, 1913-1923.

Zilitinkevich, S.S., and A. Baklanov, 2002: Calculation of the height of the stable boundary layer in practical applications. *Bound.-Layer Meteor.*, **105**, 389-409.

Zilitinkevich, S.S., and I.N. Esau, 2003: The effect of baroclinicity on the equilibrium depth of the neutral and stable planetary boundary layers. *Quart. J. Roy. Meteor. Soc.*, **129**, 3339-3356.

Zilitinkevich, S.S., V.L. Perov, and J.C. King, 2002: Near-surface turbulent fluxes in stable stratification: Calculation techniques for use in general circulation models. *Quart. J. Roy. Meteor. Soc.*, **128**, 1571-1587.

Zilitinkevich, S.S., A. Baklanov, J. Rost, A.S. Smedman, V. Lykosov, and P. Calanca, 2002: Diagnostic and prognostic equations for the height of the stably stratified Ekman boundary layer. *Quart. J. Roy. Meteor. Soc.*, **128**, 25-46.

Samenvatting

Dit proefschrift gaat over het begrijpen en het modelleren van de nachtelijke stabiele grenslaag boven land. Een stabiele grenslaag treedt op als de potentiële temperatuur toeneemt met de hoogte. Dit gebeurt veelal 's nachts, en boven polaire gebieden in de winter. De motivatie voor het onderzoek is ontstaan uit het feit dat weersverwachting- en klimaatmodellen grote systematische fouten maken voor stabiele omstandigheden, zonder dat goed is begrepen waarom. Een belangrijke oorzaak van deze slechte representatie van de stabiele grenslaag is dat veel verschillende fysische processen een rol spelen. De belangrijkste relevante processen zijn turbulente menging, stralingstransport, de koppeling met het landoppervlak en onderliggende bodem, zwaartekrachtsgolven, effecten van heterogeniteit van landgebruik, barocliniciteit, het nachtelijk windmaximum, en eventueel mist. Al deze processen en hun onderlinge interacties moeten door modellen goed beschreven worden om een betrouwbare verwachting te krijgen. In het algemeen gebruiken deze modellen nu meer turbulente menging dan mag worden gebaseerd op locale turbulentiewaarnemingen. Daarnaast tonen deze modellen een sterke gevoeligheid voor kleinere verandering in de beschrijving van de turbulente menging. Omdat de stabiele grenslaag een dunne laag is (typisch 100-200 m), en weermodellen maar beperkte verticale resolutie hebben is het oplossend vermogen van dergelijke modellen beperkt m.b.t. de stabiele grenslaag. Dit alles brengt grote onzekerheden met zich mee omtrent weersverwachtingen voor de minimumtemperatuur, mist, nachtvorst, en voor klimaatprojecties en toepassingen in verspreidingsmodellen.

Om stabiele grenslagen beter te begrijpen en haar modellering te verbeteren worden in dit proefschrift kortweg de volgende vragen aan de orde gesteld:

1. Wat is de rol van de koppeling met het landoppervlak op de stabiele grenslaag.
2. Kan de stabiele grenslaag locaal goed worden gemodelleerd indien alle relevante processen worden meegenomen en hoge resolutie wordt gebruikt.
3. Zijn orografisch gegenereerde zwaartekrachtsgolven een mogelijke verklaring voor de benodigde extra wrijving grootschalige modellen
4. Is een robuuste en verbeterde formulering voor de dikte van stabiele grenslaag mogelijk?

Grofweg bestrijkt het proefschrift drie paden. Het eerste pad wordt gevormd door een drietal modelstudies met een kolomsmodel. Het tweede pad bestaat uit een aantal studies over de 3D aspecten van het modelleren van de stabiele grenslaag. Als laatste worden formuleringen van de stabiele grenslaaghoogte geëvalueerd en verbeterd.

Hoofdstuk 2 bouwt voort op de 1e GABLS modelvergelijkingsstudie, waarin modeluitkomsten van een reeks kolomsmodellen onderling worden vergelijken voor een matig stabiele grenslaag met voorgeschreven koeling. Echter, een voorgeschreven koeling is geen realisti-

sche randvoorwaarde voor de stabiele grenslaag. In werkelijkheid is de grenslaag direct ge-koppeld aan het landoppervlak, zodat een compenserende warmtestroom uit de bodem wordt meegenomen. Een gevoeligheidsstudie laat zien dat de structuur, diepte en geïntegreerde koe-ling sterk afhangt van de mate van koppeling met het landoppervlak. De vraag rijst nu hoe ge-voelig de resultaten zijn voor model resolutie, zowel in de bodem als in de atmosfeer, en aan welk proces (bodem of atmosfeer) de meeste rekencapaciteit moet worden gealloceerd. De stabiele grenslaag blijkt sterk gevoelig voor de gekozen resolutie in de bodem. Effecten van te grove resolutie in de bodem lijken gecompenseerd te kunnen worden door extra turbulente menging. Daarnaast wordt in dit hoofdstuk de lengteschaalformulering voor turbulente men-ging vergeleken met een ensemble van Large Eddy Simulatie uikomsten. Het blijkt dat de structuur van de grenslaag beter voorspeld wordt als naast de hoogte z ook een lengteschaal wordt meegenomen die de locale eigenschappen van de turbulente stroming beschrijft, bij-voorbeeld u_*/N.

Hoofdstuk 3 behandelt een processtudie waarin een serie van 3 dagelijkse gangen die sterk verschillen in de mate van mechanische forcering (wind) gemodelleerd wordt met een kolom-smodel op hoge resolutie. De nachten zijn respectievelijk intermittent turbulent, volledig tur-bulent en niet turbulent en zijn geselecteerd uit de CASES-99 meetcampagne boven prairie grasland in Kansas (U.S.A.). Het doel van de studie is te begrijpen of we locaal (dus gegeven de locaal gemeten bodemruwheid, bodem- en vegetatie-eigenschappen, geostrofische wind, en de advectie termen) de stabiele grenslaag voldoende nauwkeurig kunnen modelleren als we geen restricties aan resolutie opleggen, en toch alle fysisch relevante processen, zoals turbu-lente menging, stralingsdivergentie en de interactie met het landoppervlak meenemen. Het blijkt dat zowel de verticale structuur en de oppervlaktefluxen zeer nauwkeurig kunnen wor-den gesimuleerd (mede ook door de hoge kwaliteit van de waarnemingen). Aspecten die niet nauwkeurig konden worden gesimuleerd zijn het intermittent gedrag van de turbulentie, en het nachtelijk windmaximum.

In hoofdstuk 4 vertalen we de kennis uit hoofdstuk 3 van een kolomsmodel naar een aantal driedimensionale modellen voor dezelfde case studie. Tevens wordt het werk binnen de GABLS context uitgebreid naar driedimensionale modellen. De veelgebruikte mesoschaal-modellen MM5, HIRLAM (KNMI) en COAMPS worden vergeleken met observaties voor verschillende typen nachten. Verder zoeken we welke systematische fouten deze modellen gemeen hebben, en onder welke atmosferische omstandigheden deze optreden. In het alge-meen tonen deze modellen een onderschatting van de oppervlaktekoeling, van de dagelijkse gang van temperatuur en windsnelheid, en van de stabiele grenslaagdikte. Daarnaast hebben alle modellen problemen met het forecasten van de low-level jet. Een voldoende groot reken-domein is noodzakelijk voor een goede representatie van de locale barocliniciteit en het bijbe-horende het nachtelijk windmaximum. Oppervlaktelaagschema's die voorzien zijn van een vegetatielaag zijn aanzienlijk in het voordeel bij het voorspellen van de minimumtemperatuur.

Dit geldt ook het enige model met een lengteschaal op basis van locale turbulente eigenschappen ($\sqrt{TKE}/N$ in HIRLAM). Een additionele gevoeligheidsstudie met diverse stralingsschema's gaf tot 6 K verschil in minimumtemperatuur in nachten zonder wind. Uiteindelijk laten we zien dat aanzienlijke verbetering voor de verwachting van de minimumtemperatuur mogelijk is door het invoeren van een realistische formulering van de bodemwarmtestroom, de vegetatielaag en turbulente menging op basis van locale schaling.

Hoofdstuk 5 behandelt de wrijving op de stabiele grenslaag veroorzaakt door kleinschalige orografie. Hoofdstuk 3 heeft laten zien dat de stabiele grenslaag vanuit het locaal perspectief redelijk goed kan worden gemodelleerd, voor contrasterende windregimes. De vraag rijst nu waarom grootschalige weermodellen veel meer turbulente wrijving nodig hebben, dan op grond van locale turbulente metingen mag worden verwacht. Zonder deze extra wrijving worden depressies te diep. In dit hoofdstuk onderzoeken we de potentiële rol van orografisch geforceerde wrijving op de stabiele grenslaag. Weermodellen houden nu alleen rekening met grootschalige orografie zoals gebergtes. Eerste orde schattingen op basis van schalingsargumenten van orografische wrijving blijken voor zeer stabiele omstandigheden het verschil tussen de benodigde en gerechtvaardigde wrijving te kunnen verklaren voor het CASES-99 terrein. Het bijtellen van de divergentie van deze wrijving over de stabiele grenslaag geeft een realistisch wind- en temperatuurprofiel, en meer belangrijk, ook een voldoende crossisobarische stroming.

In hoofdstuk 6 wordt onderzocht wat de respons van de stabiele grenslaag is op het toevoegen van CO_2 in de atmosfeer. Dit onderzoek draagt bij aan de discussie of het warmteeiland effect van steden invloed heeft op de waargenomen temperatuursstijging in langjarige temperatuurobservaties. Analyse hiervan gaf aan dat de temperatuursstijging onafhankelijk is van de windsnelheid. Anderzijds is dit vreemd omdat de stabiele grenslaag structuur erg verschilt voor windstille en winderige condities. Klimaatsceptici grijpen dit aan om de zuiverheid van de waarnemingen in twijfel te trekken. De modelstudie in dit hoofdstuk geeft inderdaad aan dat de temperatuursstijging door interne feedbacks onafhankelijk is van de windsnelheid.

De laatste 2 hoofdstukken van het proefschrift hebben betrekking op het voorspellen van de stabiele grenslaagdikte. Voor tal van toepassingen (met name voor verspreidingsmodellen voor luchtkwaliteit) is er behoefte aan een robuuste beschrijving van de stabiele grenslaagdikte, zonder radiosondes te hoeven oplaten. In hoofdstuk 7 evalueren we een aantal formules voor de stabiele grenslaagdikte tegen waarnemingen uit een brede range van landgebruik, bodemruwheid, breedtegraad. Vele van deze beschrijvingen (hoewel gestoeld op theorie) werken niet goed, met name voor dunne grenslagen (en dus hoge concentraties van verontreinigingen). Door gebruik te maken van dimensie-analyse van de relevante grootheden, konden re relevante dimensieloze groepen aan elkaar worden gerelateerd. Dit leverde een uitdrukking voor de stabiele grenslaagdikte die zich robuust gedraagt voor een meerdere observaties.

Daarnaast wordt de relevantie van de Coriolisparameter voor de stabiele grenslaagdikte be-studeerd. Zowel uit een principal component analysis als dimensie-analyse blijkt dat de Corio-lisparameter geen vereiste parameter is om de stabiele grenslaagdikte in de praktijk te be-schrijven.

Hoofdstuk 8 bouwt voort op hoofdstuk 7 waarin wederom de stabiele grenslaagdikte centraal staat. Eerder werk baseerde de stabiele grenslaaghoogte als een gewogen interpolatie van lengteschalen die drie prototype grenslagen representeren: de nachtelijke grenslaag, de geheel neutrale grenslaag en de conventioneel neutrale grenslaag. In dit hoofdstuk becommentariëren we dit werk, en stellen we dat als deze effecten van verschillende grenslaagtypes inderdaad tegelijkertijd samenwerken, beter de bulk eddy-diffusiviteit kan worden geïnterpoleerd dan de individueel resulterende lengteschalen. Dit geeft een alternatieve uitdrukking voor de stabiele grenslaagdikte die zich beter laat vergelijken met observaties dan het oorspronkelijke werk.

Curriculum Vitae

Gerard Johannes (Gert-Jan) Steeneveld werd geboren op 25 juni 1978 te Delft tijdens de door Nederland verloren WK-voetbal finale tegen Argentinië. Na de basisschool doorliep hij 2 jaar MAVO, 3 jaar HAVO en 2 jaar VWO (cum laude) op Scholengemeenschap College 't Loo te Pijnacker en Voorburg. In 1997 begon hij aan de studie Bodem, Water en Atmosfeer aan de toenmalige Landbouwuniversiteit Wageningen. Aanvankelijk lag zijn interesse vooral bij de synoptische meteorologie, maar de colleges micrometeorologie (Henk de Bruin), grenslaag-meteorologie, en het veldpracticum brachten daar flink verandering in. Een afstudeervak bij prof. Bert Holtslag over convectieve grenslaagschaling volgde. Daarna bracht een stage over het modelleren van de uitwisseling door bossen van warmte, vocht en CO_2 met een plantfysiologische methode hem in 2001 naar het KNMI (prof. Bart van den Hurk). Na een afstudeervak (onder begeleiding van Jordi Vilà en Bas van de Wiel) waarin de kwaliteit van het weermodel MM5 voor nachtelijke omstandigheden werd geëvalueerd, behaalde hij het BWA diploma (cum laude) in 2002. Direct aansluitend hierop startte hij het promotie onderzoek, wederom over het modelleren van nachtelijke stabiele grenslagen. Een belangrijk onderdeel hiervan is de samenwerking binnen GABLS (GEWEX Atmospheric Boundary Layer Study) modelvergelijkingsexperiment, in het kader waarvan een werkbezoek aan Stockholm Universiteit werd afgelegd. Na deze PhD studie wordt het grenslaagwerk gecontinueerd in een Post-Doc positie op het gebied van grenslaagmodellering.

Publications

Peer-reviewed

Steeneveld, G.J., A.A.M. Holtslag, and H.A.R. de Bruin, 2005: Fluxes and gradients in the convective surface layer and the possible role of the boundary-layer depth and entrainment flux, *Bound.-Layer Meteor.*, **116**, 237-252.

Cuxart, J., Holtslag, A.A.M., Beare, R.J., Bazile, E., Beljaars, A.C.M., Cheng, A., Conangla, L., Ek, M., Freedman, F., Hamdi, R., Kerstein, A., Kitagawa, H., Lenderink, G., Lewellen, D., Mailhot, J., Mauritsen, T., Perov, V., Schayes, G., Steeneveld, G.J., Svensson, G., Taylor, P.A., Weng, W., Wunsch, S., and Xu, K-M., 2006: A single-column model intercomparison for a stably stratified atmospheric boundary layer, *Bound.-Layer Meteor.,* **118**, 273-303.

Steeneveld, G.J., B.J.H. van de Wiel, and A.A.M. Holtslag, 2006: Modelling the Arctic stable boundary layer and its coupling to the surface, *Bound.-Layer Meteor.*, **118**, 357-378.

Steeneveld, G.J., B.J.H. van de Wiel, and A.AM. Holtslag, 2006: Modelling the evolution of the nocturnal boundary-layer coupled to the land surface for three contrasting nights in CASES-99, *J. Atmos. Sci.*, **63**, 920-935.

Baas, P., G.J. Steeneveld, B.J.H. van de Wiel, and A.A.M. Holtslag, 2006: Exploring self-correlation in flux-gradient relationships for stably stratified conditions, *J. Atmos Sci.*, **63**, 3045-3054.

Steeneveld, G.J., B.J.H. van de Wiel, A.AM. Holtslag, 2007: Diagnostic Equations for the stable boundary layer height: evaluation and dimensional analysis, *J. Appl. Meteor. Clim.*, **46**, 212-225.

Steeneveld, G.J., B.J.H. van de Wiel, and A.A.M. Holtslag, 2007: Comments on deriving the equilibrium height of the stable boundary layer, *Quart. J. Roy. Meteor. Soc.*, **133**, 261-264.

Van de Wiel, B.J.H, A.F. Moene, G.J. Steeneveld, O.K. Hartogensis and A.A.M. Holtslag, 2007: Predicting the Collapse of Turbulence in Stably Stratified Boundary Layers, *Flow, Turbulence, and Combustion*, accepted.

Steeneveld, G.J., T. Mauritsen, E.I.F. de Bruijn, J. Vilà-Guerau de Arellano, G. Svensson, and A.A.M. Holtslag, 2007: Evaluation of limited area models for the representation of the diurnal cycle and contrasting nights in CASES-99, *J. Appl. Meteor. Clim.*, accepted

Holtslag, A.A.M., G.J. Steeneveld, and B.J.H. van de Wiel, 2007: Role of land-surface feedback on model performance for the stable boundary layer. *Bound.-Layer Meteor.*, accepted.

Steeneveld, G.J., A.A.M. Holtslag, C.J. Nappo, B.J.H. van de Wiel, and L. Mahrt, 2007: Exploring the possible role of small scale gravity wave drag on stable boundary layers over land, *J. Appl. Meteor. Clim.*, submitted.

Steeneveld, G.J., and A.A.M. Holtslag, 2007: On land surface temperature trends in calm and windy nights, in preparation.

Popular Scientific

Steeneveld, Gert-Jan, Bas van de Wiel, Jordi Vilà-Guerau de Arellano en Bert Holtslag, 2003: 'In het holst van de nacht…, Evaluatie van een mesoschaalmodel voor de stabiele grenslaag boven land', *Meteorologica*, **12** (2), 14-20. (In Dutch).

Steeneveld, G.J, D. van As, S. Houweling, Y. Meijer, H. Moolenaar, C. von Randow, C. Reijmer, S. de Roode, 2004: Atmosferisch onderzoek in Nederland, een samenvatting van het Buys Ballot symposium 2004, *Meteorologica*, **13**(4), 27-30 (in Dutch).

Holtslag, A.A.M., G.J. Steeneveld, A.F. Moene and B.J.H van de Wiel, 2005: Turbulente nachten in het klimaat, *Meteorologica*, **14**(1), 10-13 (in Dutch).

Steeneveld, G.J., B.J.H van de Wiel and A.A.M. Holtslag, 2005: Recordnacht: mist laat model in de kou staan, *Meteorologica*, **14**(2), 33-36 (in Dutch).

Gert-Jan Steeneveld , Simon Axelsen, Remco van de Beek, Willem-Jan van de Berg, Bastiaan van Diedenhoven, Monica Górska, Mxolisi Shongwe, Hidde Leijnse, Sjoukje Philip, Holger Tost, Bas van de Wiel, 2005: Nederlands onderzoek naar weer en klimaat: een selectie van het Buys Ballot symposium 2005, *Meteorologica*, **14** (4), 19-22 (in Dutch).

Jules Beersma, Willem Jan van de Berg, Jeroen Derksen, Peter Kuipers Munneke, Jennifer Mathies, Aart Overeem, Gerben Pieterse, Joel Schröter, Ivan Vigano, Nicolette Vis-Star and Gert-Jan Steeneveld, 2007: Het Buys Ballot symposium 2006, *Meteorologica*, **16** (1), 13-17 (in Dutch).

Buys-Ballot Research School Education Statement Form

Review of Literature

Nieuwstadt, F.T.M., 1998: *Turbulentie, inleiding in de theorie en toepassingen van turbulente stromingen*, Epsilon Uitgaven, Utrecht, 211 pp.

Nappo, C.J., 2002: *An Introduction to Atmospheric Gravity Waves*, Academic press, London, 276 pp.

Oke, T. R., 1978: *Boundary Layer Climates.* Methuen and Co., London, 372 pp.

Post Graduate Courses

June 2003	*Techniques for writing and presenting a scientific paper*, prof. M. Grossmann, PHLO, Wageningen.
June 2003	*Mathematical techniques and tools for data analysis and modelling of intermittent structures*, prof. F.T.M. Nieuwstadt, Lorentz Centre, Leiden, The Netherlands.
Oct 2003	*Advising and organizing a MSc thesis*, Education Support Wageningen University, Wageningen, The Netherlands.
Feb 2004	*Spatial Statistics*, Wageningen University, The Netherlands.
Mar 2004	*Parameterisation of diabatic processes,* European Centre for Medium Range Weather Forecasts (ECMWF), Reading, United Kingdom.
July 2004	*Environmental Stably Stratified Flows,* International Centre for Mechanical Sciences (CISM), Udine, Italy.
Jan. 2005	*Oral lecturing*, Education Support Wageningen University, Wageningen, The Netherlands.
Feb 2005	Large Eddy Simulation course, intern course at Wageningen University.
June 2005	*Summer school on Boundary Layers over complex and vegetated terrain,* Finnish Meteorological Institute, Sodankyla, Finland.

International Symposia, Workshops and Conferences

GEWEX-GABLS Workshop on Stable Boundary Layers, Mallorca, *Spain*, 20-25 September 2003.

16th Symposium on Boundary Layers and Turbulence, Portland, Maine, *USA,* 9-13 August 2004, American Meteorological Society.

4th Annual Meeting of the European Meteorological Society, Nice*, France,* 26-30 September 2004.

5th Annual Meeting of the European Meteorological Society, Utrecht*, The Netherlands,* 12-16 September 2005.

6th Annual Meeting of the European Meteorological Society, Lubljana*, Slovenia,* 4-8 September 2006.

GLASS-GABLS workshop on local land-atmosphere coupling, De Bilt, *The Netherlands*, 19-21 September 2005

17th Conference on Boundary Layers and Turbulence, San Diego, California, *USA*, 22-25 May 2006, American Meteorological Society.

7th Annual Meeting of the European Meteorological Society, Madrid*, Spain,* 1-5 October 2007.

Dustconf 2007, Maastricht, *The Netherlands*, 23-24 April 2007.

GEWEX-GABLS Workshop on Stable Boundary Layers, Stockholm, *Sweden*, 19-21 June 2007.

**Buys Ballot Research School Meetings and Seminars**

BBOS autumn symposia 2002-2006
BBOS spring symposium 2004, "History and Future of Climate Observations", 12 May 2006
BBOS spring symposium 2006, "Gas What!!", 27 April 2006
Organisation BBOS spring symposium 2007, "Another one bites the dust?", 10 May 2007
BBOS boundary-layer workshop, 24 September 2004, KNMI, De Bilt.
BBOS boundary-layer workshop, 21 November 2005, Wageningen Univ., Wageningen.

Buys Ballot Research School
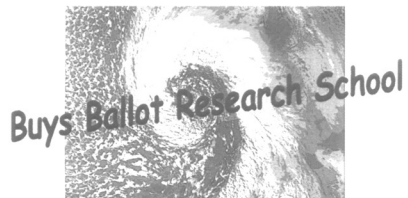
A school for the study of fundamental processes in the climate system

Director:	Prof. dr. ir. J. D. Opsteegh
Address:	IMAU, Princetonplein 5, 3584 CC Utrecht, The Netherlands
Telephone:	+31 30 253 3275
Email:	IMAU@phys.uu.nl
Web site:	http://www.phys.uu.nl/~wwwimau/education/bbos/home.html

Utrecht, 14 juni 2007

Beste Gert-Jan,

Hiermee verklaar ik dat jij in de afgelopen vier jaar met goed gevolg het opleidingsprogramma van de Buys Ballot Onderzoekschool behorende bij het promotietraject hebt doorlopen. Je kunt tot de verdediging van het proefschrift worden toegelaten.

Vriendelijke groet,

Prof. Dr. J.D. Opsteegh,
directeur Buys Ballot Onderzoekschool

members	Institute for Marine and Atmospheric Research, Utrecht University (penvoerder)
	Department of Meteorology and Air Quality, Wageningen University
associate members	Royal Netherlands Meteorological Institute (KNMI)
	Royal Netherlands Institute for Sea Research (NIOZ)
	Research Group of Atmospheric Physics, Eindhoven University
	National Institute of Public Health and the Environment (RIVM)
	Max-Planck-Institut für Chemie, Mainz

Photo front cover: Wageningen in a fog layer at night, 7 December 1998.